Stony Brook University

Structure-Property Relationships in Polyolefin Blends and Copolymers

A Dissertation Presented

by

Feng Zuo

to

The Graduate School

In Partial Fulfillment of the

Requirements

for the Degree of

Doctor of Philosophy

in

Chemistry

Stony Brook University

August 2009

Stony Brook University

The Graduate School

Feng Zuo

We, the dissertation committee for the above candidate for the
Doctor of Philosophy degree, hereby recommend
acceptance of this dissertation.

Benjamin S. Hsiao, Dissertation Advisor
Professor, Department of Chemistry

Jiangyong Jia, Chairperson of the Defense
Assistant Professor, Department of Chemistry

Benjamin Chu, Third Member
Distinguished Professor, Department of Chemistry

Andy H. Tsou, Outside Member
Section Head, ExxonMobile Research and Enginnering Company

This dissertation is accepted by the Graduate School

Lawrence Martin
Dean of the Graduate School

Abstract of the Dissertation

Structure-Property Relationships in Polyolefin Blends and Copolymers

by

Feng Zuo

Doctor of Philosophy

in

Chemistry

Stony Brook University

2009

Polymers have become the primary materials of mankind since the second half of last century. The annual global production of polymers increases with the increasing world demand, and it has reached to about 200 million metric tons recently. The overwhelming success of polymers is the result of their unique combination of properties, such as light weight, stable, economical, and easy to process. Polyolefins, mainly including polyethylene, polypropylene, and ethylene-α-olefin block and random copolymers, hold more than half of the polymer market due to their versatile applications e.g. packaging films, containers, bags, and molded parts etc. Thus understanding their structure-property relationships is essential for an efficient tailor of polyolefin products to meet specific needs.

Since polyolefins usually can partially crystallize and the crystallization behavior will directly influence the properties of polyolefins in the solid state, studies were carried out using in-situ synchrotron X-ray techniques combined with Linkam shear stage and Instron tensile machine, which were used to observe the structure changes of polyolefins under simulated processing conditions and to evaluate their mechanical performance, respectively. Formation of initial crystallization precursor structure, shish-kebab, and the kinetic and thermodynamic aspects of flow-induced and quiescent crystallization of polyolefins were investigated. This also has many practical implications to industrial polymer processing methods such as extrusion, injection molding and spinning, which involve external flow field. Meanwhile, mechanical properties, such as modulus, strength, elongation, and relaxation, of these polyolefins in the form of films and fibers, crosslinked and non-crosslinked, were obtained as well as the phase behavior and structure development during the uniaxial deformation according to the analysis of wide-angle and small-angle X-ray scattering data. The relationships between different mechanical properties and various structural parameters, for example, chain architecture, block distribution, comonomer content, crystal structure, morphology, and orientation, were revealed.

Table of Contents

List of Tables

List of Figures

Acknowledgements

Foremost, I would like to express my deep gratitude to my advisor Prof. Benjamin S. Hsiao for his wisdom, advice, generous support, and soul-stirring encouragement at all times. More than five years of graduate study under his supervision is an invaluable experience for me. His attitude and assiduity in scientific research is what I should always remember in my future career.

I would also like to thank my committee members, Profs. Benjamin Chu, Jin Wang, Jiangyong Jia, and Dr. Andy H. Tsou, for their time, comments, and suggestions on my way to the Ph.D. degree. Many thanks to my current group members Yimin Mao, Xiaowei Li, Yang Liu, Ran Wang, Xiao Wang, Shifen Han, Lewis Yung, Drs. Christian Burger, Dufei Fang, Hongyang Ma, Lixia Rong, Jie Zhu, Shigeyuki Toki, Jonathan Chiu, and my former group members Nan Li, Drs. Jongkahk Keum, Hongwen Zhou, Xuming Chen, Pranav Nawani, Igors Sics, Rajesh Somani, Ling Yang, Jun Zhang, Fen Wan, Carlos-Alberto Avila-Orta, Michael Gelfer, Lizhi Liu, Shaofeng Ran. I also want to thank our secretary, Jane Wainio, for her great assistance in the past a few years. Special appreciation is given to outside collaborators Prof. Lei Zhu in Case Western and Drs. Hongyu Chen in Dow Chemical, Rossana Iervolino from Italy. In addition, this research would not be possible without the financial support from National Science Foundation and The Dow Chemical Company.

Finally, I would like to thank my wife, my parents, and all other family members and friends for their understanding and endless support, which is the source of energy and powerful backing inspiring me to finish my Ph.D. studies and pursue further achievement.

Chapter 1. Thermal Stability of Shear-Induced Shish-Kebab Precursor Structure from High Molecular Weight Polyethylene Chains

1.1 Introduction

The molecular mechanism, responsible for the formation of the initial crystallization precursor structure (i.e., shish-kebabs) induced by flow prior to the full scale crystallization process in entangled polymer melts, is an important subject, having many practical implications to polymer processing and property manipulation. It is thought that the topological arrangement of the shish-kebab precursors can directly influence the subsequent developments of crystallinity, crystallization rate and morphology [1-7]. However, the subject is still not well understood. Recent studies from different laboratories all indicated that, the high molecular weight species in the molecular weight distribution play an essential role of forming the precursor structure under flow in an entangled and supercooled melt [8-14]. In this study, our goals are thus twofold: (1) to demonstrate that, beyond any doubt, the shish-kebab structure is induced by the high molecular weight chains (even with a rather narrow polydispersity of 1.1) in a bimodal blend of low and high molecular weight polyethylene model samples; (2) to explore the relationship between the thermal stability of the shear-induced shish-kebab structure and the relaxation behavior of deformed entangled high molecular weight chains at varying temperatures.

It is necessary to point out that the current state of theoretical development for the shish-kebab formation in entangled polymer melts under flow is primarily based on the concept of stretch-coil transition for dilute polymer solutions proposed by de Gennes [15].

Keller adopted the stretch-coil transition concept for polymer melts and proposed the existence of a critical orientation molecular weight (M^*) under a particular flow field (e.g. extensional flow) [16-17]. That is, the linear polymer chain having a molecular weight above the M^* value can remain in the stretched state after flow due to its long relaxation time, while shorter chains will relax back to the coiled state due to the corresponding short relaxation time. The critical molecular weight is related to the elongation rate as $\dot{\varepsilon}_c \propto (M^*)^{-\beta}$. Based on this argument, the high molecular weight species, which can remain in the stretched state upon deformation, are mainly responsible for the shish-kebab formation. However, Keller did not rationalize the obvious consequence of the high molecular weight chains, i.e., they possess a large number of chain entanglements. It is very unlikely that the stretch-coil transition can take place at the level of individual chain because multiple steps of chain disentanglement cannot occur under the typical flow conditions. Recently, the simulation work carried out by Muthukumar et al. showed that the shish-kebab structure can be formed by stretched and coiled chains, which co-exist without stable intermediate conformations, in a monodispersed system under flow [18]. Of course, if one considers the scale of chain length for the high molecular weight species, the use of short monodispersed chains in simulation does not reflect the reality. However, if one considers the scenario of chain entanglement, the simulation with monodispersed chains would make perfect sense, as the average chain length between the entanglement points must be, statistically, about the same. Furthermore, if the entangled chains in a supercooled state can be considered as a network structure with slow dynamics, a uniaxial deformation field will induce orientation in the chain segments along the flow direction, resulting in the stretched chain segments between the entanglement points, but it will not affect the chain segments arranged perpendicularly to the flow.

In the literature, the melting behavior of the shish-kebab structure has been investigated quite extensively [19-29]. For example, Keller studied the changes of the shish-kebab structure in polyethylene using transmission electron microscopy (TEM) before, during and after the melting process by rapid quenching or isothermal crystallization [24-26]. When the shish-kebab structure was heated to 130 ^{o}C, some kebabs started to melt and formed beads, while the shish fibril became smooth or blobby. Above 145 ^{o}C, kebabs totally disappeared, evidenced by the disappearance of the corresponding crystal reflections. If the molten sample was quenched, a smooth fiber could be obtained; but if the sample was slowly cooled and crystallized at a lower temperature, the molten beads could restore themselves into kebabs. It appeared that the chains within the melt - hairdressed like fibrils could transform back to the initial shish-kebab structure, and the shish could retain the previous orientation. Petermann et al. also studied the partial melting of the shish-kebab structure of isotactic polystyrene with TEM [27-29]. Their results confirmed the existence of several components in the shish-kebab structure, including the central extended-chain microshish, the partially extended-chain macroshish, the microkebabs, and the overgrown macrokebabs. The macrokebabs that grew on the microkebabs templates were less thermally stable than microkebabs and, upon heating, became segmented and discontinuous; but the shish cores remained intact. It was thought that microkebabs originated from the firmly attached cilia to the shish backbone, having parts intrinsically implanted in the shish. These kebabs had a higher melting temperature and at a high temperature, all kebabs completely melt leaving behind only the more stable extended-chain shish. In fact, they observed that the shish could melt at a temperature beyond the equilibrium temperature of infinitely thick extended-chain crystals. Therefore, they argued that, since some kebabs have many tie chains that resemble micellar type of crystal structure, the hairdressing structure in Keller's model, which only accounts for the folded-chain kebab crystal growth, was incomplete. Upon cooling to lower temperatures, the partially melted kebabs reform again during isothermal crystallization. Although we

do not disagree with the above viewpoints by Keller et al. and Peterman et al., in this study, we have attempted to further understand the molecular mechanism responsible for the thermal stability of the shish-kebab structure in an entangled melt, especially from the viewpoint of the relaxation of a deformed entangled polymer network.

To carry out this study properly, we have chosen a unique bimodal polyethylene blend, containing a very narrowly distributed high molecular weight component ($\overline{M}_w$ = 1,500,000 g/mol, polydispersity = 1.1), termed HMWPE, and a low molecular weight matrix ($\overline{M}_w$ = 53,000 g/mol, polydispersity = 2.2), termed LMWPE. The molecular weight of HMWPE is above the critical orientation molecular weight according to our group's previous work [30-31], while the molecular weight of the LMWPE matrix is definitely below it. In addition, the chosen experimental temperature was such that LMWPE did not crystallize, only HMWPE crystallized. Thus, the bimodal blend was analogous to a dilute polymer solution having a high molecular weight crystallizing component with very slow chain dynamics (or long relaxation times) in a low molecular weight amorphous polymer matrix under the experimental conditions. The formation of the shish-kebab structure in the HMWPE component under shear and the corresponding shish-kebab structure thermal stability, by a thermal cycling method under planar constraints [32], were investigated by *in-situ* rheo-SAXS (small-angle X-ray scattering) and rheo-WAXD (wide-angle X-ray diffraction) techniques with synchrotron radiation. As this study allowed us to follow only the crystallization, melting and relaxation of HMWPE chains, some new insights into the shish-kebab formation under flow and its relationship with the dynamics of entangled melt of high molecular weight chains were obtained.

1.2 Experimental

1.2.1 Materials and Sample Preparation

Two polyethylene samples (LMWPE and HMWPE) were chosen for this study. LMWPE was an experimental polyethylene copolymer ($\overline{M}_w$ = 53,000 g/mol, polydispersity = 2.2), containing 2 mol% of hexane unit, and was provided by the ExxonMobil Research and Engineering Co., Annandale, NJ. The HMWPE sample ($\overline{M}_w$ = 1,500,000 g/mol, polydispersity = 1.1) was purchased from the Chevron Phillips Chemical Company LP, Woodlands, TX. This sample was produced by a fractionation method. The sample information such as molecular weight, molecular weight distribution ($\overline{M}_w / \overline{M}_n$), nominal melting temperature and end melting temperature ($T_{m,end}$ from DSC) are shown in Table 1.1, and their GPC profiles are shown in Figure 1.1. These model samples, all prepared by a metallocene catalyst, were used to prepare the bimodal polyethylene blend. The blend sample had a 2 wt% concentration of the HMWPE, which was higher than the overlap concentration (c*) of HMWPE (c* = 0.35 wt% according to the equation $c^* = \frac{3\overline{M}_w}{4\pi[< R_g^2 >^{1/2}]^3 N_a}$, where $< R_g^2 >^{1/2} / \overline{M}_w{}^{1/2}$ was about 0.46, estimated form the SANS measurement). [33-34]

The polymer blend was prepared by a solution mixing procedure to ensure the intimate blending of different species at the molecular level. The detailed mixing procedures can be found in our previous publication [35]. A control sample of pure LMWPE without the addition of HMWPE was also prepared using the same procedure. Polymer films of about 0.5 mm thickness were prepared by compression molding at 150 ^oC. Samples in the form of a ring (inner diameter = 10 mm, outer diameter = 20 mm) were cut from the melt pressed films for rheo-X-ray measurements.

1.2.2 Instrumentation

A Linkam CSS-450 optical shear stage, modified for *in-situ* rheo-X-ray studies was used to apply controlled shear conditions to the polymer melt. The details of this modified shear apparatus have been described elsewhere [36]. Briefly, the sample was placed in the gap between two X-ray windows (i.e., a diamond window and a Kapton window) and completely enclosed in cavity of the measuring cell. WAXD and SAXS measurements were carried out at the X27C beamline in the National Synchrotron Light Source (NSLS), Brookhaven National Laboratory (BNL). The wavelength of the synchrotron radiation was 1.371 Å. 2D SAXS/WAXD patterns were collected by MAR CCD X-ray detector (MAR-USA), which had a resolution of 1024×1024 pixels (pixel size = 158.44 μm). For SAXS measurements, the sample-to-detector distance was 2014 mm and the scattering angle was calibrated by silver behenate (AgBe); for WAXD measurements, the sample-to-detector distance was 109 mm and the diffraction angle was calibrated by aluminum oxide (Al_2O_3). All X-ray images (SAXS and WAXD) were corrected for background scattering, air scattering and beam fluctuations.

Differential scanning calorimetry (DSC) measurements were carried out using a Perkin-Elmer DSC 7 instrument. The chosen heating and cooling rates were the same, i.e., 30 ^oC/min. All DSC runs were carried out under a nitrogen gas flow to minimize sample oxidation. An indium standard was used to calibrate the temperature.

1.2.3 Experimental Procedure

In order to ensure that the polymer melt was free of any memory effects associated with the prior thermal and mechanical history, all polymer samples were subjected to the temperature protocol shown in Figure 1.2. The sample was first heated to 165 ^oC

(substantially above the equilibrium melting temperature of polyethylene, $T_m^o \approx 145\ ^oC$, as well as the relaxation temperature of the entanglement network for HMWPE chains at 154 ^oC, which will be discussed later) and held for 5 min. The melt was then cooled to the chosen crystallization temperature of 126.5 ^oC at a 30 ^oC/min rate. Upon reaching the crystallization temperature, a SAXS or WAXD pattern was collected before the application of shear. Time-resolved X-ray images were subsequently taken upon the cessation of the applied shear (shear rate = 125 s^{-1}, shear duration = 20 s; shear duration was long enough to be in the zone of the steady state behavior). The data acquisition time was 15 s and the data storage time was 5 s for each scattering pattern for SAXS measurements; the data acquisition time was 22.5 s and the data storage time was 7.5 s for WAXD measurements. After 1 hour at the isothermal condition, thermal cycles were applied on the once-sheared melt under planar constraints in the Linkam stage to examine the thermal stability of shish-kebabs and its relationship with the relaxation of the deformed entanglement network of HMWPE chains. In the first thermal cycle, the shear melt was heated at a heating rate of 1 ^oC/min, but discontinuously or in several steps, to a temperature of 133.5 ^oC. At each intermediate step or temperature, the sample was held for 5 min for completion of the melting process. After the final step of melting at 133.5^oC, the sample was cooled down to 126.5 ^oC at 30 ^oC/min and held there for 60 min. A sequential cycling thermal treatment for the study of the thermal stability of the shish kebab structure was introduced as follows. In the next or second thermal cycle, the temperature was elevated at a 3 ^oC/min heating rate to a temperature that was about 2-2.5 ^oC higher than the highest temperature of the previous cycle (i.e. the cycle number and the corresponding highest temperature were as follows: for 1st cycle: 133.5 ^oC; 2nd cycle: 136 ^oC; 3rd cycle: 138 ^oC and so on). At the final temperature of each cycle (2nd and higher), the melt was always equilibrated for 3 min, and then subsequently cooled down at a 10 ^oC/min rate to 124 ^oC, under which the melt was allowed to crystallize for 10 min. The sample was subjected to sequential thermal cycles until the final temperature of 154

^{o}C, as shown in Figure 1.2. SAXS images were continuously collected during each cycle. The usefulness of the adopted, rather complex, thermal protocol was that, it allowed us to precisely track melting and re-crystallization (which can be related to the relaxation and memory of the constituent chain sections) of each component of the shish-kebab structure; namely, shish, microkebabs and macrokebabs.

1.3 Results and Discussion

1.3.1 DSC Evaluation of Referenced Thermal Behavior in Sheared Samples

DSC melting thermograms for quiescently crystallized samples of pure LMWPE and the LMWPE/HMWPE blend (98:2) are shown in Figure 1.3. The samples were first heated to 165 ^{o}C for 5 min to erase thermal history and then cooled down at 30 ^{o}C/min to room temperature. Both samples exhibited the same melting behavior, i.e., having a melting point around 115.8 ^{o}C, neither the second endotherm peak nor the broadening of the first endotherm peak was observed. This indicates that LMWPE and HMWPE were completely mixed at the molecular level and might have co-crystallized upon cooling (we note that the pure HMWPE sample exhibited a much higher melting point at 132.0 ^{o}C in DSC, data are not shown here). DSC melting thermograms for the shear-induced crystallized pure LMWPE and LMWPE/HMWPE blend samples are also shown in Figure 1.3. The initial samples were also heated to 165 ^{o}C for 5 min to erase thermal history, but after being cooled down at 30 ^{o}C/min to 126.5 ^{o}C, they were subjected to a step shear (shear rate = 125 s^{-1}, shear duration = 20 s), held there 60 min for crystallization, and then cooled down again at 30 ^{o}C/min to room temperature. The endotherm of the sheared LMWPE sample was almost the same as those of LMWPE and LMWPE/HMWPE blend crystallized under the quiescent state. However, the thermal behavior of the sheared LMWPE/HMWPE blend was very different, where two discrete

peaks were seen during heating. The peak at lower temperature (115.8 ^{o}C) was due to the melting LMWPE, whereas the peak at higher temperature (128.4 ^{o}C) could be attributed to the shear-induced shish-kebab structure of HMWPE.

1.3.2 WAXD Examination of Shear-Induced Crystallization by HMWPE

Time-resolved WAXD patterns were collected for both LMWPE and LMWPE/HMWPE blend samples, which were crystallized at 126.5 ^{o}C for 60 min under both conditions with and without the application of shear at the beginning of crystallization. All WAXD patterns for LMWPE exhibited a diffuse scattering halo with no sign of crystal diffraction, confirming that the LMWPE chains remained in the molten amorphous state at 126.5 ^{o}C under and after shear. WAXD patterns for the LMWPE/HMWPE blend without shear exhibited a single isotropic crystal diffraction ring, which could be indexed as the (110) reflection at $2\theta = 25.54^{o}$ (the wavelength was converted to 1.54 Å) from HMWPE crystals without preferred orientation.

Figure 1.4 shows selective 2D WAXD patterns of LMWPE/HMWPE blend before and during shear-induced crystallization at different times after the cessation of shear (shear rate = 125 s^{-1}, shear duration = 20 s, temperature = 126.5 ^{o}C). The first pattern collected before the application of shear exhibited a diffuse scattering halo, similar to that of the molten LMWPE matrix. This observation indicated the presence of a completely amorphous melt, confirming the thermal clearing of all residual crystalline structures. The first appearance of the crystal diffraction (i.e. the equatorial (110) reflection) in WAXD from an orientated structure was seen at 2 min after the cessation of shear. This pattern exhibited a pair of sharp equatorial (110) reflections, which could be attributed to the shish formation with extended-chain crystals. A pair of weak (200) reflections was also detected, but its intensity was too low to be analyzed even after crystallization for 60

min. At longer times (e.g. t = 10 min), the azimuthal breadth of the (110) reflection was found to broaden significantly; a closer inspection revealed that it consisted of two discrete peaks with the corresponding azimuthal distribution: (1) the initially formed peak with a narrow azimuthal distribution (point like), and (2) the subsequently developed peak with a broad azimuthal distribution (arc like). The evolution of the diffraction pattern suggested the sequential formation of the shish-kebab structure, i.e., shish formed first followed by the growth of kebabs. This behavior is consistent with our previous observations of another similar blend that consisted of non-crystallizing LMWPE (termed MB-50K in the previous study) and crystallizing ultra-high molecular weight polyethylene chains [41]. As no off-axis (110) reflection was observed, we concluded that the subsequently formed kebabs were not twisted because the twisted lamellae (kebabs) should produce four-arc off-axis (110) reflections. As expected, the total intensity of the reflections became stronger with time. At the end of the crystallization (time = 60 min), the total crystallinity estimated from the diffraction profile reached about 1%. This supports our hypothesis that LMWPE remains as an amorphous melt under the experimental conditions and the observed crystallinity mainly results from HMWPE. It is reasonable to extrapolate the situation at longer crystallization times, where the crystallinity would be higher but less than 2 %, which is the composition limit of the blend.

1.3.3 Confirmation of the Shish-Kebab Structure by SAXS

SAXS patterns of pure LMWPE with and without shear and those of the LMWPE/HMWPE blend without shear were first collected as reference experiments. These SAXS results were consistent with WAXD results, whereby all collected SAXS patterns did not exhibit any scattering features, indicating the absence of any ordered

structures in the LMWPE melt with or without shear, and in the LMWPE/HMWPE melt without shear at 126.5 ^{o}C.

Selective 2D SAXS patterns of LMWPE/HMWPE blend before and after shear (shear rate = 125 s^{-1}, shear duration = 20 s, temperature = 126.5 ^{o}C) are shown in Figure 1.5. The SAXS pattern of the sheared LMWPE/HMWPE blend exhibited a clear equatorial streak arising immediately after the cessation of shear (at t = 30 s). The appearance of the equatorial streak indicated the formation of shish (microfibrils), containing extended crystals formed from the bundles of stretched chain segments parallel to the flow direction. The SAXS results were consistent with the WAXD results. Soon after the shish formation, strong scattering maxima appeared on the meridian. The meridional maximum could be attributed to the kebab growth, resulted from folded-chain crystallization. The oriented scattering features from the shish-kebab structure became stronger with the increase in time. Time evolution of the integrated scattered intensities from the shish and kebab fractions (I_{shish} and I_{kebab}) is illustrated in Figure 1.6. Both scattered intensities increased with the growth of shish-kebab structure. The higher I_{shish} value at the very beginning of the shear-induced crystallization than the corresponding I_{kebab} value (see Figure 1.6 inset) was because the shish was formed first and then the kebabs. The ratio of I_{kebab} to I_{shish} became about 3 at the end of crystallization.

Time evolution of the average diameter of kebab is shown in Figure 1.7. These were estimated from a shish-kebab model analysis of the meridional intensity profile. The details of the analytical schemes were given elsewhere and would not be repeated here [37]. It was found that the average diameter of the kebab increased with time, but not in a linear fashion (i.e. the kebab growth rate was not constant). The profile of the kebab growth rate (G = dD/dt, where D represents the kebab diameter and t is time) *versus* time on a logarithmic scale is plotted in Figure 1.8. The line in Figure 1.8 has a slope of - 0.76,

it roughly follows the relationship of log $G \propto (-0.5)\log t$ for a diffusion-controlled growth process, predicted by Muthukumar et al [18].

1.3.4 Melting and Reformation of the Shish-Kebab Structure

After crystallization for 60 min at 126.5 ^{o}C, the once-sheared LMWPE/HMWPE sample was subjected to the first thermal cycle. Selected 2D SAXS patterns during this cycle are shown in Figure 1.9. It was found that with the increase of temperature, the scattered intensity from the shish-kebab structure decreased accordingly, due to melting. The integrated scattered intensity (I_{shish} and I_{kebab}) at the end of each holding temperature are plotted in Figure 1.10(A), showing that both values of I_{shish} and I_{kebab} decreased with the increasing temperature. When the temperature was elevated to 133.5 ^{o}C, both I_{shish} and I_{kebab} became zero. Although this appears to indicate the complete melting of the shish-kebab structure, it is not a conclusive evidence of whether the constituent chains have completely relaxed, as discussed below.

Figure 1.10(B) illustrates the time evolution of I_{shish} and I_{kebab} during heating and holding at the late stage of the first thermal cycle. It was interesting to see that during the heating process in this cycle, even with the increase of 1 ^{o}C, corresponding scattered intensities from shish and kebabs decreased rapidly. However, as soon as the sample was equilibrated at a constant temperature for a period of 5 min, both scattered intensities (I_{shish} and I_{kebab}) increased slightly, indicating the reformation of some melted crystals. Overall, the changes of integrated scattered intensities for I_{shish} and I_{kebab} exhibited a step-like behavior, consistent with the steps in the thermal cycles. Figure 1.10(C) illustrates the ratio of I_{kebab} and I_{shish} at the end of each holding temperature, in which the ratio decreased slowly at lower temperatures and more rapidly (from 3 to 2) when the temperature approached to 133.5 ^{o}C. It was interesting to note that the corresponding

long period remained about constant at 40 nm during the heating and holding steps in the first thermal cycle (Figure 1.11). The above observations suggests the following sequence of events during melting of the shish-kebab structures; the less thermally stable macrokebabs melt first, followed by the simultaneous melting of shish and more thermally stable microkebabs. The detailed explanations for the above results are given in the discussion section.

At the end of the first thermal cycle, the once-sheared sheared LMWPE/HMWPE blend was cooled down continuously from 133.5 ^{o}C to 126.5 ^{o}C at 30 ^{o}C/min. This step revealed a very interesting behavior of the previously melted shish-kebabs. It was found that the shish-kebab structure reformed. The SAXS patterns in Figure 1.9 (bottom) clearly evidenced a substantial reformation of the prior structure. The overall scattering feature of the reformed SAXS pattern at 126.5 ^{o}C was similar to that of the initial SAXS pattern. On the other hand, there were some subtle but important differences between the two. Comparison of the SAXS patterns collected at 30 s and 126.5 ^{o}C, one after shear (Figure 1.5) and one during re-crystallization (Figure 1.9), showed that the crystallization rate in the early stage of the re-crystallization was much faster than that after shear. In fact, the scattered intensity of the SAXS pattern at 30 s during the re-crystallization period was very close to that obtained about 4 min after shear. This could be explained by the difference in the state of orientation in the stretched chain segments, immediately after shear and after the melting of shish crystals. Let us first consider the process of melting. We argue that it follows a more or less reversible path; i.e., the structures that grew late melt first. Also, even after melting of the crystalline structures, the relaxation dynamics of the constituent chains of the underlying network/scaffold is very slow at the experimental conditions of temperature compared with the holding time. Chronologically, the chains in the initially formed structures; especially the primary nuclei (shish) will be the last to loose their state of orientation or conformation. Thus, a

high fraction of the primary nuclei survive in the supercooled melt. In contrast, immediately after shear, it takes a certain time for the oriented chain segments to organize and form primary nuclei. As a result, crystallization kinetics in the re-crystallization process was faster than that after shear. Also, it was found that the long period decreased slightly at the initial stage of re-crystallization, and it reached a constant value at about 46 nm that was larger than the long period before the first thermal cycle (~ 40 nm). Since crystallization was carried out at the same temperature (126.5 ^{o}C) and the same duration (1 hour) for both stages, the lamellar thickness (which is a strong function of super cooling) should remain the same. So, the larger long period at the re-crystallization indicates that a lesser amount of crystals was formed (i.e., the lamellae were more sparsely spaced). This can be attributed to the reduction in the total amount of the oriented, crystallizable chain segments after the melting process. However, we envision that some chains indeed completely relax and cannot participate in the re-crystallization process.

The second thermal cycle was carried out at the end of 60 min re-crystallization at 126.5 ^{o}C (immediately after the end of the first cycle). As mentioned in the experimental section, in second and subsequent cycles, the sample was not subjected to step-wise heating, instead it was heated continuously to the highest temperature of the corresponding cycle at a 3 ^{o}C/min rate (See Figure 1.2; for example, 136 ^{o}C in the second cycle). During heating in the second cycle, the observed melting behavior was very similar to that in the first cycle. Both scattered intensities from shish and kebabs decreased with the increase of temperature. It was found that the long period remained about constant (46 nm) before 131 ^{o}C and it started to increase afterward (Figure 1.11); again due to the relaxation/non-participation of some of the chains in the re-crystallization process. The final long period was 48.5 nm at 133 ^{o}C; beyond 133 ^{o}C, it was difficult to determine the long spacing due to the weak meridional maximum.

The subsequent cycles showed similar trend in the shish and kebab intensities as well as the long period. In the third and fourth thermal cycles, the initial scattered intensities of shish and kebabs all became lower, due to the reduction in the total mass fraction of the shish-kebab structure after each thermal cycle. In the third cycle, the scattered intensity of the kebabs decreased rapidly during heating and it approached zero at 132 ^{o}C, whereas the corresponding long period, illustrated in Figure 1.11, increased immediately upon heating. Generally speaking, the long period increased with the order of the thermal cycles at the same final crystallization temperature. The long period changes during cooling in the third and forth cycles were similar to that in the second cycle, except for a larger initial long period at the beginning of cooling in the high order cycle.

Figure 1.12 illustrates the final SAXS patterns collected at the end of re-crystallization in all thermal cycles (note that the crystallization temperature was 126.5 ^{o}C for the first cycle and 124 ^{o}C for all other cycles). In this figure, the equatorial streak could still be seen in the first two patterns (i.e., the first and second cycles with the highest temperature of 133.5 and 136 ^{o}C, respectively), but the later patterns only exhibited a meridional scattering feature. The scattered intensity decreased notably after each cycle. In the later cycles, since crystallization took place at the same temperature (124 ^{o}C) for the same duration of time (10 min), the decrease in scattered intensity could be attributed to the decreasing number of primary nuclei (from the stretched chain segments) for creation of kebabs. The final SAXS pattern at the end of eleventh thermal cycle did not show any sign of the shish-kebab structure. This cycle had the highest temperature of 154 ^{o}C; thus, it appears that here the complete relaxation of the stretched chain segments (or the deformed entanglement network) took place. The long period and integrated scattered intensities (total, shish and kebabs) determined from the final SAXS pattern obtained after each cycle are plotted as a function of the highest temperature in

the cycle in Figure 1.13(A) and (B), respectively. It was found that the long period increased in the first six cycles (no long period could be identified after heating about 144 ^{o}C as there was no indication of scattering maximum, but some meridional scattering feature persisted). Along with the decrease in the scattered intensity in Figure 1.13(B) confirmed that the fraction oriented shish-kebab structure decreased after each thermal cycle.

1.3.5 The Shish-Kebab Formation from HMWPE Chains

One of the unique features in this study is the careful selection of molecular weight, polydispersity and molecular architecture for the two polyethylene samples. As shown in Figure 1.1, $\overline{M}_w$ of LMWPE was about 53,000 g/mol having a polydispersity of 2.2, and $\overline{M}_w$ of HMWPE was 1,500,000 g/mol having a polydispersity of 1.1. Both samples do not overlap in the molecular weight region at around 300,000 g/mol, which is near the critical orientation molecular weight at the similar degree of super cooling, as estimated from our previous work for PE and iPP [30-31,35]. As LMWPE is a random copolymer of ethylene (98 mol%) and hexane (2 mol%), it does not crystallize at the experimental temperatures (i.e. $\geq$ 124 ^{o}C). In addition, at the chosen shear conditions (temperature = 126.5 ^{o}C, shear rate $\dot{\gamma}$ = 125 s^{-1}), the characteristic relaxation times; i.e., the Rouse time, τ_r, chain disentanglement or Reptation time, τ_D, of the LMWPE chains are significantly shorter than the experimental time scale (i.e., $1/\dot{\gamma}$) [38-39], indicating that all relatively short matrix chains would relax back to the coiled state after shear. Thus, the LMWPE matrix behaves mainly as a solvent, where the only crystallizing component is HMWPE. This hypothesis is further supported by both SAXS and WAXD results.

The development of crystalline shish and kebab structures, all from the narrow distribution of HMWPE chains, requires explanation of rational molecular mechanism. In the supercooled melt, HMWPE chains are in the entangled state, whose entanglement density is mainly a function of concentration but not of temperature [40]. In other words, the average chain length between the entanglement points (or the entanglement molecular weight M_e) does not change with temperature but change with concentration. Thus, the entanglement density of the chosen blend (2 wt% HMWPE) should remain about constant under all experimental conditions (i.e., during and after shear). There are several characteristic time scales that determine the state of orientation and extension for chain segments between the entanglement points in HMWPE during and after cessation of shear. These time scales include: (1) the imposed shear (flow) time scale (τ_{exp}), which is inversely proportional to the shear rate ($\tau_{exp} \propto \dot{\gamma}^{-1}$), (2) the Rouse time ($\tau_R$), which is related to the relaxation of the chain segments between the entanglement points, and (3) the Reptation time (τ_d), which is related to the relaxation of monodispersed chain [38-39]. In addition, there are other "breathing" modes; such as contour length fluctuation (CLF), convective constraint release (CCR), that can relax chain or segment orientation. At very low shear rates or $\tau_{exp} >> \tau_d$, reptation along with CLF dominate the relaxation process and almost no chain segments should remain oriented; here the stretched state is, obviously, not at all possible. At intermediate shear rates or $\tau_{exp} \sim \tau_d$, the chain segments between the entanglements can be oriented but not stretched. At very high shear rates or when $\tau_R > \tau_{exp}$, the chain segments between the entanglements can be both oriented and stretched. At the chosen shear conditions, the scenario of $\tau_R > \tau_{exp}$ (= 0.08 s) must have been met; the evolution of shish evidence straight, or oriented and stretched chain sections between the entanglement points. This scenario will be further discussed elsewhere. It is clear that the crystallization process will alter the state of the entanglement topology. That is, in the crystalline region, the entanglement is largely

eliminated, however, the entanglement density should increase in the amorphous region surrounding the lamellae.

If one considers the entangled melt as a network structure, containing entanglement points at dynamic equilibrium as physical crosslinks, then the deformation field (i.e. flow) would generate two populations of chain segments conformation, as illustrated in Figure 1.14: (1) stretched segments oriented along the flow direction and confined by the entanglement points, and (2) un-oriented and -stretched segments (or coiled segments) perpendicular to the flow direction. Unlike the deformation of chemically crosslinked network material, the extent of the stretched segments in the entangled melt under flow is also a function of strain. Under the supercooled state, both stretched and coiled segments can crystallize, most likely following the pathway proposed by Muthukumar et al. for monodispersed stretched and coiled chains [18]. That is the stretched segments can rapidly crystallize into shish with extended-chain conformation (we note that the characteristic time scale of extended-chain crystallization should be order of magnitudes faster than the experimental time scale or the relaxation time scale in entangled HMWPE chains), and the coiled segments can crystallize into the kebabs with folded-chain conformation. Muthukumar et al. have predicted that the growth rate (G) of kebabs should follow a diffusion-controlled mechanism (i.e. $G \propto t^{-0.5}$). This prediction is consistent with our experimental observations that the (overall) kebab growth rate from coiled HMWPE chain segments was indeed not constant. The difference between the predicted exponent of -0.5 (i.e. for diffusion-controlled growth under ideal conditions) and the experimental exponent of -0.76 may be due to the connectivity of chain segments in the entangled melt or the possible difference between the growths of microkebabs and macrokebabs. The latter hypothesis is not clear and will be the subject of our future study.

1.3.6 Thermal Stability of the Shish-Kebab Structure

During heating in the first thermal cycle, we noted the decrease in the I_{shish} and I_{kebab} values as well as in the I_{kebab}/I_{shish} ratio, but a constant long period, with the increase of temperature. Based on these observations, we composed a model to describe the thermal stability of the shish-kebab structure (illustrated in Figure 1.15), modified from the one proposed by Petermann [27-29]. Diagram A represents a well-formed shish-kebab structure before heating. The microkebabs have fractions of chain segments embedding in the shish; while the macrokebabs grow from the microkebab templates perpendicular to the shish. Upon heating, the outer macrokebabs melt first and relax back to the random coil state, but the inner microkebabs persist with the thermally stable shish. Diagram B illustrates the partially melted shish-kebab structure, surrounded by coiled chain segments in the molten state (both Diagrams B and C omit the chain connectivity between the molten coiled segments and the residual shish-kebab structure). When the temperature is increased above the nominal melting point, both microkebabs and shish would lose their crystalline registrations. The chain segments melted from microkebabs will relax back into the coiled state, but the chain segmented melted from shish will remain in the stretched state (Diagram C), unless the deformed entanglement network structure is relaxed back, due to high temperature or long hold times, to the un-deformed initial state. In Figures 1.14 and 1.15, we omitted the presence of LMWPE chains because they could not crystallize under the experimental conditions. Since the LMWPE phase was the dominant matrix, the molten amorphous region would consist of both LMWPE (the major component) and HMWPE (the minor component) chains. When the blend was cooled down to the experimental temperature (126.5 ^{o}C), only HMWPE chains could crystallize; whereas LMWPE chains would remain in the amorphous region, resulting in an increase in the composition ratio for LMWPE.

The relaxation time scale for the stretched chain segments of shish is order of magnitude higher than that of kebabs. The stretched chain segments can quickly re-crystallize into crystalline shish, if cooled down to low temperatures, which can subsequently nucleate microkebabs. Thus, the residual shish-kebab structure at the end of each cycle is a direct reflection of the state of the stretched and coiled chain segments upon heating under the confined planar constraints to the highest temperature of the cycle. It is seen that the kebab long period increased but the corresponding scattered intensity decreased with the increase of the highest temperature in each cycle (Figures 1.11 and 1.12). This can be attributed to the relaxation of the deformed entanglement network, which reduces the extent of the stretched segments after each thermal cycle to a higher temperature. As the amount of the stretched segments decreases, the amount of the shish reformation would decrease, resulting in a less amount of kebabs and a larger value of long period between kebabs. In the last thermal cycle with the holding temperature of 154 ^{o}C for 3 min, the shish and kebabs reformation did not take place, indicating the complete relaxation of the deformed entanglement network.

We noticed that the final SAXS patterns taken at the end of the first and the second cycles (Figure 1.12) all exhibited an equatorial streak together with meridional peaks, whereas the rest patterns only showed meridional scattering feature. In our earlier study [35], we argued that the lack of equatorial streak does not mean that the shish formation did not take place, it simply means that the concentration of the shish might be too low or the diameter of the shish too thin to be detected by SAXS. However, with our recent observation of multiple shish [41] in the shish-kebab structure induced by shear in a similar bimodal blend, we speculate that the appearance of equatorial streak in SAXS may be related to the occurrence of multiple shish, which has a more enhanced contrast than typical single shish. This hypothesis will be thoroughly tested in our future study.

1.4 Conclusion

From the shear-induced crystallization study of a special polymer blend containing 98 wt% non-crystallizing LMWPE and 2 wt% narrowly distributed crystallizing HMWPE using *in-situ* SAXS and WAXD techniques, we obtained several new insights into the formation, melting and reformation of the shish-kebab structure under planar constraints. These new insights can be summarized as follows.

1. Under shear flow, stretched and coiled chain segments co-exist even in near monodispersed HMWPE chains. The different states of chain segments are caused by the deformation of the network like structure in highly entangled polymer melt with each entanglement point acting as a physical crosslink.
2. The stretched and coiled segments are responsible for the formation of the shish-kebab structure, where the kebab growth seems to follow a diffusion-controlled process, as predicted by Muthukumar et al. [18]
3. Upon heating, the melting of macrokebabs takes place before the melting of microkebabs and shish, which vanish simultaneously as an integrated entity into coiled and stretched chain segments. The shish-kebab structure can reform upon cooling, mainly due to the survival of stretched chain segments confined by the entanglement points.

4: The reformed shish-kebab structure directly reflects the state of stretched and coiled segments upon heating under the confined planar constraints. With increase of temperature, the relaxation of the deformed entanglement network results in the decrease in the extent of stretched segments and the shish-kebab fraction, and the increase of the kebab long period.

5: Upon thermal annealing at 154 ^{o}C for 3 min, no shish-kebab structure could be reformed, indicating the complete relaxation of the deformed entanglement network.

List of References

1. Keller, A.; Kolnaar, H. W. *Mater. Sci. Technol*, **1997**, vol 18, 189.
2. Ward, I. M. *Structure and Properties of Oriented Polymers*, Wiley, New York, **1975**.
3. Wunderlich, B. *Macromolecular physics*, vol 2, Academic Press, New York, **1973**.
4. Wilkinson, A. N. and Ryan, A. J. (Eds.), *Polymer Processing and Structure Development*, Kluwer, Dodrecht, **1998**.
5. Eder, G.; Janeschitz-Kriegl, H. *Mater. Sci. Technol.*, **1997**, 18, 268.
6. Hobbs, J. K.; Humphris, A. D. L.; Miles, M. J. *Macromolecules*, **2001**, 34, 5508.
7. Bashir, Z.; Odell, J. A.; Keller, A. *J. Mater. Sci.*, **1986**, 21, 3993.
8. Somani, R. H.; Hsiao, B. S.; Nogales, A.; Srinivas, S.; Tsou, A. H.; Sics, I.; Balta-Calleja, F. J.; Ezquerra, T. A. *Macromolecules*, **2000**, 33, 9385.
9. Jerschow, P.; Janeschitz-Kriegl, H. *Int. Polym. Process*. **1997**, 12, 72.
10. Sherwood, C.; Price, F.; Stein, R. J. *Polym. Sci. (Polym Symp.)*, **1978**, 63, 77.
11. Lagasse, R. R.; Maxwell, B. *Polym. Eng. Sci.*, **1976**, 16, 189.
12. Vleeshouwers, S.; Meijer, H. *Rheol. Acta*, **1996**, 35, 391.
13. Duplay, C.; Monasse, B.; Haudin, J. M.; Costa, J. L. *J. Mater. Sci.,* **2000**, 35, 6093.
14. Seki, M.; Thurman, D. W.; Oberhauser, J. P.; Kornfield, J. A. *Macromolecules*, **2002**, 35, 2583.
15. de Gennes, P. G.; *J. Chem. Phys.*, **1974**, 60, 5030.
16. Pope, D. P.; Keller, A. *Colloid Polym. Sci.*, **1978**, 256, 751.
17. Miles, M. J.; Keller, A. *Polymer*, **1980**, 21, 1295.

18. Dukovski, I.; Muthukumar, M. *J. Chem. Phys.*, **2003**, 118, 6648.
19. Na, B., Wang, Y.; Zhang, Q.; Fu, Q. *Polymer*, **2004**, 45, 6245.
20. Yamazaki, S.; Hikosaka, M.; Toda, A.; Wataoka, I.; Yamada, K.; Tagashira, K. *J. Macromol. Sci. Phys.*, **2003**, B42, 499.
21. Isayev, A. I.; Chan, T. W.; Shimojo, K.; Gmerek, M. *J. Appl. Polym. Sci.*, **1995**, 55, 807.
22. Gutierrez, M. G.; Alfonso, G. C.; Riekel, C.; Azzurri, F. *Macromolecules*, **2004**, 37, 478.
23. Azzurri, F.; Alfonso, G. C. *Macromolecules*, **2005**,38, 1723.
24. Hill, M. J.; Barbam, P. J.; Keller, A. *Colloid Polym. Sci.*, **1980**, 258, 1023.
25. Hill, M. J.; Keller, A. *Colloid Polym. Sci.*, **1981**, 259, 335.
26. Hill, M. J.; Barbam, P. J.; Keller, A. *Colloid Polym. Sci.*, **1983**, 261, 721.
27. Liu, T.; Petermann, J.; He, C.; Liu, Z.; Chung, T. *Macromolecules*, **2001**, 34, 4305.
28. Liu, T.; Lieberwirth, I.; Petermann, J. *Macromol. Chem. Phys.*, **2001**, 202, 2921.
29. Liu, T.; Tjiu, W. C.; Petermann, J. *J. Crystal Growth*, **2002**, 243, 218.
30. Somani, R. H.; Hsiao, B. S.; Nogales, A.; Fruitwala, H.; Srinivas, S.; Tsou, A. H. *Macromolecules*, **2001**, 34, 5902.
31. Nogales, A.; Hsiao, B. S.; Somani, R. H.; Srinivas, S.; Tsou, A. H.; Balta-Calleja, F. J.; Ezquerra, T. A. *Polymer*, **2001**, 42, 5247.
32. Keum, J.; Somani, R. H.; Zuo, F.; Burger, C.; Sics, I.; Hsiao, B. S.; Chen, H.; Kolb, R.; Lue, C. *Macromolecules*, **2005**, 38, 5128.
33. de Gennes, P. G.; *Scaling Concepts in Polymer Physics*, Cornell University Press, Ithaca, New York, **1979**.
34. Ballard, D. G. H.; Cheshier, P.; Longman, G. W.; Schelten, J. *Polymer*, **1978**, 19, 379.
35. Yang, L; Somani, R. H.; Sics, I.; Hsiao, B. S.; Kolb, R.; Fruitwala, H.; Ong, C. *Macromolecules*, **2004**, 37, 4845.

36. Somani, R. H.; Hsiao, B. S.; Nogales, A.; Srinivas, S.; Tsou, A. H.; Scis, I,; Balta-Calleja, F. J.; Ezquerra, T. A. *Macromolecules*, **2000**, 33, 9385.
37. Keum, J.; Burger, C.; Hsiao, B. S.; Somani, R. H.; Yang, L.; Chu, B.; Kolb, R.; Chen, H.; Lue, C. *Prog. Colloid Polym. Sci.*, **2005**, 130, 114.
38. Milner, S. T.; McLeish, T. C. B. *Phys. Rev. Lett.*, **1998**, 31, 725.
39. Bent, J.; Hutchings, L. R.; Richards, R. W.; Gough, T.; Spares, R.; Coates, P. D.; Grillo, I.; Harlen, O. G.; Read, J. D.; Garham, R. S.; Likhtman, A. E.; Groves, D. J.; Nicholson, T. M.; McLeish, T. C. B. *Science*, **2003**, 301, 1692.
40. Doi, M.; Edwards, S. F. *The Theory of Polymer Dynamics*, Oxford Science Publications, Oxford, **1986**.
41. Hsiao, B. S.; Yang, L.; Somani, R. H.; Carlos, A. A.; Zhu, L. *Phys. Rev. Lett*, **2005**, 94, 117802.

List of Tables

Table 1.1. Information about the molecular weight and the melting temperature of LMWPE and HMWPE.

Samples	$\overline{M}_w$ (g/mol)	MWD ($\overline{M}_w / \overline{M}_n$)	T_m (^oC)[b]	$T_{m,end}$ (^oC)[c]
LMWPE[a]	53,000	2.2	116	124
HMWPE	1,500,000	1.1	132	145

[a] Polymerized with 2 mol% of hexene comonomer using a metallocene catalyst.

[b,c] The melting peak and end-of-melting temperature were obtained from DSC at a heating rate of 30 ^{o}C/min.

List of Figures

Figure 1.1. GPC profiles of LMWPE and HMWPE before blending. The range of M_w^* represents the rough molecular weight values, which are near the critical orientation molecular weight according to our previous studies.

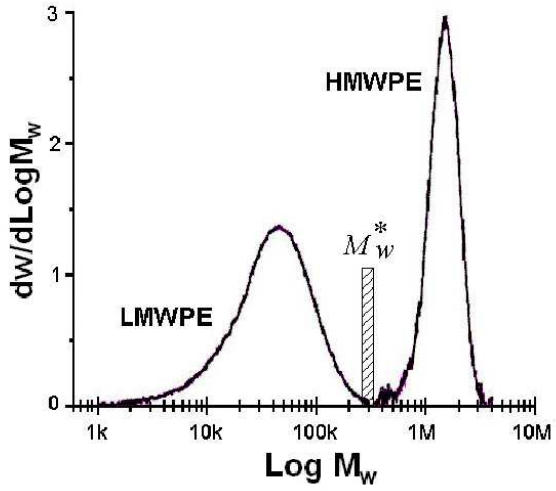

Figure 1.2. Thermal cycling protocol of this study. A step shear pulse was applied for 20 s (shear rate = 125 s^{-1}), after the collection of first SAXS or WAXD image upon the melt being cooled down from 165 ^{o}C to 126.5 ^{o}C.

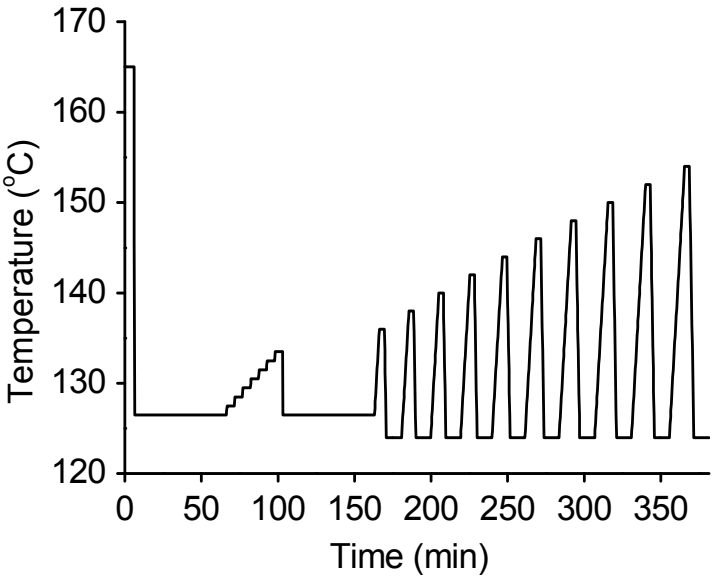

Figure 1.3. DSC melting thermograms of quiescently crystallized and shear-induced crystallized LMWPE and LMWPE/HMWPE blend samples (heating rate = 30 ^{o}C/min)

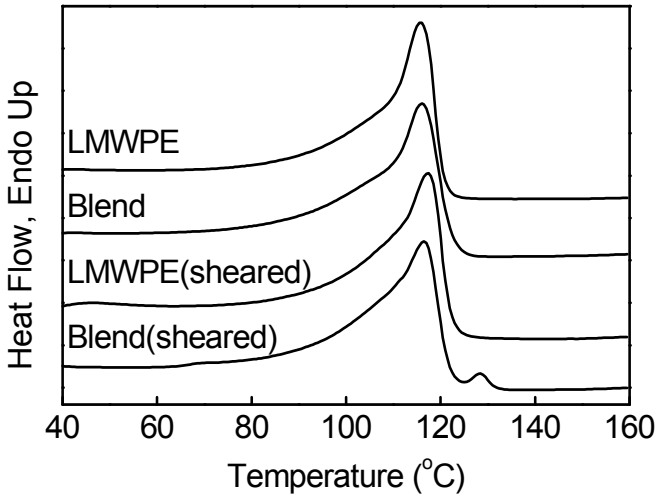

Figure 1.4. Selected 2D WAXD patterns (the (110) reflection peaks are filled in red to give a better contrast) of LMWPE/HMWPE blend before the application of shear and during isothermal crystallization at 126.5 ^{o}C after cessation of shear (shear rate = 125 s^{-1}, shear duration = 20 s).

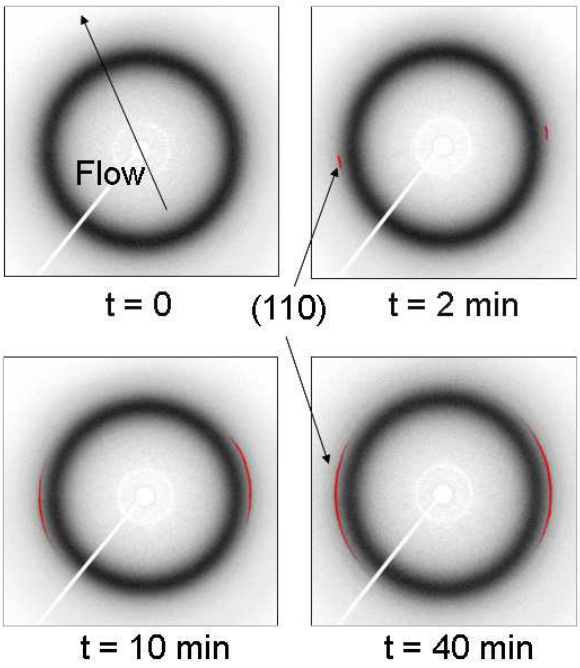

Figure 1.5. Selected 2D SAXS patterns of LMWPE/HMWPE blend before the application of shear and during isothermal crystallization at 126.5 ^{o}C after the cessation of shear (shear rate = 125 s^{-1}, shear duration = 20 s).

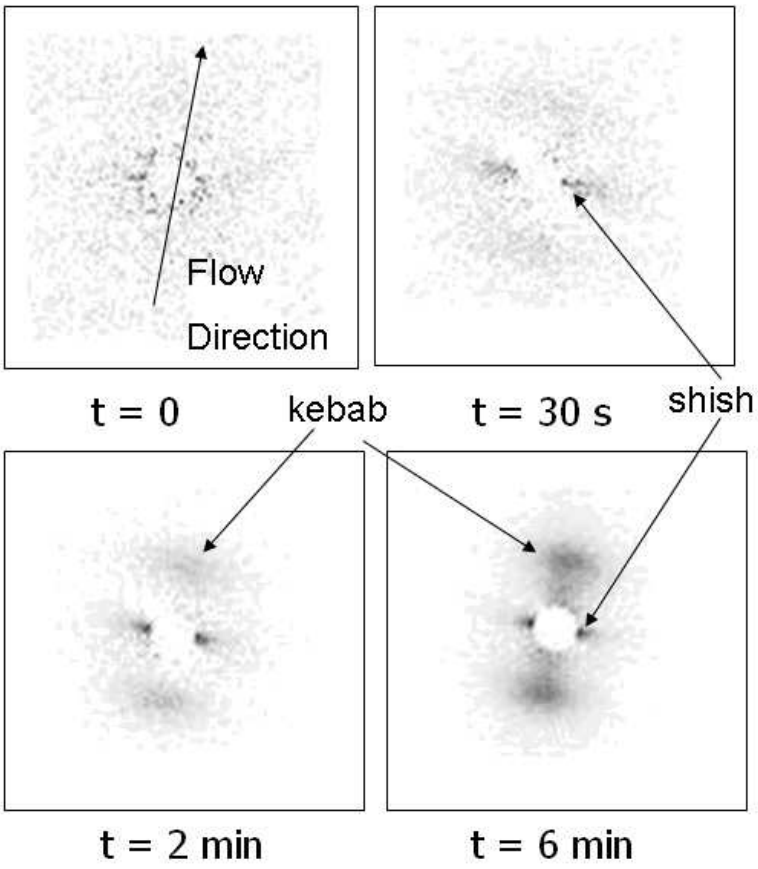

Figure 1.6. Time evolution of the integrated SAXS intensities from shish and kebabs in LMWPE/HMWPE blend after shear. The inset shows the initial stage (shear rate = 125 s^{-1}, shear duration = 20 s).

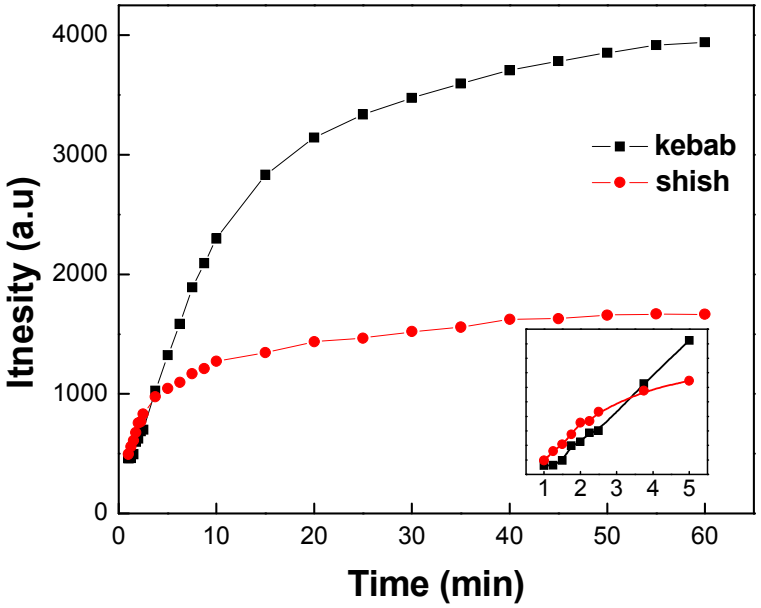

Figure 1.7. Time evolution of the average kebab diameter in LMWPE/HMWPE blend after shear (shear rate = 125 s^{-1}, shear duration = 20 s).

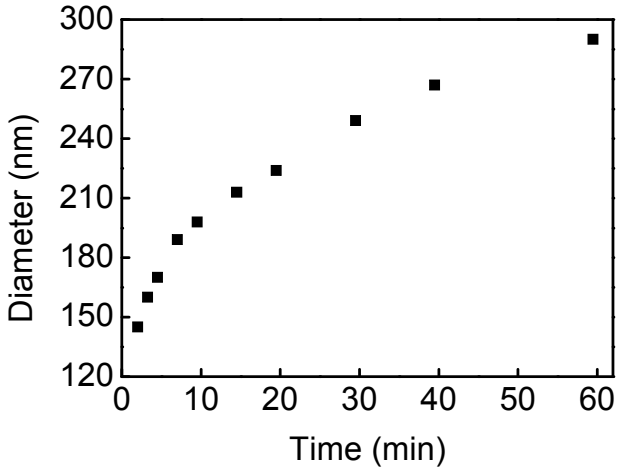

Figure 1.8. The average growth rate G of the kebab diameter in LMWPE/HMWPE blend after shear. Results indicate the kebab growth follows diffusion-controlled like process.

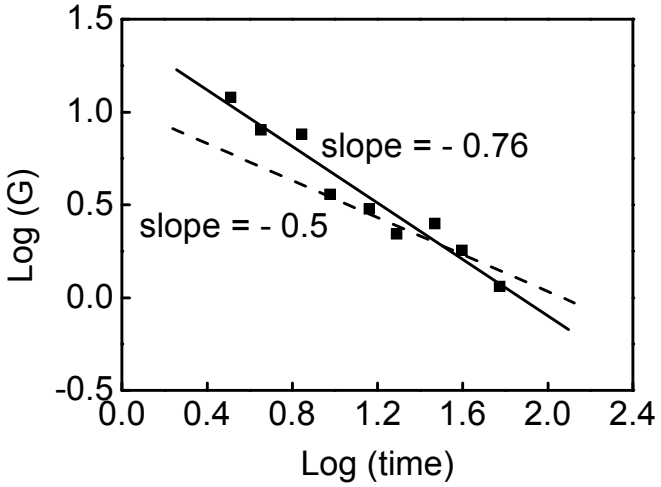

Figure 1.9. Selected 2D SAXS patterns of the LMWPE/HMWPE blend during the first thermal cycle (the patterns shown below were taken after 5 min hold at the corresponding temperature).

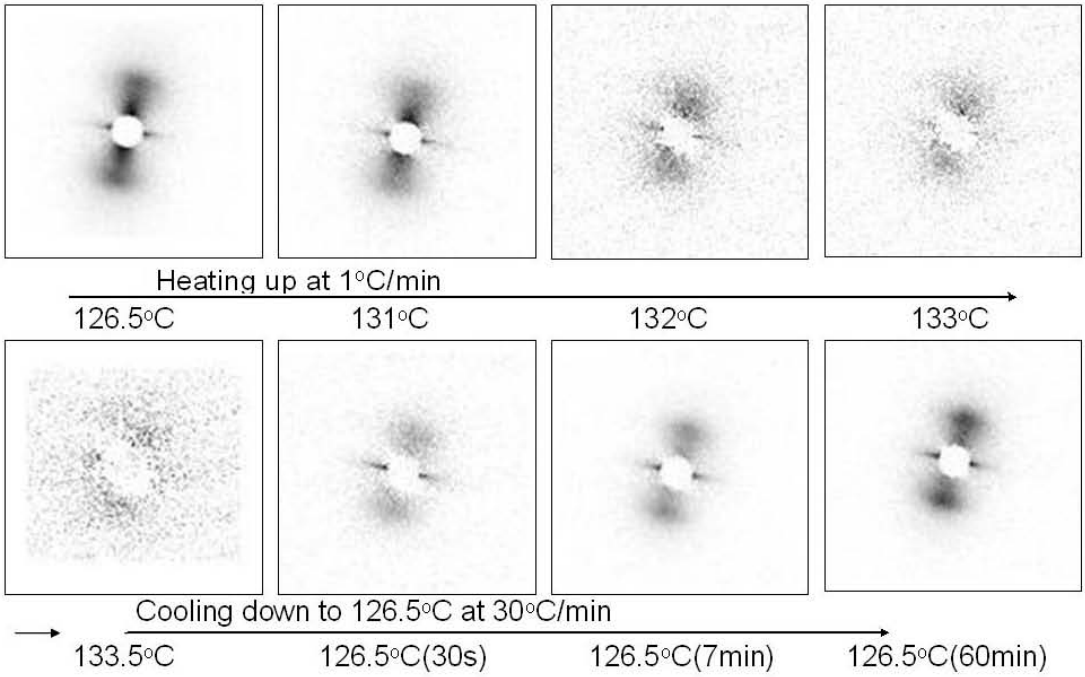

Figure 1.10. (A) Integrated SAXS intensities from shish and kebabs at the end of each holding temperature in the first thermal cycle. (B) Time evolution of integrated SAXS intensities from shish and kebabs at the late stage of the first thermal cycle. (C) The ratio of I_{kebab} to I_{shish} at the end of each holding temperature in the first thermal cycle.

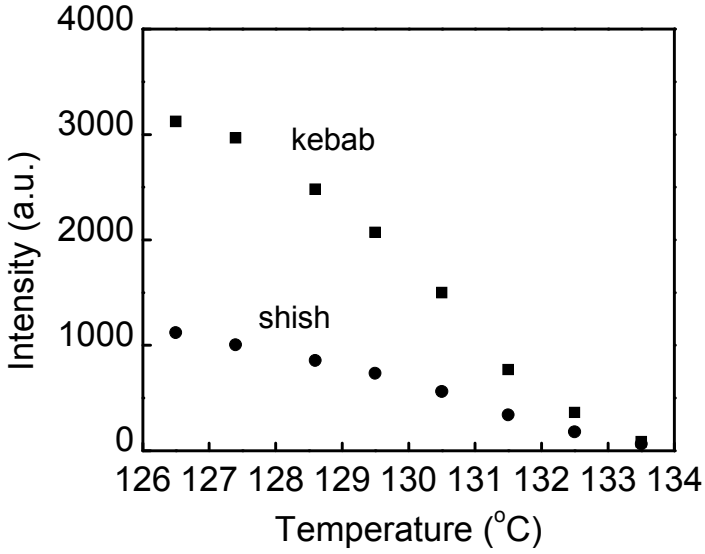

(A)

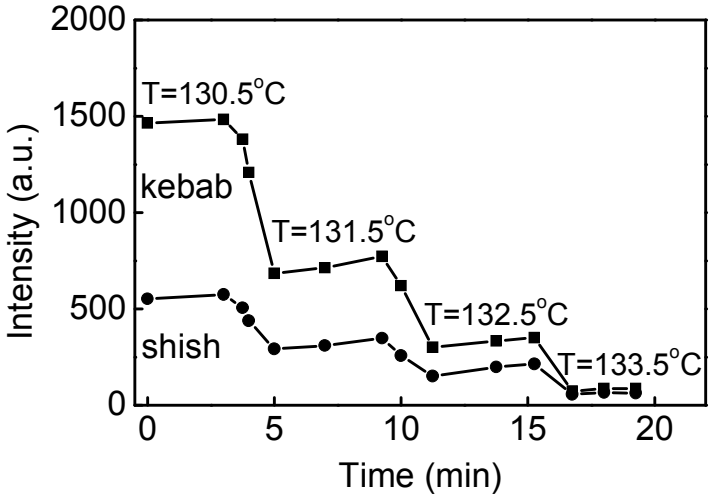

(B)

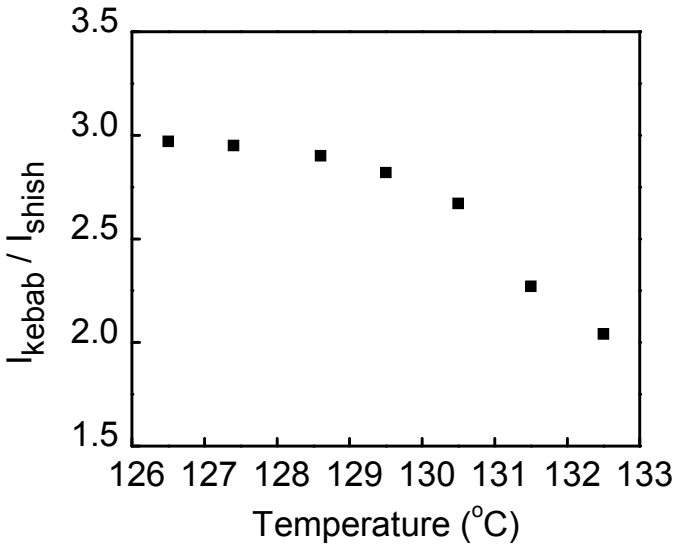
3.5
3.0
2.5
2.0
1.5
I_{kebab} / I_{shish}
126 127 128 129 130 131 132 133
Temperature (^{o}C)

(C)

Figure 1.11. The changes of long periods of shish-kebab structure in LMWPE/HMWPE blend during the heating stages in the first four thermal cycles.

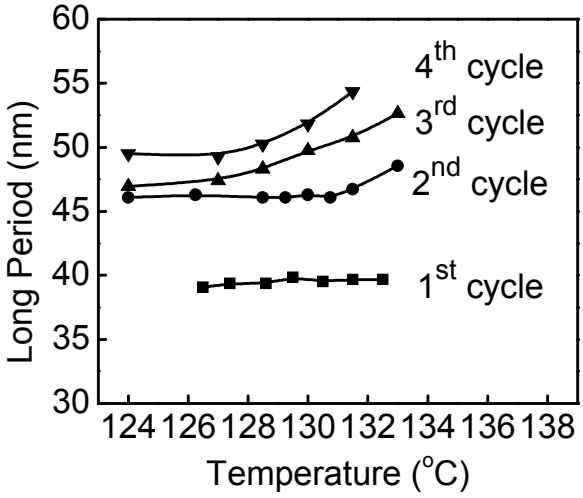

Figure 1.12. Selected 2D SAXS patterns collected at the end of re-crystallization in each thermal cycle. The temperature shown below the pattern is the highest temperature during the heating stage in corresponding thermal cycle. The crystallization temperature is 126.5 ^{o}C for the first cycle, and 124 ^{o}C for others.

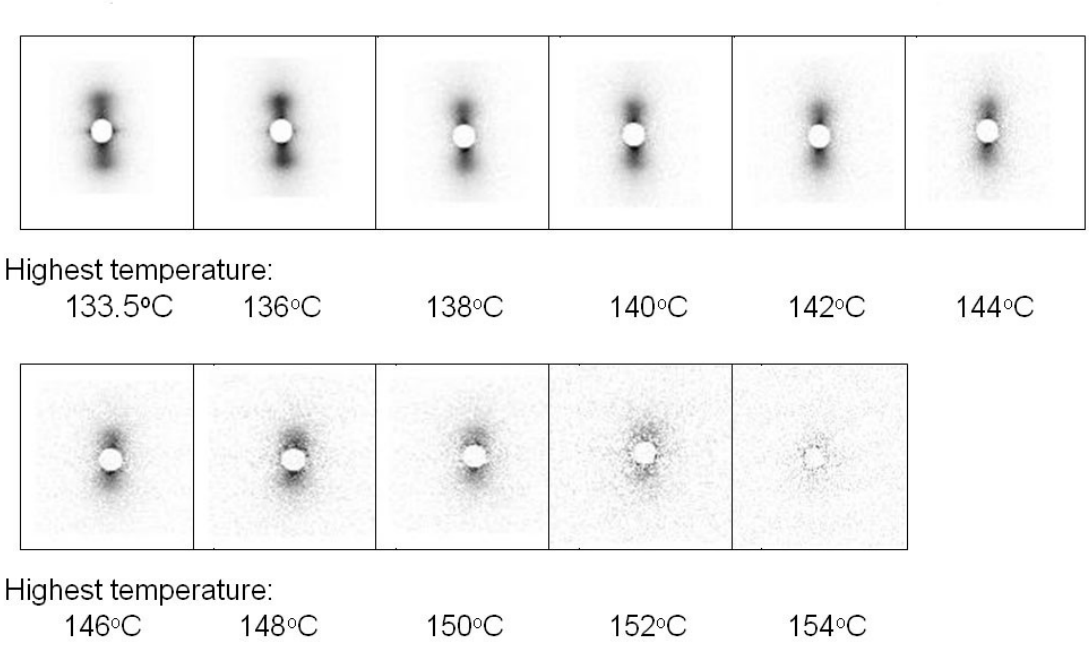

Figure 1.13. The long periods (A), and integrated SAXS intensities from shish, kebabs and total (B) obtained after re-crystallization as a function of the highest equilibrium temperatures. The crystallization temperature is 126.5 ^{o}C for the first cycle, 124 ^{o}C for others.

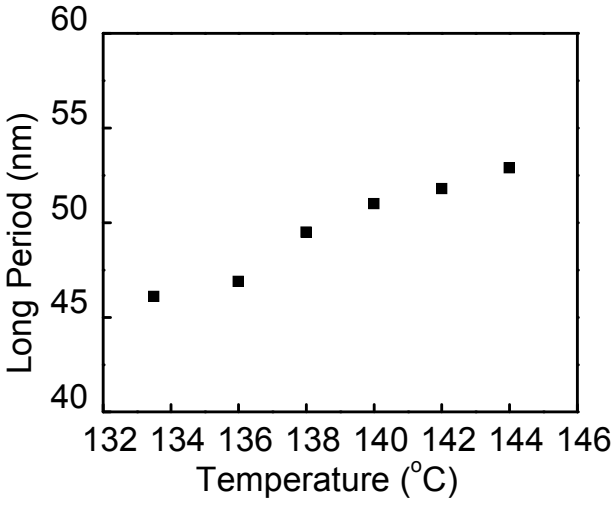

(A)

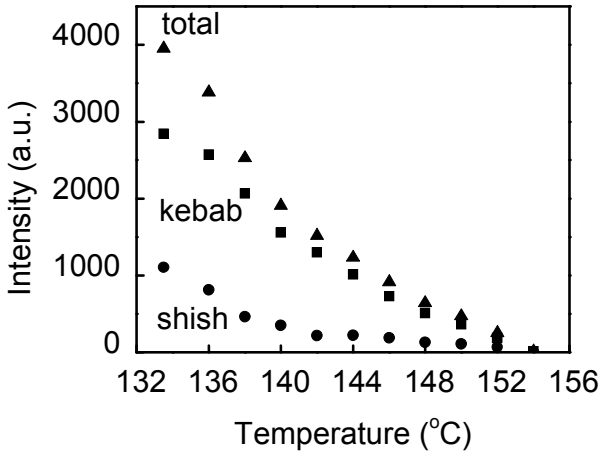

(B)

Figure 1.14. Schematic representation of the entanglement network of HMWPE chains (A) under uniaxial deformation (LMWPE chains are not shown here). Upon shearing, some chain segments between entanglements (shown as round dots) are stretched along the flow direction, but most segments remained in the coiled state (B). The stretched segments form the precursors for the shish formation, and the coiled segments can grow into kebabs.

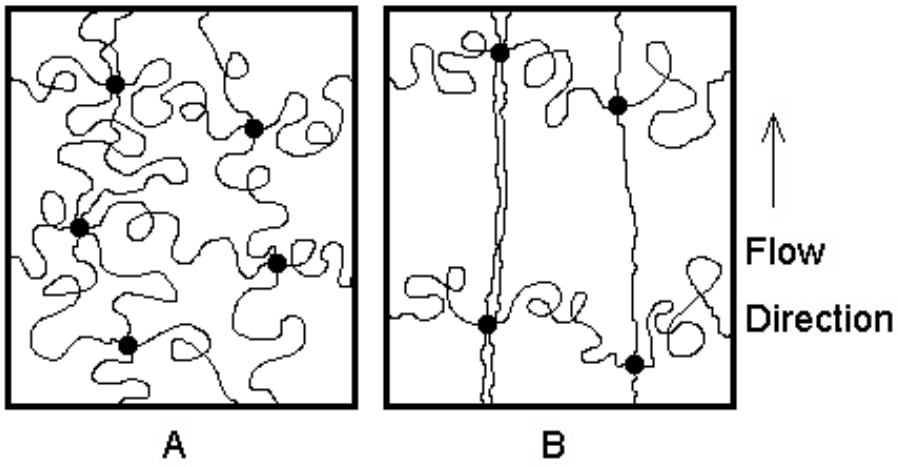

Figure 1.15. Schematic representation of the shish-kebab structure at the different stages (LMWPE chains are not shown here): (A) stable shish-kebab structure after isothermal crystallization, (B) the melting of macrokebabs during heating, (C) the melting of microkebabs and shish as an integrated entity at a higher temperature. (In (B) and (C), only chain segments are shown and the segment connectivity is omitted.)

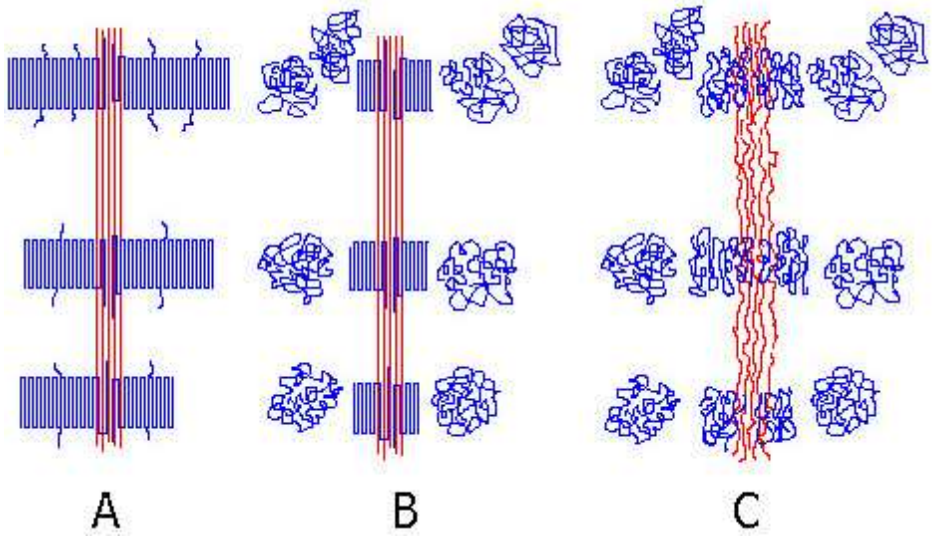

Chapter 2. The Role of Interlamellar Chain Entanglement in Deformation-Induced Structure Changes during Uniaxial Stretching of Isotactic Polypropylene

2.1. Introduction

It is well understood that molten polymer chains are entangled in a dynamic manner, where the variation of temperature does not alter the average length between the adjacent entanglement points (i.e., the entanglement length) or the entanglement density [1-2]. However, during crystallization, chain entanglements are pushed into the interlamellar amorphous region because the entanglement cannot be incorporated in the crystalline structure. Thus typical crystallization process in semi-crystalline polymers would result in an increase of entanglement density in the amorphous domain [3].

In the past, the mechanical behavior of semi-crystalline polymers has often been related to crystallinity, crystalline structure and morphology [4-9], amorphous chain orientation, as well as distribution and concentration of tie chains in the interlamellar amorphous region [10-18]. In these variables, the concept of tie chains is the most illusive one, since tie chains cannot be easily measured experimentally or predicted by current theoretical frameworks. In this study, we hypothesize that the entanglement network of amorphous chains in the interlamellar region can directly result in the formation of tie chains, thus playing a vital role to affect the overall mechanical properties and deformation-induced structure/morphology changes. Of course, some tie chains are not resulted from chain entanglements, but we speculate that the fraction of such species is small. The advantage of the entanglement-induced tie chains concept is that it can allow

us to relate the final topology of entangled chains in the interlamellar region in the solid state with molecular theories of rheology in the molten state. Although the experimental design in the present study did not allow us to directly test the effect of interlamellar chain entanglement on the mechanical properties (this will be carried out later using samples of bimodal blends with different molecular weights, where the entanglement density can be systematically change), the results indeed confirmed that the concept of entanglement-induced tie chains in the interlamellar region is consistent with the deformation-induced structure changes.

In this study, isotactic polypropylene (iPP) was chosen as a model compound for the following reasons. It is well known that iPP contains hierarchical structures, including micro-scale spherulites, nano-scale crystalline lamellae and atomic-scale crystal unit cells, typical of semi-crystalline polymers. The relationship between mechanical deformation and structure change at different length scales in iPP has been well-documented. For example, Keller et al studied the deformation behavior of micro-scale spherulites. They observed both homogenous and inhomogeneous deformation pathways within and between the spherulites [19]. Shimamura investigated the temperature dependence of spherulite change during deformation. They reported that deformation began in the equatorial region of spherulite at low temperatures, but in the meridional region at high temperatures [20]. The finding suggests that the applied stress was quite localized in the spherulite, which might reflect the variation of chain topology in the lamellar morphology. The stress localization can occur when some chain defects are pushed out from the crystalline region during crystallization. These defects will include the dangling chain ends that cannot carry stress, but they will not include stereo defects and self-looping that can carry stress. The stress localization can also occur when some amorphous chains (e.g. tie chains) that can carried more stress than the rest of the chains.

In iPP, the deformation-induced morphology and structure changes have also been well documented. On a larger scale, Peterlin et al [21, 22] reported that spherulites could be transformed into oriented fibrils above the yield point, passing through the stages of elastic deformation, plastic deformation, fragmentation of the lamellar structure, formation of fibrillar structure at high strains. From the conventional viewpoint, the deformation mechanism in semi-crystalline polymers usually includes interlamellar and intralamellar slipping of the superstructure, chain pulling-out from the folded-chain lamellae (sometimes termed mechanically-induced melting), and recrystallization and formation of oriented extended-chain crystals [23-31]. Strobl et al [32] argued that tensile deformation of semi-crystalline polymers can be considered as stretching of interpenetrated network of crystalline domains (blocks). In their model, the crystalline block can slip at small strains; but it will disintegrate and recrystallize above a critical stress. During deformation of some polymers, polymorphic transformations are also known to take place. The metastable crystal structure can prevail under strained conditions because of the reduced entropy. This behavior has been seen in iPP [33, 34] and poly(ethylene terephthalate) [35-38].

The mesomorphic form of iPP was first discovered by Natta et al [39, 40] through quenching of the melt into ice water. Later it was found that the mesomorphic phase can also be obtained by cold drawing of iPP films at room temperature [41, 42]. The mesomorphic form can be identified by the appearance of two broad peaks in the wide-angle X-ray powder diffraction pattern (or a 6-point feature in the fiber diffraction pattern), located at 2θ angles of 14.8^{o} and 21.2^{o} (based on CuKα radiation), respectively. The location of the 14.8^{o} peak is close to that of the diffuse amorphous peak from the iPP melt, but the presence of the 21.2 ^{o} peak indicates a higher order of structure from the helical chains. The infrared spectra indicated that the mesomorphic phase contains the 3_1 helical chain conformation that is very similar to that in the monoclinic crystal structure

[43-46]. The mesomorphic phase in iPP can transform into the monoclinic α-form when annealed at temperatures above 60 ^{o}C [47-50], although there seems to be a saturation level associated with the annealing time, which is a function of temperature.

Recently, there have been several in-situ and ex-situ deformation studies on polyolefin (including iPP and polyethylene, PE) using synchrotron X-ray, atomic forced microscopy (AFM), birefringence, optical microscopy (OM), electron microscopy (EM) and infrared spectroscopy (IR) techniques [51-63]. These studies revealed the different effects of varying molecular variables, such as tacticity, crystal forms, catalyst used, MWD (molecular weight distribution) on the deformation behavior of olefin-based semi-crystalline polymers. In the current study, we carried out an in-situ deformation study of iPP using combined synchrotron X-ray scattering and diffraction methods. The general results were found to be consistent with the model proposed by Peterlin et al [21, 22]. However, the difference between low and high temperature results suggested the distinct role of interlamellar chain entanglement in deformation-induced structure changes. In iPP, the unique transformation from folded-chain □-form crystals to extended-chain mesomorphic phase was the key that permitted us to make such an observation, whereas the lack of unique structure change in PE would make the similar investigation very difficult.

Based on the experimental results, we hypothesize that the existence of chain entanglements in the interlamellar amorphous region dictates the distribution of tie chains; where the strength of the entanglement network can directly affect the stability of adjacent crystal lamellae. Two likely scenarios that can be further used to rationalize this hypothesis. (1) The interlamellar amorphous region contains entangled chains, whose entanglement density is probably higher than that in the initial amorphous bulk. (2) Temperature does not change the interlamellar entanglement density, but it will

significantly alter the chain mobility. At low temperatures, the entanglement can be considered frozen because the chain dynamics is very slow; at high temperatures, the disentanglement may occur during stretching, probably by slipping. It is conceivable that the above mechanism may be a universal behavior in all semi-crystalline polymers.

2.2. Experimental

2.2.1. Materials and Preparation

In this study, a conventional Ziegler-Natta isotactic polypropylene (iPP) homopolymer was used. The material had a melt flow index of 3.2 (at 230 ˚C, 2.16 kg) and a DSC melting point of about 165 ˚C. This commercial material had an average molecular weight (M_w) of about 300 kg/mol and was used in the form of partially oriented film. The films were produced from a 20 mm 25 D extruder, equipped with a horizontal flat die and a 3 roll calendar stack. The extrusion was carried out at 240 ˚C and 10 mm/s, where the film was cast onto a chill roll with direct contact from the top roll.

2.2.2 Characterization Methods

In-situ wide-angle X-ray diffraction (WAXD) and small-angle X-ray scattering (SAXS) studies were carried out at the X27C beam line in the National Synchrotron Light Source (NSLS), Brookhaven National Laboratory (BNL). The wavelength of the synchrotron radiation was 1.371 Å. A three-pinhole collimation system was used to reduce the beam size to 0.6 mm in diameter. Two-dimensional (2D) WAXD and SAXS patterns were collected by a MAR CCD X-ray detector (MAR-USA), which had a resolution of 1024×1024 pixels (pixel size = 158.44 μm). The typical image acquisition time was 20 s for each data frame. The sample-to-detector distance was around 1850 mm

for SAXS (calibrated by a silver behenate (AgBe) standard), and was around 100 mm for WAXD (calibrated by an aluminum oxide (Al_2O_3) standard). All X-ray images were corrected for background scattering, air scattering and beam fluctuations.

Uniaxial tensile deformation was performed with a modified Instron 4442 tensile apparatus, which could stretch the film symmetrically. The symmetric stretching guaranteed that the focused X-ray beam could illuminate the same sample position during deformation. The original length of the sample between the Instron clamps was 14 mm. A constant deformation rate, 10 mm/min, was applied to the specimen throughout the deformation study. The deformation experiments were carried out at room temperature (about 25 ^{o}C), 60 ^{o}C and 160 ^{o}C, respectively. The stress and strain mentioned in this study are all engineering stress and engineering strain measured directly from the Instron machine. The heating chamber for this Instron apparatus was about 240 mm in length, which meant that the highest attainable engineering strain was only about 16.0.

2.2.3 X-ray Data Analysis

A semi-quantitative SAXS analysis was carried out to determine the changes of lamellar structure (e.g. long spacing) from the meridional scattering peaks, and the formation of fibrillar structure from the equatorial streak that might be tainted with the occurrence of micro-voids [64-66]. As the emphasis in this study was on the structure change, the WAXD results were analyzed quite extensively using the following procedures.

All 2D WAXD patterns were first corrected by the Fraser method to compensate the effect of flat-plate detection [67], and then for the background and air scattering. The corrected pattern was deconvoluted into two parts, isotropic and anisotropic contributions

(see Figure 2.1), using a "halo method" [68]. The isotropic contribution can be attributed to unoriented species, including amorphous and unoriented crystal phases; while the anisotropic contribution can be attributed to oriented species, including oriented mesomorphic and crystal phases. The principle for this deconvolution approach is that the azimuthally independent component in the total scattered profile is directly proportional to the unoriented fraction of the scatterer, which can be determined as follows. For each azimuthal scan at a specific scattering angle (2θ), the minimum value of the intensity profile can be considered as the envelope intensity of the unoriented species at that angle. By extracting all the minimum values at all scattering angles, a 2D image of the isotropic contribution is generated. This isotropic contribution is then subtracted from the total scattering image, yielding the oriented contribution. Assuming that stretched samples have a cylindrical rotational symmetry, which was true especially for samples at high strain (patterns, not shown here, taken from three orthogonal directions prove that the sample has cylindrical rotational symmetry), and a 2D pattern could contain the complete information to describe the intensity distribution in reciprocal space, and integrating over such 2D sections through 3D reciprocal space will produce the fractions of each phase. The anisotropic fraction is circularly averaged into a linear intensity profile, which can be deconvoluted into crystal and mesomorphic fractions by using the method of one-dimensional peak fitting. The same method is also applied to analyze the isotropic contribution, where the fractions of unoriented crystal and amorphous phases can be obtained. The total crystallinity index (termed crystallinity hereafter, as they are proportional to each other) is estimated by the sum of the fractions from oriented and unoriented crystal phases.

2.3. Results and Discussion

2.3.1 Uniaxial Tensile Deformation at Room Temperature

The engineering stress-strain curve of iPP film during uniaxial tensile deformation at room temperature (about 25 ^{o}C), together with selected 2D WAXD and SAXS patterns collected at different applied strains, are shown in Figure 2.2. It is seen that the orientation of the initial sample was very low. In the first 2D WAXD pattern, several nearly isotropic diffraction rings were detected, which could be indexed as (110), (040), (130) and (111)/(041), respectively (from inner to outer) using the α-form monoclinic iPP crystal structure. The corresponding SAXS pattern also exhibited a nearly isotropic ring, indicating the existence of a lamellar structure with a slight orientation. This observation is consistent with the initial spherulitic structure observed by AFM, which will be discussed later. The long period, that is the average distance between the adjacent lamellae, was estimated from the position of scattering peak using Bragg's law. The estimated long period in the iPP sample at room temperature before deformation was about 11 nm.

A yield point was seen soon after deformation began, at a strain of 0.1. The subsequent stress dropped rapidly and then increased with strain, where a two-staged linear stress-strain response was seen. The initial stage (at strains between 0.1 and 3.0) exhibited a small stress-strain ratio, which could be attributed to the necking of the sample. The final stage (at strains between 3.0 and 7.0) exhibited a large stress-strain ratio, which could be attributed to the dominant process of strain-induced crystallization (sometimes termed the strain-hardening stage). It was found that the corresponding 2D WAXD patterns changed dramatically after the yield point. Not only did the azimuthal spreads of all isotropic diffraction rings become narrower, but also the diffraction peak widths became broader, especially along the equator. The azimuthal spread of the (110) reflection peak and the linear diffraction intensity profile taken along the equator from WAXD at different strains is illustrated in Figures 2.3(A) and 2.3(B), respectively. In

Figure 2.3(B), four distinct diffraction peaks: (110), (040), (130) and (111)/(041) (from left to right), were seen in the un-deformed sample. The diffraction intensity from the (110) reflection was strong but it was nearly azimuthally independent, indicating the presence of a small degree of preferred orientation. Upon deformation, the intensities of these diffraction peaks decreased notably. In particular, at strain = 0.4, the (110) reflection on the meridian vanished rapidly, resulting in four peaks at the off-axis (Figure 2.3(A)). Such a behavior, along with the observation of decreasing intensity in the (110) reflection (Figure 2.3(B)), suggested that selective melting and rearranging of the residual structure took place. At strain = 0.6, a notable change in the structure was seen, as evidenced by the drastic increase of the equatorial (110) peak, while two off-axis shoulders remained visible (Figure 2.3(A)). The appearance of the strong equatorial (110) peak was probably due to the combined contributions of highly reoriented "original" crystals, strain-induced "new" crystals and the mesomorphic phase. The presence of weak off-axis (110) shoulders was probably dominated by the diffraction of partially oriented "original" crystals. The corresponding linear WAXD profile along the equator showed one broad peak, covering the angular range of (110), (040) and (130). The other two diffraction peaks, (111) and (041), vanished on the equator but became stronger on off-axis. The peak broadening on the equator could be attributed to the formation of the oriented mesomorphic phase, which will be discussed later. At higher strains (> 0.6 till break), the off-axis (110) peaks weakened significantly due to the further melting or/and reorientation of partially oriented "original" crystals, while the equatorial (110) peak increased and became broader due to the growth of the oriented mesomorphic phase. The corresponding 3D WAXD patterns are illustrated in Figure 2.4. These patterns showed a clear structure change from crystal to mesomorphic phases.

The changes of mass fractions from different phases are illustrated in Figure 2.5. It was seen that, at the initial stage of uniaxial tensile deformation (strain < 1.0), both

fractions of crystal and amorphous phases decreased with strain, while the corresponding fraction of oriented mesomorphic phase increased rapidly. This suggests that, at room temperature, some crystals were destroyed, where the oriented mesomorphic phase was formed from both stretched amorphous phase and destroyed crystal phase. The possible mechanism of this transition will be discussed later. At strains above 1.0, the fraction of crystal phase began to increase at a rate similar to that of the oriented mesomorphic phase. The slight increase of the crystals fraction can be attributed to several coupled effects: (1) destruction of "original" crystals, (2) reorientation of "original" crystals (since the fraction of unoriented crystals continued to decrease) and (3) formation of highly oriented "new" crystals (may be in the form of extended-chain crystals). It is interesting to note that the fraction of oriented crystal phase exhibited a minimum value at the strain about 1.0, whereas the fraction of unoriented crystal phase decreased monotonically. At high strains (i.e., > 5.0), the unoriented crystals vanished completely, leaving behind only unoriented amorphous, oriented crystal and oriented mesomorphic phases (the fraction of mesomorphic phase was above 60%, the fraction of oriented crystal phase was about 30%, and the fraction of unoriented amorphous phase was less than 10%).

Selected 3D SAXS patterns during deformation are illustrated in Figure 2.6. It was seen that upon stretching, the initial isotropic scattering ring in the SAXS pattern became two-bar like, which gradually disappeared with increasing strain. This is reasonable since the density of the crystal phase is slightly larger than that of the mesomorphic phase, the formation of oriented mesomorphic phase would gradually decrease the scattered intensity. The two-bar SAXS pattern on the meridian indicates two possible scenarios. (1) The "original" lamellar stacks that were parallel to the stretching direction were destroyed (e.g. by chain pulling-out). (2) The "original" lamellar stacks became fragmented and reoriented along the direction perpendicular to the stretching direction. It was found that the long period increased from 11.1 nm to 11.8 nm and 12.8 nm at strains

of 0.0, 0.1 and 0.4, respectively. Uniaxial tensile deformation clearly enlarged the average distance between the lamellae along the stretching direction. However, due to the small density difference between the mesomorphic and crystal phases at room temperature as well as the reduced thickness of the sample during deformation, the SAXS intensity became quite weak. At the later stage of deformation, the SAXS pattern exhibited a strong equatorial streak, probably due to stress-induced microvoids (the dominant contribution) and strain-induced crystalline fibrils (the minor contribution) arising during deformation until the stretched iPP film was broken at a strain of about 6.8.

2.3.2. Uniaxial Tensile Deformation at High Temperatures

Uniaxial tensile deformation of iPP film was also carried out at two higher temperatures: 60 and 160 ^{o}C. The engineering stress-strain curve and selected 2D WAXD and SAXS patterns obtained at 60 ^{o}C are illustrated in Figure 2.7. The observed engineering stress-strain curve was generally similar to that obtained at room temperature. However, distinct structure differences were also seen. The linear WAXD profiles along the equatorial direction extracted from Figure 2.7 are illustrated in Figure 2.8. It was found that the orientation of iPP crystal structure occurred at a much higher strain than that at room temperature, evidenced by the disappearance of the (111)/(041) doublet peak on the equator. At room temperature, this doublet migrated to off-axis position at a strain about 1.0, while this shift took place at a strain about 2.0 at 60 ^{o}C. It was interesting to note that the □-form crystal structure never vanished during deformation, where three distinct diffraction peaks ((110), (040) and (130)) can be seen even at a high strain of 9.0 before breaking. However, these three peaks overlapped with each other to some extent, indicating that both crystal and mesomorphic phases co-existed at high strains.

The mass fractions of different phases (amorphous, mesomorphic and crystal, including oriented and unoriented crystals) during deformation are illustrated in Figure 2.9. Similar to the case at room temperature, the fraction of oriented mesomorphic phase increased with strain. However, the fraction of the total crystal phase increased slightly at strains > 1.0, instead of decreasing as seen at room temperature. The total crystallinity increase was mainly due to the increase in oriented crystals, since the fraction of unoriented crystals decreased upon deformation. This suggests that the crystal destruction was a minor event. The major events were the orientation of some "originated" crystals and formation of "new" crystals. The notable increase of the oriented mesomorphic phase could be mainly attributed to the decrease in the amorphous phase fraction.

Uniaxial tensile deformation was also carried out at 160 ^{o}C, near the melting point of iPP, and the results are shown in Figure 2.10. Under this condition, the elongation-to-break ratio (at a strain > 16.0, which was the limit of our heating chamber) was significantly larger than those at lower temperatures. From corresponding 2D WAXD and SAXS patterns, the azimuthal spreads for both diffraction and scattering peaks became quite narrow with increasing strain, indicating the increase in orientation at both crystal structure and lamellar scales. The linear WAXD profiles taken along the equatorial direction are illustrated in Figure 2.11. Different from the cases under room temperature and 60 ^{o}C, no peak broadening was found during deformation at 160 ^{o}C. It was seen that the intensities of all equatorial peaks increased drastically with strain, and the apparent crystallinity remained high even near the melting point. At strains higher than 10.0, the (111) and (041) doublet peaks disappeared from the equator (they moved to the off-axis); but (150) and (060), corresponding to 2θ at 21.9^{o}, and (200) reflection, corresponding to 2θ at 24.2^{o}, remained visible. The full widths at half maximum (FWHM) of reflections from (110) (040) and (130) crystal planes all showed a two-staged increase with strain (a rapid increase at low stains and a slow increase at high strains) at all temperatures during

deformation. The value of FWHM is related to the combined effects of crystal size and lattice distortion.

From the 2D SAXS patterns in Figure 2.10, the following observations were made. Above the "yield" point (at strain about 1.0), the scattering maxima quickly converged onto the meridian, forming a two-bar pattern, indicating that the crystal fragmentation also occurred at 160 ^{o}C. However, by comparing with the SAXS patterns at 60 ^{o}C, the high temperature SAXS pattern showed a smaller scattering bar, indicating a larger lamellar structure. It appeared that less crystal fragmentation took place at 160 ^{o}C than that at low temperatures (room temperature and 60 ^{o}C). The total scattered intensity was found to increase with strain, probably due to the partial melting of small crystals or/and the decrease of the mesomorphic fraction, and both could enhance the scattering contrast. The average long period along the meridian during deformation at 160 ^{o}C was larger than those at lower temperatures. It was interesting to note that an equatorial streak appeared at strains above 2.0 and it increased with increasing strain. This streak feature, judging by its much weaker intensity (than those of room temperature and 60 ^{o}C), was probably resulted mainly from the fibrillar morphology instead of micro-voids. This is because the scattered intensity from micro-voids should be significantly higher due to the larger density contrast (we note that the streak intensity at 160 ^{o}C was only about several percent of those at room temperature and 60 ^{o}C).

The linear intensity profiles taken along the meridional direction of the 2D SAXS patterns are illustrated in Figure 2.12(A). It is interesting to note that at the initial stage of deformation, the position of the scattering peak shifted to a lower q value; upon further deformation, it shifted back to near the original position [52]. The corresponding long period for the lamellae structure estimated by Bragg's law is plotted in Figure 2.12(B). The increase in long period at strains < 1.0 could be attributed to the elastic deformation

of iPP crystals. The long period was found to decrease at strains between 1.0 and 3.0 (the maximum long period value was seen at strain = 1.0), and then it reached a plateau value of 32 nm at strains between 3.0 and 11.0. This behavior can be explained by the fragmentation and the strain-induced crystallization coupled with slippage process between fragmented crystal and strain-induced melting. Based on the WAXD results, we argue that the formed strain-induced crystals at 160 ^{o}C are in the form of lamellae with folded-chain conformation. The long period was found to decrease again at strains >11.0, which might be due to the limitation of slippage.

The evolution of mass fractions for different phases during deformation at 160 ^{o}C is shown in Figure 2.13. It was seen that the fraction of amorphous phase decreased continuously and nearly disappeared at strain = 16.0, but we do observe a clear SAXS pattern at the end of deformation indicating the electron density difference between amorphous and crystal phase. The reason is probably due to the limitation of our analysis method, since the amorphous phase can also oriented slightly resulting in more scattering intensity at the equator which was attributed to the mesophase during analysis. The total crystal fraction showed a two-staged increase with a faster rate at low strains (< 2.0) and a slower rate at high strains (> 2.0). The change of oriented crystal fraction was similar to that of total crystal fraction, but with an enhanced magnitude at the initial stage. The difference was due to the variation of unoriented crystal fraction, which showed a maximum value at strain = 1.0. This response was consistent with the observed maximum long period also at strain = 1.0. In contrast to the large increase at lower temperatures (room temperature and 60 ^{o}C), the fraction of mesomorphic phase was about constant (at about 35%) during deformation at 160 ^{o}C. This suggests that the major transition induced by deformation at this temperature is mainly between the amorphous and crystal phases. The above findings are consistent with the hypothesis that entangled coiled chains are crystallized into lamellar crystals with folded-chain conformation [69] under low strains

near the nominal melting point (160 ^{o}C), and can be disentangled at very high strains (e.g. at strain = 16.0).

2.3.3. Morphology and Crystal Orientation at Various Temperatures

In order to develop a reasonable molecular mechanism to explain the above observations, we have also compared the AFM results with combined SAXS and WAXD images of three representative morphologies from quenched samples prepared under different deformation conditions. The comparisons are shown in Figure 2.14. In the undeformed initial iPP sample, a distinct spherulitic morphology with very slight orientation was seen (probably caused by an uneven squeeze flow during melt pressing). This was consistent with WAXD and SAXS images, which also showed slightly oriented diffraction and scattering rings. When the iPP film was stretched to a strain of 4.0 at 60 ^{o}C, the AFM image exhibited a distinct fibrillar structure with fibrils aligned parallel to each other along the stretching direction, consistent with the two meridional scattering bars in the SAXS pattern arising due to the well oriented and correlated layered-like folded-chain lamellae. The narrow azimuthal spreads of the WAXD peaks indicated that the crystal□-form) orientation increased with the draw ratio. However, the analysis showed that the mass faction of oriented mesomorphic phase was larger than 50 % and that of oriented crystal phase was about 40%, indicating the co-existence of mixed lamellar crystals (in □-form) and mesomorphic (with no preferred registration of helical hands) structures. We note that it is not possible to distinguish the crystal and mesomorphic phases from AFM measurements. This is because there is not much difference in the modulus and hardness between the two phases, where the AFM technique cannot probe into the structures of the ordered domains. Nevertheless, the structure difference became very distinct by the X-ray diffraction technique. It is interesting to see that when the iPP film was stretched to the strain of 16.0 at 160 ^{o}C, a

very weak equatorial streak was still remained, which could be attributed to the presence of extended-chain mesomorphic microfibrils instead of micro-voids since the latter could not be found by AFM measurements of the quenched iPP film. The existence of the two-bar pattern at a lower scattering angle indicated the persistence of a highly oriented crystal lamellar structure with a larger spacing. This was also consistent with the WAXD pattern exhibiting well-oriented □-form crystals.

The chain orientation (*f*) in the crystal structure can be calculated by Hermans' orientation function [70]:

$$f = \frac{3\langle \cos^2 \phi \rangle - 1}{2}$$

where ϕ is the angle between the chain axis and the reference axis (stretching direction). $\langle \cos^2 \phi \rangle$ is defined as:

$$\langle \cos^2 \phi \rangle = \frac{\int_0^{\pi/2} I(\phi) \cos^2 \phi \sin \phi d\phi}{\int_0^{\pi/2} I(\phi) \sin \phi d\phi}$$

where $I(\phi)$ is the scattered intensity along the angle ϕ. However, since there is no plane of symmetry perpendicular to the chain axis, $\langle \cos^2 \phi \rangle$ is calculated from the crystal (110) and (040) reflections.

$$\langle \cos^2 \phi \rangle = 1 - 1.090 \langle \cos^2 \phi_{110} \rangle - 0.901 \langle \cos^2 \phi_{040} \rangle$$

The calculated Hermans' orientation factors are shown in Figure 2.15. It was seen that the initial sample possessed a value of about zero, representing a random orientation of polymer crystals (in the lamellar form). During stretching, the crystal alignment increased asymptotically toward the value of one, representing the perfect alignment of polymer chains in lamellar crystals along the stretching direction. The rate of crystal alignment during deformation at high temperatures was found to be slower than that at low

temperature, but the final orientation during deformation at high temperatures was higher due to the higher applied strain.

2.3.4 The role of interlamellar chain entanglement

It the past, the mechanical properties of semi-crystalline polymers were often considered from the viewpoint of crystallinity, crystalline morphology and tie chains. Tie chains are viewed as tightly stretched chain segments connecting the adjacent crystals. The higher tie chain concentration can lead to a stronger mechanical property in semi-crystalline polymers. The concept of tie chains is clearly related to the subject of this study, but it can only be used to explain parts of the experimental results. This is because the presence of tie chains can initiate the fragmentation of folded-chain lamellae at high strains, which is consistent with the results from deformation at lower temperatures, but it should not increase the fraction of folded-chain lamellar crystals at high temperatures and high strains.

Based on experimental observations in this study, we present a new mechanism that can sufficiently explain deformation results at both low and high temperatures. This mechanism considers the role of chain entanglement in the interlamellar amorphous layers. As described earlier, since the total entanglement density in the sample is not likely to decrease by folded-chain crystallization, the resulting entanglement density in the interlamellar amorphous region after crystallization must be higher than that in the initial melt. We hypothesize that tie chains are mainly due to the consequence of chain entanglements, which carry the major mechanical load in the interlamellar amorphous region. Of course, some tie chains can also occur without the presence of chain entanglement, but the fraction may be small. In the above scenario, two features should be noted (1) the distribution of tie chains may be quite heterogeneous in the interlamellar

region, and its concentrated mostly around the vicinity of the entanglement, and (2) some amorphous chains without the influence of chain entanglement may not carry any mechanical load during the initial stage of mechanical deformation. The second feature is consistent with the persistent observation of the amorphous fraction at low strains under both low and high temperatures.

The role of chain entanglement and its relationship with tie chains during deformation-induced structure change in semi-crystalline polymers is schematically illustrated in Figure 2.16. In the middle diagram, a typical folded-chain lamellar assembly (colored in green) is shown, where the entanglement points (colored in blue) are contained in the interlamellar amorphous region. During deformation at low temperatures (e.g. room temperature), the poor chain mobility would restrict the motion of chain slipping and thus the disentanglement process. As a result, the overall stability of the entanglement network will be stronger than that of the crystalline network. With increasing strains, some polymer chains in the crystal lamella may be pulled out due to the tie chains from the entanglement, resulting in the process of lamellar fragmentation or mechanical-induced melting. In iPP, the stretched-out chains can transform into the oriented mesomorphic phase (colored in yellow, left diagram of Figure 2.16) having extended-chain conformation but no regular registration of helical hands as in the crystals. At high temperatures (e.g. at 160 ^{o}C), the enhanced chain mobility can significantly weaken the amorphous entanglement network, thus the crystalline network becomes the dominant structure. As a result, the tensile deformation would affect mainly the amorphous region, where stretching can lead to disentanglement through chain slipping and can reduce the constraints of further folded-chain crystallization from other coiled segments. The process of an increase in folded-chain crystallization during deformation at high temperatures is shown in the right diagram of Figure 2.16. Thus, the total fraction of the folded-chain lamellar crystals (in □-form) can increase with strain,

which was seen experimentally (Figure 2.13). We note that the fraction of the mesomorphic phase remained about constant during deformation at 160 ^{o}C, suggesting that the pre-existing structure of the mesomorphic phase might not be significantly affected by deformation, except that it became much more oriented. In the case of deformation at an intermediate temperature, the scenario may be in between the two cases described above, depending on the relative strength difference between the entanglement network and the crystalline network. We note that the structure change during deformation at 60 ^{o}C is more similar to that at room temperature, instead of at 160 ^{o}C.

2.4 Conclusions

From the deformation study of iPP at three different temperatures (i.e., room temperature, 60 and 160 ^{o}C), we conclude that the role of chain entanglement in the interlamellar amorphous region plays an important role in affecting the structure changes. At low temperatures, as the chain mobility is low, the relative strength of the interlamellar entanglement network is stronger than that of the surrounding crystalline structure. As a result, the tie chains from the entanglement may initiate fragmentation of lamellar crystals upon deformation, forming an oriented mesomorphic phase in the form of extended-chain conformation. This is consistent with both WAXD and SAXS results from deformation of iPP at room temperature and 60 ^{o}C. At high temperatures, as the chain mobility is high, the crystalline network becomes the dominant structure. Deformation can facilitate the chain disentanglement process allowing the occurrence of more folded-chain crystallization from coiled segments. As a result, the fraction of the folded-chain crystal increases with strain, which is the case for deformation at 160 ^{o}C. In the conventional view point, the presence of tie chains is difficult to predict. However, the concept of chain entanglement-induced tie chains will permit us to connect melt rheology to the solid state amorphous chain topology and thus final properties.

List of References

1. Doi, M.; Edwards, S. F. *The Theory of Polymer Dynamics* (Clarendon Press, Oxford, 1986).
2. De Gennes, P. G. *Scaling Concepts in Polymer Physics* (Cornell Univ. Press, Ithaca, 1979).
3. Rastogi, S.; Lippits, D. R.; Peters, G. W. M.; Graf, R.; Yao, Y.; Spiess, H. W. *Natural Materials* **2005**, *4*, 635.
4. Yamada, K.; Kamezawa, M.; Takayanagi, M. *J. Appl. Polym. Sci.* **1981**, *26*, 49.
5. De Rosa, C.; Auriemma, F.; De Lucia, G.; Resconi, L. *Polymer* **2005**, *46*, 9461.
6. Hong, K.; Rastogi, A.; Strobl, G. *Macromolecules* **2004**, *37*, 10174.
7. Al-Hussein, M.; Strobl, G. *Macromolecules* **2002**, *35*, 8515.
8. Schrauwen, B. A. G.; Janssen, R. P. M.; Govaert, L. E.; Meijer, H. E. H. *Macromolecules* **2004**, *37*, 6069.
9. Schrauwen, B. A. G.; Breemen, L. C. A.; Spoelstra, A. B.; Govaert, L. E.; Peters, G. W M.; Meijer, H. E. H. *Macromolecules* **2004**, *37*, 8618.
10. Keith, H. D.; Padden, F. J. Jr.; Vadimsky, R. G. *J. Polym. Sci., Polym. Phys. Ed.* **1966**, *4*, 267.
11. Lustiger, A.; Markham, R. L. *Polymer* **1983**, *24*, 1647.
12. Huang, Y.; Brown, N. *J. Polym. Sci., Part B: Polym. Phys.* **1991**, *29*, 129.

13. Porter, R. S.; Wang, L. *J. Macromol. Sci., Rev. in Macromol. Chem. Phys.* **1995**, *C35*, 63.

14. Ishikawa, M.; Ushui, K.; Kondo, Y.; Hatada, K.; Gima, S. *Polymer* **1996**, *37*, 5375.

15. Nitta, K.; Takayanagi, M. *J. Polym. Sci., Part B: Polym. Phys.* **1999**, *37*, 357.

16. Janimak, J. J.; Stevens, G. C. *J. Mater. Sci.* **2001**, *36*, 1879.

17. Spitalsky, Z; Bleha, T. *Polymer* **2003**, *44*, 1603.

18. Seguela, R. *J. Polym. Sci. Part B: Polym. Phys.* **2005**, *43*, 1729.

19. Hay, I. L.; Keller, A. *Kolloid. Z. Z. Polym* **1965**, *204*, 43.

20. Shimamura, K. *In Morphology of Polymers. Proceedings 17th Europhysics Conference on Macromolecular Physics Pargue, Czechoslovakia,,* **1985**.

21. Peterlin, A. *J. Mater. Sci.* **1971**, *6*, 490.

22. Peterlin, A. *Colloid Polym. Sci.* **1987**, *265*, 357.

23. Flory, P.; Yoon, D. *Nature (London)* **1978**, *272*, 226.

24. Bowden, P.; Young, R. *J. Mater. Sci.* **1974**, *9*, 2034.

25. Popli, R.; Mandelkern, L. *J. Polym. Sci. Polym. Phys. Ed.* **1987**, *25*, 441.

26. Galeski, A. *Prog. Polym. Sci.* **2003**, *28*, 1643.

27. Hiss, R.; Hobeika, S.; Lynn, C.; Strobl, G. *Macromolecules* **1999**, *32*, 4390.

28. Ferreiro, V.; Coulon, G. *J. Polym. Sci., Polym. Phys. Ed.* **2004**, *42*, 687.

29. Hu, W. G.; Schmidt-Rohr, K. *Acta. Polym.* **1999**, *50*, 271.

30. De Rosa, C.; Auriemma, F.; de Ballesteros, O. R. *Phys. Rev. Lett.* **2006**, *96*, 167801.

31. Men, Y.; Riger, J.; Homeyer, J. *Macromolecules* **2004**, *37*, 9481.

32. Men, Y.; Rieger, J.; Strobl, G. *Phys. Rev. Lett.* **2003**, *91*, 095502.

33. Ran, S.; Zong, X.; Fang, D.; Hsiao, B. S.; Chu, B.; Phillips, R. A. *Macromolecules* **2001**, *34*, 2569.

34. Ran, S.; Zong, X.; Fang, D.; Hsiao, B. S.; Chu, B.; Cunniff P. M.; Phillips, R. A. *J. Materials Sci.* **2001**, *36*, 3071.

35. Ran, S.; Wang, Z.; Burger, C.; Chu, B.; Hsiao, B. S. *Macromolecules* **2002**, *35*, 10102.

36. Kawakami, D.; Ran, S.; Burger, C.; Fu, B.; Sics, I.; Hsiao, B. S. *Macromolecules* **2003**, *36*, 9275.

37. Kawakami, D.; Ran, S.; Burger, C.; Fu, B.; Sics, I; Hsiao, B. S.; Kikutani, T. *Polymer* **2004**, *45*, 905.

38. Kawakami, D.; Hsiao, B. S.; Ran, S.; Burger, C.; Avila-Orta, C.; Sics, I.; Kikutani, T.; Jacob, K.; Chu, B. *Macromolecules* **2005**, *38*, 91.

39. Natta, G.; Peraldo, M.; Corradini, P. *Rend. Accad. Naz. Lincei* **1959**, *26*, 14.

40. Natta, G.; Corradini, P. *Nuovo Cimento, Suppl.* **1960**, *15*, 40.

41. Wyckoff, H. W. *J. Polym. Sci.* **1962**, *62*, 83.

42. Morosoff, N.; Peterlin, A. *J. Polym. Sci.* **1972**, *A-2(10)*, 1237.

43. Jones, A. T.; Aizlewood, J. M.; Beckett, D. R. *Makromolekulare Chemie* **1964**, *75*, 134.

44. Brucker, S.; Meille, S. V.; Petraccone, V.; Pirozzi, B. *Prog. Polym. Sci.* **1991**, *16*, 361.

45. Lotz, B.; Wittmann, J. C.; Lovinger, A. J. *Polymer* **1996**, *37*, 4979.

46. Miller, R. L. *Polymer* **1960**, *1*, 135.

47. Zannetti, R.; Celotti, G.; Fichera, A. Francesconi, R. *Makromol. Chem*. **1969**, *128*, 137.

48. Zannetti, R.; Celotti, G.; Armigliato, A. *Eur. Polym. J.* **1970**, *6*, 879.

49. De Candia, F.; Iannelli, P.; Staulo, G.; Vittoria, V. *Colloid Polym. Sci.* **1988**, *266*, 608.

50. Vittoria, V. *J. Macromol. Sci. Phys.* **1989**, *B28(2&3)*, 489.

51. Song, Y.; Nitta, K.; Nemoto, N. *Macromolecules* **2003**, *36*, 1955.

52. Nozue, Y.; Shinohara, Y.; Ogawa, Y.; Sakurai, T.; Hori, H.; Kasahara, T.; Yamaguchi, N.; Yagi, N.; Amemiya, Y *Macromolecules* **2007**, *40*, 2036.

53. Sakurai, T.; Nozue, Y.; Kasahara, T.; Mizunuma, K.; Yamaguchi, N.; Tashiro, K.; Amemiya, Y. *Polymer* **2005**, *46*, 8846.

54. Koike, Y.; Cakmak, M. *Macromolecules* **2004**, *37*, 2171.

55. Koike, Y.; Cakmak, M. *Polymer* **2003**, *44*, 4249.

56. Koike, Y.; Cakmak, *J. Polym. Sci., Polym. Phys.* **2006**, *44*, 925.

57. Li, J. X.; Cheung, W. L.; Chan, C. M. *Polymer* **1999**, *40*, 3641.

58. Li, J. X.; Cheung, W. L.; Chan, C. M. *Polymer* **1999**, *40*, 2089.

59. Aboulfaraj, M.; G'Sell, C.; Ulrich, B.; Dahoun, A. *Polymer* **1995**, *36*, 731.

60. Zhang, X. C.; Butler, M. F.; Cameron, R. E. *Polymer* **2000**, *41*, 3797.

61. Chu, F.; Yamaoka, T.; Kimura, Y. *Polymer* **1995**, *36*, 2523.

62. Huy, T. A.; Adhikari, R.; Lupke, T.; Henning, S.; Michler, G. H. *J. Polym. Sci., Polym. Phys.* **2004**, *42*, 4478.

63. Hong, K.; Strobl, G. *Macromolecules* **2006**, *39*, 268.

64. Wu, J. *Polymer* **2003**, *44*, 8033.

65. Aerts, J. *J. Appl. Cryst.* **1991**, *24*, 709.

66. Wu, J.; Schultz, J. M.; Yeh, F.; Hsiao, B. S.; Chu, B. *Macromolecules* **2002**, *33*, 1765.

67. Fraser, R. D. B.; Macrae, T. P.; Miller, A.; Rowlands, R. J. *J. Appl. Cryst.* **1976**, *9*, 81.

68. Ran, S.; Zong, X.; Fang, D.; Hsiao, B. S.; Chu, B.; Ross, R. *J. Appl. Cryst.* **2000**, *33*, 1031.

69. Dukovski, I.; Muthukumar, M. *J. Chem. Phys.* **2003**, *118*, 6648.

70. Wilchinsky, W. Z. *J. Appl. Phys*. **1960**, *31*, 1969.

List of Figures

Figure 2.1. Procedures for deconvolution of isotropic and anisotropic contributions from a Fraser-corrected 2D WAXD pattern.

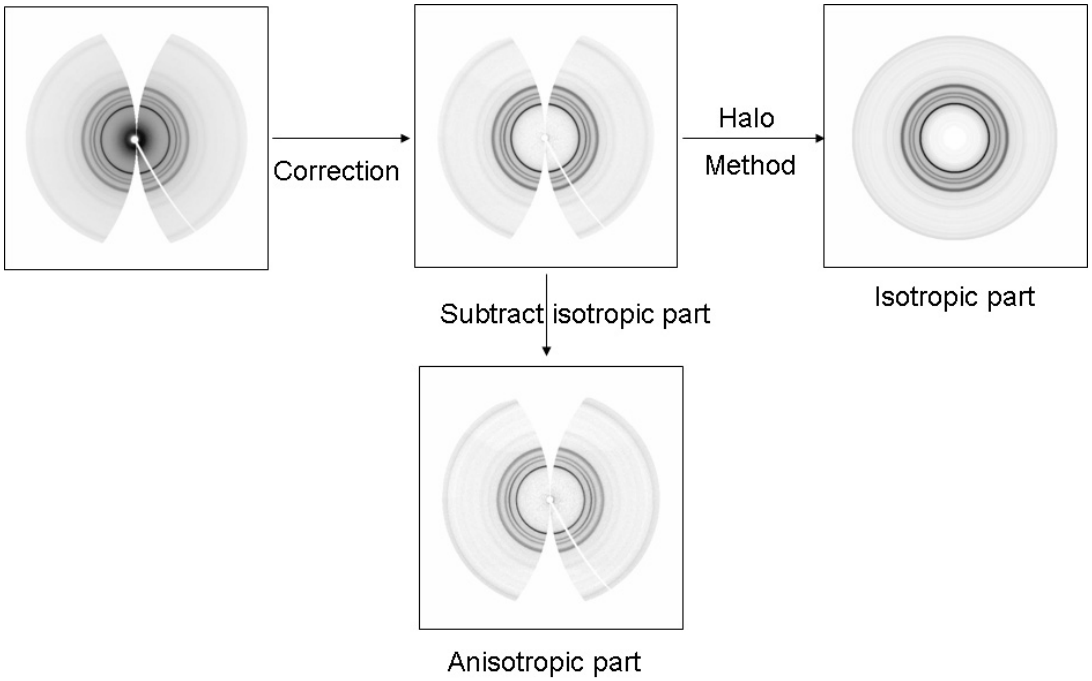

Figure 2.2. Engineering stress-strain curve and selected 2D SAXS and WAXD patterns acquired during uniaxial tensile deformation of iPP films at room temperature.

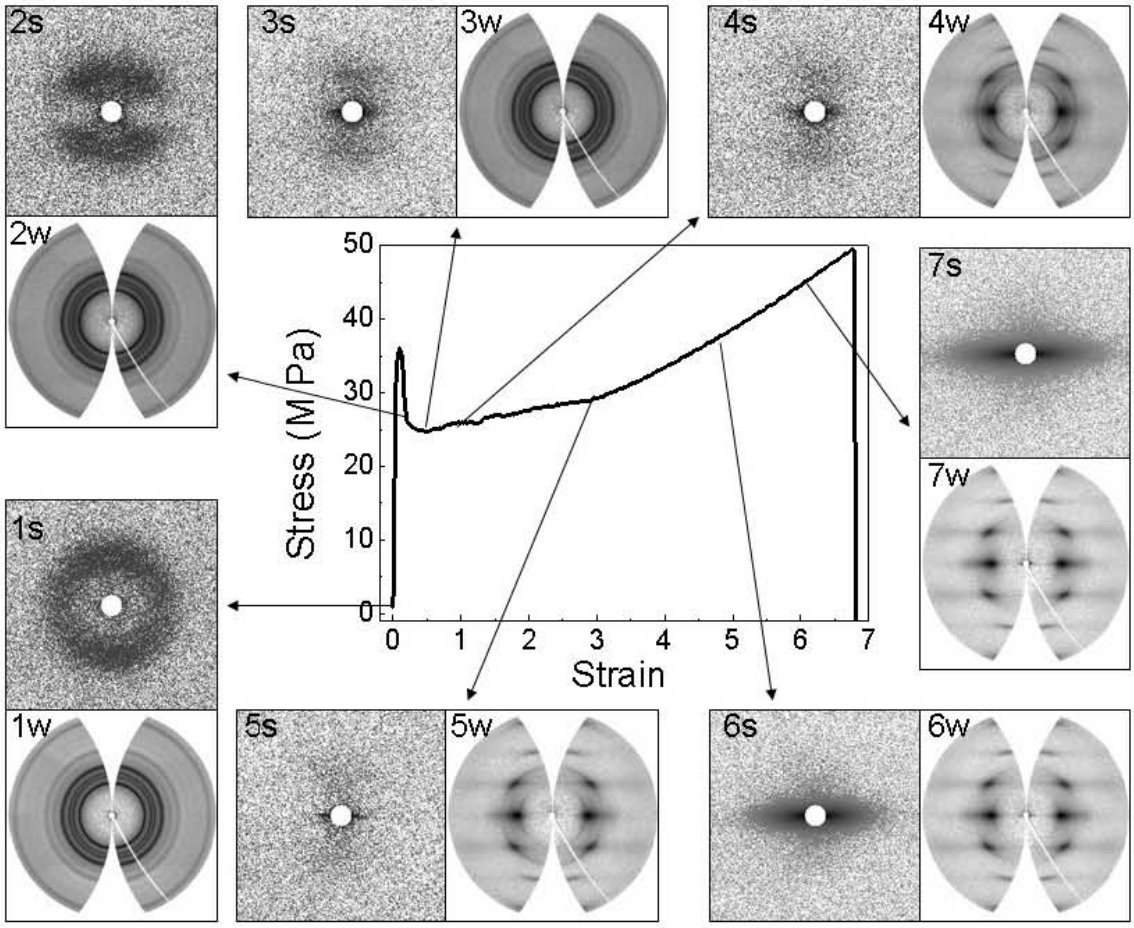

Figure 2.3. (A) The azimuthal spread of the (110) peak at varying strains, (B) linear diffraction intensity profiles taken along the equatorial direction at different strains.

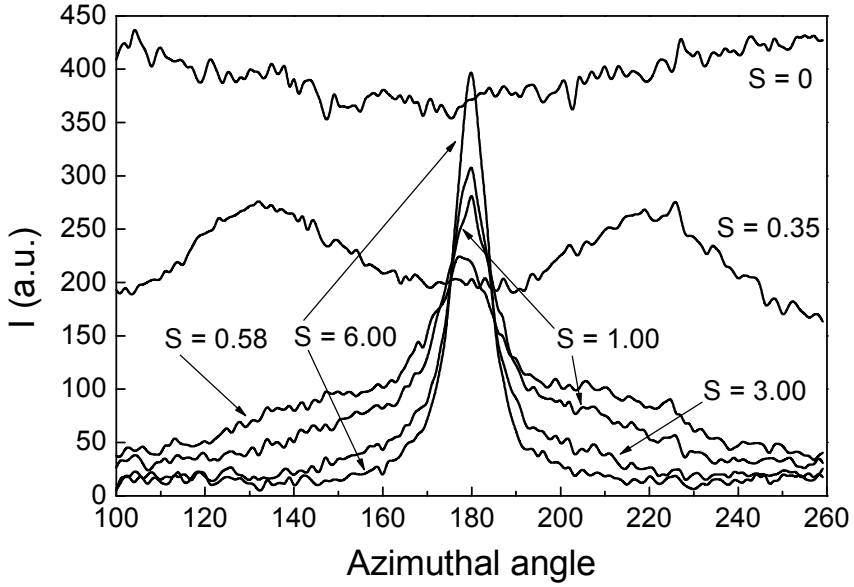

(A)

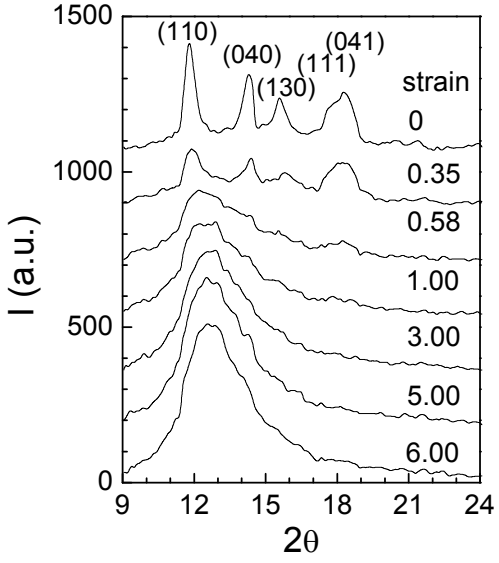

(B)

Figure 2.4. 3D WAXD patterns during uniaxial tensile deformation at room temperature.

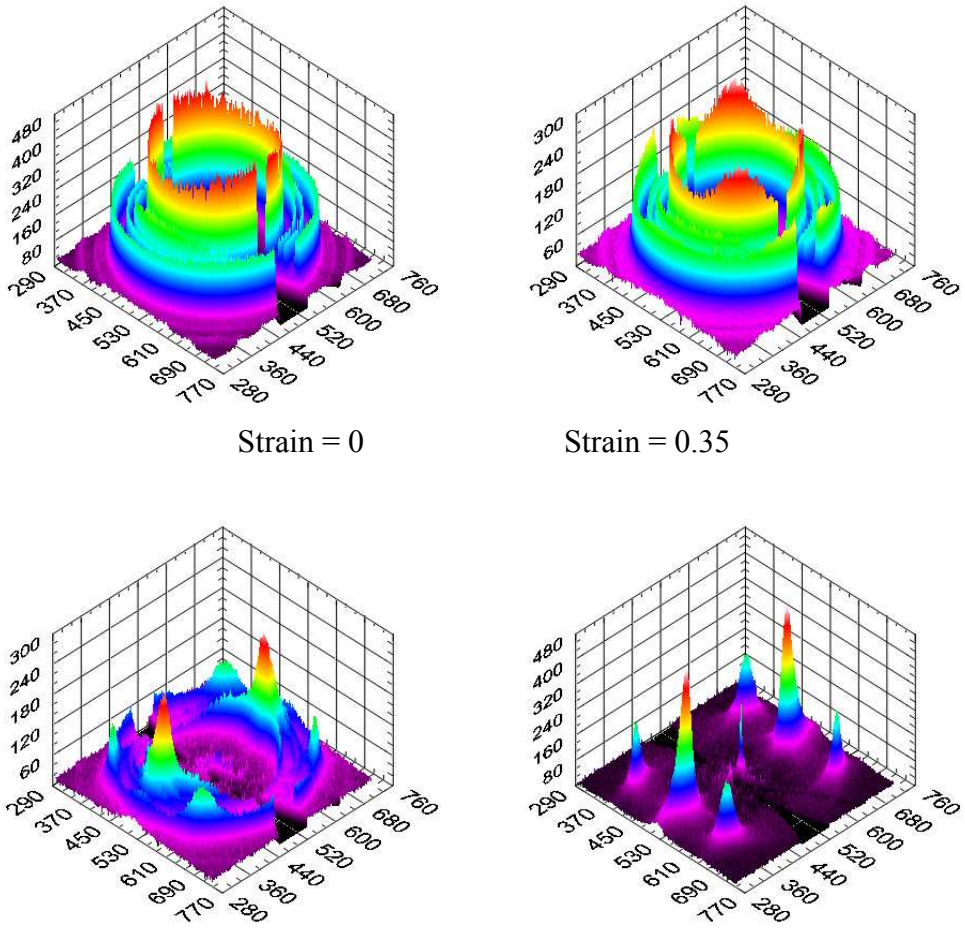

Strain = 0 Strain = 0.35

Strain = 0.58 Strain = 6.8

Figure 2.5. Evolution of the fractions of amorphous, mesomorphic and crystal (including oriented crystal and unoriented crystal) phases in the iPP film during uniaxial tensile deformation at room temperature.

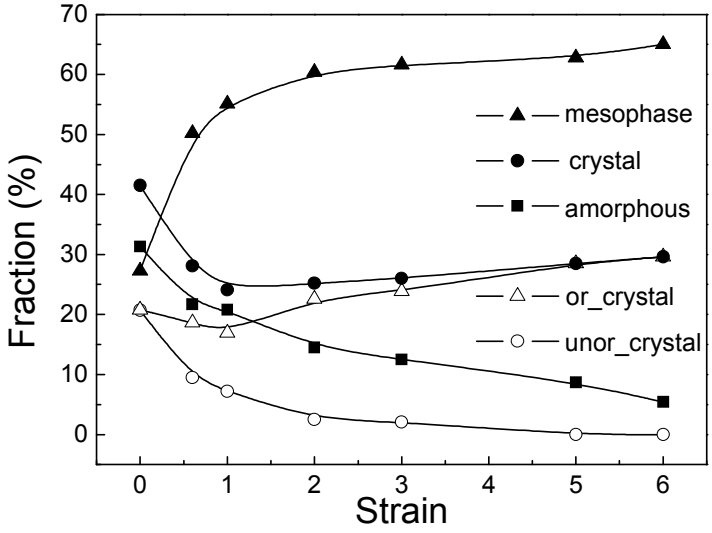

Figure 2.6. 3D SAXS patterns during uniaxial tensile deformation at room temperature.

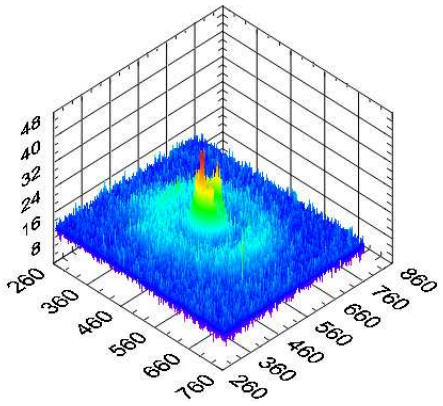

Strain = 0

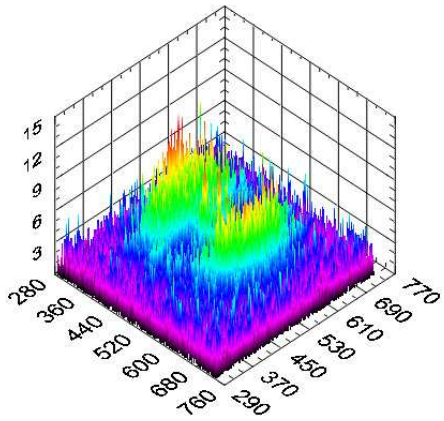

Strain = 0.12

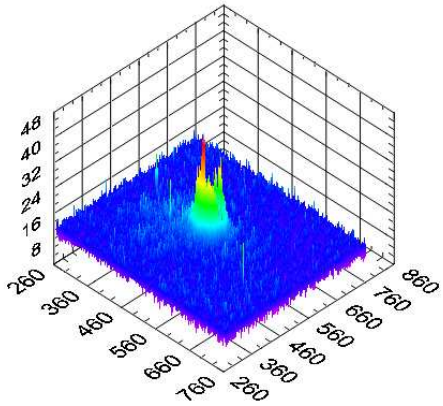

Strain = 1

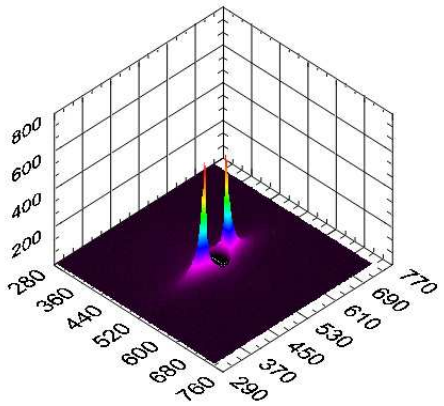

Strain = 6.8

Figure 2.7. Engineering stress-strain curve and selected 2D SAXS and WAXD patterns acquired during uniaxial tensile deformation of iPP films at 60 ^{o}C.

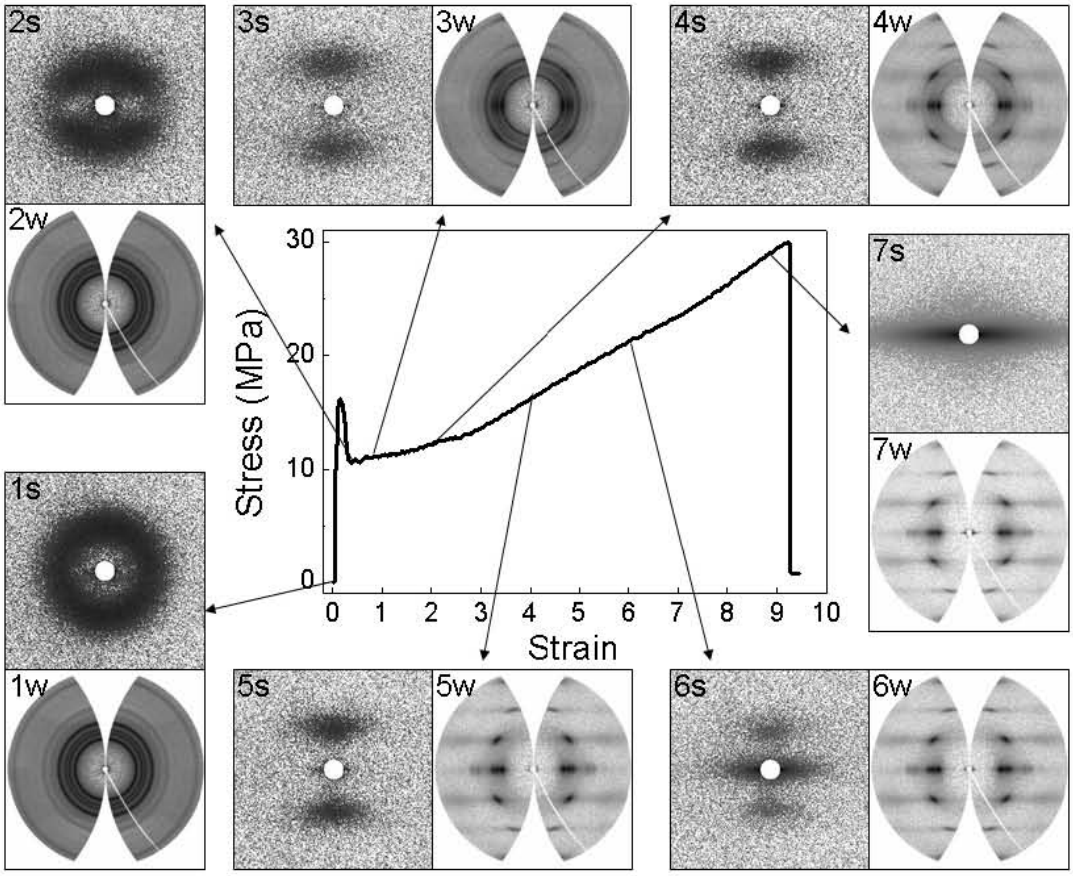

Figure 2.8. Linear WAXD profiles along the equatorial direction at different strains during uniaxial tensile deformation.

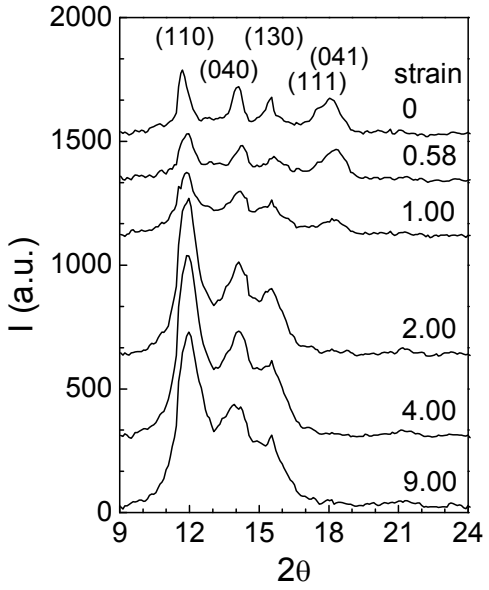

Figure 2.9. Evolution of mass fractions of amorphous, mesomorphic and crystal (including oriented crystal and unoriented crystal) phases in the iPP film during uniaxial tensile deformation at 60 ^{o}C.

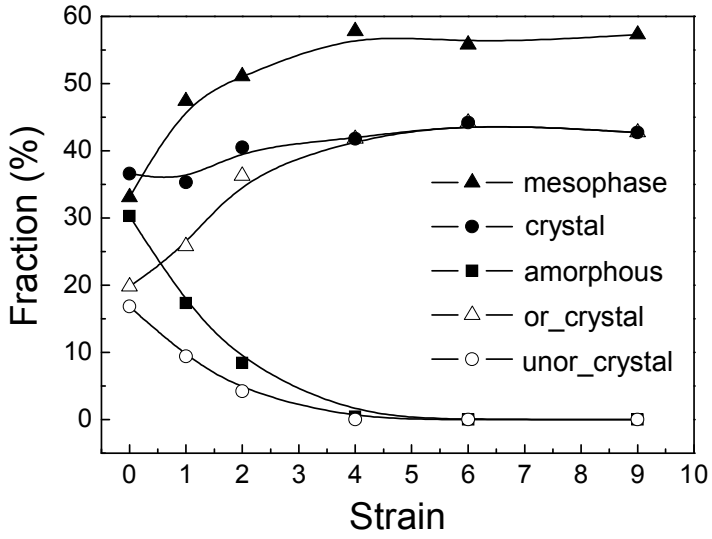

Figure 2.10. Engineering stress-strain curve and selected 2D SAXS and WAXD patterns acquired during stretching of iPP films at 160 ^{o}C.

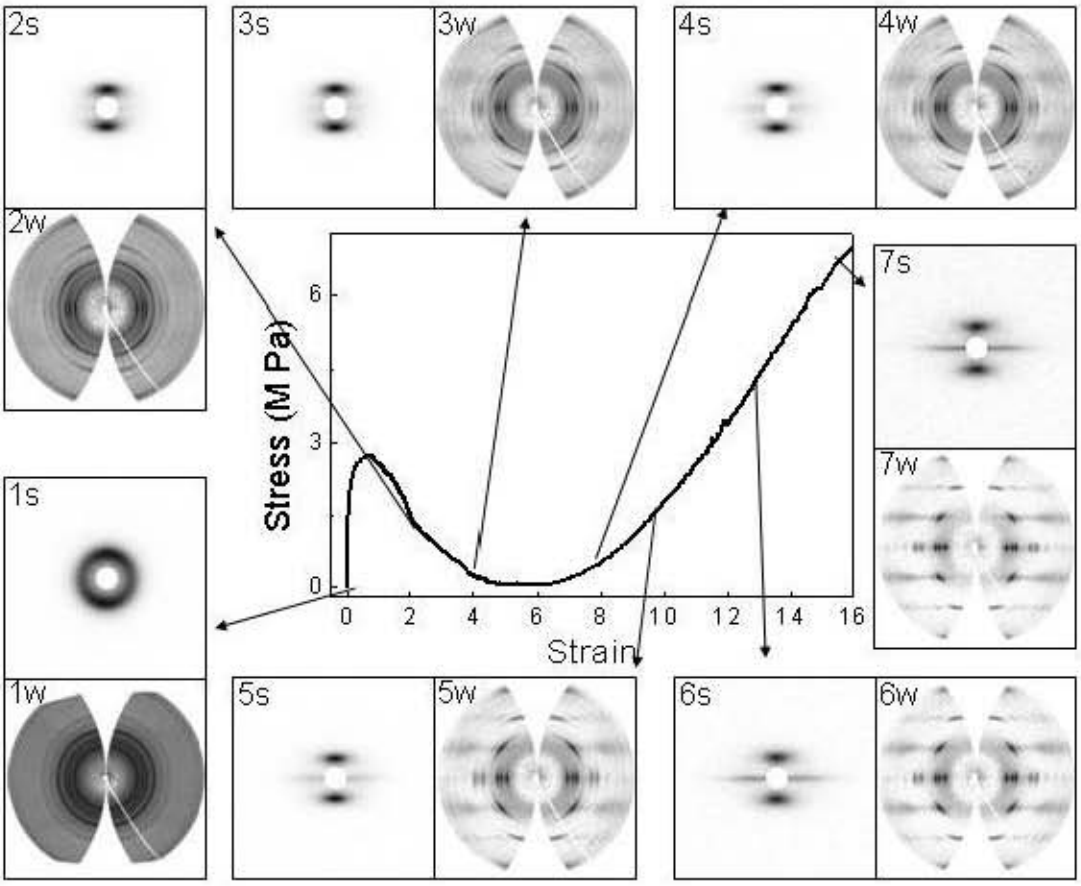

Figure 2.11. Linear WAXD profiles along the equatorial direction at different strains during stretching of iPP film at 160 ^{o}C.

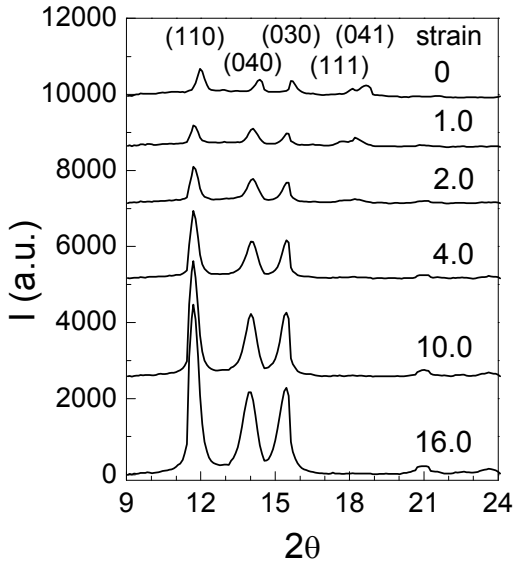

Figure 2.12. (A) Linear SAXS intensity profiles taken along the meridional direction at different strains during uniaxial tensile deformation, and (B) corresponding change of long period as a function of strain.

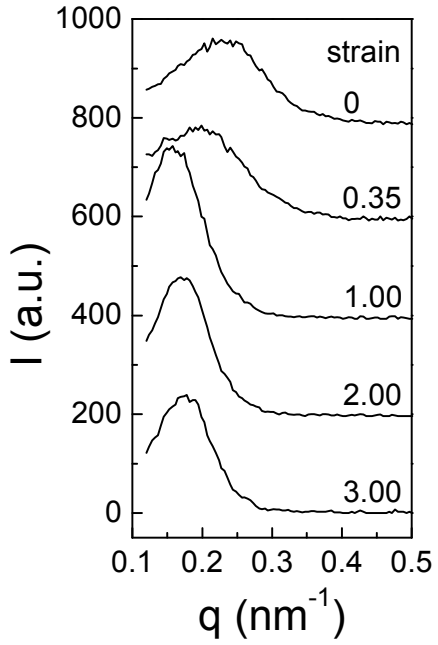

(A)

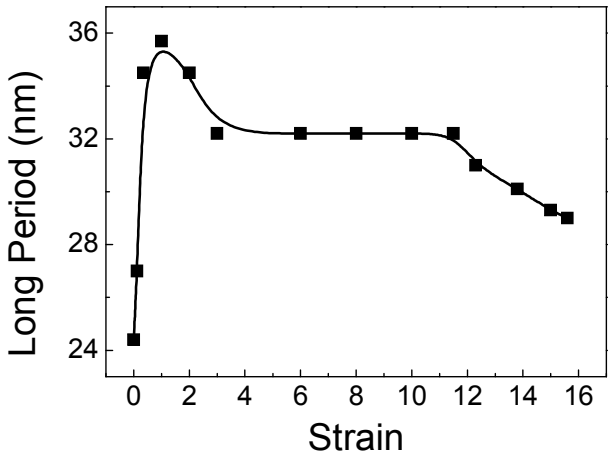

(B)

Figure 2.13. Evolution of mass fractions of amorphous, mesomorphic and crystal (including oriented crystal and unoriented crystal) phases in the iPP film during uniaxial tensile deformation at 160 ^{o}C.

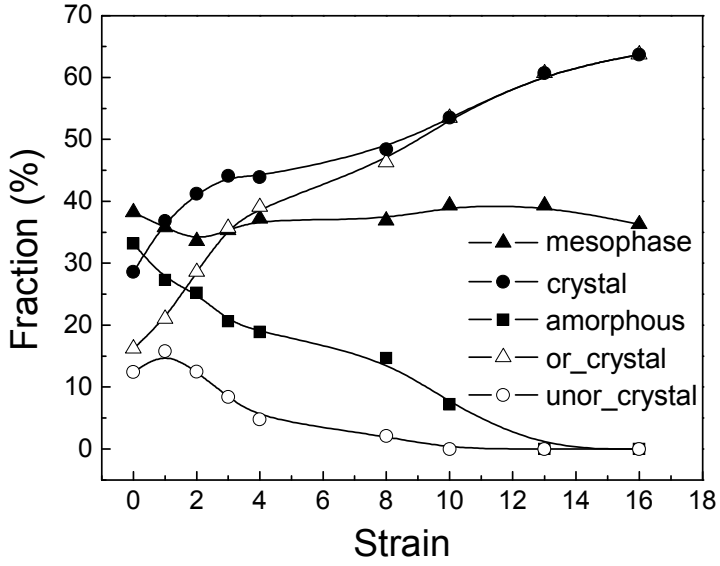

Figure 2.14. AFM, WAXD and SAXS images of iPP film under different conditions. Left column: spherulitical morphology (strain = 0.0, T = RT); center column: fibrillar structure (strain = 4.0, T = 60 ^{o}C); right column: voids and transverse bands (strain = 16.0, T = 160 ^{o}C). (AFM scale: 40 μm)

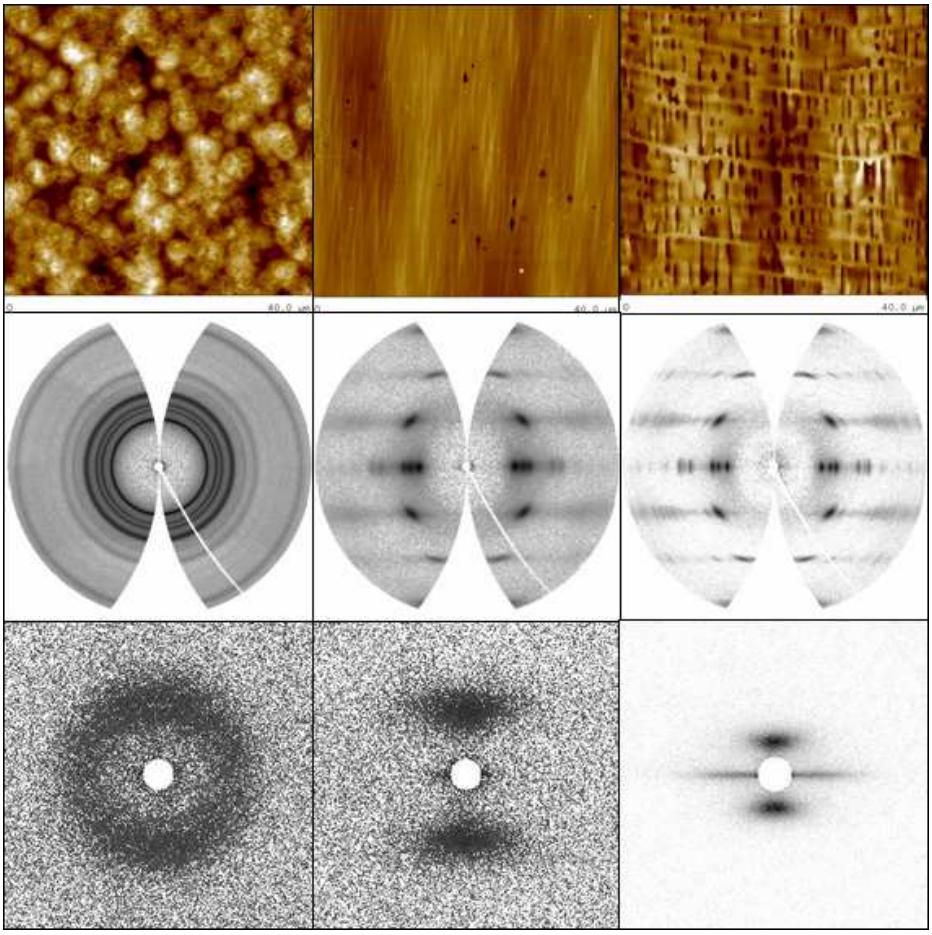

Figure 2.15. Hermans' orientation factors of crystal chain axis as a function of strain for iPP film at different temperatures.

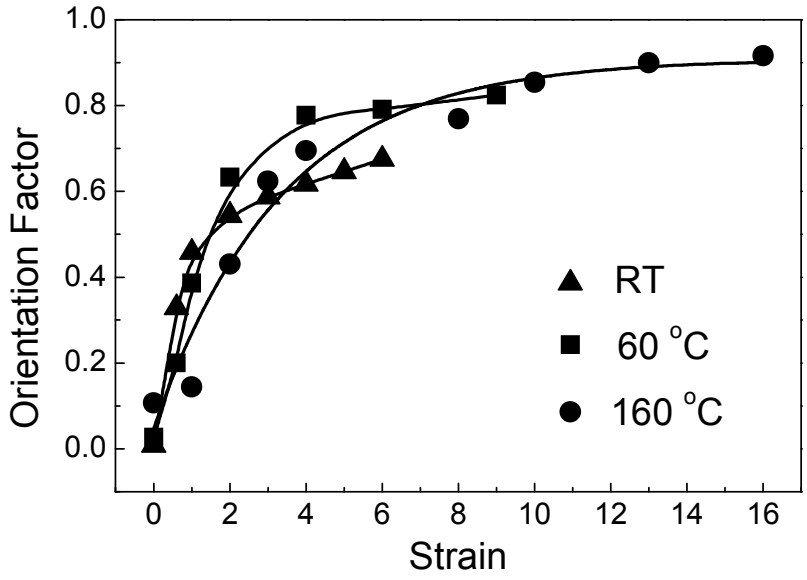

Figure 2.16. The deformation of the crystal and amorphous phases during uniaxial tensile deformation at low and high temperatures.

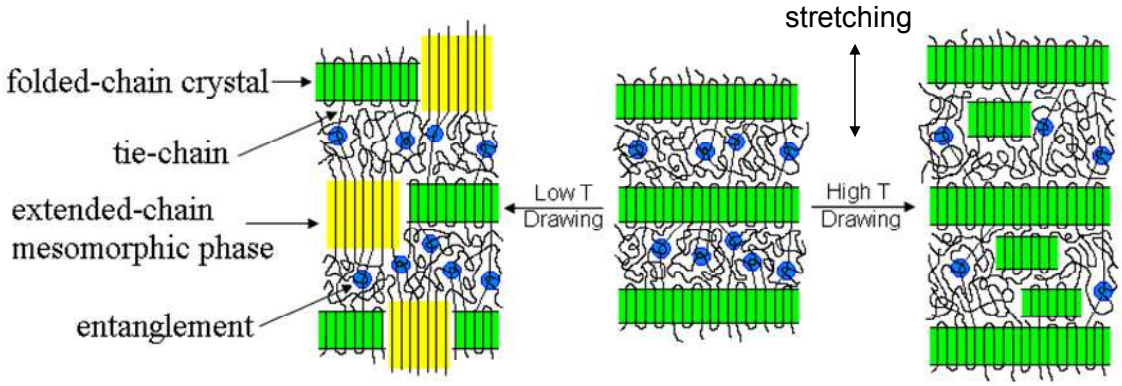

Chapter 3. Shear-induced Crystallization and Crystallization-induced Phase Separation of Olefin Block Copolymers

3.1 Introduction

Semi-crystalline polymers together with amorphous polymers are the most important commercially useful polymers for various applications. In semi-crystalline polymers, due to the distinct differences between crystal and amorphous phases, crystallization will affect their properties in almost all aspects, for instance, thermal, optical, mechanical properties, etc. Meanwhile, during the industrial processing, including extrusion, injection, fiber spinning and film blowing of polymers, external flow-fields (shear, extension and mixed) are always involved. These fields can significantly affect the crystallization kinetics and orientation of the polymer chains, then the formation of the crystal structure.[1-3] Thus understanding the crystallization mechanism of polymers, especially how external flow-fields affect the crystallization behavior, is essential for their applications and further investigation is needed to benefit the industrial processing.

Polyethylene was used as a model polymer system for studies in polymer crystallization behavior due to its simplicity in structure. Numerous reports can be found in literature, including both quiescent and flow-induced crystallization, using many techniques, for instance, scattering, microscopy, and thermal analysis.[4-7] If copolymerized with α-olefins, the short chain branches introduced will interrupt the folding and packing of linear chains into crystals and influence the crystallization behavior. Various parameters, such as comonomer type, whether it is propylene, butene, hexene, or octene,[8-

[12] and comonomer content, i.e. distribution of the short branches,[13-17] affects the crystallization behavior. Even more complicated situations will occur if the crystallizable chain segments are incorporated into the polymer chain with other chain segments to form block copolymer.[18-22] Block copolymers are of interests to many researchers, because its flexibility in modifying the structure by connecting different polymer chains to adjust the properties of the final products, such as ABS plastic, SBS rubber, etc. For conventional block copolymers, segregation due to the incompatibility between covalent-bonded blocks which are distinct in chemical compositions is the most important characteristic. The strength of segregation is governed by the product of Flory-Huggins interaction parameter χ and the degree of polymerization N.[23] Given diblock copolymer with equal volume fraction of two blocks, phase separation occurs when χN is greater than 10.5. [24]

Olefin block copolymers (OBCs) produced by The Dow Chemical Company via novel chain shuttling technology consist of two kinds of blocks.[25] Both are ethylene and α-olefin copolymer block, but the α-olefin comonomer content in each block is different. The successful synthesis of this block copolymer is attributed to the two catalysts with distinct selectivity to produce ethylene copolymer blocks of different comonomer content and thus the density with the help of chain shuttling agents that can transfer the growing chains between catalysts to form the blocky structure. By choosing specific catalyst, the commoner content in the block could be more than 20 mol%, and the density of the block could vary from high density around 0.94 g/cm^3 to low density about 0.85 g/cm^3. So for the OBCs, the χ must increase when the density difference between hard and soft segment increased as the incompatibility was more severe. The length of the blocks or the number of the blocks in each polymer chain can also be adjusted by changing the amount of chain shuttling agents in the polymerization reactor. Less chain shuttling agents used, the less frequently the growing chain transferred between the catalysts, and the longer the

blocks. A longer block means larger N, which will favor the phase segregation between blocks. However, whether the minimum requirement of the product of N and χ for the phase separation to occur is achieved or not and how the incompatibility of different blocks affects the crystallization deserve elaborate studies.[26]

In this study, we investigated the quiescent and shear-induced crystallization of several ethylene-octene block copolymers. The selected OBC samples were different in both block length and the comonomer content in the soft segment, i.e. different N and χ. In-situ wide-angle X-ray diffraction and small-angle X-ray scattering data were collect during the crystallization. The time-evolution of the crystallinity and the phase development were revealed. The influences of N and χ on the crystallization behavior were clarified through the analysis.

3.2 Experimental

3.2.1 Materials

Five olefin block copolymer samples polymerized from ethylene and octene by chain shuttling technology were provided by The Dow Chemical Company, and were named OBC-LS, OBC-H, OBC-M, OBC-L, and OBC-HS, respectively, according to their characteristics which were summarized in Table 3.1. The major difference between OBC-LS and OBC-HS was the content of chain shuttling agent used during polymerization processes. OBC-LS, representing low shuttling, was synthesized with chain shuttling agent content of 0.4 per 1000 ethylene, while this content was 1.3 for OBC-HS, meaning high shuttling. The rest of OBCs, i.e. OBC-H, OBC-M, and OBC-L, had the same medium level of chain shuttling agent content of 0.6, and the most distinct difference among these three OBCs was actually the octene comonomer content in the soft segment.

OBC-H had the highest comonomer content, 16.0 mol%, while OBC-L had the lowest comonomer content, 11.2 mol%, and the comonomer content of OBC-M was in between at 13.4 mol%. The isotropic OBC films of about 0.5 mm thickness were prepared by compression-molding at 165 ^{o}C, and then quenched to the room temperature. Samples in the form of a ring (inner diameter = 10 mm, outer diameter = 20 mm) were cut from the melt-pressed films for rheo-X-ray experiment.

3.2.2 Instrumentation

Linkam CSS-450 shear stage, modified for in-situ rheo-X-ray studies, was used to apply controlled shear conditions to the polymer melt. The details of this modified shear apparatus was described elsewhere. Briefly, the ring-shaped OBC sample was placed in the gap between two X-ray windows (i.e., a diamond window and a Kapton film window) and completely enclosed in cavity of the measuring cell. The samples crystallized at different temperatures under both quiescent and shear-induced conditions with X-ray scattering data collected simultaneously.

WAXD and SAXS measurements were carried out at the X27C beamline in the National Synchrotron Light Source (NSLS), Brookhaven National Laboratory (BNL). The wavelength of the synchrotron radiation was 1.371 Å. 2D SAXS/WAXD patterns were collected by MAR CCD X-ray detector (MAR-USA), which had a resolution of 1024 times 1024 pixels (pixel size = 158.44 μm). For SAXS measurements, the sample-todetector distance was around 1900 mm, and the scattering angle was calibrated by silver behenate (AgBe); for WAXD measurements, the sample-to-detector distance was around 110 mm, and the diffraction angle was calibrated by aluminum oxide (Al_2O_3). All X-ray images (SAXS and WAXD) were corrected for background scattering, air scattering, and beam fluctuations.

3.2.3 Experimental Procedure

To ensure that the OBC melts were free of any memory effects associated with the prior thermal and mechanical history, all OBC samples were first heated to 165 °C (substantially above the equilibrium melting temperature of polyethylene, $T_m° \sim 145$ °C) and held for 5 minutes. The melts were then cooled to the chosen crystallization temperatures at a 30 °C/min rate. Upon reaching the crystallization temperature, a SAXS or WAXD pattern was collected before the application of shear. Time-resolved X-ray images were subsequently taken upon the cessation of shear (shear rate = 45 s^{-1}, shear duration = 5 s). The data acquisition time was 15 s and the data storage time was 5 s for each scattering pattern. For quiescent crystallization experiment, there was no application of shear, but the rest of procedures were the same. The crystallization duration was usually up to 30 minutes.

3.3 Results and Discussion

3.3.1 Molecular Structure of OBCs

According to the information in Table 3.1, we would like to discuss more on the molecular structure of OBCs studied. OBCs consisted of two kinds of blocks. Both blocks can be individually seemed as ethylene-octene random copolymer segment. The one with quite small amount of octene comonomer, 0.4 mol%, was hard segment, and the other one was soft segment with much higher octene comonomer. The density of each segment was determined by this octene comonomer content which was controllable during polymerization by changing the incorporation ability of two catalysts. The densities of hard segments were the same for all OBCs, while soft segments densities

varied from 0.857 to 0.871 g/cm^3, as the octene content ranged from 16.6 to 11.2 mol%. The number and length of blocks in one polymer chain can be determined by the ratio of chain shuttling agent to ethylene in reactor. The more chain shuttling agents in the reactor, the more frequent the transfers of growing polymer chain between catalysts. Thus OBC-HS will have more but shorter blocks in each chain than OBC-LS. Schematic diagrams of the chain structure of these segmented OBCs were illustrated in Figure 3.1. The change of densities of hard or soft segments was indicated by a color scale with blue meaning low density and red meaning high density. The length of each segment can be roughly estimated from the information provided if the small differences in volume fraction of each segment and molecular weight were neglected. The length of hard segment in OBC-HS was in the order of 50 nm, while in OBC-LS it was about 100 to 150 nm. The length of soft segment was roughly three times of the hard segment. The length of hard segment was longer than the regular thickness of polyethylene lamella, thus hard segment should be able to fold back and forth to form lamellar crystal upon crystallization without difficulty. However, due to the relatively low density of soft segments, they might not be able to crystallize especially at high temperature slightly below melt point or exhibit very poor crystallizability. According to the above description, we can easily deduce that in the sequence of OBC-H, OBC-M, and OBC-L, N was constant, but χ was decreasing. For OBC-HS, N was the smallest one, but the χ was the same as in OBC-LS, larger than other three OBCs. The value of χN should be the largest for OBC-LS, since it had the longest blocks and largest density difference. However, even for OBC-LS the phase separation was not observed at temperature higher than melting point.

3.3.2 Quiescent Crystallization Temperatures of OBCs

Typical 2D SAXS and WAXD patterns of all OBCs were quite similar, thus we only showed the patterns of OBC-H in Figure 3.2. On the right were the SAXS and WAXD patterns obtained after 30-minute quiescent crystallization at 125 ^{o}C. The sample was still completely amorphous without any indication of crystal structure in WAXD pattern. The SAXS did not show any scattering. Because the scattering intensity in SAXS was from electron density contrast, this indicated the polymer melt was homogenous without phase separation between soft and hard segments, which implied the χN was still not large enough to induce the phase separation in melt. However, if the melt crystallized quiescently at temperature 1 ^{o}C lower, i.e.124 ^{o}C, OBC-H can crystallize well within the 30-minute experimental duration. The 2D WAXD pattern on the left showed two crystal reflections which can be assigned to (110) and (200) peaks from orthorhombic polyethylene crystal and a diffused halo from amorphous phase. The SAXS pattern was somewhat different from regular polyethylene samples. There was no prominent and clear first order scattering maximum from lamellar structure. The scattering intensity decreased monotonically starting from the beam stop.

By carrying out quiescent and isothermal crystallization experiment of OBCs at different temperatures, the starting quiescent crystallization temperatures of all OBCs can be obtained, that was the temperature under which the polymer can crystallize within 30 min. The results were listed in Table 3.2. OBC-LS can crystallize at temperature as high as 126 ^{o}C, while OBC-HS can only crystallize when temperature was cooled down to 122 ^{o}C. Other three OBCs had the same starting crystallization temperature at 124 ^{o}C. From the above experimental observations, one can easily find the relationship between the starting crystallization temperature with the chain shuttling agent content, that was low chain shuttling leading to a high crystallization temperature.

3.3.3 Quiescent and Shear-induced Crystallization

More selected 2D SAXS patterns of OBC-H during quiescent crystallization and shear-induced crystallization at 124 ^{o}C and 120 ^{o}C were shown in Figure 3.3. All SAXS patterns had the same feature as we mentioned above, that was monotonically decreased intensity. The isotropic SAXS patterns indicated that quiescently crystallized samples were isotropic without any preferred orientation in the large length scale, and the orientation of the sheared sample was also too weak to show distinguishable anisotropic scattering. Time-evolution of integrated linear SAXS profiles of OBC-H under quiescent crystallization at 120 ^{o}C was shown in Figure 3.4 (A). It can be seen that there was a shoulder along the strong and decreasing scattering curve. This implied that lamellar crystals did form under experimental condition. To locate the scattering maximum, Lorentz-correction, plot of Is^2 versus s, was carried out as shown in Figure 3.4(B). The s value at the scattering maximum was 0.027 nm^{-1} and its reciprocal value, 37 nm, was the long period of the lamellar structure. The long period remained as a constant during the crystallization.

2D WAXD patterns corresponding to the 2D SAXS in Figure 3.3 were shown in Figure 3.5, and typical time-evolution of integrated linear WAXD profiles were shown in Figure 3.6. The peak positions of two crystal reflections were consistent with orthorhombic polyethylene crystals, indicating hard segments in melt can crystallize well without the interruption of soft segments. The WAXD pattern after 10-minute quiescent crystallization at 124 ^{o}C still showed only the amorphous halo, while the melt started to crystallize even 1 min after shear (shear rate = 45 s^{-1}, shear duration = 5 s). The shear-induced crystallization at 120 ^{o}C gave the most intense crystal reflection peaks. The stronger scattering intensity at low temperature or after the shear suggested that application of shear can enhance the crystallization in both kinetic and dynamic aspects with the similar effects of lowering temperature. The orientation of small length scale

crystals was also very weak, as the (110) and (200) reflections was relatively isotropic ring comparing with arch-like scattering peaks that can be found in neat polyethylene melt. However, there did exist slightly orientation preference for OBCs crystallized under shear.

3.3.4 Time-Evolution of Crystallinity Index

As shown in Figure 3.6, (110), (200) reflections and broad amorphous peak were separated from each others, thus they can be deconvoluted by 1D peak fitting method. The ratio of integrated area under crystal peaks to the total area was the crystallinity index, which we termed as crystallinity later on. The development of crystallinity in all OBCs during both quiescent and shear-induced crystallization was calculated and plotted in Figure 3.7. The crystallization temperature chosen was the corresponding starting quiescent crystallization temperature (T_{qc}) of each OBC, i.e. 126 ^{o}C for OBC-LS, 124 ^{o}C for OBC-H, -M, -L, and 122 ^{o}C for OBC-HS. Besides, all OBCs were also crystallized under the same temperature, 120 ^{o}C. The crystallization induction time was about 10 to 15 minutes at T_{qc} without application of shear, before that no crystals were detected by WAXD. Later, crystallinity started to increase slowly in a linear manner. Till the end of crystallization duration, crystallinity was about 1 to 3 %, and can still increase further. Upon the application of shear at T_{qc}, crystallization process was changed in terms of two aspects. First, the crystallization induction time was greatly shortened. Crystallization of all OBCs occurred almost instantaneously after the cessation of shear. Second, crystallization rate was accelerated and crystallinity was higher than quiescent crystallization. For some OBCs, such as OBC-H, the growth rate was initially fast and leveled off gradually later, which meant the shear-induced crystallization was almost complete. While for others, such as OBC-LS, crystallinity increased exponentially through the entire 30-minute duration indicating a relatively slow growth rate.

Since both applying shear and decreasing temperature can speed up crystallization process, we can compare the difference between these two effects. For OBC-LS and OBC-HS, lower temperature that led to the similar crystallization behavior as shear-induced crystallization at T_{qc} in terms of the kinetics and dynamics was found to be 124 ^{o}C and 118 ^{o}C, respectively. The corresponding crystallization curves were also plotted in Figure 3.7(A) and (E). The shear-induced crystallization showed a faster rate and higher crystallization at the very beginning stage, but then it was exceeded by melt under quiescent state at low temperature. Same phenomenon was found for OBC-H, -M, and -L under shear-induced crystallization at 124 ^{o}C and quiescent crystallization at 120 ^{o}C. This can be attributed to the two components of crystallization process, nucleation and growth. Application of shear can induce the orientation of the polymer chains, aligned chain segments can act as nucleation sites for the crystallization. So comparing the shear-induced crystallization and quiescent crystallization, the nucleation density was higher in the former one right after shear, thus the initial increase of crystallization was faster, while the later diffusion-controlled growth of the crystals depended more on the temperature. The growth rate was faster in quiescent melt at low temperature, leading to the crossover of two crystallization curves. It was interesting to note that the effects of shear on the OBC-LS at T_{qc} were almost similar to a decrease of 2 ^{o}C in crystallization temperature, while it was 4 ^{o}C in OBC-HS. And for other three OBCs, it was in an intermediate region. This could be due to reason that at lower temperature, the relaxation of polymer chains was more difficult to happen, thus the same shear rate and duration can result in more effective orientated precursors or nucleation sites for the crystallization to occur.

3.3.5 Crystallization-induced Phase Separation

The observed SAXS without pronounced scattering peak but having a decreased intensity with only a scattering shoulder from lamellar structure was due to the crystallization-induced phase separation in the OBCs. The homogenous melt before crystallization can be proved from SAXS pattern, which did not have any scatterings indicating no electron density fluctuation. Thus the hard segments and soft segments were distributed evenly and entangled with each other homogenous and freely. Their neighboring polymer chain segments had the same possibility to be soft and hard segments. Under this kind of situation, it was difficult for hard segments to crystallize due to the existence of nearby non-crystallizable soft segments. Thus the phase separation had to occur to form the favorable environment for hard segments to crystallize. So the surrounding soft segments were pushed away from hard segments, while hard segments would aggregate together to form hard segment rich domains to prepare for the following crystallization. The excluded soft segments could also possibly form a soft segment rich sphere domain, which was in the order of around 10 nm. Since not all of the hard segments can crystallize, there also existed continuous and major domains consisting of homogenous hard and soft chain segments as in the melt. To summarize, there were three phases in the current samples, lamellar crystals, soft segment rich domains, and homogenous amorphous phase. These soft segment rich nano domains which were not correlated to each other were the cause of intense SAXS scattering and hidden scattering peak from lamellar structure. Our uniaxial deformation studies of OBC films indicated that these soft segment nano domains were deformed under stress to elliptical shape and later needle shape with a length of hundreds of nanometers and only several nanometers in diameter, exhibited by strong equatorial scattering streaks. The scattering intensity was mainly from the density contrast between soft segment rich domains and homogenous amorphous phase.

3.3.6 Effects of N on Phase Separation

For OBCs polymerized with different chain shuttling agent content, the crystallization temperatures were different. OBC-LS with low chain shuttling can crystallize at 126 ^{o}C, while OBC-HS with high chain shuttling can only crystallize at 122 ^{o}C, and other three OBCs with intermediate shuttling crystallized at 124 ^{o}C. Whether it was the different in the length of the hard segment or the phase separation that directly led to the different crystallizability and crystallization temperatures need to be clarified. Considering the length scale of hard segments in OBCs, as we calculated before, the hard segment in OBC-LS was around 125 nm and the molecular weight of this hard segment was about 13,000 g/mol, while for hard segment in OBC-HS was around 50 nm with molecular weight about 5,200 g/mol. Both segments exceeded the lamellar thickness of about 10 nm, suggesting they can fold back and forth without much problem. Thus the same density of all hard segments should result in the same crystallization temperature. Then the crystallization temperature difference must come from the ability in the induction of phase separation. As we discussed above, the crystallization can only happen by forcing the phase separation simultaneously, thus the occurrence of phase separation induced by crystallization will determined the starting crystallization temperature. The same octene comonomer content in hard segments gave rise to the same density, and also should be the same crystallization ability. Then the key point relied on the segregation between hard and soft segments. According to the conventional block copolymer theory the segregation depends on χN, and obviously, for our samples, N was the dominant factor. In OBC-LS, the largest N represented the easiest segregation between hard and soft segments, while the smallest N in OBC-HS represented the most difficult segregation. As temperature decreased, the hard and soft segments in the homogenous melt in OBC-LS were the first to be able to segregate under the driven force of crystallization and form the phase rich domains and thus crystallize. The starting quiescent crystallization temperature was a good indication of the segregation tendency between hard and soft segments and to prove

that the dominant factor determining the crystallization-induced phase separation is segmental length N.

3.3.7 Effects of χ on Phase Separation

Despite the dominant factor N, the influence of χ in the crystallization-induced phase separation can also be examined. OBC-H, OBC-M, and OBC-L had the same N as they were produced with same chain shuttling agent content but different χ as the octene comonomer content in the soft segments was different. By comparing the evolution of crystallinity of these OBCs in Figure 3.8(A), we can see that at the same quiescent crystallization temperatures, 124 ^{o}C and 120 ^{o}C, OBC-H crystallized faster and to a higher crystallinity of 3% and 9%, respectively, while OBC-L was the last one in both kinetics and thermal dynamics. It was clear that high octene comonomer content in soft segment in OBC-H resulted in a larger density difference between soft and hard segment and thus a larger χ. So the segregation is stronger in OBC-H, and upon the crystallization the phase separation would be easier and favor the crystallization. The experimental observations proved that the χ was a less dominant factor than N, or in other words, the variation in the densities of soft segment from 0.859 to 0.871 g/cm^3 was not large enough to influence the crystallization of the hard segment effectively as variation in N.

3.3.8 Shear-induced Orientation

Comparing the crystallization of these three OBCs after the application shear, things were slightly different. As shown in Figure 3.8(B), crystallinity index of OBC-H was still higher than the other two, but those of OBC-M and OBC-L switched the position. We believed that both the volume fraction of hard segments and the orientation of the polymer chains after shear were responsible for the observations. OBC-H was the one

having much larger fraction of hard segment, 24%, than OBC-M, 18%, and OBC-L, 19%. This meant that OBC-H contained one third more crystallizable hard segments, and thus crystallinity was still the highest among the three. However, for the rest two OBCs, which contained almost the same amount of hard segments, the effects of shear-induced orientation were more pronounced. Even though we did not see clear arch-like scattering peaks from oriented crystal chains in 2D WAXD patterns in Figure 3.5, there did exist the orientation difference in OBC-M and OBC-L. In Figure 3.9 (A), 3D WAXD pattern of OBC-L crystallized at 120 ^{o}C after shear showed a weak distribution of (110) scattering along the azimuthal direction. Comparison was made between OBC-M and OBC-L in Figure 3.9 (B) and (C). As can be seen, at lower temperature of 120 ^{o}C, the orientation of polymer chains was higher indicated by a narrower spread of (110) scattering in Figure 3.9 (B) than (C), which was related to the slow relaxation of polymer chains at low temperature. Besides, the OBC-L was oriented to a higher extent than OBC-M at both temperatures. Higher orientation led to more nucleation sites and thus an enhanced crystallization for OBC-L. This shear-induced orientation was the reason why OBC-L behaved different with OBC-M under different experimental conditions. The reason of this different orientation obtained in two samples under the same shear rate and duration should be also due to the phase separation. Empirically from our studies in shear-induced crystallization of polyolefins, we found polymer chains in OBCs can hardly orient after shear comparing to polyethylene, polypropylene, and random ethylene-α-olefin copolymers. It must be because of the crystallization-induced phase separation in OBCs, chain segments will try to coil together to reduced exclusion between different phase domains rather than freely extended chains in non-block polyolefins, thus the phase separation inhibited the chains to orient in OBC melts. Thus the more severe segregation in OBC-M resulted in lower degree of orientation than OBC-L, and the shear-induced orientation of the chains in melt was more effective in OBC-L to obtain a higher orientation and then favored the crystallization process.

3.4 Conclusions

Quiescent and shear-induced crystallization of different OBCs revealed the relationships between structure and crystallization behavior of polymers. The OBCs consisted of hard and soft ethylene-octene random copolymer segments can vary in the segmental length and soft segment density which represented the different N and χ affecting the segregation between two segments. The polymer melts were homogenous before crystallization proved by SAXS, but the nearby soft segments had to be excluded away from hard segment upon crystallization, which induced microphase separation with non-correlated soft segment rich sphere domains in the length scale of 10 nm. The hard segments thus aggregated and crystallized into orthorhombic polyethylene lamellar crystals. Quiescent crystallization indicated that N was more dominant as OBC with longer segments can crystallize at a higher temperature due to the easy occurrence of phase separation driven by crystallization, while χ was not larger enough to cause any difference in starting quiescent crystallization temperature, but it still can influence the crystallization of OBCs having the same value of N at the same crystallization temperature. Application of shear accelerated the crystallization through the alignment of polymer chains even though the degree of orientation was relatively low due to the crystallization-induced phase separation.

List of References

1. Keller, A.; Kolnaar, H. W. H. *Processing of Polymers*, **1997**, 18, 189-268.
2. Kornfield, J. A.; Kumaraswamy, G.; Issaian, A. M. *Ind. Eng. Chem. Res.*, **2002**, 41, 6383-6392.
3. Somani, R. H.; Yang, L.; Zhu, L.; Hsiao, B. S. *Polymer*, **2005**, 46, 8587-8623.
4. Pople, J. A.; Mitchell, G. R.; Chai, C. K.; *Polymer*, **1996**, 37, 4187-4191.
5. Androsch, R. *Polymer*, **1999**, 40, 2805-2812.
6. Stribeck, N; Camarillo, A. A.; Cunis, S.; Bayer, R. K.; Gehrke, R. *Macromol. Chem. Phys.*, **2004**, 205, 1445-1454.
7. Fukushima, H.; Ogino, Y.; Matsuba, G.; Nishida, K.; Kanaya, T. *Polymer*, **2005**, 46, 1878-1885.
8. Crist, B.; Howard, P. R. *Macromolecules*, **1999**, 32, 3057-3067.
9. Hu, W.; Srinivas, S.; Sirota, E. B. *Macromolecules*, **2002**, 35, 5013-5024.
10. Matsuba, G.; Shimizu, K.; Wang, H.; Wang, Z.; Han, C. C. *Polymer*, **2003**, 44, 7459-7465.
11. Silvestre, C.; Cimmino, S.; Triolo, R. *J. Polym. Sci.: Part B: Polym. Phys.*, **2003**, 41, 493-500.
12. Hafele, A.; Heck, B.; Kawai, T.; Kohn, P.; Strobl, G. *Eur. Phys, J. E*, **2005**, 16, 207-216.
13. Kim, M.; Phillips, P. J. *J Appl. Polym. Sci.*, **1998**, 70, 1893-1905.
14. Alizadeh, A.; Richardson, L.; Xu, J.; McCartney, S.; Marand, H.; Cheung, Y. W.; Chum, S. *Macromolecules*, **1999**, 32 6221-6235.
15. Zhang, M.; Lynch, D. T.; Wanke, S. E. *Polymer*, **2001**, 42, 3067-3075.
16. Zhang, F.; Liu, J.; Xie, F.; Fu, Q. ; He, T. *J. Polym. Sci.: Part B: Polym. Phys.*, **2002**, 40, 822-830.
17. Bustos, F.; Cassagnau, P.; Fulchiron, R. *J. Polym. Sci.: Part B: Polym. Phys.*, **2006**,

44, 1597-1607.

18. Rangarajan, P.; Register, R. A.; Adamson, D. H.; Fetters, L. J.; Bras, W.; Naylor, S.; Ryan, A. J. *Macromolecules*, **1995**, 28, 1422-1428.
19. Rangarajan, P.; Register, R. A.; Fetters, L. J.; Bras, W.; Naylor, S.; Ryan, A. J. *Macromolecules*, **1995**, 28, 4932-4938.
20. Ryan, A. J.; Hamley, I. W.; Bras, W.; Bates, F. S. *Macromolecules*, **1995**, 28, 3860-3868.
21. Hamley, I. W.; Fairclough, J. P. A.; Ryan, A. J.; Bates, F. S.; Towns-Andrews, E. *Polymer*, **1996**, 37, 4425-4429.
22. Hamley, I. W.; Fairclough, J. P. A.; Bates, F. S.; Ryan, A. J. *Polymer*, **1998**, 39, 1429-1437.
23. Flory, P. J. *Principles of polymer chemistry*, Cornell University Press, **1953**, Ithaca.
24. Hamley, I. W.; *The Physics of Block Copolymers*, Oxford University Press, **1998**, Oxford.
25. Arriola, D. J.; Carnahan, E. M.; Hustad, P. D.; Kuhlman, R. L.; Wenzel, T. T. *Science*, **2006**, 312, 714-719.
26. Khariwala, D. U.; Taha, A.; Chum, S. P.; Hiltner, A.; Baer, E. *Polymer*, **2008**, 1365-1375.

List of Tables

Table 3.1. Characteristics of OBCs.

	CSA	C_8H_{16} in Soft (mol%)	Soft Segment Density	Hard Segment Density	wt% hard	M_w (kg/mol)	MWD
OBC-LS	0.4	16.6	0.857	0.932	21	124	3.1
OBC-H	0.6	16.0	0.859	0.933	24	145	2.6
OBC-M	0.6	13.4	0.865	0.933	18	133	2.6
OBC-L	0.6	11.2	0.871	0.933	19	129	2.8
OBC-HS	1.3	16.6	0.857	0.932	22	118	2.2

CSA: Chain Shuttling Agent content ([Zn]/[C_2H_4]*1000) during the polymerization process.

Table 3.2. Quiescent crystallization temperatures of OBCs observed by WAXD within 30-minute experimental duration.

	OBC-LS	OBC-H	OBC-M	OBC-L	OBC-HS
T_{qc} (^{o}C)	126	124	124	124	122

List of Figures

Figure 3.1. Schematic diagrams of the chain structure of OBCs.

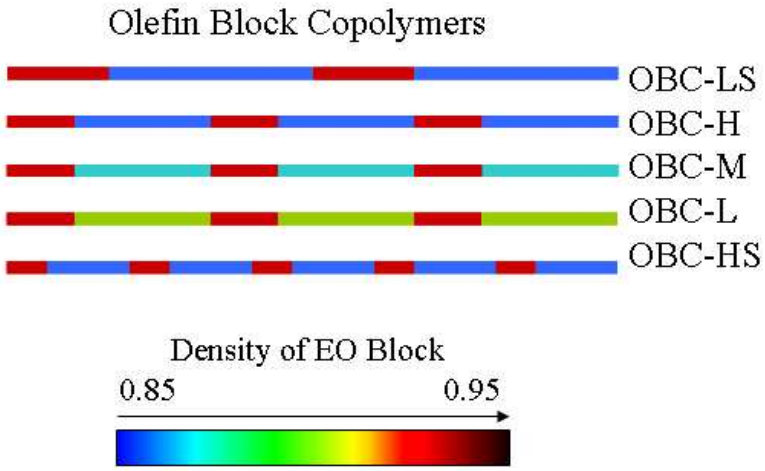

Figure 3.2. 2D SAXS (top) and WAXD (bottom) patterns of OBC-H quiescently crystallized for 30 minutes at 124 ^{o}C (left) and 125 ^{o}C (right).

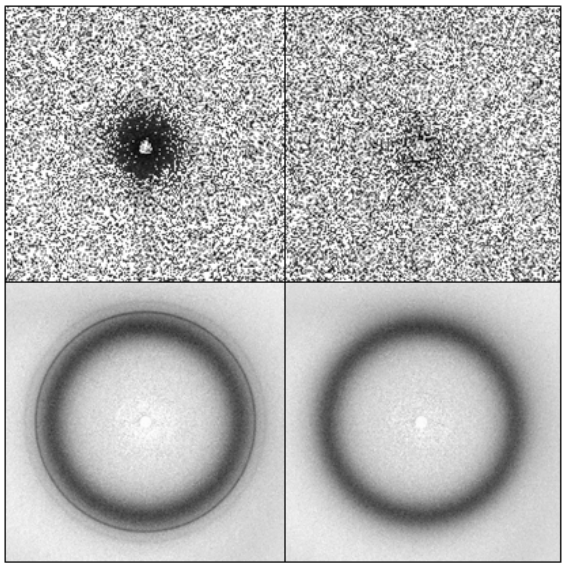

Figure 3.3. Selected 2D SAXS patterns of OBC-H during crystallization at 124 ^{o}C and 120 ^{o}C with or withour shear.

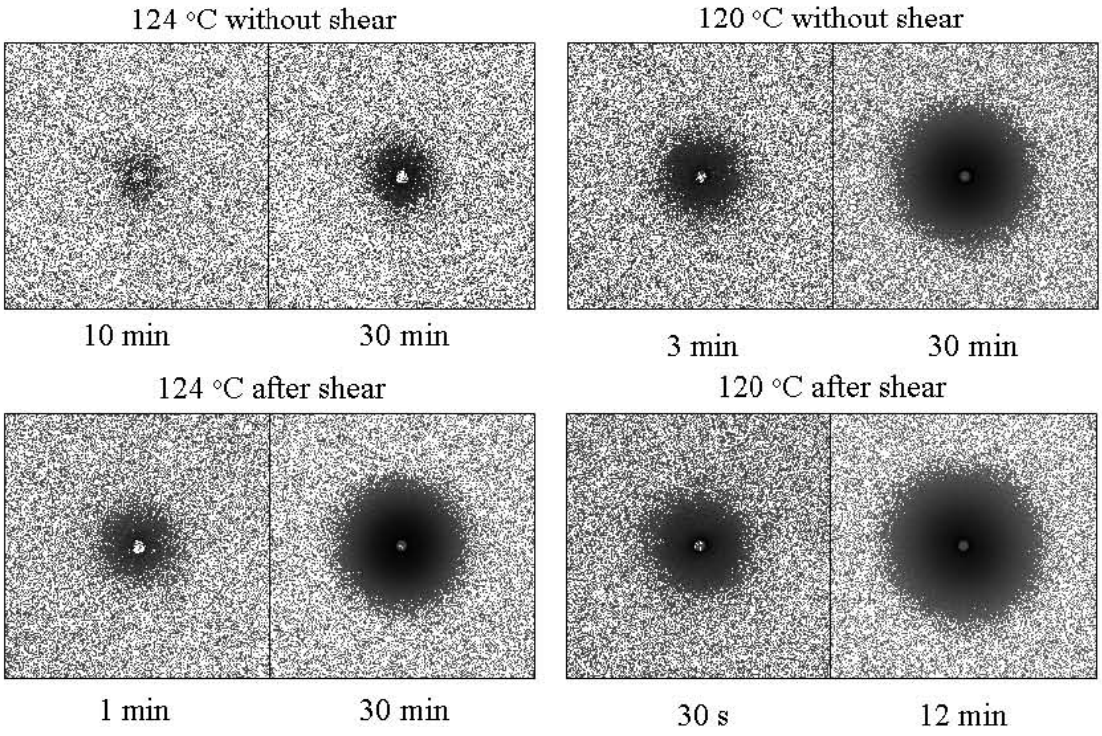

Figure 3.4. Evolution of linear SAXS profiles (A) of OBC-H quiescently crystallized at 120 ^{o}C and corresponding Lorentz-corrected plot (B).

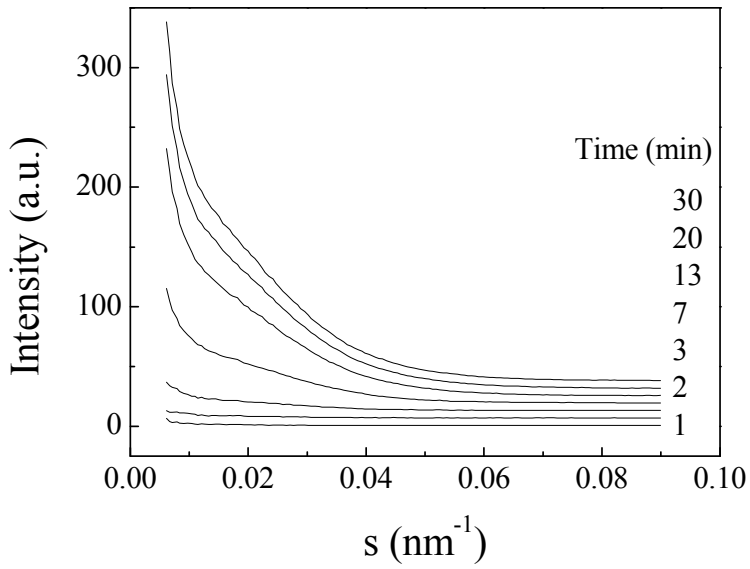

(A)

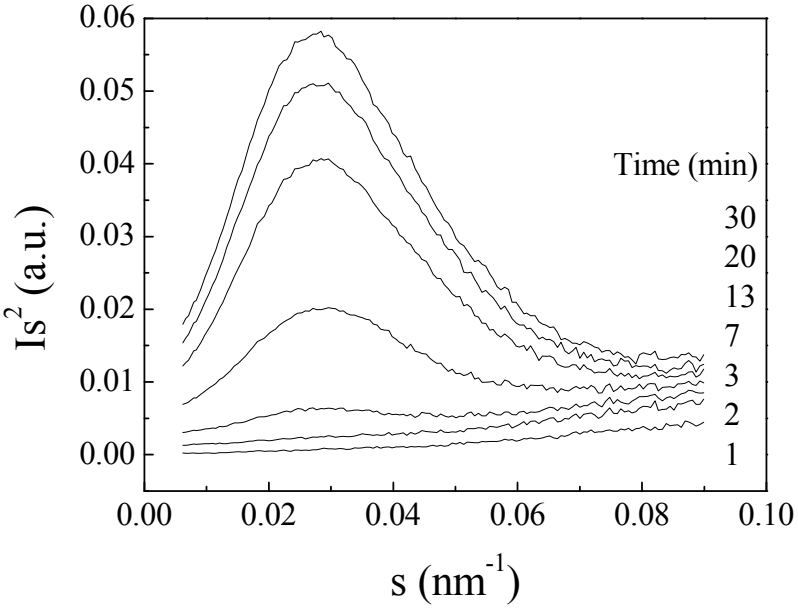

(B)

Figure 3.5. Selected 2D WAXD patterns of OBC-H during crystallization at 124 ^{o}C and 120 ^{o}C with or withour shear.

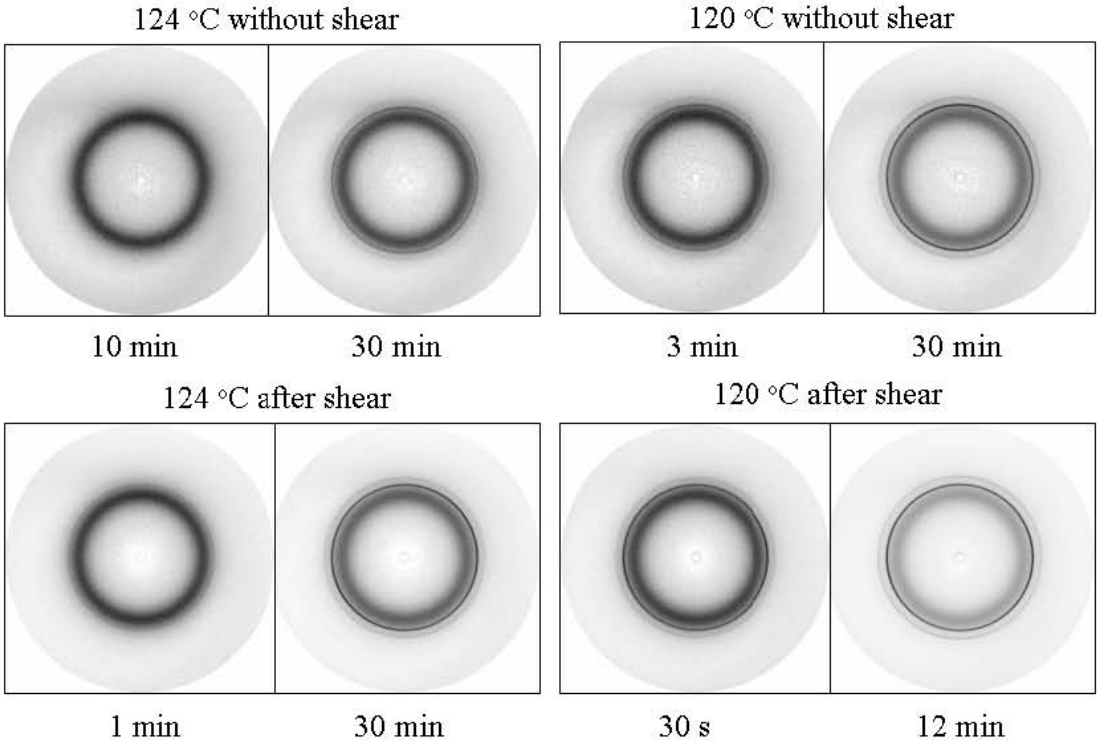

Figure 3.6. Evolution of linear WAXD profiles of OBC-H quiescently crystallized at 120 ^{o}C.

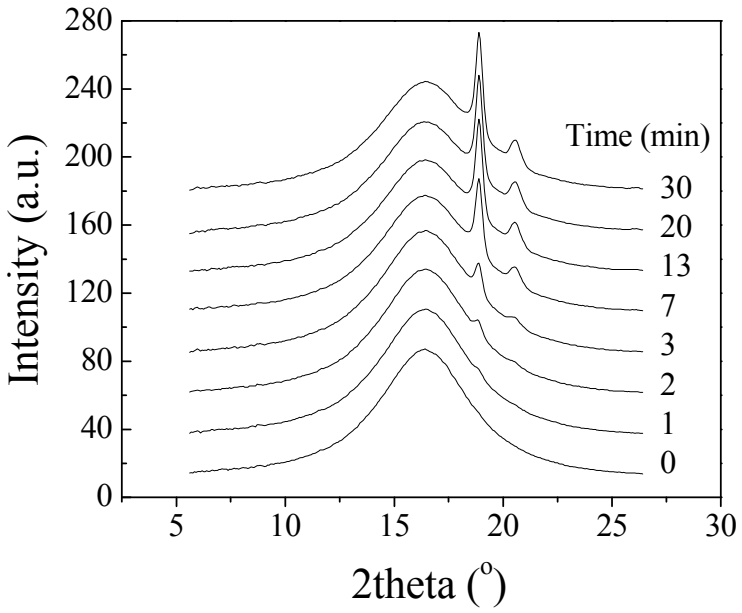

Figure 3.7. Evolution of crystallinity of OBC-LS (A), OBC-H (B), OBC-M (C), OBC-L (D), and OBC-HS (E) under different experimental conditions.

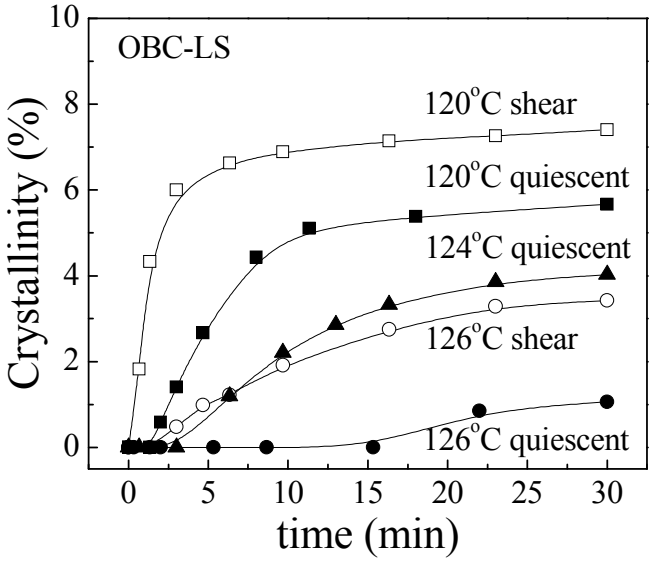

(A)

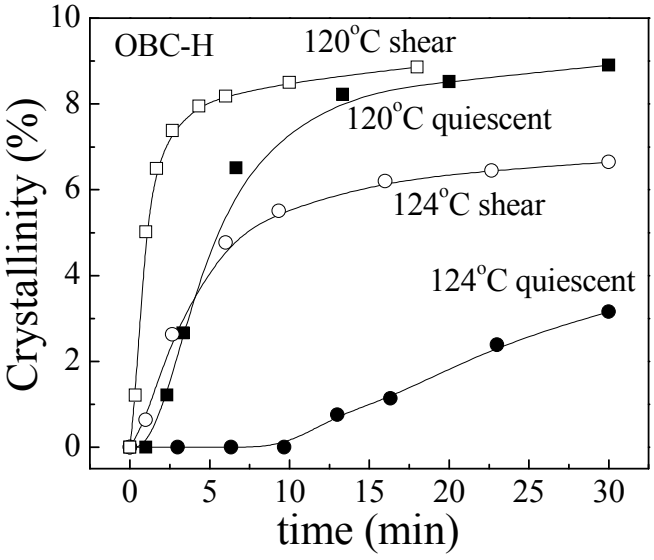

(B)

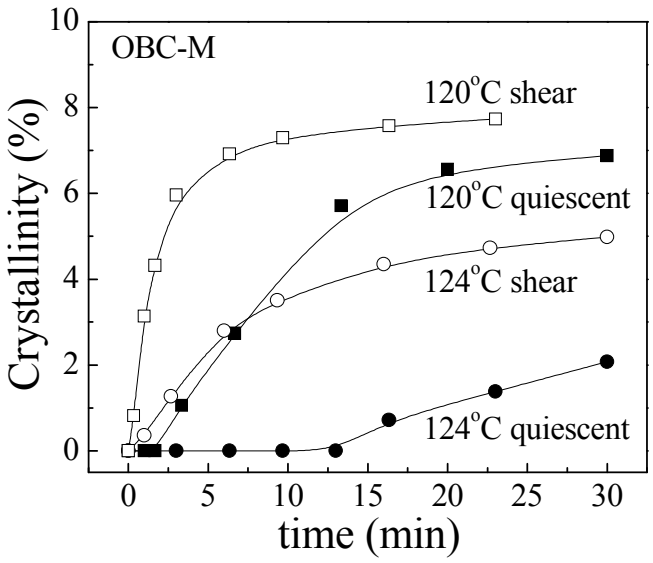
OBC-M
120°C shear
120°C quiescent
124°C shear
124°C quiescent
Crystallinity (%)
time (min)
0
2
4
6
8
10
0
5
10
15
20
25
30

(C)

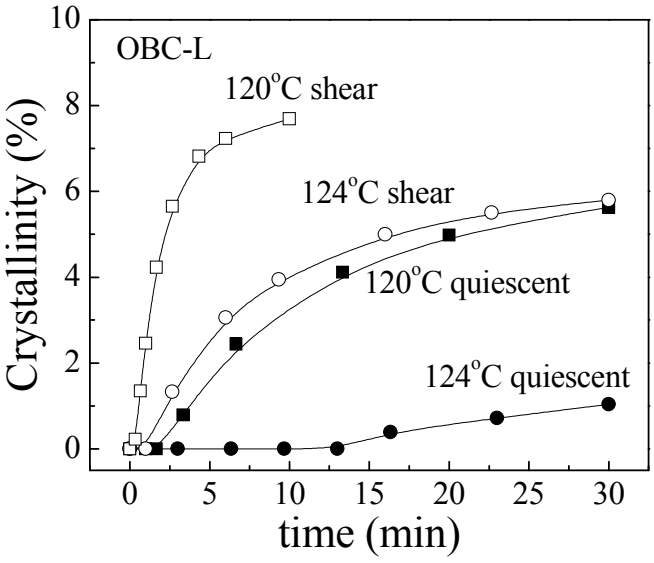
OBC-L
120°C shear
124°C shear
120°C quiescent
124°C quiescent
Crystallinity (%)
time (min)
0
2
4
6
8
10
0
5
10
15
20
25
30

(D)

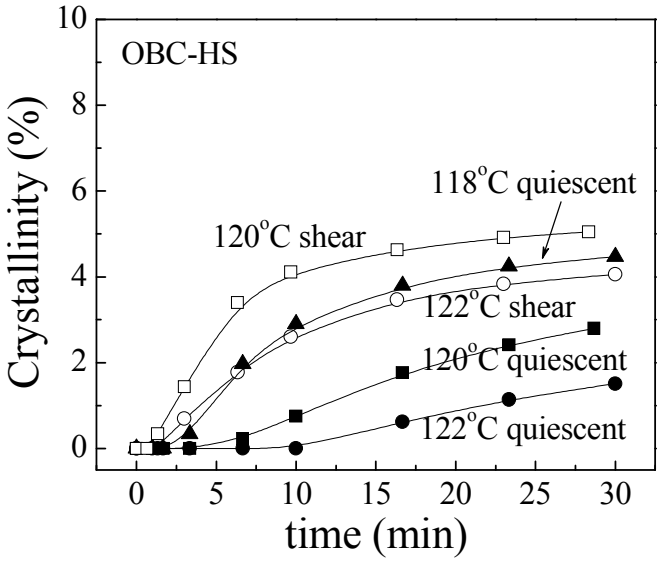
OBC-HS
Crystallinity (%)
time (min)
118°C quiescent
120°C shear
122°C shear
120°C quiescent
122°C quiescent
0
2
4
6
8
10
0
5
10
15
20
25
30

(E)

Figure 3.8. Comparison of crystallinity development among OBC-H, OBC-M, and OBC-L during quiescent (A) and shear-induced (B) crystallization at 120 ^{o}C and 124 ^{o}C.

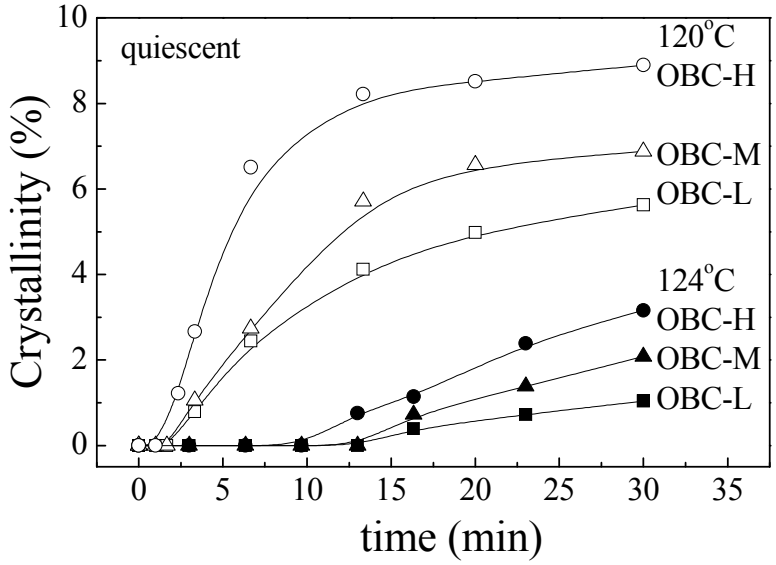

(A)

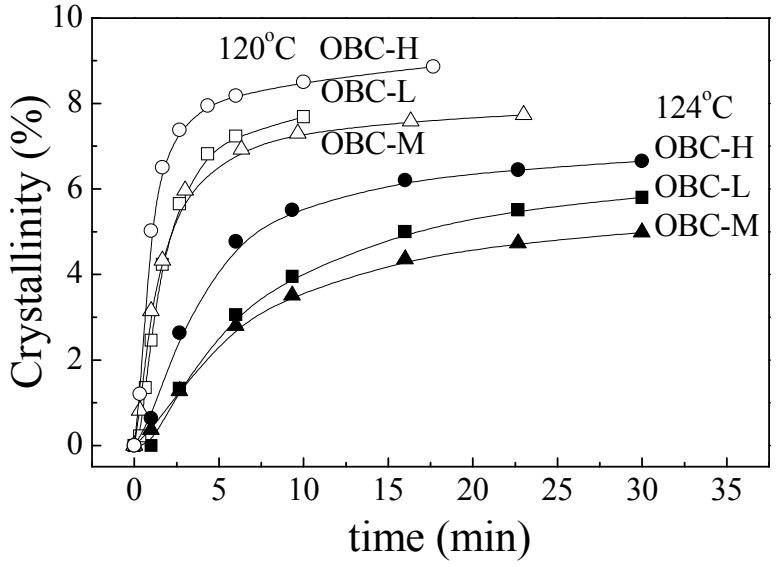

(B)

Figure 3.9. 3D WAXD pattern (A) of OBC-L crystallized for 10 minutes at 120 ^{o}C after shear. Comparison of azimuthal intensity distribution of (110) reflection of OBC-M and OBC-L crystallized 10 minutes at 120 ^{o}C (B) and 124 ^{o}C (C) after shear.

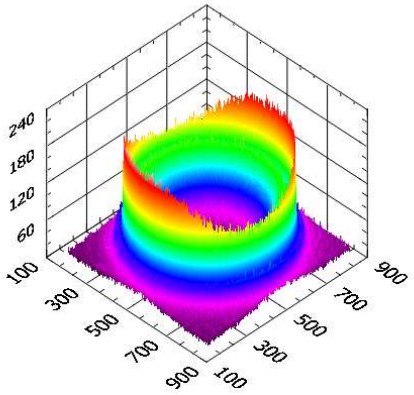

(A)

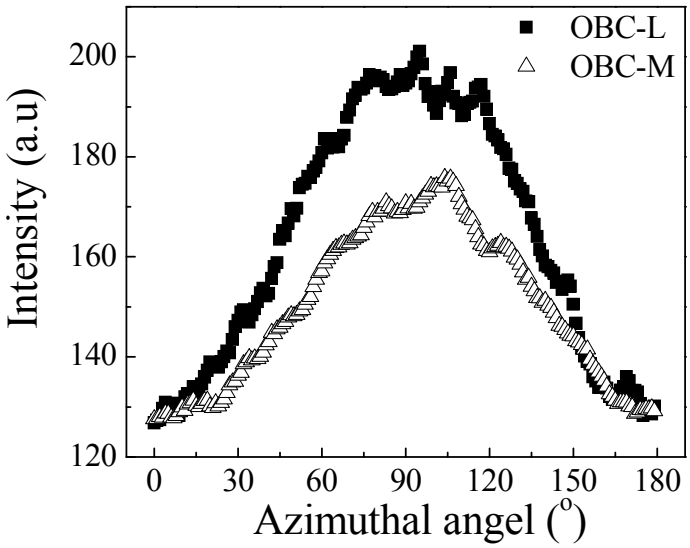

(B)

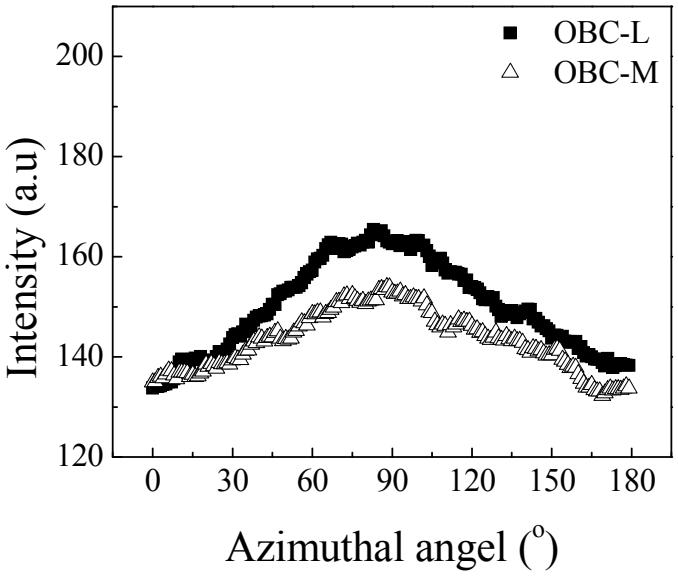
OBC-L
OBC-M
Intensity (a.u)
200
180
160
140
120
0
30
60
90
120
150
180
Azimuthal angel (°)

(C)

Chapter 4. Studies on the Uniaxial Deformation of Olefin Block and Random Copolymers

4.1 Introduction

In the polymerization processes of olefin random copolymers, the content of comonomer, such as propene and octene etc., directly determines the properties of the finial products. The more the comonomer content, the better the elastomeric property of the random copolymer. However, the melting temperature drops with the increase of comonomer content, which limits the application at high temperature. Novel olefin block copolymer was produced using a new chain shuttling technology developed by The Dow Chemical Company.[1-3] The chain shuttling technology involves two catalysts, which are good and poor incorporates, and one chain shuttling agent, which reversibly transfers the growing chains between two catalysts. The produced OBC consists of alternating hard segment of high or medium density and soft segment of low density. The hard segment containing low comonomer content has a high melting point, while the soft segment containing high comonomer content has a low glass transition temperature. So the most advantage of OBC is that it combines both properties of soft and hard segments together and can exhibit excellent elastomeric property at high temperature up to 120 ^{o}C, which is far higher than the normal melting point of olefin random copolymer around 70 ^{o}C. Besides, there are more the controllable parameters during the production of OBC than in random copolymer, such as block length, block distribution, number of blocks, and comonomer contents in the hard and soft segments, which makes the various tailors of OBC possible and more efficient and thus achieves desired properties easily according to

the customer's specific needs. In addition, OBC exhibits better recovery, abrasion resistance, and compression set than random copolymer, which proves that OBC is potentially promising for many applications.

The structure and mechanical properties of olefin random copolymers, especially ethylene-octene random copolymers, had been studied extensively before.[4-11] To understand the relationships between chain architecture, structure, morphology and properties in OBCs and their difference with random copolymers will be benefit for improving the design of OBC and thus produce more desirable products for different uses. With this goal, current study investigated the structure and morphology changes of ethylene-octene block and random copolymers during the uniaxial deformation at room temperature and high temperature using in-situ synchrotron X-ray. By comparing the evolution of two dimension (2D) wide-angle X-ray diffraction (WAXD) and small-angle X-ray scattering (SAXS), we clarified the difference in structure and morphology changes between two samples and proposed probable reasons arising from the chain architecture.

4.2 Experimental

4.2.1 Materials

In this study, we had two samples provided by The Dow Chemical Company. One was OBC from ethylene and octene, and the other one was ethylene octene random copolymer, Affinity KC8852. The information about overall density, weight averaged molecular weight, and the molecular weight distribution was shown in Table 4.1. Both OBC and Affinity had similar molecular characteristics. However, OBC contained 79 wt% of hard segment with density of 0.932 g/cm^3 and 21 wt% of soft segment with

density of 0.857 g/cm^3. Thus, in terms of the density, only hard segment in the OBC can crystallize, while soft segment almost can not crystallize. The lower density of homogeneous random copolymer Affinity, 0.875 g/cm^3, indicated the poor crystallizability comparing to the hard segment in OBC. The isotropic films of both samples were obtained by melting-compression at 165 ^{o}C in a dumbbell shape mold, and then quenched to the room temperature. The dumbbell shape sample was 35 mm long, 6 mm wide and 1 mm thick.

4.2.2 Instrumentation

In-situ WAXD and SAXS studies were carried out at the X27C beam line in the National Synchrotron Light Source (NSLS), Brookhaven National Laboratory (BNL). The wavelength of the synchrotron radiation was 1.371 Å. A three-pinhole collimation system was used to reduce the beam size to 0.6 mm in diameter. 2D WAXD and SAXS patterns were collected by a MAR CCD X-ray detector (MAR-USA), which had a resolution of 1024×1024 pixels (pixel size = 158.44 μm). The typical image acquisition time was 20 s for each data frame. The sample-to-detector distance was around 1900 mm for SAXS (calibrated by a silver behenate (AgBe) standard), and the sample-to-detector distance was around 110 mm for WAXD (calibrated by an aluminum oxide (Al_2O_3) standard). All X-ray images were corrected for background scattering, air scattering and beam fluctuations.

Uniaxial tensile deformation was performed with a modified Instron 4442 tensile apparatus, which could stretch the film symmetrically. The symmetric stretching guaranteed that the focused X-ray beam could illuminate the same sample position during deformation. The original length of the sample between the Instron clamps was 15 mm. A constant deformation rate, 4.5 mm/min (30 %/min), was applied to the specimen

throughout the deformation study. The deformation experiments were carried out at room temperature and 60 ^{o}C. The stress and strain mentioned through the article were all engineering stress and engineering strain measured directly between clamps. The heating chamber for this Instron apparatus is about 200 mm in length, which means that the highest attainable engineering strain was only about 13.

4.3 Results and Discussion

4.3.1 Stress-Strain Curves

Figure 4.1 showed the engineering stress-strain curves of OBC and Affinity during the uniaxial deformation at room temperature and 60 ^{o}C. The mechanical data were summarized in Table 4.2. Both Affinity and OBC showed similar stress-strain curves with typical characteristics of elastomers, i.e. non-distinct yielding point upon deformation, steady increase of stress in the early stage, and strain hardening at late stage of deformation. The difference was that Affinity exhibited higher strength than OBC during the deformation at room temperature, but it became lower at 60 ^{o}C, which was closed to the melting point of the Affinity. Besides, the fracture strain of OBC was similar with Affinity at room temperature but quite different at 60 ^{o}C, which was because of the easy disentanglement of the entanglement points due to the increasing mobility of amorphous chains and the less effective tie chains in OBC due to the segmented chain architecture.

4.3.2 Formation of Monoclinic Crystals

The 2D SAXS and WAXD patterns of OBC at selected strains during the uniaxial deformation at room temperature were shown in Figure 4.2. Before deformation, we can

observe a broad peak from amorphous in the WAXD. Other two reflections from inner to outer can be assigned to (110) and (200) from orthorhombic polyethylene crystal, respectively. All reflections were initially isotropic, indicating both amorphous and crystals were unoriented. Upon deformation, reflections became arc-like along the azimuthal direction suggesting a better orientation, in other words more crystals were aligned with preferred orientation. The crystal reflections changed from four-arc at off-axis to two-arc at equatorial upon further deformation, which meant that the crystal has a b-axis orientation first and later c-axis orientation.[12] As the strain further increased, azimuthal spread of all reflections became narrow since the orientation was higher. At the middle and late stage of the deformation, two highly oriented but broad point reflections at scattering angle slightly lower than that of (110) and slightly higher than that of amorphous were seen at the equator. As shown in Figure 4.3, the new reflection was clearly distinct from (110) reflection (colored in fresh red) and amorphous halo (colored in light blue and green). This new reflection can be attributed to the (010) from monoclinic polyethylene crystal, which was formed during the deformation. Monoclinic crystal is one of the three crystal forms of polyethylene, while the other two are orthorhombic and hexagonal. The orthorhombic is the most common and stable one, hexagonal is usually occurred in the defected crystal, such as random copolymer with high octene content, while the monoclinic phase is usually formed under the condition of tension or compression. The lattice structure of orthorhombic and monoclinic crystal was illustrated in Figure 4.4. Several mechanisms of the transformation from orthorhombic to monoclinic were proposed, such as slipping and twinning.[13-19] Besides, the calculated WAXD pattern for a mixture of orthorhombic and monoclinic crystals without amorphous halo was shown in Figure 4.5(A), with proper orientation of the crystals to satisfy the intensity distribution of all reflections. This was very consistent with the experimental pattern (Figure 4.5(B)), which also confirmed that orthorhombic crystals formed during the uniaxial deformation.

4.3.3 Morphology during Deformation

2D SAXS pattern (in Figure 4.2) from undeformed OBC exhibited a different feature compared with common pattern of semi-crystalline polyethylene. In regular semi-crystalline polyethylene there was a first order scattering peak from layered lamellar structure due to the folded chain crystals with long period in the order of tens of nanometer. However, in OBC, the scattering intensity decreased with scattering vector. This feature can be due to the microphase separation in OBC induced by melt crystallization. The soft segment and hard segment are different in chain architecture and density, even though the difference is small and both segments are miscible at temperature high enough, but once when the melt was cooled down close to melting temperature, most crystallizable hard segments tend to aggregate together for effective crystallization and the non-crystallizable soft segments are push away and some portion of them can aggregate with each others. The soft segment rich domains are small, around a couple of tens nanometers, and they are not correlated to each other, leading to the diffused scattering. However, the lamellar crystals do exist in the samples. After the Lorentz-correction, a scattering peak can be seen (Figure 4.8B), which comes from the first order scattering of the lamellar stacks in the OBC samples. As the strain increased, the nanoscale domains of soft segments were stretched into needle-shape and aligned along the drawing direction with about hundreds of nm in length and several nm in width, thus the scattering intensity moved toward to the equator and led to the equatorial streak. While the lamellar stacks were stretched perpendicular to the drawing direction, and the scattering intensity concentrated to the meridional direction. When the orientation was very high, two scatterings were separated in the 2D SAXS patterns.

4.3.4 Comparison between OBC and Affinity

The selected 2D WAXD and SAXS patterns of random copolymer Affinity during the uniaxial deformation under the same condition were shown in Figure 4.6. It can be seen that the crystallizability of random copolymer was weaker than OBC. We only observed the (110) reflection, while (200) reflection was too weak to be seen. The crystal size was thinner and smaller, leading to the broad distribution of the reflection. The integrated WAXD profiles were shown in Figure 4.7(A). The peak positions of (110) and (200) reflections were the same in both Affinity and OBC consistent with orthorhombic polyethylene crystal. However, the peak positions of broad amorphous peaks were different. The peak shifted to the high angle in Affinity, getting closer to the hexagonal (100) reflection, which indicated that some crystals in hexagonal form might exist. At high strain, the orientation was developed to a high degree and the azimuthal spread of the reflections became much narrow. 2D SAXD image showed a typical lamellar scattering pattern comparing to OBC (see Figure 4.7(B)). A diffused isotropic ring before deformation indicated unoriented lamellar stacks, and they were oriented perpendicular to the stretching direction upon deformation showing two bar scattering at the meridian. No equatorial streak was observed throughout the entire deformation process.

The integrated linear WAXD profiles of OBC at different strains during the deformation were shown in Figure 4.8. As strain increased, the height of (110) peak and (200) peak in relative to the amorphous peak decreased. The amorphous peak became broad and shifted to high angle, due to overlapping with the (010) reflection from monoclinic crystal, which was newly formed during the deformation. When the strain was large than 9, it was hard to separate the (110) and (200) peaks from this broad reflection, which meant the fraction of orthorhombic phase can no longer be calculated using 1D peak fitting method. At an even higher strain, only one broad peak was observed, which should be mainly from monoclinic crystal mixed with some amorphous

and orthorhombic crystal. The Lorentz-corrected scattering intensity profile along meridian of SAXS was shown in Figure 4.8(B). The s value at the scattering maximum after Lorentz-correction was used to determine the long period between the adjacent lamellar layers. The shifting of the peaks to the right revealed that the long period was decreasing during the deformation along the meridional direction, which implied that those loosely packed and unstable lamellar structure was disintegrated. The selected linear WAXD and SAXS profiles of Affinity during deformation at room temperature were also shown in Figure 4.9. Similar with OBC, new monoclinic crystal can be induced in addition to the original orthorhombic and hexagonal ones. The reflection from monoclinic (010) plane became much more intense, resulting in a single broad peak with the maximum in between amorphous and orthorhombic (110) peak. However, the peak position of meridional scattering maximum of SAXS did not change dramatically as in OBC. The calculated long periods of OBC and Affinity along meridional direction were plotted in Figure 4.10. The long period of OBC was decreasing dramatically, while for Affinity it even increased at the early stage of deformation and then decreased slightly and later reached a plateau value. This indicated that the fragmentation of lamellar crystals was more severe in OBC.

4.3.5 Deformation at 60 ^{o}C

The uniaxial deformation was also carried out at a higher temperature, 60 ^{o}C. The evolution of the 2D WAXD and SAXS patterns was similar to the room temperature, but at a slow rate, because the high temperature resulted in a slow alignment of the polymer chains. The last 2D WAXD and SAXS patterns collected right before failure were shown in Figure 4.11. Upon fracture, OBC reached a very low orientation comparing to the deformation at room temperature, and there should be only slightly monoclinic crystals formed according to the weak (010) reflection. The final orientation in Affinity was

better, one of the reasons if that the fracture strain was obviously higher. Besides, in 2D WAXD pattern of Affinity, the strong point reflections at equator were separated from amorphous halo, and thus it should be only from orthorhombic crystal not monoclinic crystal. Comparisons between integrated WAXD profiles of Affinity obtained at room temperature and 60 ^{o}C were made in Figure 4.12. Before deformation, the peak positions of the first broad reflections at different temperatures were not the same in different temperatures. As we discussed, due to the existence of hexagonal crystals at room temperature, amorphous peak shifted to the high angle after superposing with hexagonal (100) reflection, but it shifted back to the position exactly the same as that of OBC when heated up to 60 ^{o}C. This suggested that the hexagonal phase was disappeared because of the perfection of polyethylene crystals in random copolymer due to recrystallization at high temperature. After stretched to a strain of 8 at room temperature, the peak position relocated to where the monoclinic (010) peak was, but at 60 ^{o}C we did not observe any change of the peak position. Thus it meant the monoclinic crystal was not able to be induced during deformation at 60 ^{o}C, in other words, monoclinic crystal was not stable at high temperature and probably due to the low stress on the sample during the deformation.

4.3.6 Structure Analysis during Deformation

The fractions of orthorhombic crystal in OBC and Affinity during the uniaxial deformation were calculated using 1D peak fitting method. Assuming that stretched sample had a cylindrical rotational symmetry, a 2D pattern could contain the complete information to describe the intensity distribution in reciprocal space, and integrating over such 2D sections through 3D reciprocal space would produce the fractions of each phase. Since the amorphous reflection was superimposed with monoclinic (010) reflection and can not be deconvoluted by 1D peak fitting, we can only obtain the area of orthorhombic

(110) and (200) reflections which were intense and easily separated from the broad reflection at the early stage of deformation. Thus we can obtain the fraction index of orthorhombic phase according to the area percentage of orthorhombic (110) and (200) reflections. Results were plotted in Figure 4.13. At room temperature, the fraction of orthorhombic crystal decreased from about 17% to 10% in OBC as strain increases to 8. Beyond this strain, the peaks of orthorhombic reflections can not be separated from other peaks and thus we can not calculate its fraction in the sample. The fraction of orthorhombic phase was lower in Affinity due to the disruption of octene comonomer during the crystallization. Besides, the formation of monoclinic phase in Affinity was faster upon deformation, resulting in the single broad peak from all reflections and the fraction of orthorhombic phase can not calculated when strain was greater than 1. At high temperature, a slower decreasing of the orthorhombic crystal in OBC was observed, and recrystallization even took place at 60 ^{o}C in Affinity leading to a slightly increasing of the fraction at the beginning. This was consistent with the finding that monoclinic phase was not stable at high temperature compared with orthorhombic phase.

The full width at half maximum (FWHM) of orthorhombic (110) reflection was shown in Figure 4.14. According to the Scherrer equation, the crystal size is inversely proportional to the FWHM, but during the uniaxial deformation the micro-strain and distortion of the second kind may also affect the FWHM as well. However, given that the experimental conditions were the same for both samples, the comparison of FWHM should also tell the changes and differences of the crystal size between samples during the deformation. The smaller crystals were found in Affinity, and it should be attributed to the poor crystallizability due to the disruption of the octene comonomer. The FWHM increased upon deformation which meant the crystal size decreased, and this was because lamellar crystals were fragmented due to the chain pulling-out mechanism. The decreasing rate of crystal size was higher at room temperature indicating that the

fragmentation took place easily at room temperature, consistent with our previous results in the deformation of iPP, which can all be explained from the relative strength of the entangled amorphous network at different temperatures.[20]

The degree of orientation of the amorphous and crystal phase was calculated based on Hermans' orientation function:[21]

$$f = \frac{3\langle \cos^2 \phi \rangle - 1}{2}$$

where ϕ is the angle between the chain axis and the reference axis (stretching direction). $\langle \cos^2 \phi \rangle$ is defined as:

$$\langle \cos^2 \phi \rangle = \frac{\int_0^{\pi/2} I(\phi) \cos^2 \phi \sin \phi d\phi}{\int_0^{\pi/2} I(\phi) \sin \phi d\phi}$$

where $I(\phi)$ is the scattered intensity along the angle ϕ. Since there is no plane of symmetry perpendicular to the chain axis, the c axis orientation can not be measured directly due to the absence of (00L) plane, but we can still obtain that indirectly from the (110) and (200) reflections using

$$\langle \cos^2 \phi \rangle = 1 - 1.435 \langle \cos^2 \phi_{110} \rangle - 0.565 \langle \cos^2 \phi_{200} \rangle .$$

Regarding amorphous phase, the orientation we calculated is actually that of the normal vector of the amorphous chains, so the f value is multiplied by a factor of -2 to convert that into the value representing the degree of orientation along the stretching direction. Besides, in calculating the orientation of amorphous phase, the azimuthal scan was chosen along a lower s value at 2.04 nm^{-1} than the amorphous peak at 2.13 nm^{-1} in order to reducing the contribution from (010) reflection. The value of orientation factor is between -0.5 to 1. When f = 1, it means all polymer chains align to the stretching

direction perfectly, while f = -0.5 means chains are all perpendicular to the stretching direction, and f = 0 indicates random orientation of the chains.

The calculated Hermans' orientation factors of crystal and amorphous as a function of strain were shown in Figure 4.15 (A) and (B), respectively. The orientation of both amorphous crystal phases increased asymptotically toward the value of one upon deformation, representing the better alignment of polymer chains along the stretching direction. The orientation of crystal phase was higher than the amorphous phase which could be due to the easy relaxation of the amorphous chains. It was interesting to find that the degree of orientation of both phases in Affinity was always higher than those in the OBC. Since most of the molecular characteristics in OBC and Affinity were similar, the orientation difference should be due to the chain architecture difference in OBC and Affinity. As shown in Figure 4.16 (homogenous entangled amorphous phase was neglected except for Affinity melt), Affinity was ethylene-octene random copolymer; polymer chains in Affinity were all homogeneous, so there was no problem about the miscibility among polymer chains. While for OBC, in which polymer chains consisted of soft and hard segments in an alternating order, upon the crystallization, phase separation took place, because hard segments tended to aggregate together to form a domain to crystallize later on, while soft segments were pushed out from this region. Since the segregation was very week, it can not form well defined spherical, cylindrical, or lamellar structure like in conventional block copolymers. The phase separated domains were in nano scale as shown in Figure 4.16 (hard segments were in red and soft segments were in blue), and also the extent of separation can not be thorough through out the entire polymer melt. Since the soft segment rich domain was small and contained only chain segments from a few neighboring chains comparing to Affinity, in which chains were homogeneously distributed and can entangle with many other chains and participate in many lamellar crystals if this characteristic segmental length was shorter than the hard

segments in OBC. Thus the entanglement density was reduced for OBC with segmented chain architecture due to crystallization-induced phase separation. Besides, the number of tie chains in OBC should be less than Affinity, since this OBC contained only quite a few segments each chain. Thus a more effective network in Affinity was obtained and can result in a better degree of orientation upon uniaxial deformation. The soft segment rich phase deformed into needle-like domains and contributed to the equatorial streak observed.

4.4 Conclusions

Affinity and OBC (ethylene-octene random and block copolymers, respectively) with similar overall density were uniaxially deformed at room temperature and 60 ^{o}C. Engineering stress-strain curves and 2D SAXS and WAXD patterns were collected simultaneously using in-situ synchrotron X-ray. OBC showed a better crystallizability than Affinity, which indicated that hard segment in OBC can crystallize very well. The crystals were in orthorhombic form in OBC, but there were also some hexagonal crystals coexisting with orthorhombic crystals in Affinity. Upon deformation, the fraction of orthorhombic phase decreased in both samples, more monoclinic crystals were induced easily and became dominant phase during the deformation at room temperature. However, monoclinic crystal was unstable at high temperature, at 60 ^{o}C the monoclinic crystal was difficult to form during deformation. The Hermans' orientation factors of amorphous and crystal phases were calculated. Better orientation in Affinity was due to the difference in the chain architecture. Crystallization-induced microphase separation occurred in OBC between soft and hard segments due to the density difference, which led to a lower entanglement density and less tie chains in OBC compared with random copolymer. The strong network in Affinity resulted in a better orientation upon deformation.

List of References

1. Arriola, D. J.; Carnahan, E. M.; Hustad, P. D.; Kuhlman, R. L.; Wenzel, T. T. *Science*, **2006**, *312*, 714-719.
2. Arriola, D. J.; Carnahan, E. M.; Cheung, Y. W.; Devore, D. D.; Graf, D. D.; Hustad, P. D.; Kuhlman, R. L.; Shan, C. L. P.; Poon, B. C.; Roof, G. R.; Stevens, J. C.; Stirn, P. J.; Wenzel, T. T. Catalyst composition comprising shuttling agent for ethylene multi-block copolymer formation. *WO*, **2005090427**, *2005-US8917*.
3. Wang, H. P.; Khariwala, D. U.; Cheung, W.; Chum, S. P.; Hiltner, A.; Baer, E. *Macromolecules*, **2007**, *40*, 2852-2862.
4. Androsch, R.; Blackwell, J.; Chvalun, S. N.; Wunderlich, B. *Macromolecules*, **1999**, *32*, 3735-3740.
5. Androsch, R.; Stribeck, N.; Lupke, T.; Funari, S. S. *J Polym. Sci. Part B: Polym. Phys.*, **2002**, *40*, 1919-1930.
6. Androsch, R.; Wunderlich, B.; Lupke, T.; Wutzler, A. *J Polym. Sci. Part B: Polym. Phys.*, **2002**, *40*, 1223-1235.
7. Shan, H.; White J. *Plastics, Rubber and Composites*, **2006**, *35*, 155-164.
8. Hu, W.; Srinivas, S.; Sirota, E. B. *Macromolecules*, **2002**, *35*, 5013-5024.
9. Hu, W.; Sirota, E. B. *Macromolecules*, **2003**, *36*, 5144-5149.
10. Bensason, S.; Stepanov, E. V.; Chum, S.; Hiltner, A.; Baer, E. *Macromolecules*, **1997**, *30*, 2436-2444.
11. Eynde, S. V.; Rastogi, S.; Mathot, V. B. F.; Reynaers, H. *Macromolecules*, **2000**, *33*, 9696-9704.
12. Chen, X.; Yoon, K.; Burger, C.; Sics, I.; Fang, D.; Hsiao, B. S.; Chu, B.

Macromolecules, **2005**, *38*, 3883-3893.

13. Kiho, H.; Peterlin, A.; Geil, P. H. *J. Appl. Phys.*, **1964**, *35*, 1599-1605.
14. Kiho, H.; Peterlin, A.; Geil, P. H. *Polym. Lett.*, **1965**, *3*, 157-160.
15. Seto, T.; Hara, T.; Tanaka, K.; *Japan. J. Appl. Phys.*, **1968**, *7*, 31-42.
16. Takahashi, Y.; Ishida, T. *J Polym. Sci. Part B: Polym. Phys.*, **1988**, *26*, 2267-2277.
17. Whttmann, J. C.; Lotz, B. *Polymer*, **1989**, *30*, 27-34.
18. Russell, K. E.; Hunter, B. K.; Heyding, R. D. *Polymer*, **1997**, *38*, 1409-1414.
19. Shan, H.; White, J. L. *Intern. Polymer Processing XXI*, **2006**, *4*, 361-373.
20. Zuo, F.; Keum, J. K.; Chen, X. M.; Hsiao, B. S.; Chen, H. Y.; Lai, S. Y.; Wevers, R.; Li, J. *Polymer*, Accepted.
21. Wilchinsky, W. Z. *J. Appl. Phys*. **1960**, *31*, 1969.

List of Tables

Table 4.1. Density, composition, and molecular weight information of OBC and Affinity.

	Overall density (g/cm^3)	wt% soft	Soft segment density	Hard segment density	M_w (kg/mol)	M_w/M_n
OBC	0.875	79	0.857	0.932	124	3.05
Affinity (KC8852)	0.875	Ethylene-Octene Random Copolymer			79	2.47

Table 4.2. Mechanical properties of OBC and Affinity at room temperature and 60 ^{o}C.

	fracture strain		yield stress(MPa)		fracture stress (MPa)	
	RT	60 ^{o}C	RT	60 ^{o}C	RT	60 ^{o}C
OBC	13.0	4.4	1.3	0.8	5.8	1.2
Affinity	12.5	8.3	1.4	0.6	7.6	1.1

List of Figures

Figure 4.1. Engineering stress-strain curves of OBC and Affinity at room temperature and 60 ^{o}C.

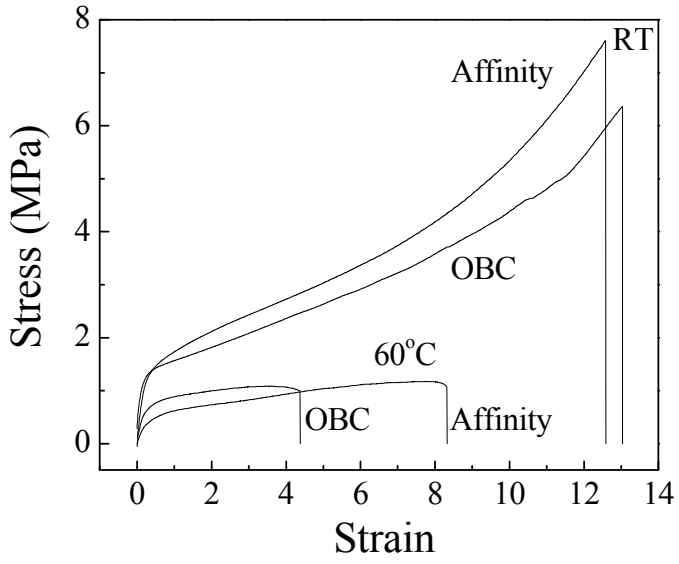

Figure 4.2. Selected 2D WAXD and SAXS patterns of OBC during uniaxial deformation at room temperature.

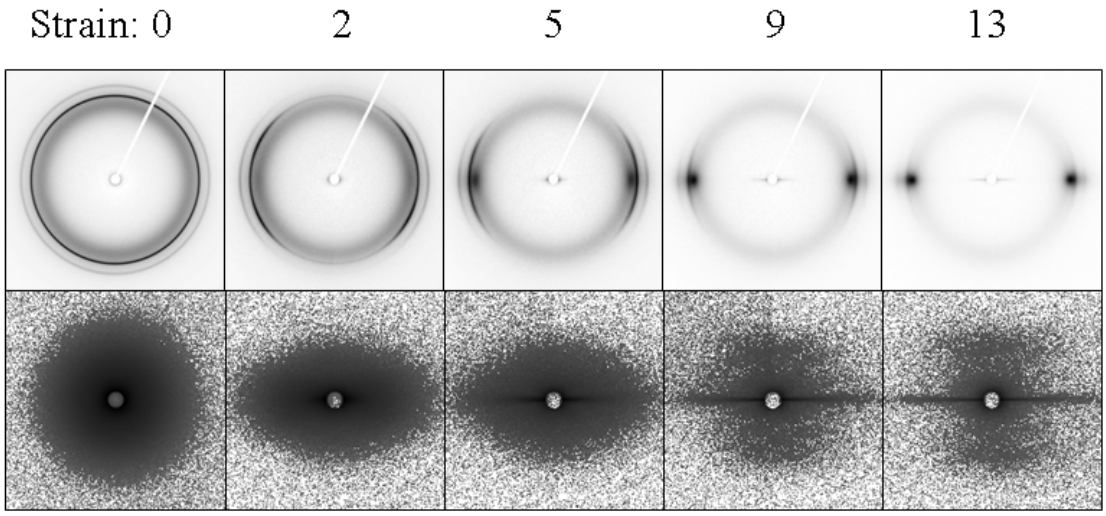

Figure 4.3. 3D WAXD pattern of equatorial region of OBC at strain = 4 at room temperature.

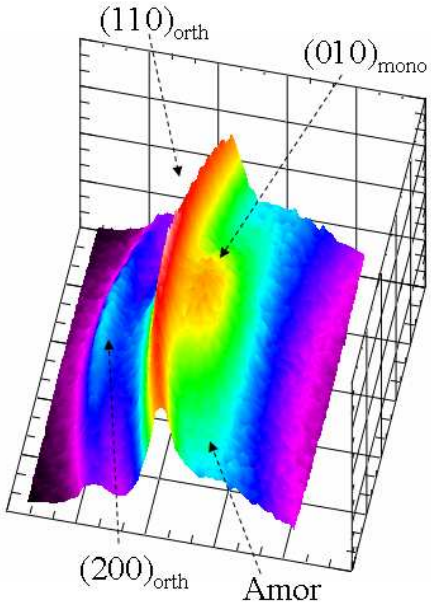

Figure 4.4. 3D structure of orthorhombic (A) and monoclinic (B) crystals.

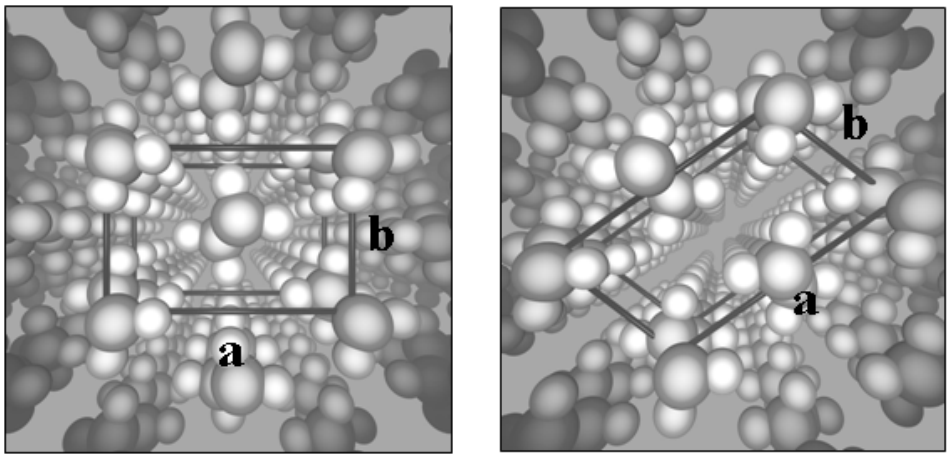

(A) (B)

Figure 4.5. (A) Calculated scattering of orthorhombic and monoclinic crystals without amorphous halo. (B) Experimental scattering pattern of OBC containing amorphous, orthorhombic and monoclinic crystals.

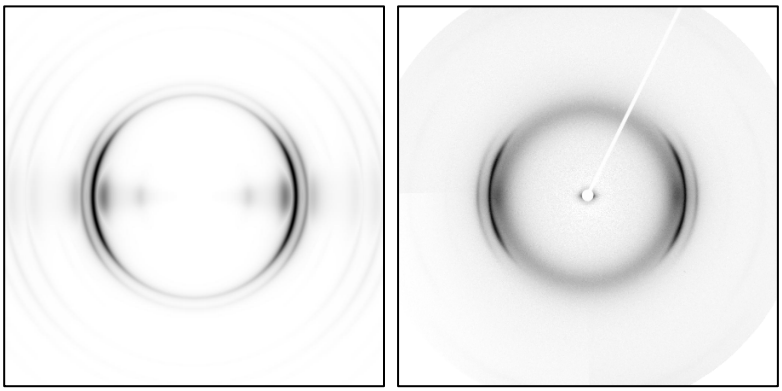

(A) (B)

Figure 4.6. Selected 2D WAXD and SAXS patterns of Affinity during uniaxial deformation at room temperature.

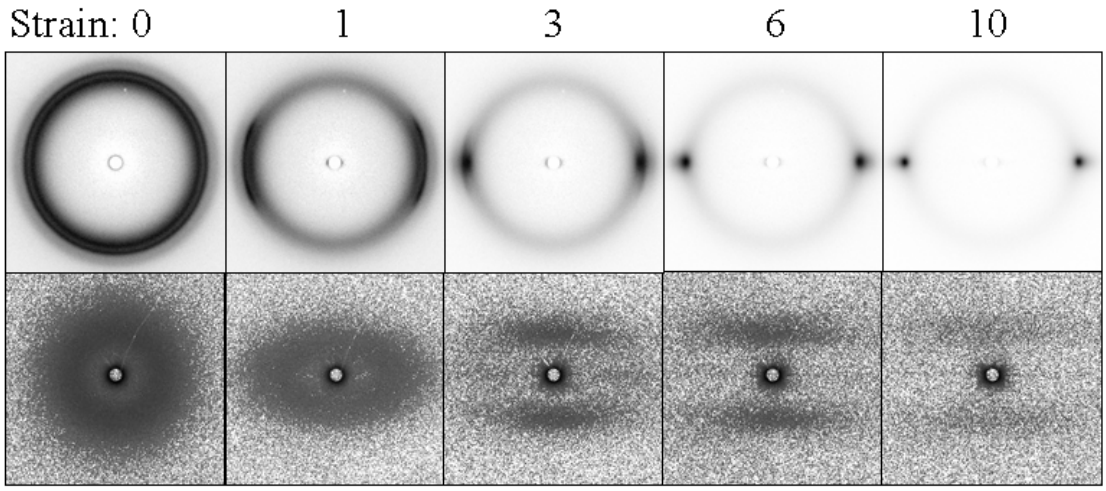

Figure 4.7. Integrated WAXD (A) and SAXS (B) profiles of OBC and Affinity at room temperature before deformation.

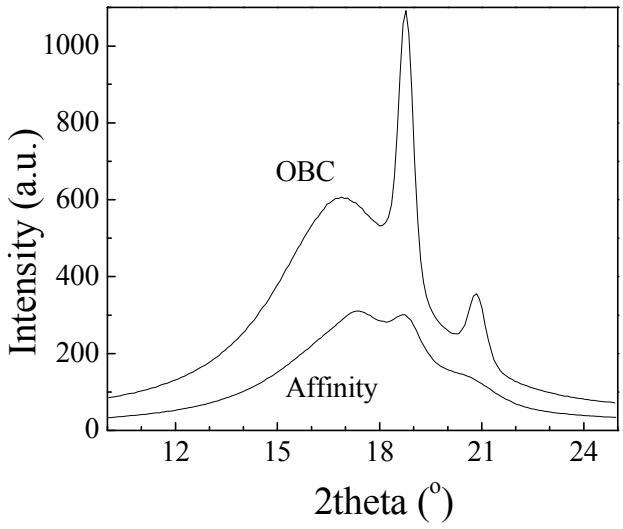

(A)

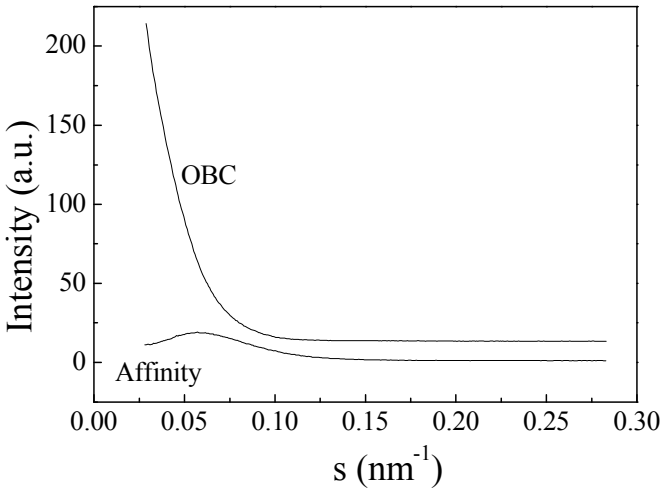

(B)

Figure 4.8. (A) Selected integrated WAXD profiles of OBC during deformation. (B) Selected Lorentz-corrected integrated SAXS profiles along meridian of OBC during deformation.

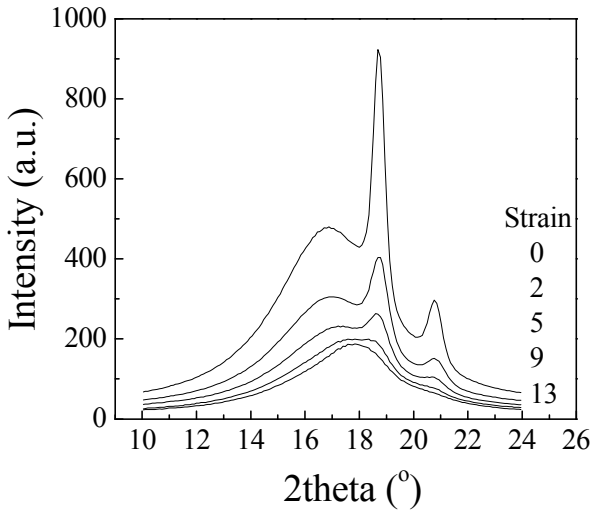

(A)

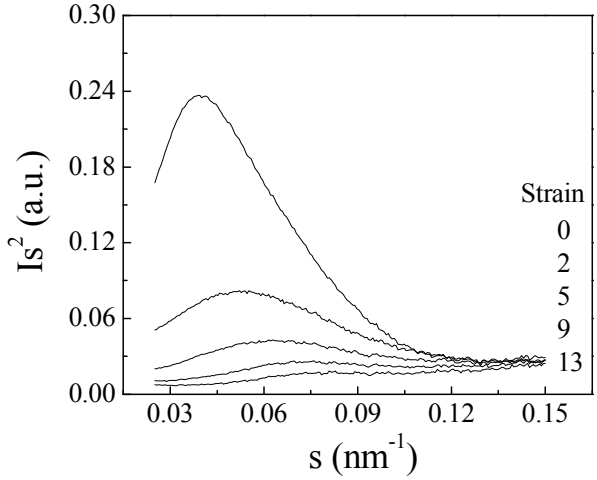

(B)

Figure 4.9. (A) Selected integrated WAXD profiles of Affinity during deformation. (B) Selected integrated SAXS profiles along meridian of Affinity during deformation.

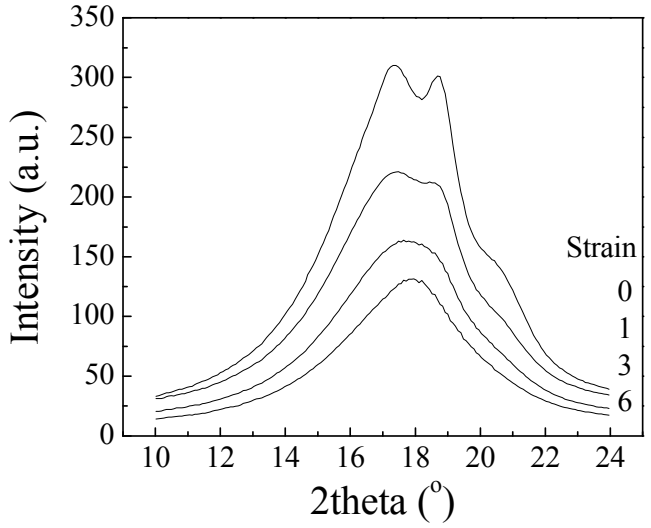

(A)

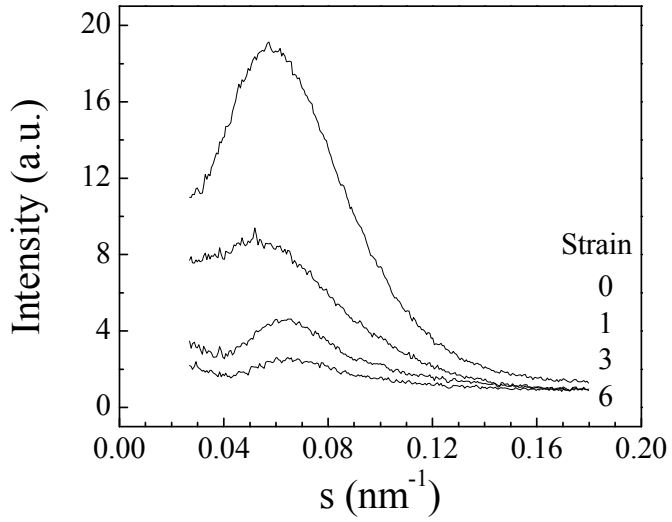

(B)

Figure 4.10. Change of meridional long period during deformation at room temperature.

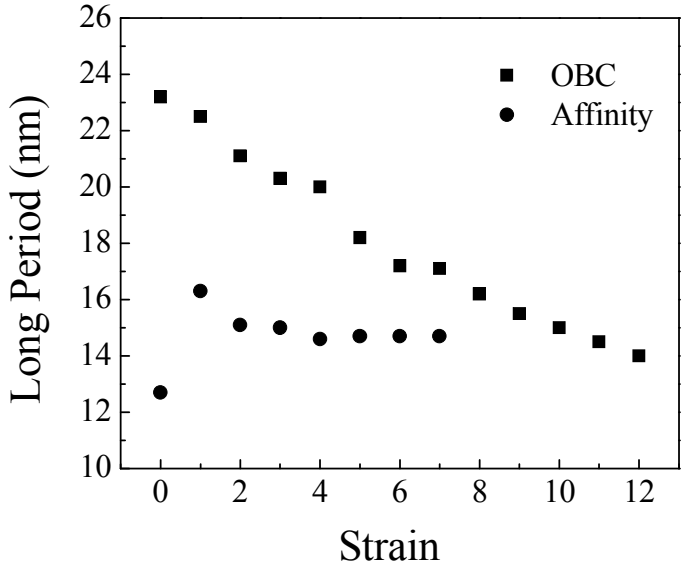

Figure 4.11. 2D SAXS and WAXD patterns of OBC (A) and Affinity (B) right before fracture during deformation at 60 ^{o}C. (Strain = 4.4, and 8.3 for OBC and Affinity, respectively.)

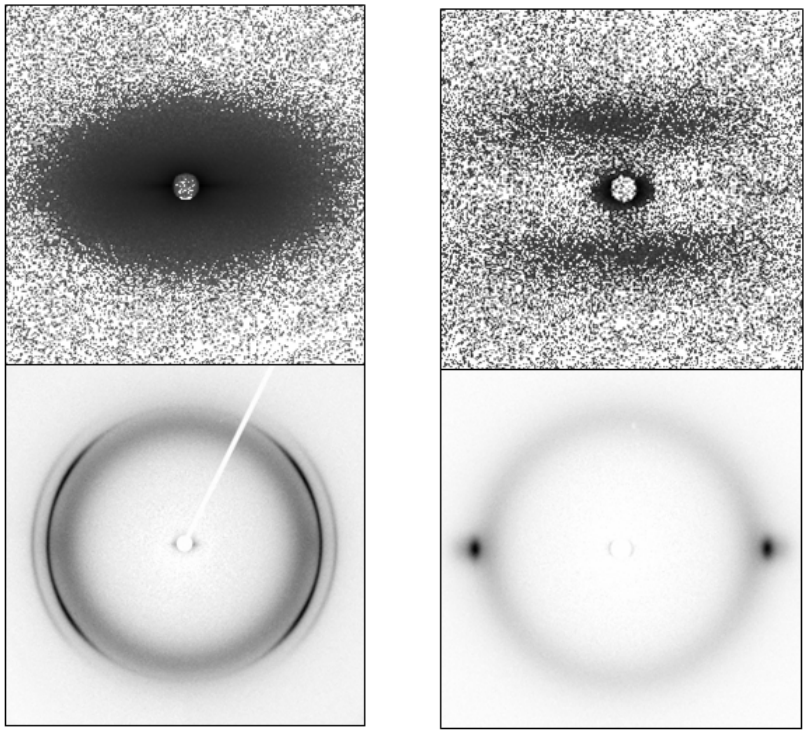

(A) (B)

Figure 4.12. Comparison of integrated WAXD profiles of Affinity at different temperatures and strains.

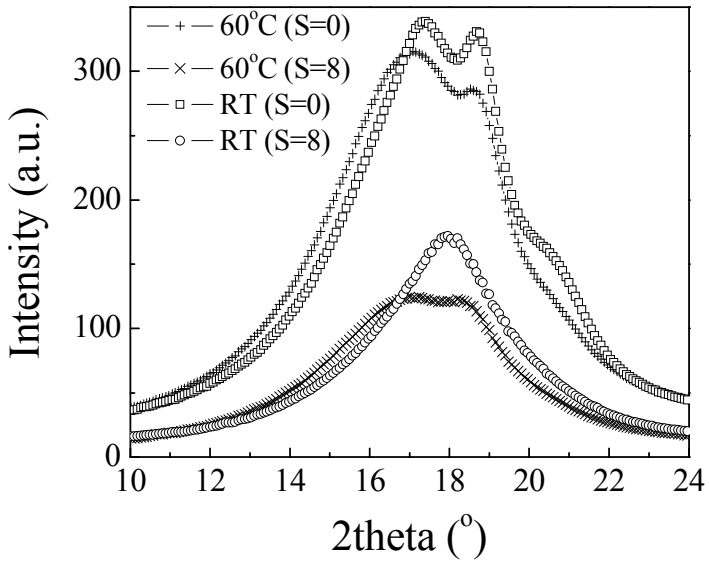

Figure 4.13. Development of fractions of orthorhombic crystals in OBC and Affinity during deformation.

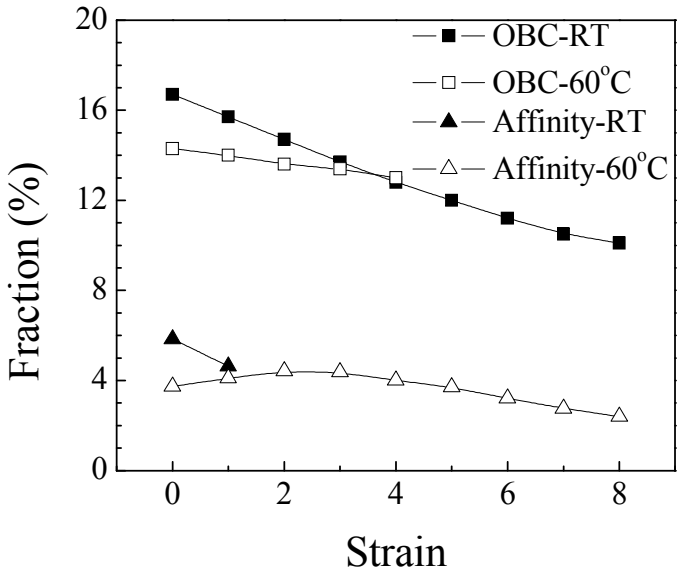

Figure 4.14. Change of FWHM during deformation.

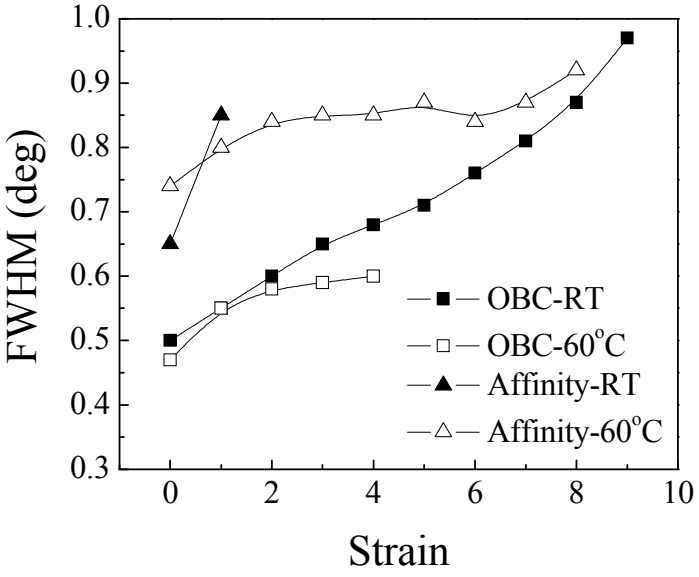

Figure 4.15. Hermans' orientation factors of crystal (A) and amorphous (B) phases as a function of strain.

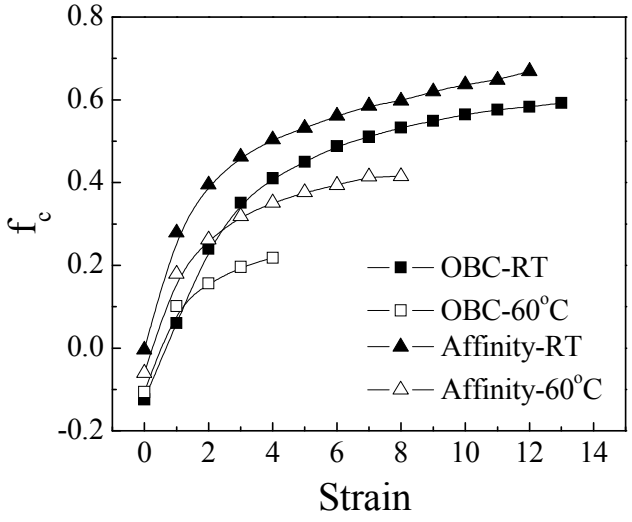

(A)

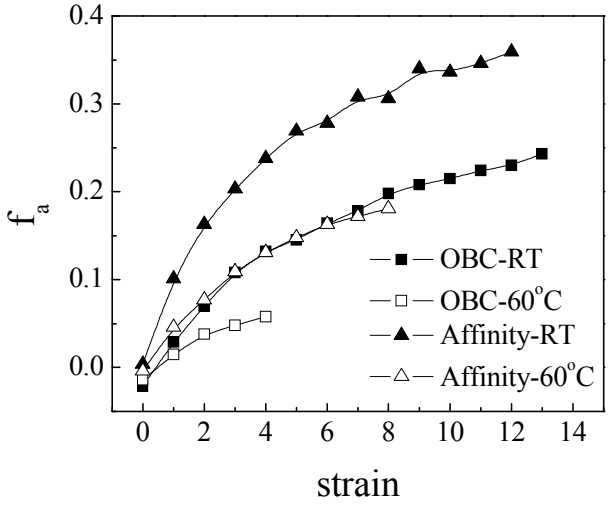

(B)

Figure 4.16. Shematic diagrams of OBC (left) and Affinity (right) in the phase separated pre-crystallization stage (top), after crystallization (mid), and after deformation (bottom). Homogenous entangled amorphous phase was not shown except in melted Affinity.

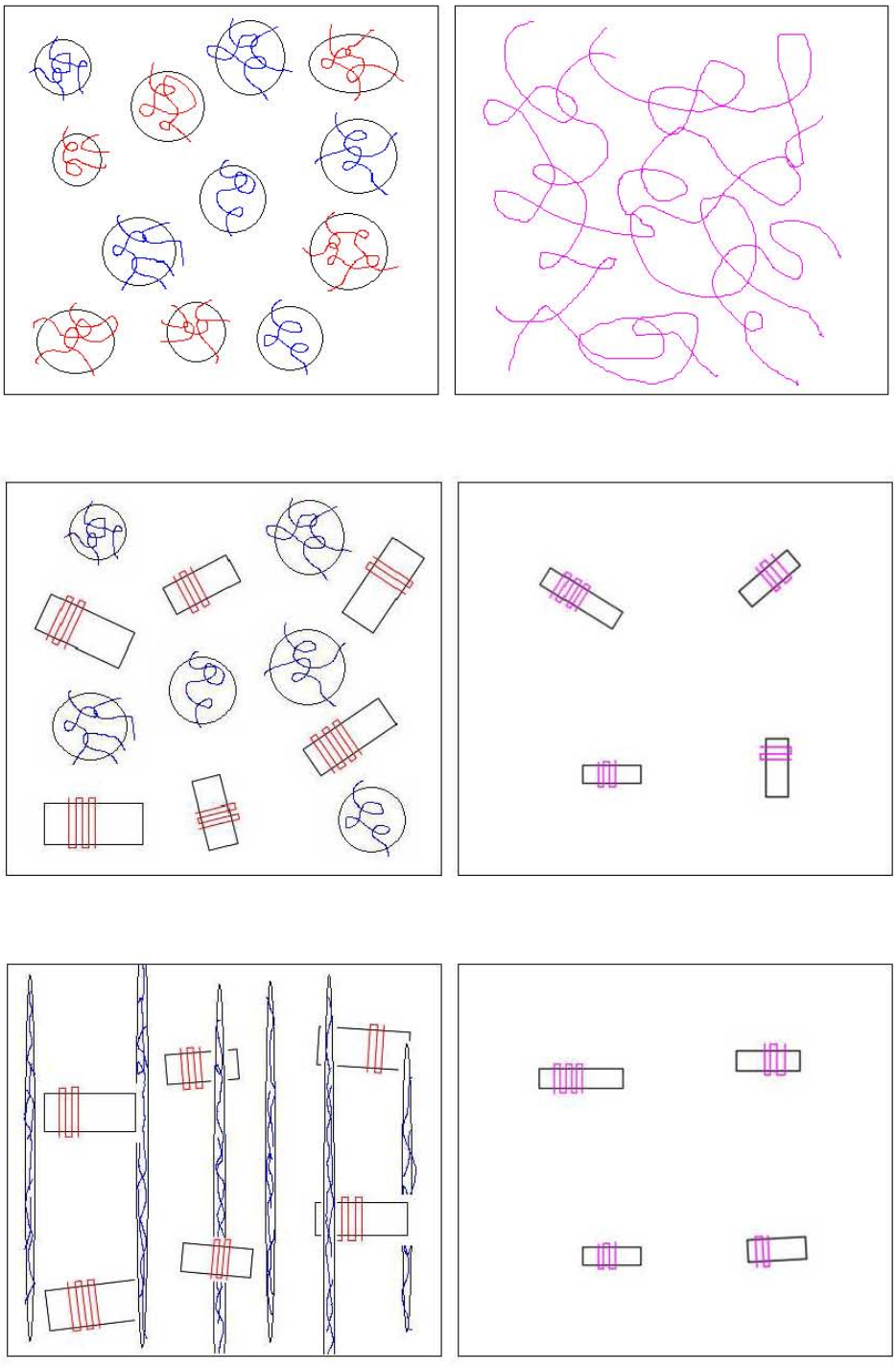

Chapter 5. Effects of Chain Shuttling Agent on the Uniaxial Deformation of Olefin Block Copolymers

5.1 Introduction

Thermoplastic elastomers are the substitutes of nature rubbers that people have been looking for during the past decades of years. They do not only exhibit the desirable elasticity of nature rubbers, but they can also be easily manufactured by simply melting and then processing via extrusion or injection molding.[1] The most common thermoplastic elastomers include some block copolymers, such as styrenics[2] and polyurethanes,[3,4] thermoplastic elastomer blends or alloys,[5] and polyolefin elastomers and plastomers.[6] Recently, one novel thermoplastic elastomer, olefin block copolymer, made from ethylene and α-olefin was produced by The Dow Chemical Company through chain shuttling technology.[7-9] The new OBC can provide much better performance than polyolefin elastomers and plastomers and competitive performance but at much low cost compared to styrenics, thermoplastic vulcanizates and so on.

As named block copolymer, polymer chains in OBCs also consisted of alternating hard and soft segments.[1] The hard segment containing low comonomer content has a medium or high density and a high melting temperature, while soft segment containing high comonomer content has a low density and a low glass transition temperature. The hard segments in OBCs can crystallize at room temperature and provide reversible physical crosslinks and filler-like reinforcement. Once heated up, crystals melt and OBCs can be thermally processed, thus fulfill the basic requirements of a thermoplastic

elastomer. Due to the procedures in producing OBCs, there are many controllable structure factors of OBCs that could be critical in affecting the property of the final products, such as the distribution of block length and number of blocks per chain, ratio of hard and soft segments, and comonomer content in the hard and soft segments,[7] thus the understanding of the relationships between chain architecture, structure, morphology and properties in OBCs deserves extensive studies in order to improve the design of OBCs and make the various tailors of OBCs possible and more efficient, and finally achieve the desirable properties according to the customer's specific needs.

Chain shuttling technology is one of the most special and interesting part during the production of OBCs. The formation of linear segmented polymer chain of OBCs in one polymerization reactor was accomplished by employing two distinct catalysts with different comonomer selectivities and one chain shuttling agent to transfer the growing chain between two kinds of catalysts reversibly to extend the polymer chains with a different segment. In this article, we will focus on the effects of chain shuttling agent content in polymerization processes on the property and structure development of OBCs during the tensile deformation. Since the content of chain shuttling agent determines the frequency of transfers of polymer chain between catalysts, thus if there are more chain shuttling agents, the polymer chain was transferred more frequently, and the time for the segment to grow up on one catalyst is shorter, which meant the segmental length produced is shorter in this case. So the influence of the chain shuttling agent content was then related to effects of length of hard and soft segments in the OBCs.

The impacts of segment on the structure, morphology, and mechanical properties of styrenics, polyurethanes, or other block copolymers have been studied before. The effects of variables in soft segment length,[10-14] hard segment length,[15-17] and content of each segment[19-21] on the morphology and property of polyurethane were investigated, and it

was believed that the phase separation which increases with segment length or the difference in segment content is the primary reason causes the other consequences, such as modulus, hysteresis, crystallinity, temperature dependence, fracture stress and strain. In present study, the chosen two olefin block copolymers had similar molecular weight and molecular weight distribution and the same fraction of different segments which were the same in density, which also meant the same content of comonomer. The only difference was the content of the chain shuttling agent used in polymerization thus the different length of segments. Instron tensile machine combined with in-situ synchrotron X-ray was used to test the mechanical property and detect the structure development of OBCs during the uniaxial deformation at different temperatures. 2D wide-angle X-ray diffraction (WAXD) and small-angle X-ray scattering (SAXS) data were collected and analyzed. One structure model was proposed to explain the structure-property relationship in terms of the different blocky architecture resulting from the content of chain shuttling agent.

5.2 Experimental

5.2.1 Materials

In this study, we had two ethylene-octene block copolymers provided by The Dow Chemical Company. One was OBC-LS produced with low chain shuttling agent content, and the other one was OBC-HS produced with high chain shuttling agent content. The information about the density, segments, chain shuttling agent content, molecular weight, and molecular weight distribution was shown in Table 5.1. Both OBCs had the same segment component, about 80% of soft segment with a density of 0.857 g/cm^3 and rest hard segment with density of 0.932 g/cm^3. The overall density, weight averaged molecular weight and molecular weight distributions were also similar to each other.

However, OBC-LS was produced with a content of 0.4 chain shuttling agent per 1000 ethylene, while for OBC-HS the content increased to 1.3. Thus, as we discussed in the introduction section, the polymer chain in OBC-LS should contain less segments than OBC-HS, and both soft and hard segments in OBC-LS were longer than those in OBC-HS. In terms of the density of each segment, only hard segment in the OBCs can crystallize, while soft segment can not. The isotropic films of the samples were obtained by melting-compression at 165 ^{o}C in a dumbbell shape mold, and then quenched to the room temperature. The dumbbell shape sample was 35 mm long, 6 mm wide and 1 mm thick.

5.2.2 Instrumentation

In-situ WAXD and SAXS studies were carried out at the X27C beam line in the National Synchrotron Light Source (NSLS), Brookhaven National Laboratory (BNL). The wavelength of the synchrotron radiation was 1.371 Å. A three-pinhole collimation system was used to reduce the beam size to 0.6 mm in diameter. 2D WAXD and SAXS patterns were collected by a MAR CCD X-ray detector (MAR-USA), which had a resolution of 1024×1024 pixels (pixel size = 158.44 μm). The typical image acquisition time was 20 s for each data frame. The sample-to-detector distance was around 1900 mm for SAXS (calibrated by a silver behenate (AgBe) standard), and the sample-to-detector distance was around 110 mm for WAXD (calibrated by an aluminum oxide (Al_2O_3) standard). All X-ray images were corrected for background scattering, air scattering and beam fluctuations.

Uniaxial tensile deformation was performed with a modified Instron 4442 tensile apparatus, which could stretch the film symmetrically. The symmetric stretching guaranteed that the focused X-ray beam could illuminate the same sample position during

deformation. The original length of the sample between the Instron clamps was 15 mm. A constant deformation rate, 4.5 mm/min (30 %/min), was applied to the specimen throughout the deformation study. The deformation experiments were carried out at room temperature and 60 ^{o}C. The stress and strain mentioned through the article were all engineering stress and engineering strain measured directly between clamps. Step-cycle mechanical tests were also carried out for both samples at room temperature. In these tests, the films were stretched at 15 mm/min (100 %/min) to a certain strain and then brought back to zero stress at the same speed, and the sample was stretched again to a higher strain and relaxed back. This loading unloading cycle was carried out several times to study the structure development.

5.3 Results and Discussion

5.3.1 Mechanical Properties of OBCs

Engineering stress-strain curves and 2D SAXS and WAXD patterns of OBC-HS and OBC-LS during the uniaxial deformation at room temperature were quite similar to each other, so here we only showed the stress-strain curve and selected patterns from OBC-HS in Figure 5.1 to demonstrate the mechanical property and structure development during the deformation. The stress-strain curve exhibited a distinguishable but not pronounced yielding point, typical of an elastomeric material. The stress was about 1.5 MPa at yielding point and then increased almost linearly with strain for a certain period. In the later stage of deformation, strain hardening was observed when stain value exceeded 10. The failure of OBC-HS film occurred at strain of 14, slightly higher than OBC-LS which had a fracture strain of 13, and the ultimate stress was around 6MPa.

5.3.2 Uniaxial Deformation at Room Temperature

The first 2D WAXD and SAXS patterns were isotropic, confirming that both large scale structure and small scale crystals were randomly arranged in the quenched OBC films before deformation. The broad diffraction peak in WAXD came from the amorphous phase of OBC, while the positions of the rest two sharp reflections were consistent with (110) and (200) reflections of orthorhombic crystals of polyethylene, which meant that hard segments containing small amount of octene comonomer can crystallize well into regular polyethylene crystals as common medium density polyethylene without being disrupted by neighboring low density soft segments. The SAXS did not show the clear first order scattering peak of lamellar stacks, which was believed to hide underneath of the scattering from uncorrelated rich domains mainly composed of soft segment. These domains in the length scale of tens of nanometers were formed because of the crystallization-induced phase separation between part of the crystallizable hard segments and non-crystallizable soft segments. After taking Lorentz-correction, the first order scattering of lamellar structure will appear indicating that folded-chain crystal lamella existed in the OBC films. As strain increased, the spherical domains were deformed into elliptical shape with long axis aligned parallel to the drawing direction, while lamellar stacks were stretched perpendicular to it. This led to the scattering intensity condensed into the equatorial and meridional direction, respectively. Finally, at high stain, scatterings from the needle-like soft domains and lamellar stacks were separated because of the high degree of orientation, resulting in equatorial streak and meridional maximum in 2D SAXS patterns. In the 2D WAXD patterns, the azimuthal spread of (110) and (200) reflections became narrow upon deformation also because of the induced orientation of the crystals. At strain of 2, the (110) reflection split into four arcs at off-axis while (200) reflection remained at the equator, indicating b-axis orientation of the polymer chain. Later, (110) reflection also moved to the equator as strain increased further, because the polymer chains aligned to an even high degree with

c-axis orientation of the polymer chain. When approaching the late stage of the uniaxial deformation, strong point-like reflection was observed at equator, which was not from oriented amorphous but from newly formed monoclinic crystal as we discussed in our previous study.

The integrated WAXD profiles were shown in Figure 5.2 (A). It can be seen that the broad amorphous peak shifted to the right toward high 2 theta angle due to the new (010) peak which was from the monoclinic phase and located in between amorphous and (110) peaks. The intensities of (110) and (200) peaks decreased a lot because the OBC film was thinner, and more important the orthorhombic crystals were deformed. Since the area of broad peak can represent the total fraction of amorphous and monoclinic phase, the fraction index of orthorhombic crystal, that was the area percentage of two sharp (110) and (200) peaks, can be calculated using peaking fitting of linear WAXD profile at low strain. However, the overlap of these peaks at high strain made the calculation of the fraction index of orthorhombic phase more difficulty because it was impossible to separate peaks by 1D peak fitting. The Lorentz-corrected linear SAXS profiles along meridian were shown in Figure 5.2 (B). The long period, which is the average distance between two lamellar layers, is the inverse of the s value at peak position. As the peak shifted to the right with strain, the long period was decreasing within the sample. We calculated the long period of the lamellar structure in OBCs along both meridional direction and equatorial direction during uniaxial deformation at room temperature deformation and plotted versus strain in Figure 5.3. The meridional long period of both OBCs decreased continuously from 25nm, because some loosely packed lamellar layers were fragmented upon drawing. Equatorial long period dropped a lot more than meridional one, not only because the reason mention above, but also due to the orientation of the lamellar stacks. When the OBCs were stretched to strain higher than 7, the scatterings from lamella can not be detected at equatorial direction, only streak was

observed, proving that lamella stacks were orientation perpendicular to the drawing direction, while soft segment rich domains were parallel to it.

5.3.3 Uniaxial Deformation at 60 ^{o}C

The uniaxial deformation was also carried out at higher temperature, 60 ^{o}C. Here we showed the engineering stress-strain curves and selected 2D WAXD and SAXS patterns of both OBC-HS and OBC-LS in Figure 5.4 and 5.5, respectively. The mechanical properties of both OBCs became much poorer at high temperature. The stress increased at the initial stage of deformation, but after passing the yielding point it kept a plateau value and even decreased to some extent before fracture. No strain hardening behavior was found. Besides, at high temperature, OBC-HS and OBC-LS behaved quite different to each other comparing with room temperature. One prominent difference was the fracture strain of OBC films. Both films can be stretched to a high strain of 13 or 14 at room temperature, but when heated to 60 ^{o}C only OBC-HS can still preserve certain good drawability and can be stretched to a high strain of 12, while that of OBC-LS was decreased dramatically than room temperature. From Figure 5.5 we can see that the fracture strain of OBC-LS was only 4.5 at 60 ^{o}C. This difference could be attributed to the enhanced mobility of the amorphous chains and the distribution of tie chains related to the special blocky chain architecture of OBCs which we will discuss more in detail later. Moreover, caused by the low fracture strain at high temperature, polymer chains and large scale lamellar structure, and soft segment rich domains in OBC-LS can only reach a low degree of orientation revealed from 2D WAXD and SAXS patterns. In embodiments, the (110) and (200) reflections were very widely spread, and the scattering from soft domains lamellar stacks in the SAXS was more closed to the isotropic state other than separated equatorial streak and meridional maximum. The (010) reflection from monoclinic phase located between (110) reflection and amorphous halo was not

observed before fracture. By comparing with the deformation process at room temperature, we can conclude that monoclinic phase was not stable and can not form under low stress and high temperature. The structure and orientation development in OBC-HS was similar to that at room temperature, except the kinetic aspects slowed down due to the elevated temperature. In detail, the deformation of soft domains, the orientation of polymer chains and lamellar stacks increased slowly than room temperature, the phase formation of monoclinic was delayed and the fraction of monoclinic phase was less while more original orthorhombic crystals remained.

5.3.4 Structure Evolution during Deformation

Fractions of orthorhombic crystals of two OBC samples at both temperatures were calculated using linear peak fitting method as mentioned before and plotted in Figure 5.6. The initial fraction was about 17% or 18% for OBCs at room temperature, which was also believed to be the crystallinity index of the initial OBCs since only the orthorhombic crystals consisted of crystal phase, this value dropped a couple of percentages at 60 ^{o}C as a result of melting of some small and defective crystals. Upon deformation at room temperature, the fraction kept decreasing to about 11% when strain reached around 7. Beyond this strain, calculations of fractions were not possible through 1D peak fitting. There was a crossover of two curves at strain equal to 5, thus the decreasing rate was faster in OBC-HS than OBC-LS, meaning that the lamellar crystal structure was easily deformed in OBC-HS. Once the temperature was elevated to 60 ^{o}C, we noted that the slope of the fraction curve of OBC-LS was not as steep as others. The reduction of the orthorhombic phase of OBC-LS was only 1%, while in OBC-HS it was about 3% till strain of 4. This indicated the high temperature affected the deformation behavior of OBC-LS more significantly than others. The reason can be also attributed to the enhanced mobility of amorphous chains and the distribution of tie chains.

The orientation factors of both amorphous and crystal phases were calculated using Hermans' orientation function:[22]

$$f = \frac{3\langle \cos^2 \phi \rangle - 1}{2}$$

where ϕ is the angle between the chain axis and the reference axis (stretching direction). $\langle \cos^2 \phi \rangle$ is defined as:

$$\langle \cos^2 \phi \rangle = \frac{\int_0^{\pi/2} I(\phi) \cos^2 \phi \sin \phi d\phi}{\int_0^{\pi/2} I(\phi) \sin \phi d\phi}$$

where $I(\phi)$ is the scattered intensity along the angle ϕ. Since there is no plane of symmetry perpendicular to the chain axis, the c axis orientation can not be measured directly due to the absence of (00L) plane, but we can still obtain that indirectly from the (110) and (200) reflections using

$$\langle \cos^2 \phi \rangle = 1 - 1.435\langle \cos^2 \phi_{110} \rangle - 0.565\langle \cos^2 \phi_{200} \rangle .$$

Regarding amorphous phase, the orientation we calculated was actually that of the normal vector of the amorphous chains, so the f value was multiplied by a factor of -2 to convert that into the value representing the degree of orientation along the stretching direction. Moreover, in calculating the orientation of amorphous phase, the azimuthal scan was chosen along a lower s value at 2.04 nm^{-1} rather than the amorphous peak at 2.13 nm^{-1} in order to reducing the contribution from (010) reflection. The value of orientation factor is between -0.5 to 1. When f = 1, it means all polymer chains align to the stretching direction perfectly, while f = -0.5 means chains are all perpendicular to the stretching direction, and f = 0 indicates random orientation of the chains. The calculated results were plotted in Figure 5.7 (A) and (B) as a function of strain. At room temperature, the orientation factor of amorphous rose from 0 to 0.25 before fracture,

much lower than that of crystal at about 0.6, which was easily understood from the point of view of easy relaxation of the amorphous chains. Besides, we can see that both orientation factors of crystal and amorphous phases of OBC-HS and OBC-LS were quite close through out the whole deformation process at room temperature, with that of OBC-HS being only slightly higher, about 10%. However, the difference between orientation factors became quite large at 60 ^{o}C, e.g. the orientation factor of OBC-HS was about twice of OBC-LS at strain of 4. This should also relate to the influence of the high temperature on the deformation behavior of OBC-LS, consistent with what we observed in the change of the fractions of the orthorhombic phase at different temperatures.

5.3.5 Effects of Chain Shuttling Agent

The experimental observations described above can be explained according to the difference in chain architecture resulted from the amount of chain shuttling agents used during the polymerization of OBCs. As the chain shuttling agents were used to transfer the growing chain from one catalyst to another to form the blocky structure, more chain shuttling agents in OBC-HS led to more frequently shuttling, thus the segmented soft or hard blocks in each polymer chain was shorter in OBC-HS than OBC-LS. On the other hand, the molecular weight was similar for both OBC-HS and OBC-LS, thus the total number of blocks in OBC-HS was greater than OBC-LS. The Figure 5.8 was a schematic diagram showing the difference in lamellar structure before and after drawing in OBCs with hard segments colored in red and soft segments colored in blue. Soft segment rich domains and entangled amorphous phase were neglected. Because the hard segments were longer and less in OBC-LS than in OBC-HS, so after crystallization from melt each polymer chain tended to go through only a couple of lamellar crystals. However, for OBC-HS, polymer chains can join in different hard segment rich domains before crystallization, and then each chain can go through more lamellar crystals after

crystallization comparing with OBC-HS. Thus the number of tie chain segments in OBC-HS was greater than OBC-LS, and tie chains in OBC-HS were also greater and more effective as they participated in more lamellar crystals. Along with the tie chains, entanglement also played an important role during the deformation. For both OBCs, the entanglement density should be roughly the same, since the volume fraction and the molecular weight of the soft segment was the similar. Considering the influences of both tie chains and entanglements on the uniaxial deformation at different temperatures, experimental observations can be explained as follows. At room temperature, disentanglement was difficult to take place as the mobility of the amorphous chains was very limited, both tie chains and entanglement points were effective in localizing the stress. The similar entanglement density in two OBC films and higher tie chain content in OBC-HS together led to the observed room temperature phenomenon that was the similar deformation behavior but slightly higher degree of orientation and efficiency in deforming the crystal structure in OBC-HS. However, at high temperature, the mobility of the amorphous chain enhanced a lot, thus it was easy for the disentanglement to occur because the amorphous chains can slide away from the entanglement points without much difficulty during the stretching. Then the effects of tie chains were more prominent in the deformation. As shown in Figure 5.8, more tie chain segments in OBC-HS resulted in severe deformation and fragmentation of lamellar crystals and a faster decrease of the fraction of orthorhombic phase, and also a more effective network and thus a higher degree of orientation. Also due to the lack of tie chains to connect lamellar layers, OBC-LS broke easily at a much lower strain as amorphous chains slide away.

5.3.6 Recoverabilities of OBCs

The step cycle tests of OBCs at room temperature were also investigated. We still only showed the 2D WAXD and SAXS patterns of OBC-HS due to its similarity with

OBC-LS. Both engineering stress-strain curves of two samples were plotted. It was clear to see that the permanent set of OBC-LS was smaller than OBC-HS, for example, after the release of load from samples stretched to a strain ratio of 4, OBC-LS can relax to strain of 0.8, and OBC-HS only returned to strain of 1.5, indicating a better recoverability of OBC-LS. From the crystal structure, we knew that there would be more lamellar crystals in OBC-HS and they were easier to be fragmented comparing with OBC-LS. Once deformed, these crystals were deconstructed and can no longer act as physical crosslink to connect the polymer chains together and thus prevented OBC-HS from shrinking back upon the release of the load. The fraction of orthorhombic crystals as a function of time during step-cycle test was plotted in Figure 5.10. The first data point was the initial state before drawing, and followed by stretched and relaxed state one by one (in turns corresponding to pattern A, a, B, b, C, c, D, d in Figure 5.9). The fraction decreased upon drawing and increased upon relaxation, demonstrating the strain-induced melting and re-crystallization mechanism or in other words the transformation between orthorhombic and monoclinic crystals. Consistent with previous straight deformation, orthorhombic fraction of OBC-HS was higher than OBC-LS at first but it declined fast and later dropped to value less than the fraction in OBC-LS. This again proved the easy fragmentation and poor recovery of OBC-HS because of its highly segmented chain structure. The orientation factors of crystal and amorphous phases though step-cycle tests in both OBCs were also shown in Figure 5.11(A) and (B). The degree of orientation was of course high when stretched and low when relaxed. Take a look at last two data points collected at strain of 4 and its relaxed analogue, when both OBC films were stretched, the orientation factors of amorphous were almost the same at 0.14, but it relaxed to 0.05 for OBC-HS and 0.02 for OBC-LS. These of crystal were also quite close around 0.45, and when film relaxed they decreased to 0.35 and 0.2 for OBC-HS and OBC-LS, respectively. It was not surprising to see the appearance of large difference between

orientation factors when the OBC films brought back to the zero stress, as we already discussed that the OBC-LS has a better recoverability.

5.4 Conclusions

Novel OBCs provided a great way to investigate the influence of structure, in specific, the segmented chain architecture, on the macroscopic properties upon deformation, as two samples studied had most of the molecular characteristics in common except the length and number of the segmented blocks, achieved by varying the content of chain shuttling agent used during production. When hard segments crystallized, polymer chains from OBC-HS can go through more lamellar crystals, because they consisted of more blocks than OBC-LS, and formed more tie chains, which were also more effective. In addition, by considering another important factor, the entanglement, we can then explain our experimental observations as follows. At room temperature the restriction on the mobility of the amorphous chains limited the occurrence of disentanglement, the integrated effect of tie chain and entanglement was that both samples behaved similarly with OBC-HS being only slightly higher in orientation and faster in the decline of orthorhombic fraction and a poor recoverability. However, at high temperature, easy disentanglement made the tie chain a dominant role affecting the deformation, leading to the distinct differences in fracture strain, orientation, and structure development between two samples comparing to room temperature.

List of References

1. Holden, G.; Kricheldorf, H. R.; Quirk, R. P. *Thermoplastic elastomers* 3rd edition; Munich: Hanser, **2004**.
2. Holden, G. *J Elastoplastics* **1970**, *2*, 234-246.
3. Hepburn, C. *Polyurethane Elastomers* 2nd edition; Elsevier Applied Science: London, **1991**.
4. Wirpsza, Z. *Polyurethanes: Chemistry, Technology and Application*; Horwood: New York, **1993**.
5. Abdou-Sabet, S.; Puydak, R. C.; Rader, C. P. *Rubber Chem. Tech.* **1996**, *69*, 476-494.
6. Batistini, A. *Macromol. Symp.* **1995**, *100*, 137-142.
7. Arriola, D. J.; Carnahan, E. M.; Hustad, P. D.; Kuhlman, R. L.; Wenzel, T. T. *Science* **2006**, *312*, 714-719.
8. Wang, H. P.; Khariwala, D. U.; Cheung, W.; Chum, S. P.; Hiltner, A.; Baer, E. *Macromolecules* **2007**, *40*, 2852-2862.
9. Khariwala, D. U.; Taha, A.; Chum, S. P.; Hiltner, A.; Baer, E. *Polymer* **2008**, *49*, 1365-1375.
10. Martin, D. J.; Meijs, G.. F.; Renwick, G. M.; McCarthy, S. J.; Gunatillake, P. A. *J. Appl. Polym. Sci.,* **1996**, *62*, 1377-1386.
11. Martin, D. J.; Meijs, G.. F.; Gunatillake, P. A.; McCarthy, S. J.; Renwick, G. M. *J. Appl. Polym. Sci.,* **1997**, *64*, 803-817.
12. Gisselfalt, K.; Helgee, B. *Macromol. Mater. Eng.* **2003**, *288*, 265-271.
13. Chu, B.; Gao, T.; Li, Y.; Wang, J.; Desper, C. R.; Byrne, C. A. *Macromolecules* **1992**, *25*, 5724-5729.
14. Kong, X.; Tan, S.; Yang, X.; Li, G.; Zhou, E.; Ma, D. *J Polym. Sci. Part B: Polym. Phys.*, **2000**, *38*, 3230-3238.

15. Miller, J. A.; Lin, S. B.; Hwang, K. K. S.; Wu, K. S.; Gibson, P. E.; Cooper, S. L. *Macromolecules* **1985**, *18*, 32-44.
16. Versteegen, R. M.; Kleppinger, R.; Sijbesma, R. P.; Meijer, E. W. *Macromolecules* **2006**, *39*, 772-783.
17. Amitay-Sadovsky, E.; Komvopoulos, K.; Ward, R.; Somorjai, G. A. *Appl. Phys. Lett.* **2003**, *83*, 3066-3068.
18. Chen, S.; Hu, J.; Liu, Y.; Liem, H.; Zhu, Y.; Liu, Y. *J Polym. Sci. Part B: Polym. Phys.* **2007**, *45*, 444-454.
19. Kim, B. K.; Shin, Y. J.; Cho, S. M.; Jeong, H. M. *J Polym. Sci. Part B: Polym. Phys.* **2000**, *38*, 2652-2657.
20. O'sickey, M. J.; Lawrey, B. D.; Wilkes, G. L. *J. Appl. Polym. Sci,* **2002**, *84*, 229-243.
21. Puskas, J. E.; Antony, P.; Fray, M. E.; Altstadt, V. *Euro. Poly. J.* **2003**, *39*, 2041-2049.
22. Wilchinsky, W. Z. J. Appl. Phys. 1960, 31, 1969.

List of Tables

Table 5.1. Density, component, chain shuttling agent content and molecular weight information of OBC samples.

	Overall density (g/cm^3)	%soft	Soft segment density	Hard segment density	Zn/[C2] *1000	M_w (kg/mol)	M_w/M_n
OBC-LS	0.875	79	0.857	0.932	0.4	124	3.05
OBC-HS	0.878	78	0.857	0.932	1.3	118	2.23

List of Figures

Figure 5.1. Engineering stress-strain curve and selected 2D WAXD and SAXS patterns of OBC-HS during uniaxial deformation at room temperature.

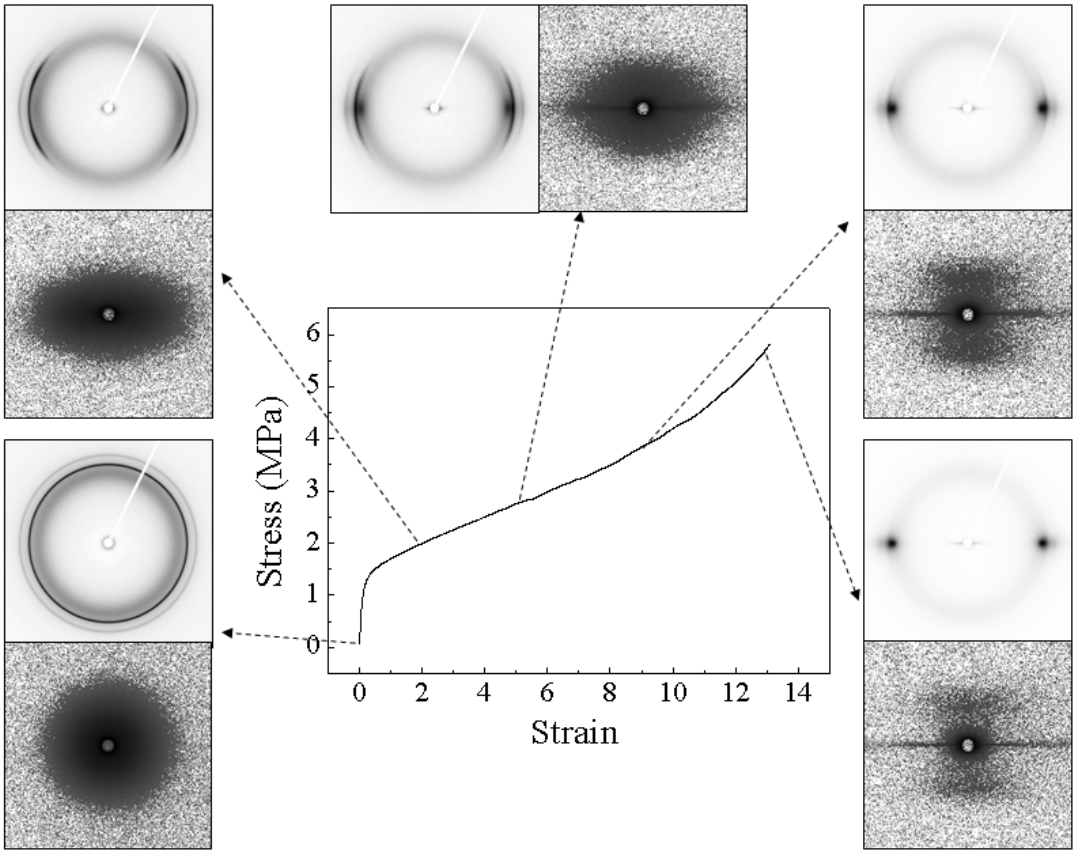

Figure 5.2. Selected integrated WAXD profiles (A) and Lorentz-corrected integrated SAXS profiles along meridian (B) of OBC-HS during uniaxial deformation at room temperature.

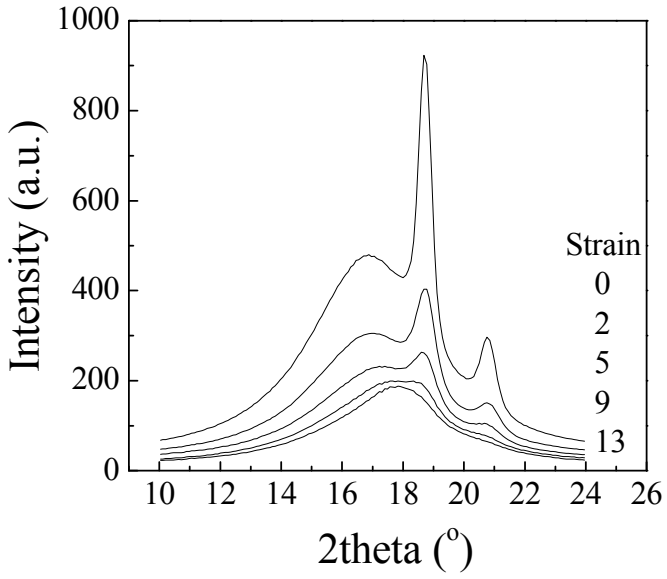

(A)

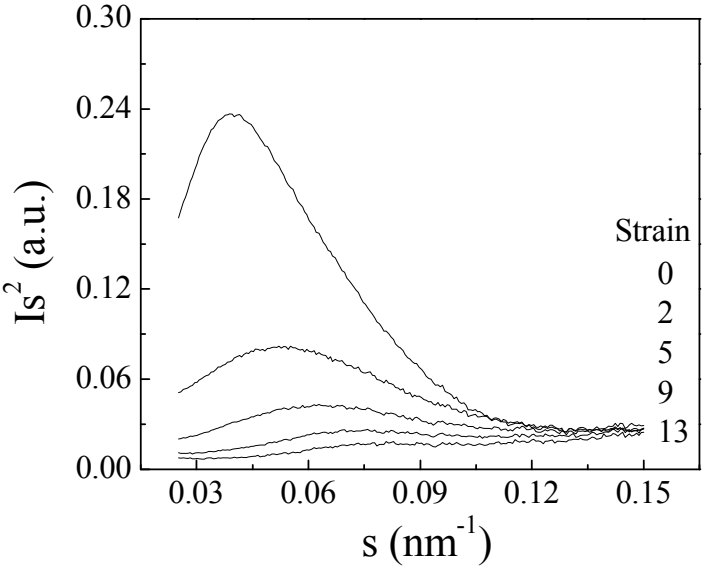

(B)

Figure 5.3. Change of equatorial and meridional long period of OBCs during uniaxial deformation at room temperature.

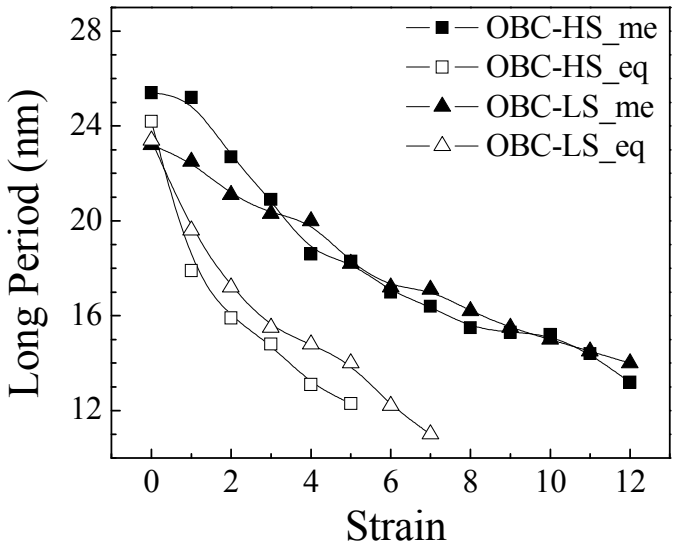

Figure 5.4. Engineering stress-strain curve and selected 2D WAXD and SAXS patterns of OBC-HS during uniaxial deformation at 60 ^{o}C.

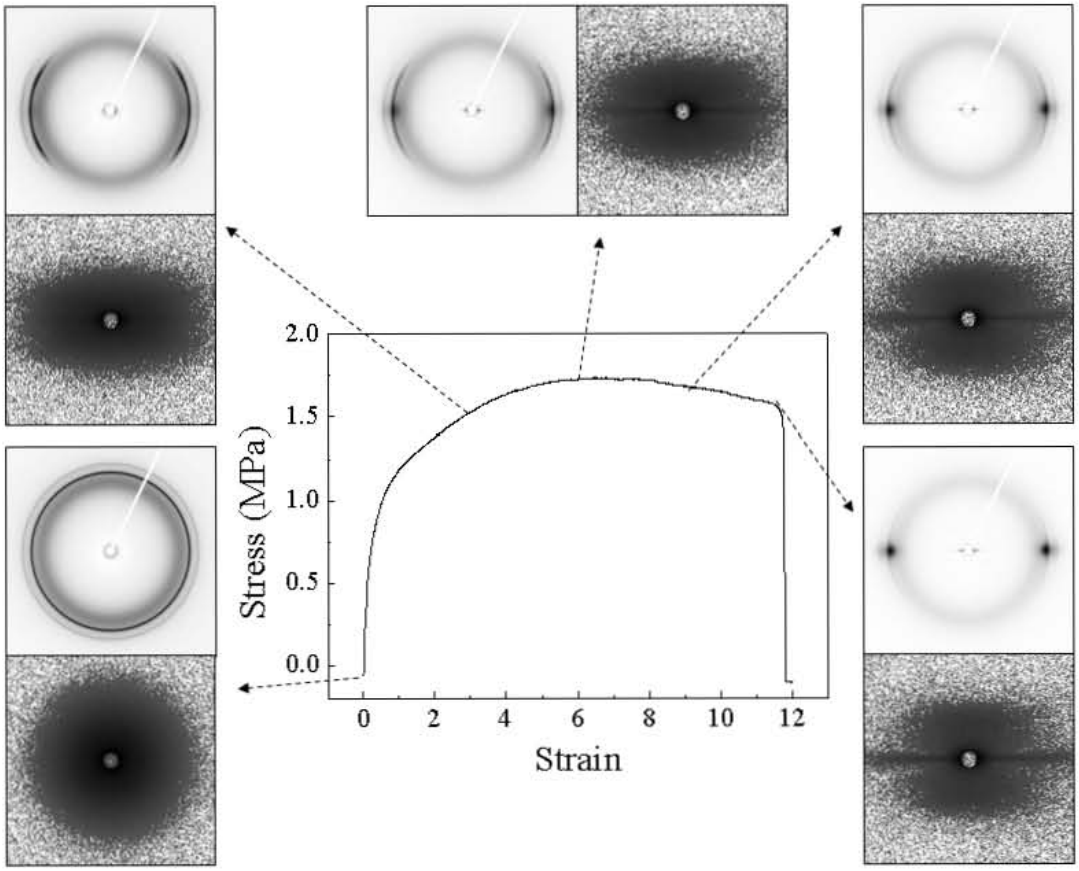

Figure 5.5. Engineering stress-strain curve and selected 2D WAXD and SAXS patterns of OBC-LS during uniaxial deformation at 60 ^{o}C.

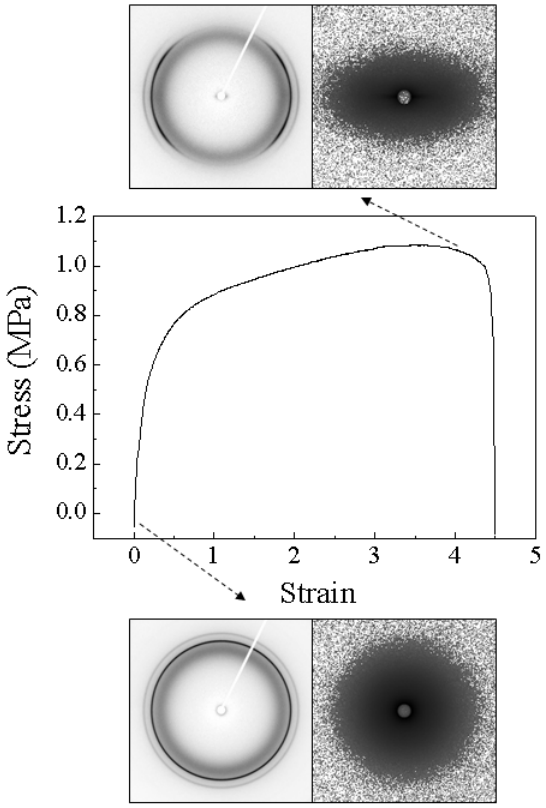

Figure 5.6. Fractions of orthorhombic crystals in OBCs during the uniaxial deformation.

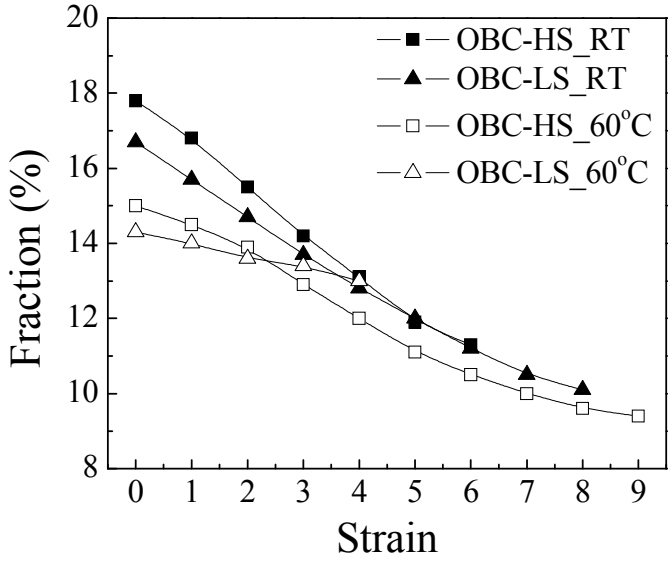

Figure 5.7. Orientation factors of amorphous (A) and crystal (B) as a function of strain in OBCs during deformation.

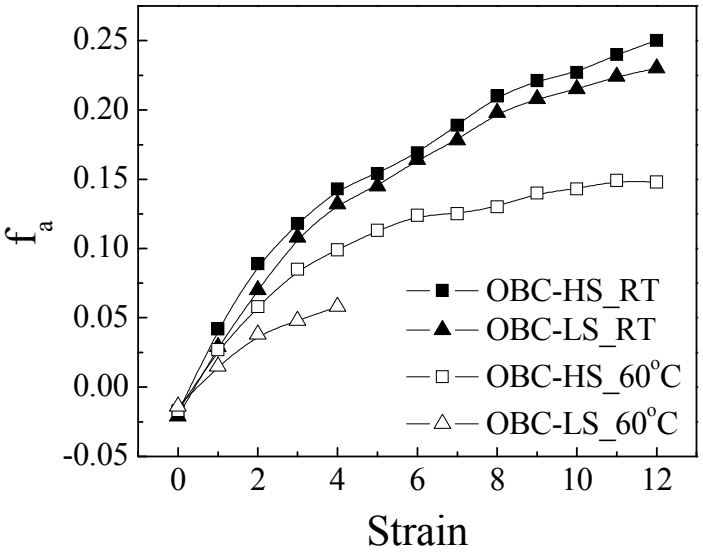

(A)

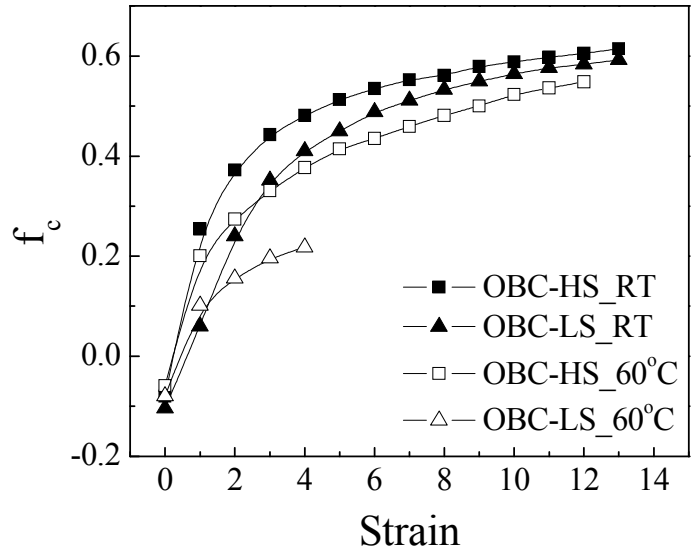

(B)

Figure 5.8. Schematic diagram of the lamellar structure in OBC-LS (left) and OBC-HS (right) before (top) and after (bottom) uniaxial deformation. Soft segment rich domains and entangled amorphous phase are neglected.

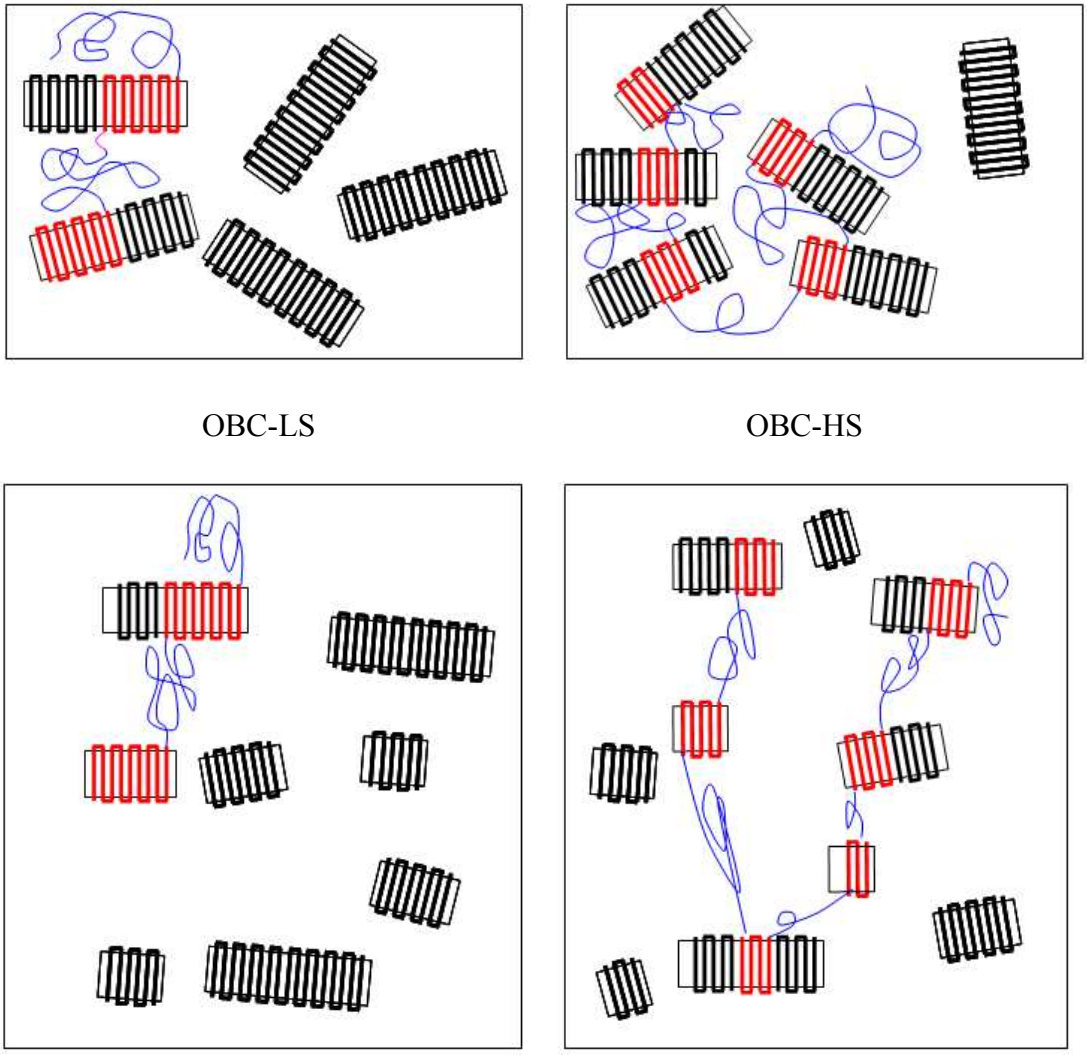

Figure 5.9. Engineering stress-strain curve and selected 2D SAXS and WAXD patterns of OBC-H during the step-cycle test at room temperature. A, B, C, and D are at stretched states with stain of 1, 2, 3, and 4, while a, b, c, and d are at relaxed states from them.

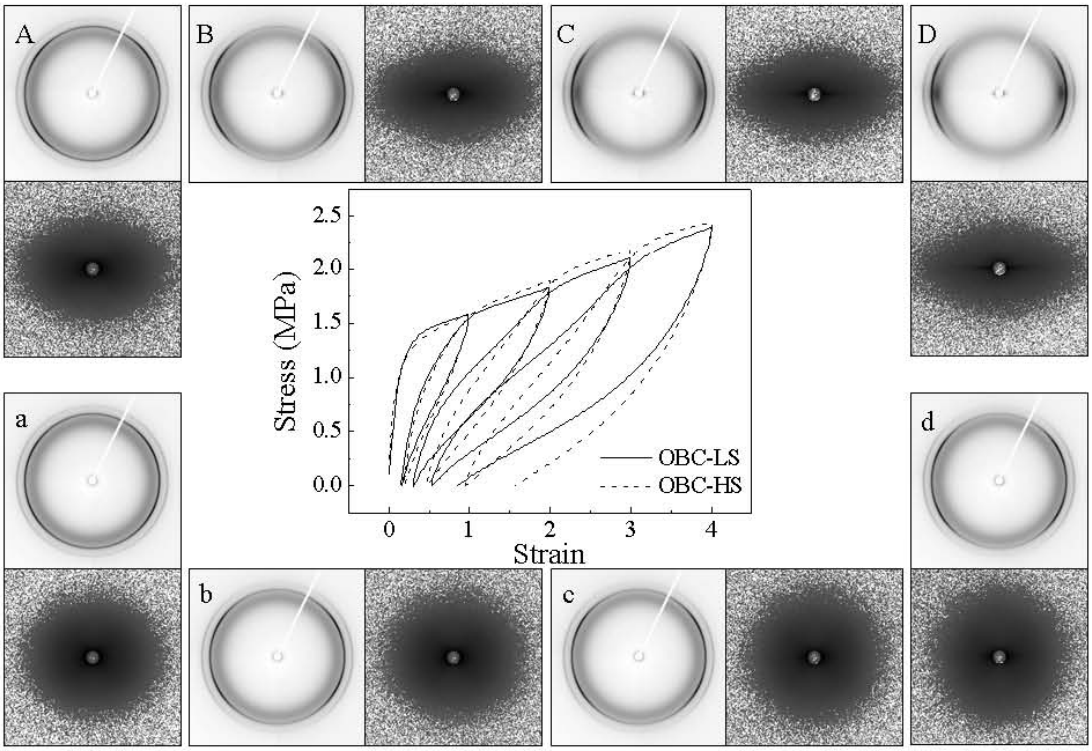

Figure 5.10. Change of fractions of orthorhombic phase during step-cycle test.

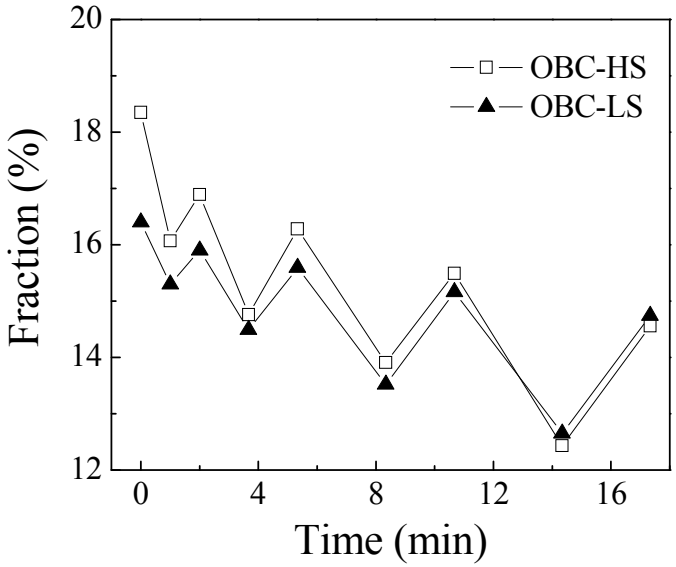

Figure 5.11. Development of orientation of amorphous (A) and crystal (B) in OBCs during the step-cycle test.

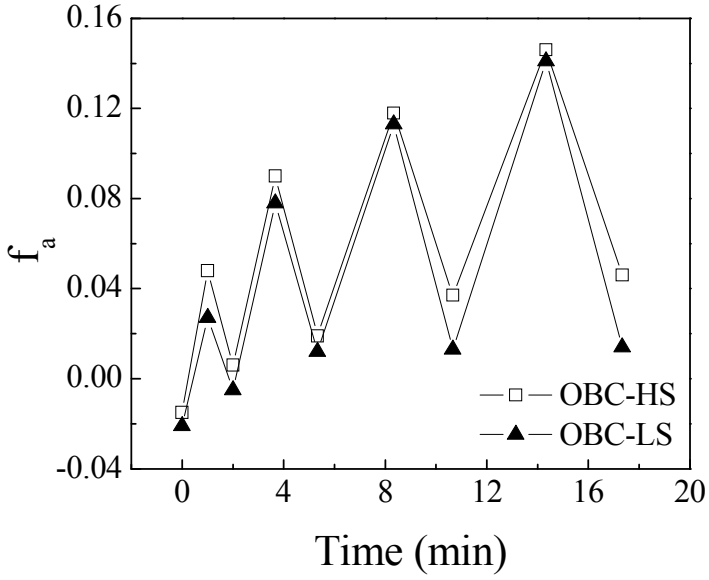

(A)

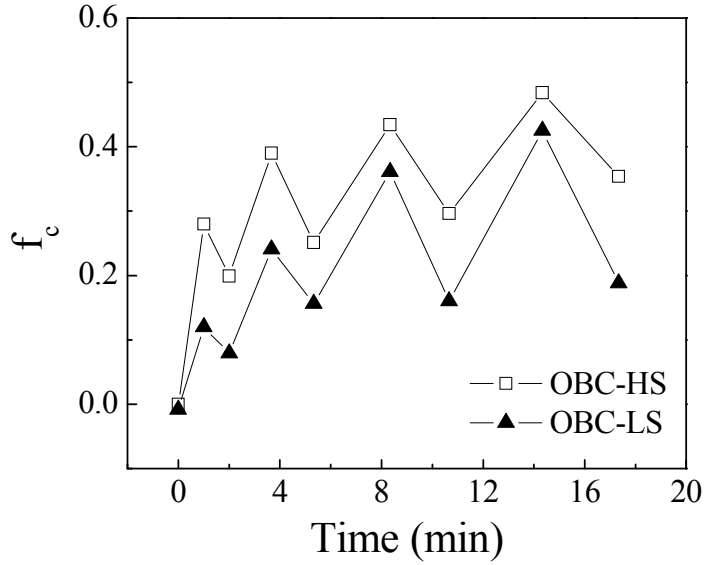

(B)

Chapter 6. Stress-Strain Behavior of Olefin Block Copolymers with Different Octene Comonomer Content in Soft Segments

6.1 Introduction

Mechanical properties, especially the tensile stress-strain behavior, of polyolefin materials are of great interests to people as they are the critical factors for determining the practical uses of these polymers in many applications, such as packaging films, containers, bags, appliances, etc. Majority polyolefins, especially polyethylene, polypropylene, and some ethylene copolymers, are semi-crystalline polymers consisting of crystal and amorphous phases. Thus understanding of crystalline structure development at the molecular and lamellar levels during deformation and the resulting influences on tensile property is essential for tailoring and improving the polyolefin products. Deformation of polyethylene, including both polyethylene homopolymers and copolymers, were studied extensively before in order to reveal the relationships among structure, morphology, and properties of ethylene-octene copolymers.[1-8] Depending on the density, chain branches, molecular weight and distributions, comonomer type and content, the polyolefins exhibit a wide spectrum of solid state properties.[9-12]

Olefin block copolymers (OBCs) produced by The Dow Chemical Company through chain shuttling technology were synthesized in a continuous process in the polymerization reactor from raw materials (ethylene and α-olefin) in the presence of catalysts and chain shuttling agents.[13] Low density soft blocks containing high comonomer content grow on the catalysts with poor ethylene incorporation ability, while

high density hard blocks containing low comonomer content grow on the catalysts with good ethylene incorporation ability. Chain shuttling agents are responsible for transferring the growing chains between two kinds of catalysts, so that the segmented blocky structure is obtained. By controlling the amount of feeding materials, chain shuttling agents, catalysts, and the selectivities of catalysts, various block copolymers with different molecular characteristics, such as the number and the length of the blocks, the comonomer content in the hard and soft segments, and the hard-to-soft segment ratio, can be produced. Thus to understand the influences of these structural variables on the properties of OBCs is necessary for designing the right product.

In our previous studies, it was found that hard segments in OBCs are long enough and can fold back and forth into the lamellar crystals in the solid state, similar to low density polyethylene. While the soft segments build up the major fraction of the amorphous phase due to the severe interruptions from the large amount of octene comonomers. The crystals are well formed orthorhombic polyethylene crystals, and the deformation of orthorhombic crystal phase can result in transformation to the monoclinic crystal phase, consistent with the early studies.[14-16] Orthorhombic crystal is one of the three major crystals found in polyethylene and it is the most stable one. The other two crystals are monoclinic and hexagonal ones, which are usually formed under elongation and in the defective crystals, respectively.[6-7,17-23] Even though the crystalline structure and possible formation mechanism were investigated,[24-26] the evolution of monoclinic phase and its stress or strain dependency during the deformation remained unclear.

The OBC samples studied in current work are similar in most of their molecular characteristics, except the octene comonomer content in the soft segments. The stress-strain behaviors, especially the phase development during the deformation was analyzed through in-situ 2D WAXD and SAXS data. The fractions of original orthorhombic

crystal phase and newly formed monoclinic crystal phase during deformation were calculated, as well as the Hermans' orientation function. The stress and strain dependence of theses variables was compared.

6.2 Experimental

6.2.1 Material

In this study, three different olefin block copolymers synthesized from ethylene and octane were provided by The Dow Chemical Company, and were named OBC-L, OBC-M, and OBC-H according to the content of octene comonomer in the soft segment. The molecular information of these OBCs including density, molecular weight, octene content in hard and soft segments, chain shuttling agent content used in production, and weight fraction of hard segment was shown in Table 6.1. All of the OBCs had the similar molecular weight and molecular weight distribution, and the same amount of chain shuttling agent was used during production, i.e. 0.6 per 1000 ethylene, so the segmental distribution was about the same. The octene comonomer content in the hard segment was fixed to 0.4 mol%, leading to a density of 0.932 g/cm^3 of the hard segment. The most distinct difference among these OBCs was the octene comonomer content in the soft segment. This number was 16.0, 13.4, and 11.2 mol% for OBC-H, OBC-M, and OBC-L, respectively. Thus, due to the decrease of comonomer content, the corresponding soft segment densities were increasing from 0.859, to 0.865, and 0.871 g/cm^3, and as a result of that, the overall densities were 0.879, 0.880, 0.888 g/cm^3 for three OBCs, respectively. The weight fraction of hard segment was 24% in OBC-H, and was slightly higher than that of OBC-M, and OBC-L. The isotropic films of the three OBC samples were obtained by melting-compression at 165 ^{o}C in a dumbbell shape mold, and then quenched to the

room temperature. The dumbbell shape sample was 35 mm long, 6 mm wide and 1 mm thick.

6.2.2 Instrumentation

In-situ WAXD and SAXS studies were carried out at the X27C beam line in the National Synchrotron Light Source (NSLS), Brookhaven National Laboratory (BNL). The wavelength of the synchrotron radiation was 1.371 Å. A three-pinhole collimation system was used to reduce the beam size to 0.6 mm in diameter. 2D WAXD and SAXS patterns were collected by a MAR CCD X-ray detector (MAR-USA), which had a resolution of 1024×1024 pixels (pixel size = 158.44 μm). The typical image acquisition time was 20 s for each data frame. The sample-to-detector distance was around 1900 mm for SAXS (calibrated by a silver behenate (AgBe) standard), and the sample-to-detector distance was around 110 mm for WAXD (calibrated by an aluminum oxide (Al_2O_3) standard). All X-ray images were corrected for background scattering, air scattering and beam fluctuations.

Uniaxial tensile deformation was performed with a modified Instron 4442 tensile apparatus, which could stretch the film symmetrically. The symmetric stretching guaranteed that the focused X-ray beam could illuminate the same sample position during deformation. The original length of the sample between the Instron clamps was 15 mm. A constant deformation rate, 4.5 mm/min (30 %/min), was applied to the specimen throughout the deformation study. All OBC samples were uniaxially deformed to a maximum strain of 7 without break, and the deformation experiment was carried out at room temperature. The stress and strain mentioned through the article were all engineering stress and engineering strain measured directly between clamps.

6.3 Results and Discussion

6.3.1 Stress-Strain Curves

Engineering stress-strain curves of OBC-L, OBC-M, and OBC-H during the uniaxial deformation at room temperature were shown in Figure 6.1. All samples had a uniform deformation with a non-distinct strain softening behavior which was similar to the conventional rubber, suggesting the elastomeric nature of three OBCs. The tensile strength decreased with increased octene comonomer content in the soft segment when subjected to the same elongation ratio, and the strain hardening was found to be more pronounced in OBC with low comonomer content in the soft segment, which also has a higher young's modulus and yield strength. Since the crystallinity index of all OBCs was similar, thus the major contribution to the strength should be from the soft segment with different octene content.

6.3.2 2D WAXD and SAXS Patterns

Selected 2D WAXD and SAXS patterns of OBCs during the uniaxial deformation at room temperature were shown in Figure 6.2 and Figure 6.3, respectively. Before deformation, the initial WAXD patterns of OBCs (not shown here) did not show any preferred orientation. Two diffraction peaks that can be assigned to (110) and (200) reflections from orthorhombic polyethylene crystal and the broad diffused scattering from amorphous phase were all isotropic along azimuthal direction, which meant that polymer chains and crystals in the films were randomly distributed. At the early stage of deformation, the orthorhombic crystals exhibit b-axis orientation, indicated by the four-point (110) reflection and equatorial (200) reflection. With the further increase of strain, c-axis orientation of the crystals was observed. Both (110) and (200) peaks were on the

equator and become narrow along the azimuthal direction with strain, indicating a higher degree of orientation. An additional reflection peak appeared gradually between (110) and amorphous peaks during deformation, and it became clear when OBCs films were uniaxially deformed to strain around 3. As we discussed in previous paper, this was due to the formation of monoclinic crystals, and the reflection was from (010) crystal plane.

Initial 2D SAXS patterns (not shown in Figure 6.3) of OBCs before deformation were also isotropic diffused scattering showing monotonically decreased intensity with the increase of scattering vector, but with a tiny shoulder at scattering vector around 0.04 nm^{-1}. This was due to the existence of folded-chain lamellar crystals and non-correlated nano scale domains mainly composed of soft segments formed due to the crystallization-induced phase separation, both of them did not have preferred orientation. Upon uniaxial deformation, the lamellar stacks were reoriented to the direction perpendicular to the drawing direction, and its scattering in 2D SAXS patterns will move to meridional direction, while the spherical nano domains were stretched along the drawing direction, and corresponding scattering will move to equatorial direction. So we can expect that when the orientation was high enough, two scatterings should be separated. This was true when strain increased, as in 2D SAXS patterns the scatterings from lamellar crystal and soft domains separated from each other and located in meridional direction as point scattering and equatorial direction as streak scattering, respectively.

6.3.3 Effects of Strain on the Deformation

As a conventional way to look into the deformation process was to see the changes as a function of strain. Thus the selected 2D WAXD and SAXS patterns of different OBCs at the same strain were shown in Figure 6.2 and 6.3. Comparison can be made among three samples by even visual examination. The increase of the degree of orientation was

the fastest in OBC-L. At each strain, the highest orientation was obtained in OBC-L, since its (110) and (200) arches were the narrowest along azimuthal direction. Besides, the formation of monoclinic phase also occurred first in OBC-L. At strain of 3, the monoclinic reflection was clearly seen at 2 theta position between (110) and amorphous peaks in OBC-L, but in OBC-H the reflection was much weaker. At the highest strain of 7, point-like reflection from monoclinic was so intense and the (110) and (200) reflections were hidden in OBC-L, which also brought difficulty to do the peak fitting to calculate the phase fraction in the method we will use later. However, in OBC-H we can still distinguish reflections from different crystal phases easily. Comparing the 2D SAXS patterns of different OBCs at the same strain in Figure 6.3, it was indicated that the separation of scatterings from lamellar crystals and phase separated domains were most efficient in OBC-L. For example, at strain of 5, scatterings from OBC-L were clearly divided into two contributions. However, in OBC-H, the two scatterings were overlapped to some extent without a distinct boundary. As for OBC-M, it always exhibited a deformation behavior in between OBC-L and OBC-H. From strain dependent WAXD and SAXS patterns in Figure 6.2 and 6.3, we saw a trend which relates the content of octene comonomer in the soft segment in the OBCs to the deformation behavior in terms of formation of new crystalline phase or the development of orientation. In detail, the lower the comonomer content in soft segment, the faster the formation of monoclinic phase and the increase of degree of orientation of crystals.

6.3.4 Effects of Stress on the Deformation

If we took one more glance of the patterns not in vertical direction but in diagonal direction in Figure 6.2 and 6.3, we saw that for patterns of OBC-L at strain of 3, OBC-M at strain of 5, and OBC-H at strain of 7 were much more similar to each other. Looking back at the stress-strain curves in Figure 6.1, it was found that these patterns were

obtained under conditions with closed stress values. Thus we again showed the 2D WAXD and SAXS patterns of OBCs under the same stress in Figure 6.4 and 6.5. This time, we did not see big differences between three OBC samples, especially at high stress of 4, 5, and 6 MPa. 2D WAXD patterns showed a comparable degree of orientation of the crystals in OBC-L, OBC-M, and OBC-H, and also the formation of monoclinic crystal phase. Meanwhile, the deformation of soft segment domains from sphere to needle shape and the orientation of large scale lamellar structure were also determined by stress rather than strain. Because the separation of their corresponding scatterings in the 2D SAXS indicated that lamellar structure and soft segment domains had a similar degree of orientation at the same stress. This implied that the orientation and the formation of monoclinic crystals were stress-dependent, the same stress localized on the crystal phase led to the same orientation of crystals and formation of monoclinic crystals. However, relatively large deviation was found at low stress. 2D WAXD and SAXS patterns of OBC-H were more anisotropic than others. This was understandable by considering the differences in the yield or strain softening behavior. OBC-L yielded at a high stress about 2.6 MPa, while OBC-H yielded at low stress about 1.4 MPa. Before yielding, the polymers were within the elastic region. The elongation was due to the chances in extension of amorphous chains via change of chain conformation and the sliding of chain segments. The crystals remained intact. Once the polymer films passed though the yielding, the crystals started to get deformed under the stress and then the monoclinic phase formed and orientation of the crystals increased. Thus the deviation found at low stress was because the samples need to overcome the yielding and thus a retardation effect.

6.3.5 X-ray Data Analysis

In order to obtain a quantitative knowledge on the development of crystallinity index, fractions of orthorhombic and monoclinic phases, and degree of orientation during the uniaxial deformation process, we carried out following methods, illustrated in Figure 6.6, to analyze 2D WAXD patterns. First, the collected 2D WAXD patterns were corrected by the Fraser method to compensate the effect of flat-plate detection and subtracted by the background and air scattering. Linear WAXD profile was then obtained by integrating the 2D pattern. Since the stretched samples should have a cylindrical rotational symmetry during the uniaxial deformation, a 2D pattern can contain the complete information to describe the intensity distribution in reciprocal space, and then integrating over such 2D sections through 3D reciprocal space will produce the fractions of each phase. Thus we can obtain the fraction of each phase if we can separate corresponding reflection peak and calculate the area underneath of it. In reality, (110) and (200) peaks from orthorhombic crystal phase were usually sharp and can be separated out using 1D peak fitting method. However, the reflection peaks from amorphous phase and monoclinic phase were superposed together and exhibited a quite broad peak. So we can only obtain the fraction of orthorhombic phase and total fraction of monoclinic and amorphous phase. The next step was to carry out "halo method" to deconvolute the 2D WAXD pattern into two parts, isotropic and anisotropic contributions. This isotropic contribution was then subtracted from the total scattering, giving the anisotropic contribution. The isotropic part was mainly due to the amorphous phase most of which was hardly to get oriented, the anisotropic part was mainly due to the crystal phase which had a high orientation upon deformation. By taking the equatorial scan of the anisotropic part, linear profiles of reflection from crystal phases along the equatorial direction can be obtained. The height of the (010) monoclinic peak and the height of the (110) orthorhombic peak were used to roughly represent the fraction of these two phases. Finally, according to the ratio of monoclinic phase to orthorhombic phase and the fraction of orthorhombic phase, we can

calculate the fraction of both phases, the sum of which was crystallinity index, termed as crystallinity later on.

6.3.6 Structure Evolution during the Uniaxial Deformation

The development of the fractions of orthorhombic and monoclinic phases and the crystallinity with increasing strain were shown in Figure 6.7. The fraction of monoclinic phase increased almost linearly with strain, and the slope represented the rate of formation, which was the fastest in OBC-L and the slowest in OBC-H. When stretched to the final strain of 7, OBC-L contained about 15% monoclinic crystals, and for OBC-H this fraction was about 10%. The decline of orthorhombic phase during deformation was illustrated in Figure 6.7(B). The fraction of orthorhombic phase before deformation, which was also equal to the initial crystallinity, should be mainly account for the crystallization of hard segments which was 19% and 18% for OBC-L and OBC-M, while it was a little bit higher in OBC-H, 24%. The soft segment might also crystallize slightly in terms of the density, and the crystalliablity decreased in the order of OBC-L, OBC-M, and OBC-H because of the reduced octane content. These two contributions led to a final crystallinity of about 18%, 16%, and 17% in OBC-L, OBC-M, and OBC-H, respectively. Upon deformation, there was a sharp decrease of orthorhombic phase in OBC-L, and the remaining fraction was about 12% for all samples after being stretched to a strain of 7. The change of crystallinity was shown in Figure 6.7 (C). During uniaxial deformation, the crystallinity of OBC-M exceeded the OBC-H, while that of OBC-L was always the highest. The crystallinity increased with the increasing strain, implying that in addition to the transformation of orthorhombic phase into monoclinic phase, the strain-induced crystallization also occurred.

In order to reveal the relationship between engineering stress and structure evolution of OBC films, crystal fractions and crystallinity were plotted versus engineering stress in Figure 6.8 rather than engineering strain. All of the data were chosen after strain softening of the films, since at small stress the OBC samples were in the linear elastic region. The increase of monoclinic phase fraction as a function of stress was shown in Figure 6.8 (A). An exponential growth of monoclinic crystal was found for all three OBC samples. By shifting the growth curves along the x-axis direction, they can superpose to some extent with each other. The reason of this stress shifting was not clear to us at this time, but it might relate to the different effective stress localized on the crystals. The decline of orthorhombic phase in Figure 6.8 (B) behaved in the same tendency, except that relatively low initial crystallinity in OBC-M resulted in small deviation of the curve at the beginning. The development of crystallinity with stress was shown in Figure 6.8 (C). Comparing with Figure 6.7 (C), the crystallinity was confined within a much smaller area, and the values were much closed for samples under the same stress. From these figures, we can conclude that the crystal transformation in OBCs films were stress dependent rather than strain dependent, which meant the formation of the monoclinic crystal was determined by the stress employed on the original orthorhombic crystals.

The degree of orientation of orthorhombic crystals and amorphous chains were also obtained and plotted versus both strain and stress in Figure 6.9 and 6.10 using Hermans' orientation function:

$$f = \frac{3\left\langle \cos^2 \phi \right\rangle - 1}{2}$$

where ϕ is the angle between the chain axis and the reference axis (stretching direction). $\left\langle \cos^2 \phi \right\rangle$ is defined as:

$$\left\langle \cos^2 \phi \right\rangle = \frac{\int_0^{\pi/2} I(\phi) \cos^2 \phi \sin \phi d\phi}{\int_0^{\pi/2} I(\phi) \sin \phi d\phi}$$

where $I(\phi)$ is the scattered intensity along the angle ϕ. Since there is no plane of symmetry perpendicular to the chain axis, the c axis orientation can not be measured directly due to the absence of (00L) plane, but we can still obtain that indirectly from the (110) and (200) reflections through

$$\left\langle \cos^2 \phi \right\rangle = 1 - 1.435 \left\langle \cos^2 \phi_{110} \right\rangle - 0.565 \left\langle \cos^2 \phi_{200} \right\rangle .$$

Regarding amorphous phase, the orientation we calculated was actually that of the normal vector of the amorphous chains, so the f value was multiplied by a factor of -2 to convert that into the value representing the degree of orientation along the stretching direction. Moreover, in calculating the orientation of amorphous phase, the azimuthal scan was chosen along a lower s value at 2.04 nm^{-1} rather than the amorphous peak at 2.13 nm^{-1} in order to reducing the contribution from (010) reflection. The value of orientation factor is between -0.5 to 1. When f = 1, it means all polymer chains align to the stretching direction perfectly, while f = -0.5 means chains are all perpendicular to the stretching direction, and f = 0 indicates random orientation of the chains. As shown in Figure 6.9 (A) and 6.10 (A), the increase of crystal and amorphous orientation was fast at the early stage of uniaxial deformation and slowed down at high strain. The highest degree of orientation was obtained in OBC-L among samples at the same strain. However, if Hermans' orientation factors were plotted as a function of stress (see Figure 6.9(B) and Figure 6.10(B)), the alignment of the orthorhombic crystals and amorphous chains was almost the same under the same stress, and reached a plateau value near the end of deformation. This again supported the assumption that stress localized in the crystal phase was responsible for the changes of crystals. The same stress will lead to the same degree of orientation of crystals. Besides, orientation of the amorphous chains should be also determined by the stress exerted on the amorphous phase, which implied

that structure evolution in amorphous phase was also stress-dependent. This was because that semi-crystalline polymer system was an interpenetrating network of amorphous phase and crystal phase via entanglements between amorphous chain segments and tie chains connecting adjacent crystals. A single polymer chain can go through both amorphous and crystalline regions and be involved in both entanglement and tie chain as well. When applying uniaxial deformation on the polymer films, amorphous and crystal phases were deformed simultaneously after yielding, and thus it was reasonable to image that their structure evolutions will be both depend on stress.

The full width at half maximum (FWHM) of (110) reflection during deformation was also calculated and shown in Figure 6.11. FWHM was usually related to the crystal size via Scherrer equation. However, during the deformation process, contributions from the micro strain on crystals to FWHM was also very important and can not be neglected, if we assume the distortion of the second kind is the same for all three samples during deformation. The same initial FWHM indicated the same crystal size from melt crystallized samples. Once the OBC films were deformed, the FWHM started to increase. From Figure 6.11, we saw a similar trend of the strain and stress dependence of the FWHM. That was different increasing rates of FWHM when expressed as a function of strain but almost the same behavior when expressed as a function of stress. Even though we can not separate the contributions from crystal size and micro strain, but it did not prevent us to conclude that the FWHM, a measurement of the nature of crystals, also depended on the stress. As long as the stress localized on the crystals was the same for every OBC films, the change of the crystals under the stress, that was the change in crystal size or micro strain, were the same.

6.4 Conclusions

Studies on the uniaxial deformation of three olefin block copolymers with different octene comonomer content in the soft segment revealed some interesting findings of the deformation behavior of semi-crystalline OBCs. The mechanical properties were well related to the octene content. Low comonomer content in soft segment led to high yield strength, tensile strength, and more pronounced strain hardening. While the structure evolution which was a concern mainly on crystals and the orientation of both crystal and amorphous phases during deformation were stress-dependent, regardless of the octene comonomer content. The formation of new monoclinic crystals and decline of original orthorhombic crystals depended on the stress localized on the crystal phase. This stress determined the change of crystals and thus FWHM. The degree of orientation of crystal and amorphous phases was also a function of applied stress, since the polymer system was an interpenetrating network of both phases via entanglements and tie chains.

List of References

1 Bensason, S.; Stepanov, E. V.; Chum, S.; Hiltner, A.; Baer, E. *Macromolecules*, **1997**, 30, 2436-2444.

2 Androsch, R.; Stribeck, N.; Lupke, T.; Funari, S. S. *J. Polym. Sci.: Part B: Polym. Phys.*, **2002**, 40, 1919-1930.

3 Liu, L.; Hsiao, B. S.; Fu, B. X.; Ran, S.; Toki, S.; Chu, B.; Tsou, A. H.; Agarwal, P. K. *Macromolecules*, **2003**, 36, 1920-1929.

4 Men, Y.; Rieger, J.; Strobl, G. *Phys. Rev. Lett.*, **2003**, 91, 095502-1-4.

5 Schrauwen, B. A. G.; Janssen, R. P. M.; Govaert, L. E.; Meijer, H. E. H. *Macromolecules*, **2004**, 37, 6069-6078.

6 Shan, H.; White, J. L. *J. Appl. Polym. Sci.*, **2004**, 93, 9-22.

7 Shan, H.; White, J. L. *Plastics, Rubber and Composites*, **2006**, 35, 155-164.

8 Hong, K.; Strobl, G. *Macromolecules*, **2006**, 39, 268-273.

9 Kennedy, M. A.; Peacock, A. J.; Failla, M. D.; Lucas, J. C.; Mandelkern, L. *Macromolecules*, **1995**, 28, 1407-1421.

10 Fatou, J. G.; Macia, I. G.; Macro, C.; Gomez, M. A.; Arribas, J. M.; Fontecha, A.; Aroca, M.; Martinez, M. C. *J Mater. Sci.*, **1996**, 31, 3095-3107.

11 Chum, P. S.; Kruper, W. J.; Guest, M. *J. Adv. Mater.*, **2000**, 12, 1759-1767.

12 Chum, P. S.; Swogger, K. W. *Prog. Polym. Sci.*, **2008**, 33, 797-819.

13 Arriola, D. J.; Carnahan, E. M.; Hustad, P. D.; Kuhlman, R. L.; Wenzel, T. T. *Science*, **2006**, 312, 714-719.

14 Kiho, H.; Peterlin, A.; Geil, P. H. *J. Appl. Phys.*, **1964**, 35, 1599-1605.

15 Kiho, H.; Peterlin, A.; Geil, P. H. *Polym. Lett.*, **1965**, 3, 157-160.

16 Seto, T.; Hara, T.; Tanaka, K. Jap. *J. Appl. Phys.*, **1968**, 7, 31-42.

17 Hendra, P. J.; Taylor, M. A.; Willis, H. A. *Polymer*, **1985**, 26, 1501-1506.

18 Tashiro, K.; Sasaki, S.; Kobayashi, M. *Macromolecules*, **1996**, 29, 7460-7469.

19 Androsch, R.; Blackwell, J.; Chvalun, S. N.; Wunderlich, B. *Macromolecules*, **1999**, 32, 3735-3740.

20 Kuwabara, K.; Horii, F. *Macromolecules*, **1999**, 32, 5600-5605.

21 Hu, W.; Srinivas, S.; Sirota, E. B. *Macromolecules*, **2002**, 35, 5013-5024.

22 Hu, W.; Sirota, E. B. *Macromolecules*, **2003**, 36, 5144-5149.

23 Liu, L.; Hsiao, B. S.; Ran, S.; Fu, B. X.; Toki, S.; Zuo, F.; Tsou, A. H.; Chu, B. *Polymer*, **2006**, 47, 2884-2893.

24 Takahashi, Y.; Ishida, T. *J. Polym. Sci.: Part B: Polym. Phys.*, **1988**, 26, 2267-2277.

25 Wittmann, J. C.; Lotz, B. *Polymer*, **1989**, 30, 27-34.

26 Russell, K. E.; Hunter, B. K.; Heyding, R. D. *Polymer*, **1997**, 38, 1409-1414.

List of Tables

Table 6.1. Density, component, and molecular weight information of three OBCs.

	Overall density g/cc	M_w kg/mol	C8 in hard mol%	C8 in Soft mol%	Soft segment density	[Zn]/[C2]*1000	Wt % Hard
OBC-L	0.888	129	0.4	11.2	0.871	0.6	19
OBC-M	0.880	133	0.4	13.4	0.865	0.6	18
OBC-H	0.879	145	0.4	16.0	0.859	0.6	24

List of Figures

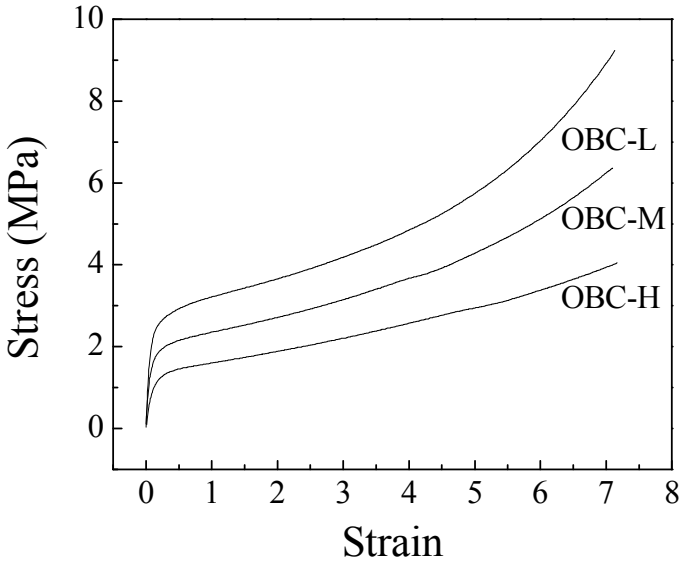

Figure 6.2. Selected 2D WAXD patterns of OBCs at the same strain during the uniaxial deformation.

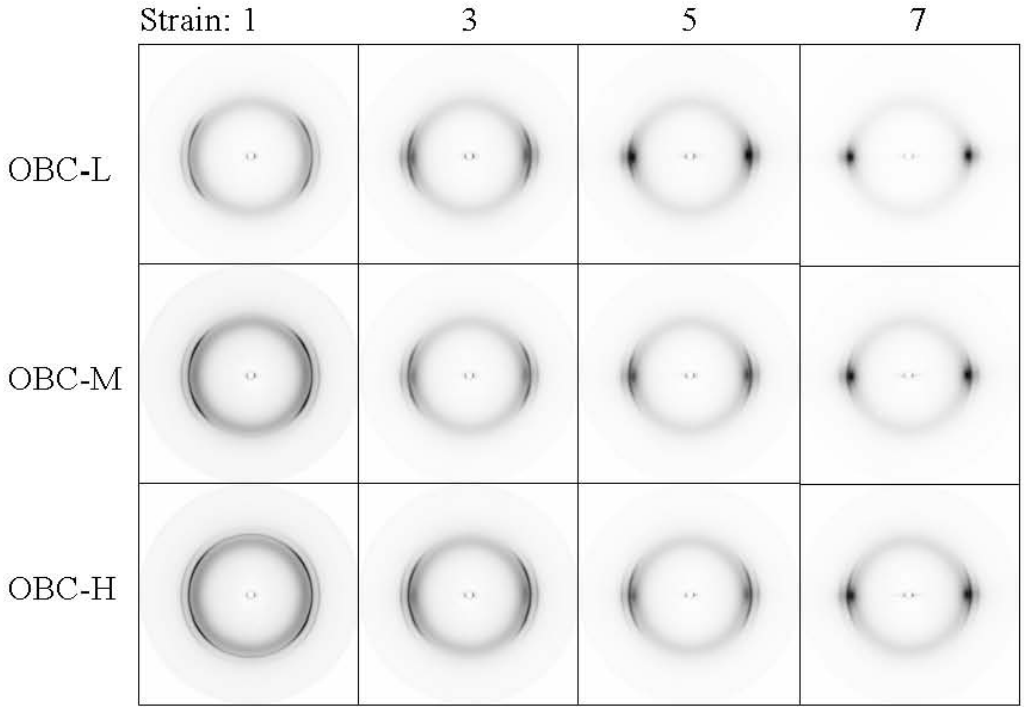

Figure 6.3. Selected 2D SAXS patterns of OBCs at the same strain during the uniaxial deformation.

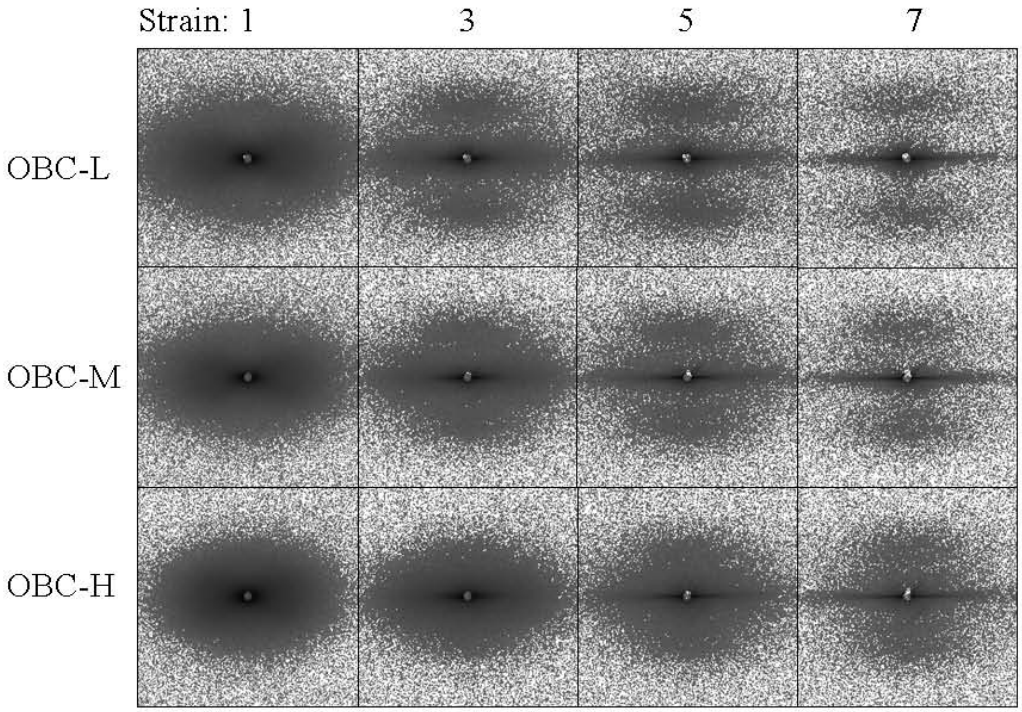

Figure 6.4. Selected 2D WAXD patterns of OBCs at the same stress during the uniaxial deformation.

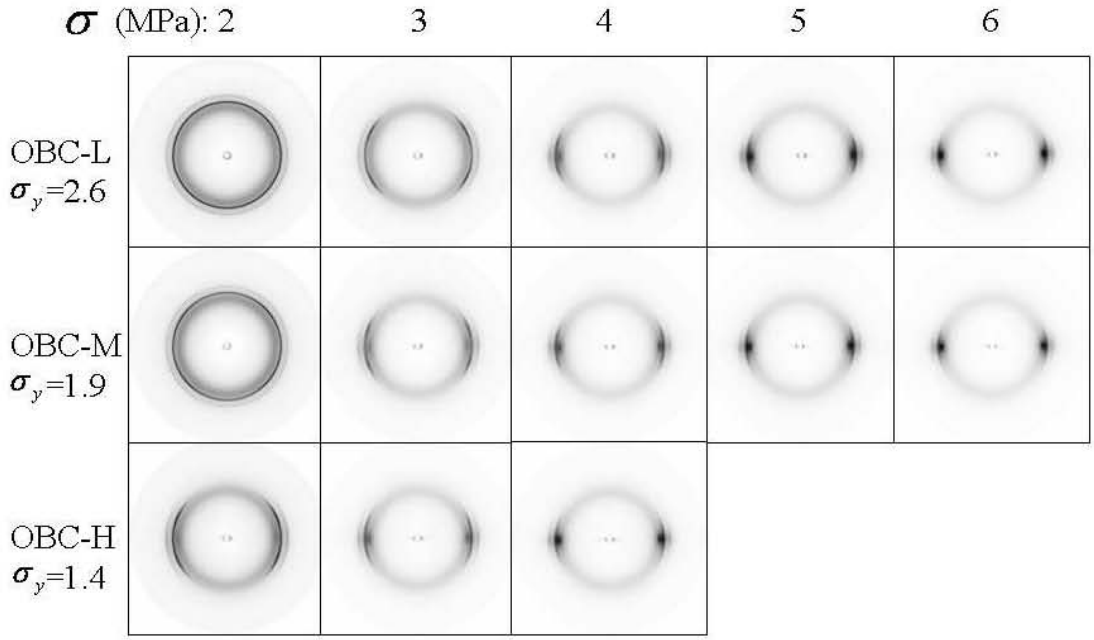

Figure 6.5. Selected 2D SAXS patterns of OBCs at the same stress during the uniaxial deformation.

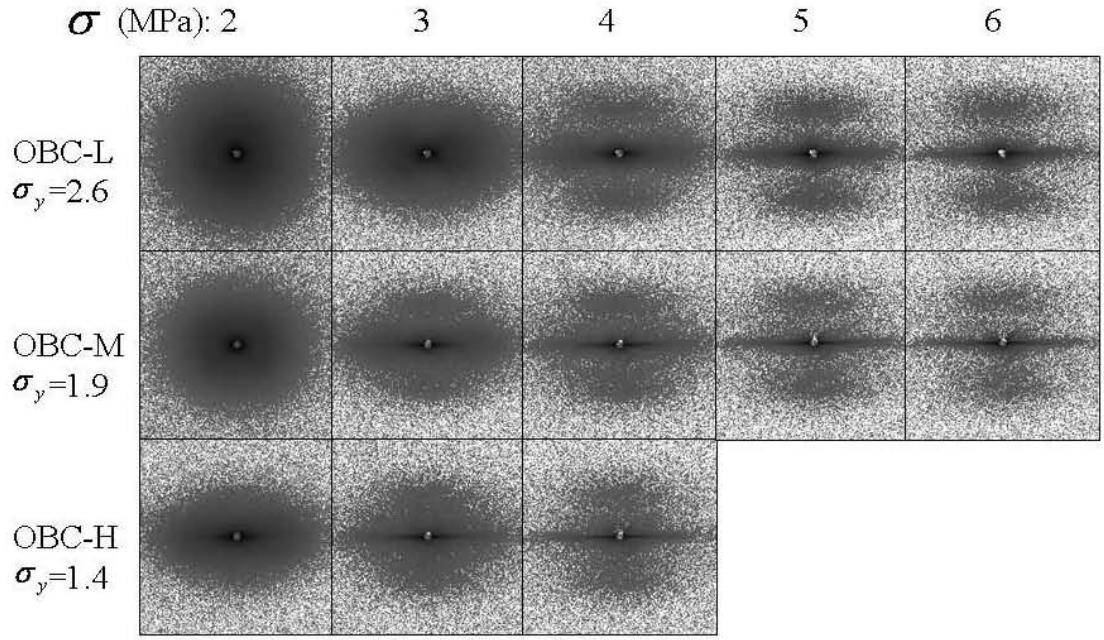

Figure 6.6. WAXD data analysis on deconvolution of amorphous, orthorhombic, and monoclinic crystal phases.

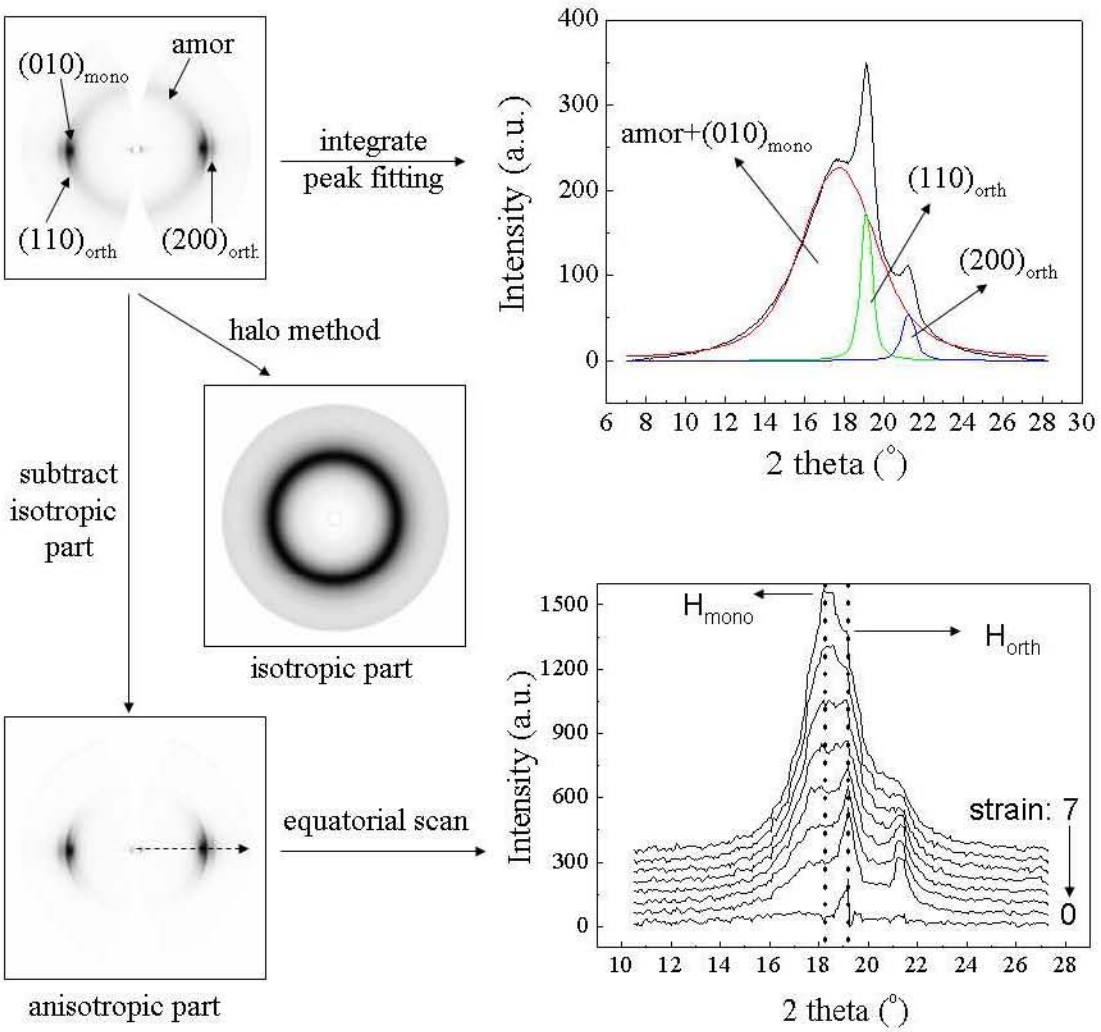

Figure 6.7. Changes of fractions of monoclinic (A) and orthorhombic (B) phases and crystallinity (C) in OBCs as a function of strain during deformation.

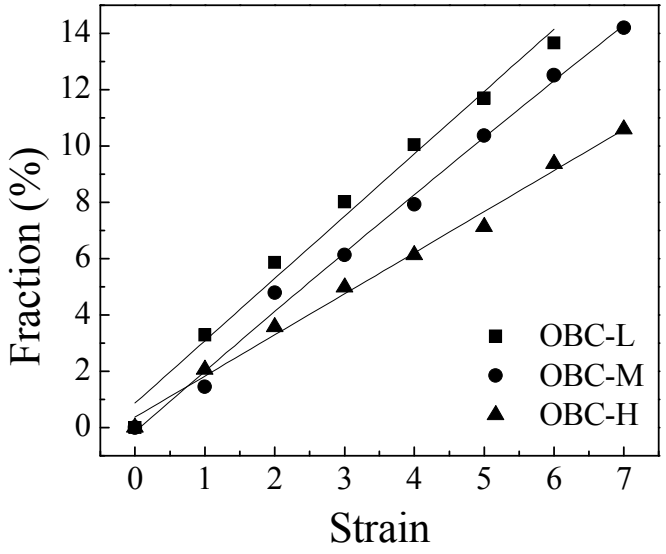

(A)

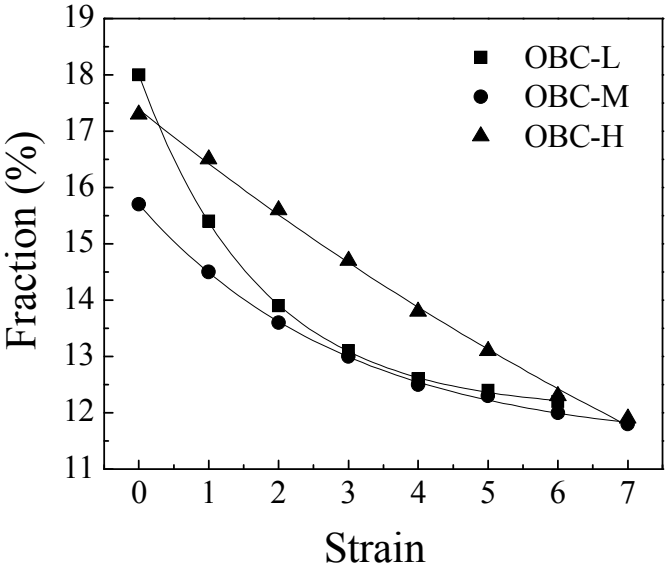

(B)

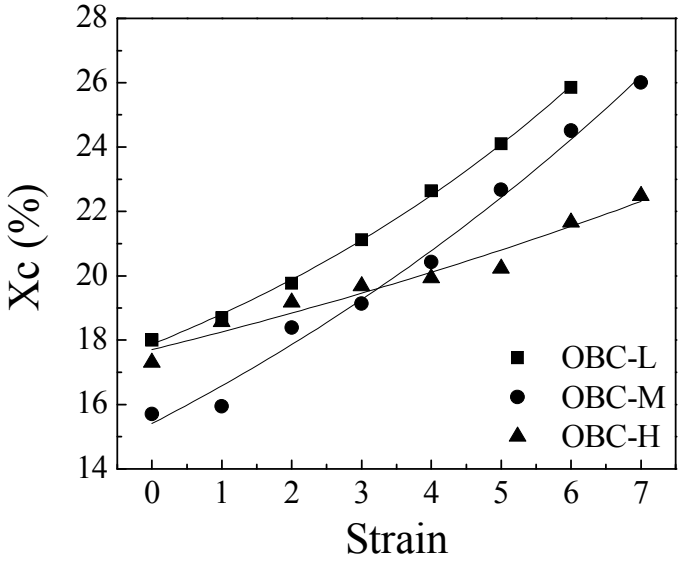

(C)

Figure 6.8. Changes of fractions of monoclinic (A) and orthorhombic (B) phases and crystallinity (C) in OBCs as a function of stress during deformation.

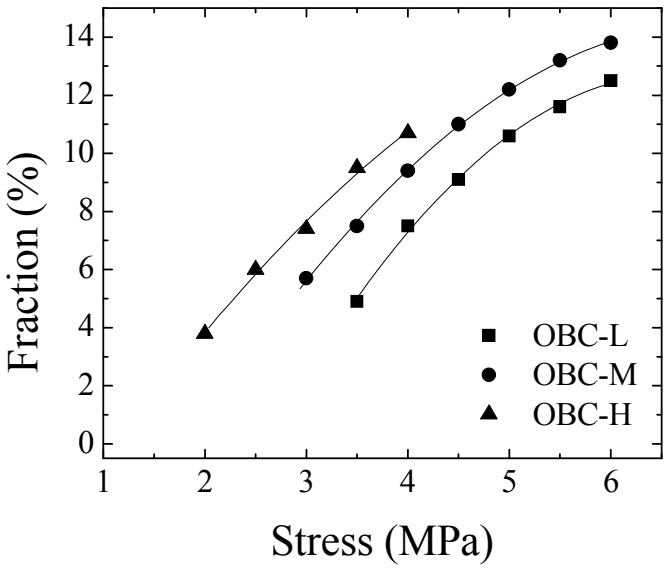

(A)

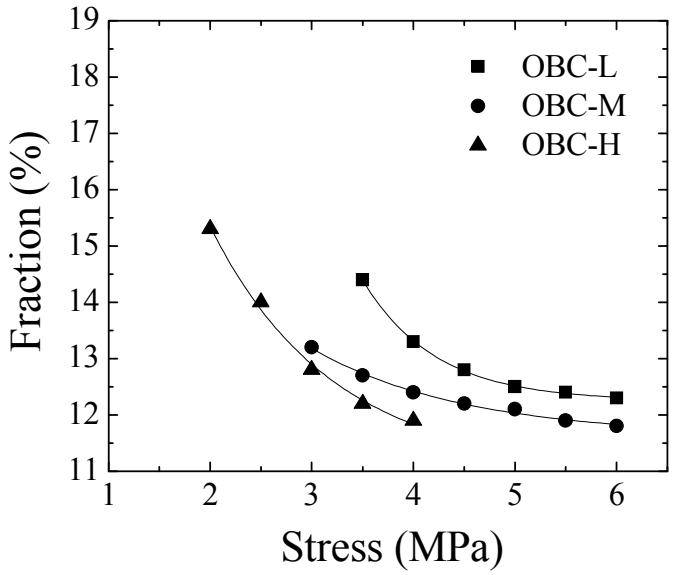

(B)

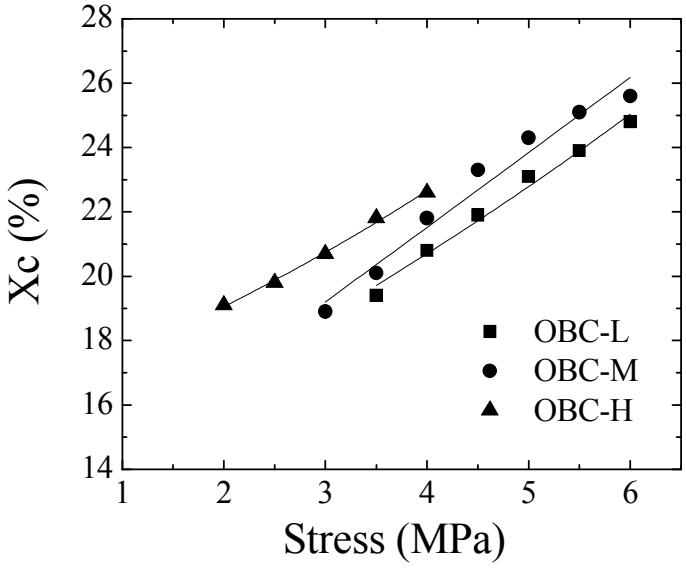

(C)

Figure 6.9. Hermans' orientation function of orthorhombic crystal phase as a function of strain (A) and stress (B).

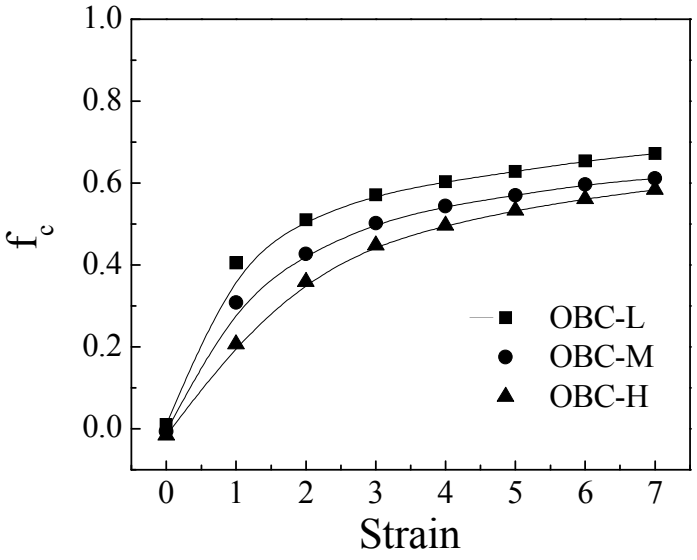

(A)

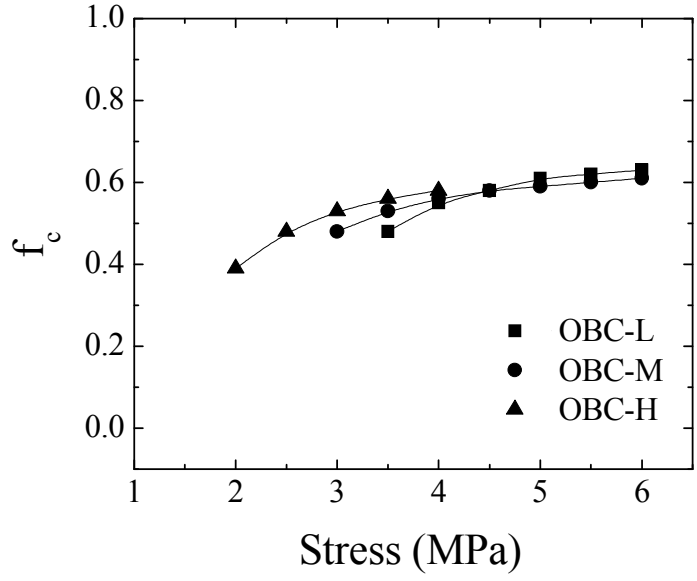

(B)

Figure 6.10. Hermans' orientation function of amorphous phase as a function of strain (A) and stress (B).

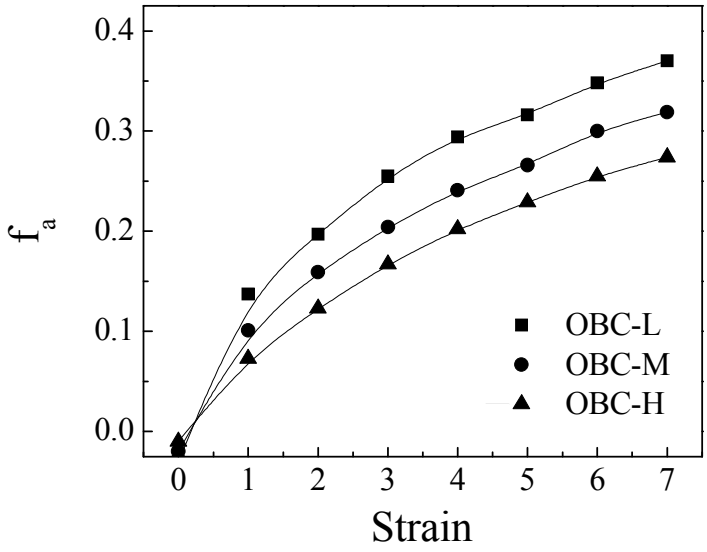

(A)

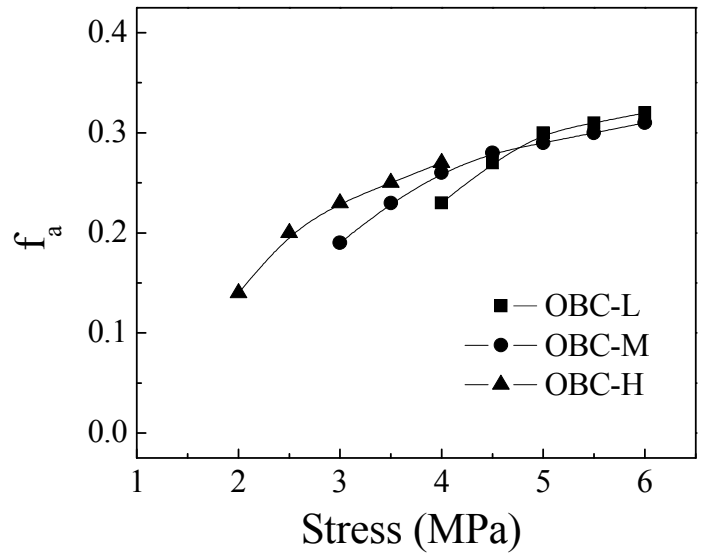

(B)

Figure 6.11. FWHM of (110) orthorhombic crystal reflection as a function of strain (A) and stress (B).

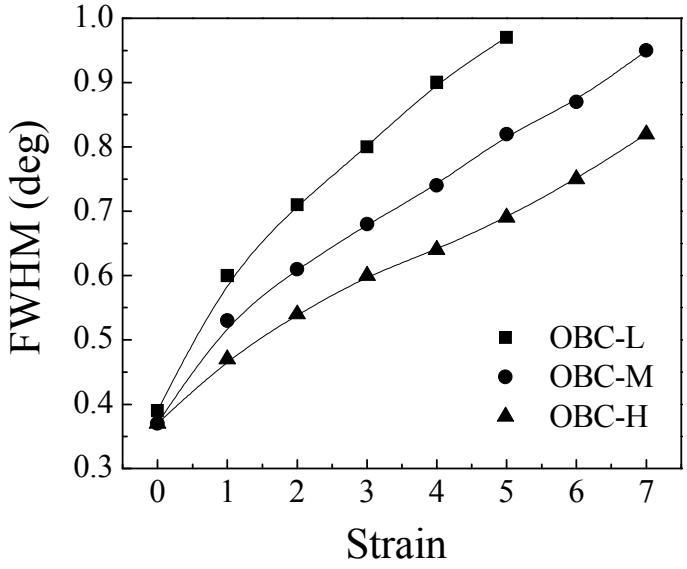

(A)

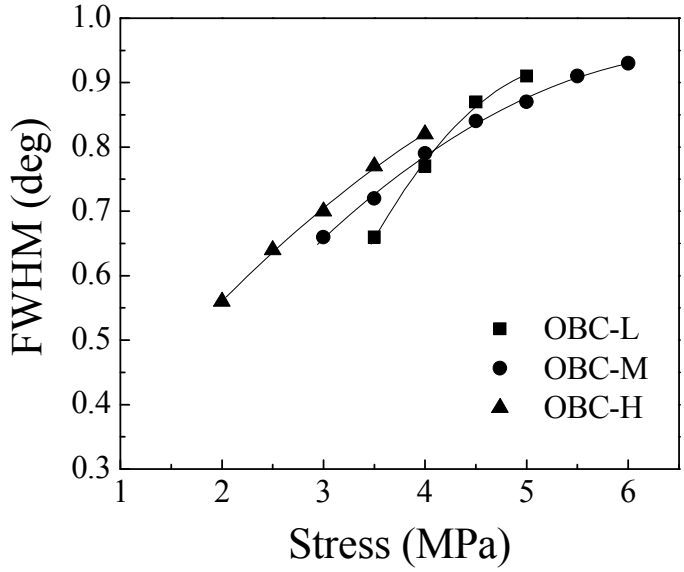

(B)

Chapter 7. Uniaxial Deformation of Electron-beam and Silane Crosslinked Olefin Block and Random Copolymers

7.1 Introduction

Crosslinking techniques are important methods in the industry for modifying chemical, physical, and mechanical properties, for examples solvent and chemical resistance, abrasion resistance, tensile and impact strength, of polymer products by connecting the adjacent polymer chain segments. The most valuable examples include vulcanized rubbers which can be utilized as tires and thermosetting materials which are crosslinked in small length scale and used as sealants and adhesives. Conventional crosslinking can use either irradiation means or chemical method.[1] The former one involves the high energy beams, such as electron beam, and the latter one uses chemical agents, such as silanes.

Electron-beam crosslinking had some advantages over silane crosslinking. There is no need of additives and do not generate wastes or by-products, and it can still achieve better performance and resistance, while silane crosslinking exhibits the great process flexibility due to less rigid siloxane bridges. There are some major differences in the process of these two methods.[1] Electron beam crosslinking can carry out in solid state polymers in air or under particular atmospheres simply by exposing polymers to the electron beam. Silane crosslinking consists of two steps. First the incorporation of silane into polymer will take place in polymer melts if monomers and vinylsilane is copolymerized in the polymerization reactor, or it can be taken in the solid state by

grafting vinylsilane onto the polymer backbone. Then it will be crosslinked in the presence of water. However, even though it can be done in the solid state for crosslinking, but the temperature is usually increased in order to accelerate the process.[2] So if the crosslinking takes place in the melt, the crosslinking junctions between polymer chains will be homogenously distributed, and will affect crystallization upon cooling. The crystallization thermodynamics[3-8] and kinetics[9-11] were studied by many researchers. In the opposite, the influences of structure on the crosslinked polymers were also investigated.[12-14] But if polymers are crosslinked in solid state, the polymer chains in crystals are closely packed in lattice and their mobility is highly restricted, crosslinking can only happen among the amorphous chains in the amorphous region.

Even though polyolefins, such as polyethylene[15-16] and ethylene octene copolymers,[17-21] are versatile and become the most widely used polymers, they still need improvement to expand their applications. Due to the low melting temperatures of polyolefins, their usages are limited to some extent, thus using crosslinking techniques to improve the temperature performance of polyolefins is desirable. Besides, polyolefins can also be crosslinked to obtain better properties for some applications such as insulating wire and cables, tubes and pipes, and foams.

There are many studies done on revealing the effects of crosslinking, chemical or irradiation means, on the structure,[22] thermal,[23-24] and mechanical[25-32] properties of polyolefins. However, most of these researches did not clarify the structure development during the mechanical testing. We carried out in-situ synchrotron X-ray experiment to investigate the structure development during the uniaxial deformation of non-crosslinked and both silane and electron-beam crosslinked polyolefins, including ethylene octene random and block copolymers, thus to understanding the relationships among crosslinking, structure development, and properties of different polyolefins.

7.2 Materials and Experiment

7.2.1 Materials

Crosslinked and non-crosslinked samples in the form of film were provided by The Dow Chemical Company with crosslinking information listed in Table 7.1. OBC (trademark: Infuse^{TM}) was ethylene octene block copolymer (density = 0.880 g/cm^3, melting temperature = 124 ^oC). EG8100 and KC8852 (trademark: Affinity^{TM}) were ethylene octene random copolymers with small differences in density (0.875 g/cm^3 for KC8852, 0.870 g/cm^3 for EG8100) and melt index (3.0 g/10 min for KC8852, 1.0 g/10 min for EG8100). OBC-0.6S, EG8100-0.6S, and EG8100-1S were obtained via silane-grafting crosslinking and were cured in presence of water at high temperature (110 ^oC for OBC-0.6S and 50 ^oC for EG8100-0.6S and EG8100-1S) to initiate crosslinking. Crosslinking agent was vinyl trimethoxysilane (VTMS), and its concentration was 0.6 wt% or 1 wt% as indicated in the nomenclature. The corresponding non-crosslinked counterparts were OBC-0S and EG8100-0S. The gel contents of crosslinked ones were also listed in the Table. Electron-beam crosslinking was applied to OBC-0E and KC8852-0E films, and the irradiation dose was 10 kGy, thus the crosslinked films were named OBC-10E and KC8852-10E, respectively.

7.2.2 Instrumentation

Uniaxial deformation was performed with a modified Instron 4442 tensile apparatus, which can stretch the films symmetrically. The symmetric stretching guaranteed that the focused X-ray beam could illuminate the same sample position during deformation. The stress and strain mentioned through the article were engineering stress and engineering

strain measured directly between clamps. The original length of the films between the Instron clamps was 30 mm. A constant deformation rate, 9 mm/min (30 %/min), was applied to the films throughout the deformation study at both room temperature and 60 ^{o}C, and the films were only deformed to a maximum strain of 5 if they were not break before that. Besides, step-cycle tests were also carried out at room temperature. In these tests, the films were stretched at 30 mm/min (100 %/min) to an integral strain and then brought back to zero stress at the same speed, and the sample was stretched again to a higher integral strain and relaxed back. Simultaneous 2D WAXD and SAXS patterns were collected during the deformation.

In-situ X-ray studies were carried out at the X27C beam line in the National Synchrotron Light Source (NSLS), Brookhaven National Laboratory (BNL). The wavelength of the synchrotron radiation was 1.371 Å. A three-pinhole collimation system was used to reduce the beam size to 0.6 mm in diameter. 2D WAXD and SAXS patterns were collected by a MAR CCD X-ray detector (MAR-USA), which had a resolution of 1024×1024 pixels (pixel size = 158.44 μm). The typical image acquisition time was 20 s for each data frame. The sample-to-detector distance was around 1900 mm for SAXS (calibrated by a silver behenate (AgBe) standard), and the sample-to-detector distance was around 110 mm for WAXD (calibrated by an aluminum oxide (Al_2O_3) standard). All X-ray images were corrected for background scattering, air scattering and beam fluctuations.

7.3 Results and Discussion

7.3.1 Deformation of Non-crosslinked and Silane Crosslinked OBCs

Engineering stress-strain curves of OBC-0S and OBC-0.6S films during deformation at room temperature and 60 ^{o}C were shown in Figure 7.1. Both films exhibited the elastomeric nature. Within the initial linear deformation region, stress-strain curves of crosslinked and non-crosslinked films were almost overlapped with each other, indicating that Young's moduli of the two were about the same. Since the Young's modulus depended most on the crystallinity, thus initial crystallinity of OBC-0S and OBC-0.6S should be very similar. After passing through the strain softening region, the stress difference between crosslinked and non-crosslinked films started to appear and increased with the strain. At later stage of deformation, the tensile stress was much greater in OBC-0.6S and its strain hardening also happened earlier. When deformed at higher temperature, the stress difference OBC-0S and OBC-0.6S became larger. Besides, OBC-0.6S had a smaller elongation-at-break ratio than OBC-0S at 60 ^{o}C, because the chain segments between crosslinked junctions were pinned and can not slip upon deformation while other polymer chains can slip, slide and disentangle due to the enhanced mobility. Thus the segments bearing too much load will be easy to break.

2D WAXD and SAXS patterns of films at the strain of 0, 2, and 5 were shown in Figure 7.2. The original sharp peaks in WAXD can be assigned to (110) and (200) to the reflections of orthorhombic polyethylene crystals and the broad halo was from amorphous phase. In SAXS the scatterings came from lamellar stacks and the micro-phase separated domains of soft segments. Films before deformation did not show any preferred orientation in both small scale and large scale structure as implied by isotropic WAXD and SAXS patterns. Upon uniaxial deformation, polymer chains started to align to the drawing direction resulting in narrowly distributed reflections along the angular direction. At higher strain, strong and highly orientated reflections from newly formed monoclinic crystal phase appeared at equatorial position. The lamellar stacks were perpendicular and soft-segment domains were parallel to the drawing direction,

respectively, as revealed by SAXS patterns consisting of meridional maximum and equatorial streaks. During the deformation, the scattering peak of that broad halo shifted to the high scattering angle, getting closed to the (010) monoclinic peak, but (110) and (200) can still be distinguished. Thus 1D peak fitting method can be used to calculate the fraction index of orthorhombic phase, as the scatterings from amorphous and monoclinic phases can be represented by one broad peak.

This fraction index of orthorhombic phase was the same value as crystallinity index when strain was equal to 0, as there were no monoclinic crystals. Besides, the meridional long period was obtained from the peak position of the Lorentz-corrected SAXS meridional profiles. The calculated orthorhombic fractions and long period were summarized in Table 7.2. Initial crystalline index was 16.4% and 17.7% of OBC-0S and OBC-0.6S, respectively. The difference was small, thus the Young's moduli mentioned above were almost the same. Slightly higher crystallinity in OBC-0.6S can be attributed to the curing at 110 ^{o}C. Crosslinking of polymers, especially in the melt, usually caused a decrease in crystallinity, as the crosslinked junction hinder the crystallization to occur upon cooling. However, for silane crosslinking via grafting and curing at high temperature, which is lower than the melting temperature (more than ten degrees in our case), the crystallization was already developed well. Curing allowed the polymer to exclude the just formed crosslinked points to the amorphous region slowly and crystallize further simultaneously. Finally, OBC-0.6S was even higher in crystallinity than non-crosslinked one. This was also consistent with the change of long period after curing. The long period of the non-crosslinked OBC-0S was 23 nm, smaller than 28 nm of OBC-0.6S. The larger long period was due to the perfection of the lamellar stacks. During the curing process, small lamellar crystals were eliminated and larger stacks grew up, resulting in the increase of long period. Upon deformation, both fraction of orthorhombic phase and the long period decreased with strain as reported in our previous work. The

extent of the decrease was very similar between both crosslinked and non-crosslinked films.

The time-evolution of angular intensity distributions of (110) reflection of OBC-0S were also illustrated in Figure 7.3. All intensities were normalized to the envelope intensity of unoriented phase. Thus the higher the intensity curve, the higher the crystal orientation along the drawing direction. At the beginning, flat curve extracted from isotropic WAXD pattern was the sign of the randomly distributed crystals. Later, two peaks rising at off-axis position (together with (200) reflections at equator) was because of b-axis orientation. Finally, it turned to c-axis orientation at high strain.

Scattering patterns of silane crosslinked films, OBC-0.6S, were similar to non-crosslinked ones. Thus we did not show the X-ray patterns but to examine some of the detailed profiles of OBC-0S and OBC-0.6S in Figure 7.4 by showing the radial intensity profiles (polar angle = 90 ^{o}) and angular intensity distributions of (110) orthorhombic reflection at strain of 2 and 5, in order to compare the crystalline structure and the development of crystal orientation between crosslinked and non-crosslinked samples. The radial profiles showed that the formation of monoclinic phase in OBC-0S was to a slightly larger extent than OBC-0.6S, especially at strain of 5. Because the broad peak containing both amorphous and (010) monoclinic reflections shifted more to the right and was a little bit stronger in intensity at that position. The angular intensity distribution had more discrepancies between the two samples. At strain of 2, both samples had b-axis orientation, and the degree of orientation was higher for OBC-0S as its peaks shifted more to the equatorial position. At even higher strain, the c-axis orientation of crystals in OBC-0S was obtained, while that of OBC-0.6S was in the middle of the transition between b-axis orientation and c-axis orientation, showing a scattering plateau.

Selected 2D WAXD of OBC-0S and OBC-0.6S during deformation at 60 ^{o}C were shown in Figure 7.5. At 60 ^{o}C, some small and defective crystals in OBCs were melted resulting in a lower initial crystallinity and a larger long period (SAXS patterns not shown here), but 60 ^{o}C was still far below the melting temperature of OBCs, most of the crystals still remained intact. Uniaxial deformation behavior of OBC-0S and OBC-0.6S at 60 ^{o}C mainly showed differences in the rate of orientation development and phase transformation comparing to room temperature. This was because the chain mobility in amorphous phase enhanced a lot and chain segments can easily disentangled upon deformation, tensile stress decreased and also the development of the orientation of crystal phase slowed down, as indicated by a broader distribution of (110) reflection in angular direction than room temperature. The formation of monoclinic crystals was more difficult, because the transformation required certain of applied load on the orthorhombic crystals to induce the unstable monoclinic crystal phase under stress. Comparison between OBC-0S and OBC-0.6S led to the same results with the deformation at room temperature, i.e. easier formation of monoclinic crystals and faster development of crystal orientation in non-crosslinked one as we saw from radial and angular intensity profiles.

7.3.2 Deformation of Non-crosslinked and Silane Crosslinked EG8100

The stress-strain curves and selected 2D WAXD and SAXS patterns of silane crosslinked ethylene octene random copolymer EG8100 were shown in Figure 7.6 and 7.7. During the deformation at room temperature, tensile stress at low strain (less than 3) and Young's muduli of crosslinked samples, EG8100-0.6S and EG8100-1S, were smaller than non-crosslinked EG8100-0S. The yielding of EG8100-0S was also distinct regarding to the crosslinked ones, which means that EG8100-0S was more plastic while crosslinked ones were more elastomeric. This can be accounted for the structure of crystalline phase of these ethylene octene random copolymers. Different from olefin block copolymers

which had relatively long hard segments that crystallize well into lamellar structure upon cooling, the random copolymers can hardly grow into well defined crystals due to the interruption of octene comonomers. As we can see from the initial WAXD patterns in Figure 7.7, the (110) reflection in EG8100-0S was broad indicating small and defective orthorhombic crystals. There were also quite a lot hexagonal crystals which caused sharp and right-shifted amorphous halo because the (010) hexagonal reflection located near the amorphous peak. The calculation of crystallinity thus became impossible due to the above reasons that led to one undeconvolutable peak in linear WAXD profiles, as shown in the radial intensity profiles in Figure 7.8.

The curing crosslinking of silane-grafted random copolymers at 50 ^{o}C can produce more perfect orthorhombic crystals suggested by the rising of (110) reflection noted with dashed line in Figure 7.8, the (200) reflection also rose up slightly. Initial SAXS patterns showed isotropic scatterings from unoriented lamellar stacks. The long period was calculated for all three samples and listed in Table 7.2. Cured samples had increased long period, consistent with the curing of OBCs. However, due to interruptions from octene comonomers and crosslinked points, the total crystallinity was still less in EG8100-0.6S and EG8100-1S even though more perfect orthorhombic crystals were obtained when they were cured at 50 ^{o}C, because the Young's modulus was greatest in EG8100-0S. As strain increased, the effects of crosslinked polymer network appeared. Tensile stress of EG8100-1S exceeded EG8100-0S first at strain about 3.5, and later at the end of deformation process EG8100-0.6S also caught up with EG8100-0S. Lamellar stacks aligned to the direction perpendicular to the drawing direction during deformation. At strain of 2, it was clear that EG8100-S had higher orientation of lamellar stacks as shown by two-point scattering at meridional, while EG8100-0.6S and EG8100-1S had elliptical scattering patterns. As strain increased more, the orientation became higher. The evolution of the WAXD demonstrated that monoclinic phase was much easier to occur

than OBCs and can be stretched to very high degree of orientation by comparing the sharpness of angular intensity distribution in Figure 7.9 with Figure 7.3. The comparison of angular intensity profiles between non-crosslinked and crosslinked EG8100 at different strain were also made in Figure 7.8. Angular distribution of EG8100-0S was narrower than crosslinked ones during deformation, which meant that orientation in EG8100-0S was higher at the same strain. The formation of monoclinic phase was also easier in EG8100-0S. All these room temperature observations between crosslinked and non-crosslinked films of ethylene octene random copolymers were consistent with ethylene octene block copolymers.

When deformed at 60 ^{o}C, which was near the melting point of EG8100, quite a fraction of small and defective crystals were melted leaving the most stable crystals. EG8100-0S without crosslinking showed lowest stress and EG8100-1S showed the highest stress. The number of crosslinked junctions or the degree of crosslinking contributed the most to the tensile stress and elongation-at-break ratio. The WAXD patterns in Figure 7.10 showed the almost the same structure development in either crosslinked or non-crosslinked EG8100. This phenomenon was different from deformation of non-crosslinked and silane crosslinked OBCs at 60 ^{o}C, and we will discuss the reason later. The hexagonal and monoclinic crystals were no longer existed in the samples. Deformed films showed sharp and well defined monoclinic reflections at the equator.

7.3.3 Deformation of Non-crosslinked and E-beam Crosslinked Samples

Electron-beam crosslinked olefin random and block copolymers were also uniaxial deformed at room temperature and 60 ^{o}C. The electron-beam crosslinking was different from silane crosslinking as it initiated crosslinking at room temperature rather than high

temperature and thus the crystalline phase usually remained intact before and after crosslinking. As shown in Figure 7.11, the engineering stress-strain curves of uniaxial deformation of non-crosslinked and electron-beam crosslinked samples exhibited similar initial deformation behavior that depends on the crystallinity. The tensile stress of crosslinked ones became greater and greater than non-crosslinked ones as strain increased. The crosslinking also caused a shorter elongation-at-break ratio at 60 ^{o}C. Long period and fraction of orthorhombic phase during deformation were calculated and listed in Table 7.3. The non-crosslinked polymer film and the one crosslinked had about the same values in these two characteristics, confirming that electron-beam crosslinking had no influences on the crystal structure. Upon uniaxial deformation, the development of the orthorhombic fraction and meridional long period were very similar like silane crosslinked polymers, suggesting the same nature of the deformation of crystal structure.

Since the in-situ WAXD and SAXS patterns of these two set of samples, OBC-0E and OBC-10E, KC8852-0E and KC8852-10E, looked like the same and similar to OBC-0S and EG8100-0S, respectively, we did not show the 2D patterns but only compared the angular and radial intensity profiles in Figure 7.12. Profiles selected were at the strain value of 2, as in the studies above, we note that at this strain, the differences between two samples were largest. However, no matter at room temperature or 60 ^{o}C, intensity profiles from crosslinked and non-crosslinked samples were almost superposed together, which meant that the crystal structure and its orientation were the same in crosslinked and non-crosslinked samples. For OBC-0E and OBC-10E, (110) and (200) reflections were well separated from diffused broad peak, which shifted to the right at room temperature due to the monoclinic phase formed. The degree of b-axis orientation for crosslinked and non-crosslinked OBCs was the same. For KC8852-0E and KC8852-10E, different temperatures affected the crystal types, i.e. hexagonal and monoclinic crystals at room

temperature and orthorhombic crystals at 60 ^{o}C, but whether the films were crosslinked or not did not influence the structure and orientation development.

7.3.4 Effects of Crosslinking and Crystalline Structure on Deformation

According to the above observations, both silane and electron-beam crosslinking can improve the strength of polymer films. At higher temperature, chain segments between crosslinked junctions can carry pronounced fraction of the load upon deformation and thus giving a higher tensile stress. This also decreased the elongation-at-break ratio significantly, since those restricted chain segments with excessive load on them will tend to break rather than sliding and disentangling of stressed polymer chains in non-crosslinked films. However, the structure development, especially the crystalline structure, during deformation was seemed to depend more on the initial crystalline phase rather than crosslinking. For non-crosslinked films and films crosslinked by electron-beam, the tensile properties were well distinguished, but the structure development during the deformation was identical as revealed by WAXD and SAXS patterns, because the electron-beam crosslinking took place in solid state polymers at room temperature and did not affect crystal structure in the films. For silane-grafting and high temperature curing crosslinked samples, there were more perfect crystals well crystallized, so they were more resistant to the deformation when external load was applied, resulting in lower degree of crystal orientation and less formation of monoclinic crystals, as we saw during the room temperature deformation of all silane crosslinked films. If the deformation temperature increased to 60 ^{o}C, silane crosslinked and non-crosslinked OBC films behaved as differently as room temperature, because the temperature was still much lower than curing temperature without much influences on the crystalline phase formed through melt-crystallization or curing at 110 ^{o}C. But for EG8100 films, 60 ^{o}C exceeded the curing temperature and getting closed to the melting point, thus the crystalline

difference between melt-crystallized EG8100-0S and EG8100s that were melt-crystallized and cured at 50 ^{o}C was eliminated, leaving crystals that were stable at 60 ^{o}C and leading to the same structure development during deformation.

7.3.5 Step-cycle Tests of Non-crosslinked and Crosslinked Samples

Elastomeric properties of all samples, i.e. olefin block and random copolymers, non-crosslinked and crosslinked by silane or electron-beam methods, were tested using step-cycle experiment under room temperature. The permanent set that is the permanent plastic deformation after the remove of applied load was used to evaluate the elasticity of the polymer films. If polymer chains were crosslinked together like in rubber, the release of external load can result in almost fully relax back of extended chains, but due to the existence of crystals in our films, the permanent set can not be zero. For non-crosslinked OBC-0E and KC8852-0E and electron-beam crosslinked OBC-10E and KC8852-10E, the permanent set after relaxation was exactly identical. This can be attributed to the same crystalline network, consistent with the analysis on the crystal structure done above. For non-crosslinked OBC-0S and EG8100-0S and silane crosslinked OBC-0.6S, EG8100-0.6S and EG8100-1S, because the curing and crosslinking was done at high temperature, the crystalline structure was slightly different, and this difference emerged out in the permanent set values during the step-cycle tests.

7.4 Conclusions

Structure development during deformation of silane and electron-beam crosslinked olefin block and random copolymers depended on the original crystalline phase. Electron-beam crosslinking took place in solid state polymers at room temperature, thus the initial crystalline structure remained intact, while crosslinking of silane-grafted

polymers took place at high temperature, the crosslinking and curing process affected more on crystalline structure comparing with melt-crystallized non-crosslinked ones, and resulted in different structure development during the deformation at room temperature. Deformation at 60 ^{o}C of silane crosslinked random copolymers eliminated the crystalline difference produced by melt-crystallization and curing, thus structure development became the same. However, 60 ^{o}C was too low regarding to the curing temperature of OBC, thus difference still existed. Crosslinked polymer chains contributed to the tensile stress a lot, especially at larger strain and high temperature, due to the highly extended polymer chain segments between the crosslinked junctions, and thus it will also reduce the elongation-at-break ratio because of the excessive stress localized on chain segments. Elasticity of electron-beam crosslinked and non-crosslinked samples were exactly the same, while silane crosslinked and non-crosslinked samples exhibit slightly difference which was due to the difference in crystalline phase.

List of References

1. Lazar, M.; Rado, R.; Rychly, J. *Adv. Polym. Sci.*, **1990**, 95, 149-197.
2. Jiao, C.; Wang, Z.; Gui, Z.; Hu, Y. *Eur. Polym. J.*, **2005**, 41, 1204.
3. Manley, T. R.; Qayyum. M. M. *Polymer*, **1972**, 13, 587-592.
4. Robertson, M. B.; Ward, I. M.; Klein, P. G.; Packer, K. J. *Macromolecules*, **1997**, 30, 6893-6898.
5. Rizzo, P.; Baione, F.; Guerra, G.; Martinotto, L.; Albizzati, E. *Macromolecules*, **2001**, 34, 5175-5179.
6. Khonakdar, H. A.; Morshedian, J.; Wagenknecht, U.; Jafari, S. H. *Polymer*, **2003**, 44, 4301-4309.
7. Khonakdar, H. A.; Jafari, S. H.; Wagenknecht, U.; Jehnichen, D. *Rad. Phys. Chem.*, **2006**, 75, 78-86.
8. Sirisinha, K.; Chimdist, S. *J. Appl. Polym. Sci.*, **2008**, 109, 2522-2528.
9. Phillips, P. J.; Kao, Y. H. *Polymer*, **1986**, 27, 1679-1686.
10. Lambert, W. S.; Phillips, P. J. *Polymer*, **1990**, 31, 2077-2082.
11. Lambert, W. S.; Phillips, P. J.; Lin, J. S. *Polymer*, **1994**, 35, 1809-1818.
12. Klein, P. G.; Gonzalez-Orozco, J. A.; Ward, I. M. *Polymer*, **1994**, 35, 2044-2048.
13. Andersson, L. H. U.; Hjertberg, T. *Polymer*, **2006**, 47, 200-210.
14. Cerrada, M. L.; Benavente, R.; Fernandez-Garcia, M.; Perez, E.; Campos, J. M. ; Ribeiro, M. R. *Polymer*, **2009**, 50, 1095-1102.
15. Chodak, I. *Prog. Polym. Sci.*, **1995**, 20, 1165-1199.
16. Chodak, I. *Prog. Polym. Sci.*, **1998**, 23, 1409-1442.
17. Sirisinha, K.; Meksawat, D. *J. Appl. Polym. Sci.*, **2004**, 93, 901-906.
18. Sirisinha, K.; Meksawat, D. *J. Appl. Polym. Sci.*, **2004**, 93, 1179-1185.
19. Kamphunthong, W.; Sirisinha, K. *J. Appl. Polym. Sci.*, **2008**, 109, 2347-2353.
20. Mishra, J. K.; Chang, Y. W.; Lee, B. C. ; Ryu, S. H. *Rad. Phys. Chem.*, **2008**, 77,

675-679.

21. Nicolas, J.; Ressia, J. A.; Valles, E. M.; Merino, J. C.; Pastor, J. M. *J. Appl. Polym. Sci.*, **2009**, 112, 2691-2700.
22. Khonakdar, H. A.; Jafari, S. H.; Taheri, M. ; Wagenknecht, U.; Jehnichen, D.; Haussler, L. *J. Appl. Polym. Sci.*, **2006**, 100, 3264-3271.
23. Turcsanyi, B.; Fekete, E.; Pukanszky, B.; Tabor, I. *J. Thermal Anal.*, **1990**, 36, 1775-1784.
24. Ke, Q.; Huang, X.; Wei, P.; Wang, G.; Jiang, P. *J. Appl. Polym. Sci.*, **2007**, 104, 1920-1927.
25. Matsuo, M.; Sawatari, C. *Macromolecules*, **1986**, 19, 2028-2035.
26. Narkis, M.; Raiters, I.; Shkolnik, S.; Siegmann, A. Eyerer, P. *J. Macromol. Sci. Phys.*, **1987**, B26(1), 37-58.
27. van der Sanden, M. C. M.; Meijer, H. E. H. *Polymer*, **1993**, 34, 5063-5072.
28. Krupa, I.; Luyt, A. S. *J. Appl. Polym. Sci.*, **2001**, 81, 973-980.
29. Bocok, T.; Zicans, J.; Kalnins, M. *Mecha. Compos. Mat.*, **2005**, 41, 161-170.
30. Zhang, G.; Wang, G.; Zhang, J.; Wei, P.; Jiang, P. *J. Appl. Polym. Sci.*, **2006**, 102, 5057-5061.
31. Ali, Z.; Youssef, H. ; Afify, T. *Polym. Compos.*, **2008**, 29, 1119-1124.
32. Nicolas, J.; Ressia, J. A.; Valles, E. M.; Merino, J. C.; Pastor, J. M. *J. Appl. Polym. Sci.*, **2009**, 112, 2691-2700.

List of Tables

Table 7.1. Samples and crosslinking information

	Crosslink	Method	Concen./Dose	Gel Content	Curing
OBC-0S	No	/	/	/	No
OBC-0.6S	Yes	Silane	0.6% VTMS	77.0%	At 110 ^{o}C
EG8100-0S	No	/	/	/	No
EG8100-0.6S	Yes	Silane	0.6% VTMS	64.2%	At 50 ^{o}C
EG8100-1S	Yes	Silane	1% VTMS	79.1%	At 50 ^{o}C
OBC-0E	No	/	/	/	No
OBC-10E	Yes	E-beam	10 kGy	N/A	No
KC8852-0E	No	/	/	/	No
KC8852-10E	Yes	E-beam	10 kGy	N/A	No

Table 7.2. Fraction of orthorhombic crystal phase and long period of silane crosslinked polymers at strain of 0, 2, and 5 under room temperature.

	f_{orth} (%)			Long Period (nm)		
	ε = 0	ε = 2	ε = 5	ε = 0	ε = 2	ε = 5
OBC-0S	16.4	11.8	9.6	23	21	17
OBC-0.6S	17.7	13.2	10.6	28	24	20
EG8100-0S	N/A			11	14	15
EG8100-0.6S				13	16	16
EG8100-1S				13	14	14

Table 7.3. Fraction of orthorhombic crystal phase and long period of E-beam crosslinked polymers at strain of 0, 2, and 5 under room temperature.

	f_{orth} (%)			Long Period (nm)		
	ε = 0	ε = 2	ε = 5	ε = 0	ε = 2	ε = 5
OBC-0E	17.9	12.7	10.1	25	22	17
OBC-10E	17.8	12.6	10.1	25	21	16
KC8852-0E	N/A			12	15	15
KC8852-10E				12	15	15

List of Figures

Figure 7.1. Engineering stress-strain curves of OBC-0S (black) and OBC-0.6S (blue) at room temperature and 60 °C.

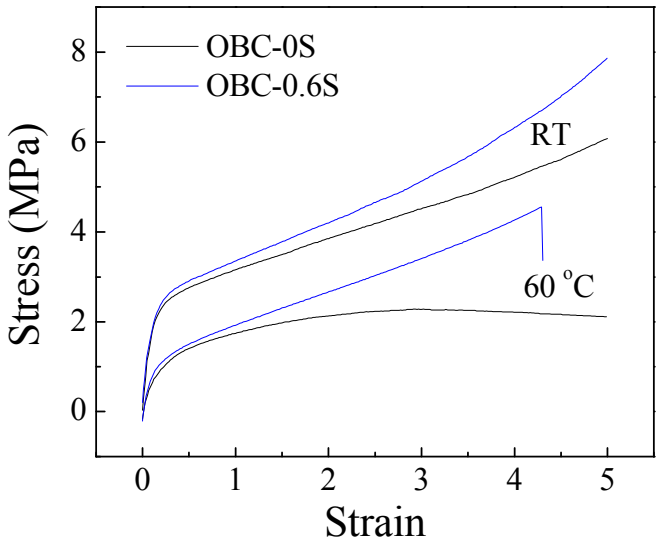

Figure 7.2. Selected 2D WAXD (A) and SAXS (B) patterns of OBC-0S and OBC-0.6S during uniaxial deformation at room temperature. Strain values were 0, 2, and 5, respectively.

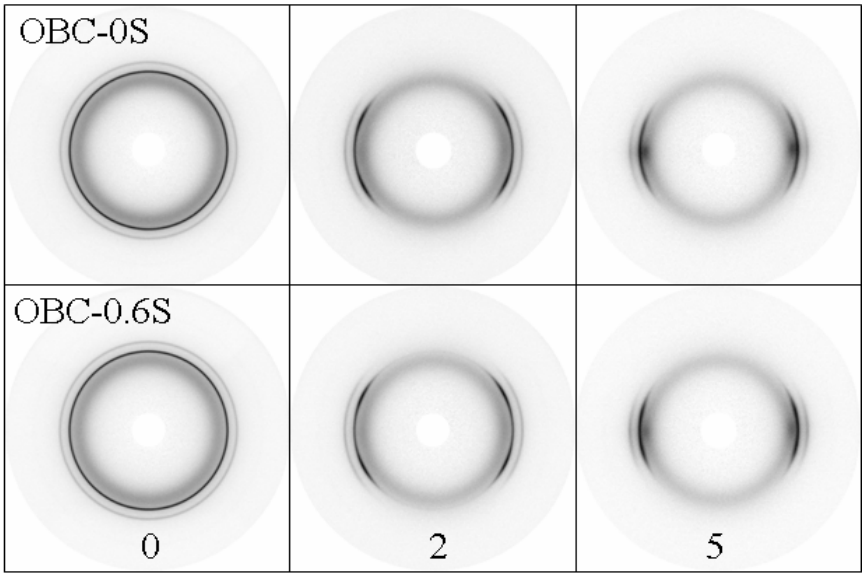

(A)

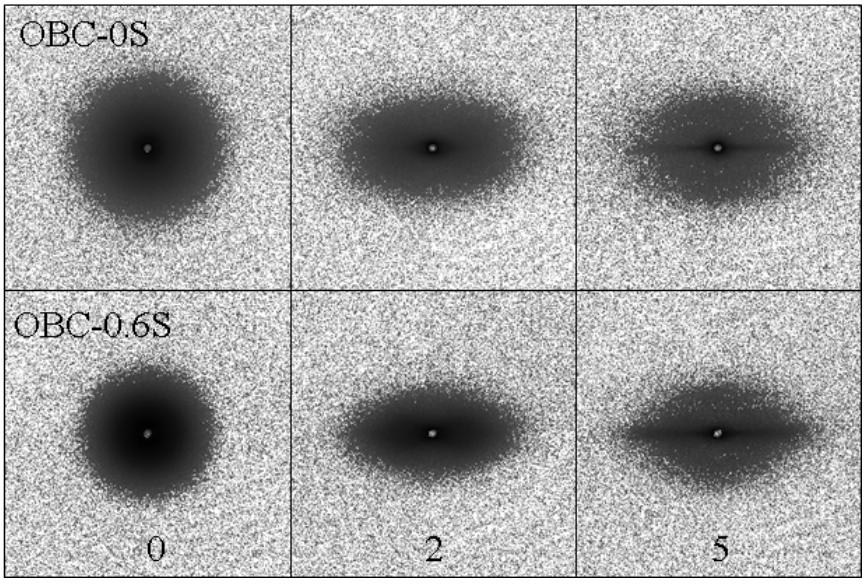

(B)

Figure 7.3. Time-evolution of angular intensity (normalized to the unoriented envelope intensity) distribution of (110) reflection during the uniaxial deformation of OBC-0S at room temperature.

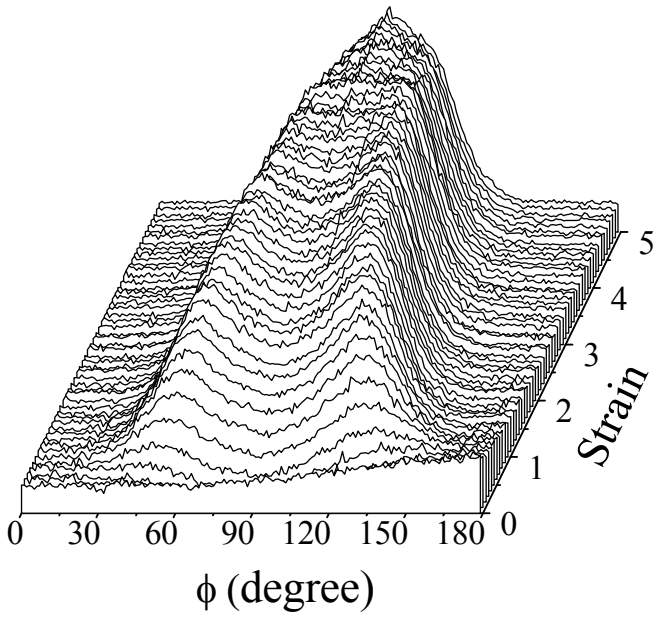

Figure 7.4. Radial (left) and angular (right) intensity profiles of OBC-0S (black) and OBC-0.6S (blue) at strain of 2 (bottom) and 5 (top).

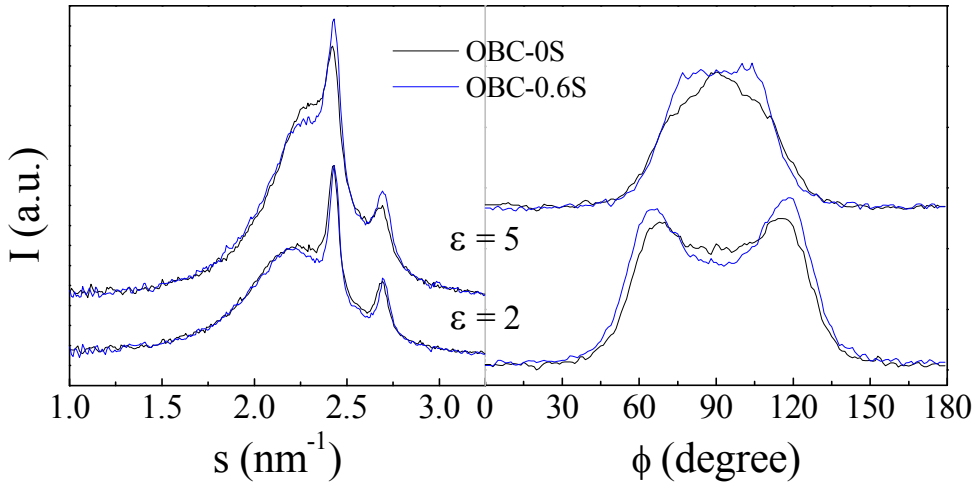

Figure 7.5. Selected 2D WAXD patterns of OBC-0S and OBC-0.6S during uniaxial deformation at 60 ^{o}C. Strain values were 0, 2, and 5, respectively.

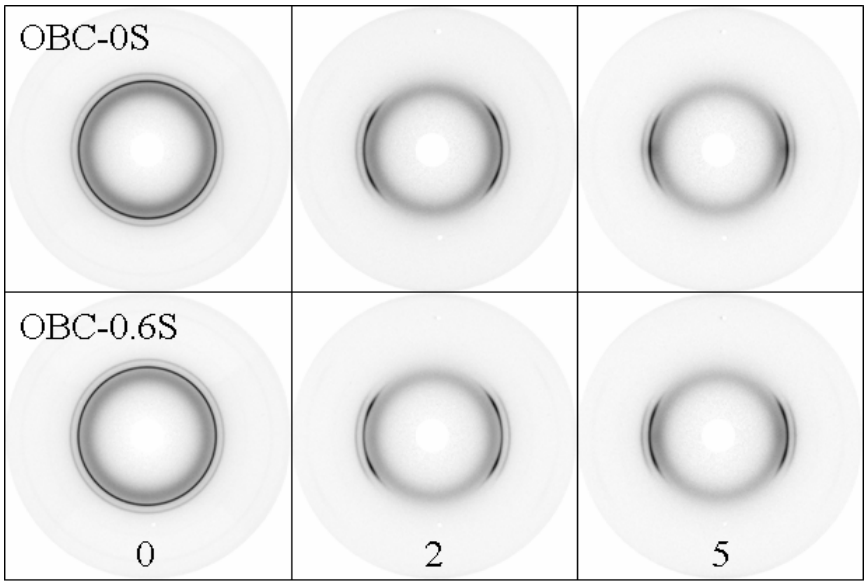

Figure 7.6. Engineering stress-strain curves of EG8100-0S (black), EG8100-0.6S (blue), and EG8100-1S (red) at room temperature and 60 ^{o}C.

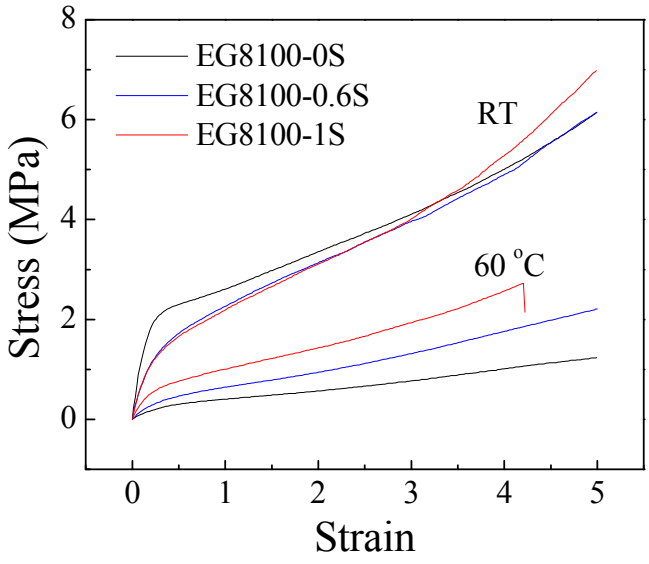

Figure 7.7. Selected 2D WAXD (A) and SAXS (B) patterns of EG8100-0S, EG8100-0.6S, and EG8100-1S during uniaxial deformation at room temperature. Strain values were 0, 2, and 5, respectively.

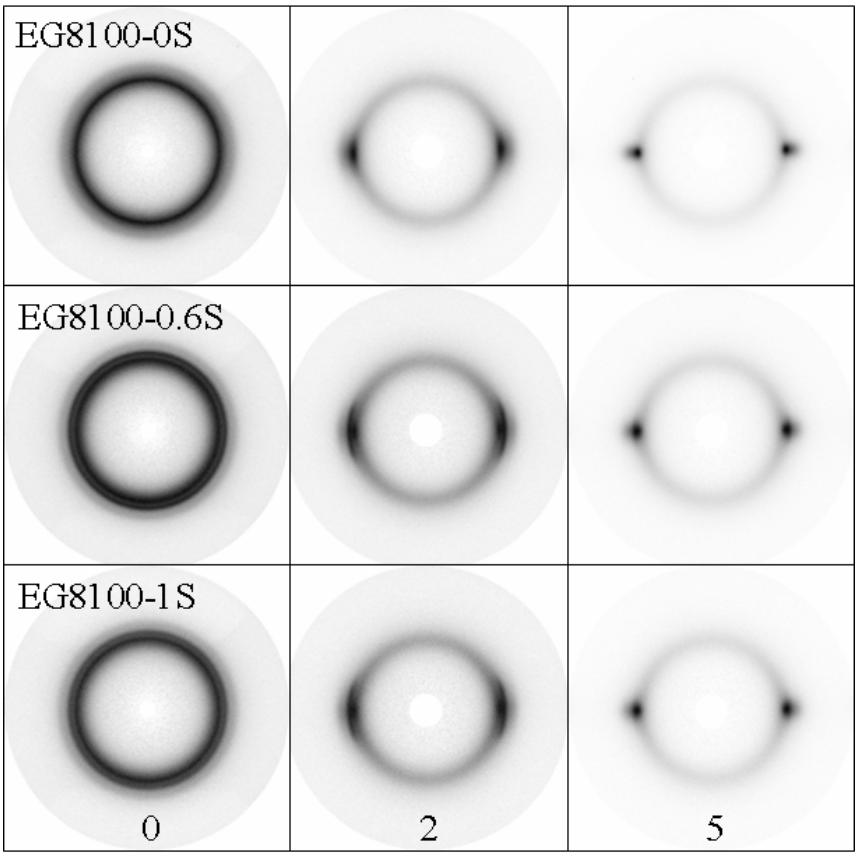

(A)

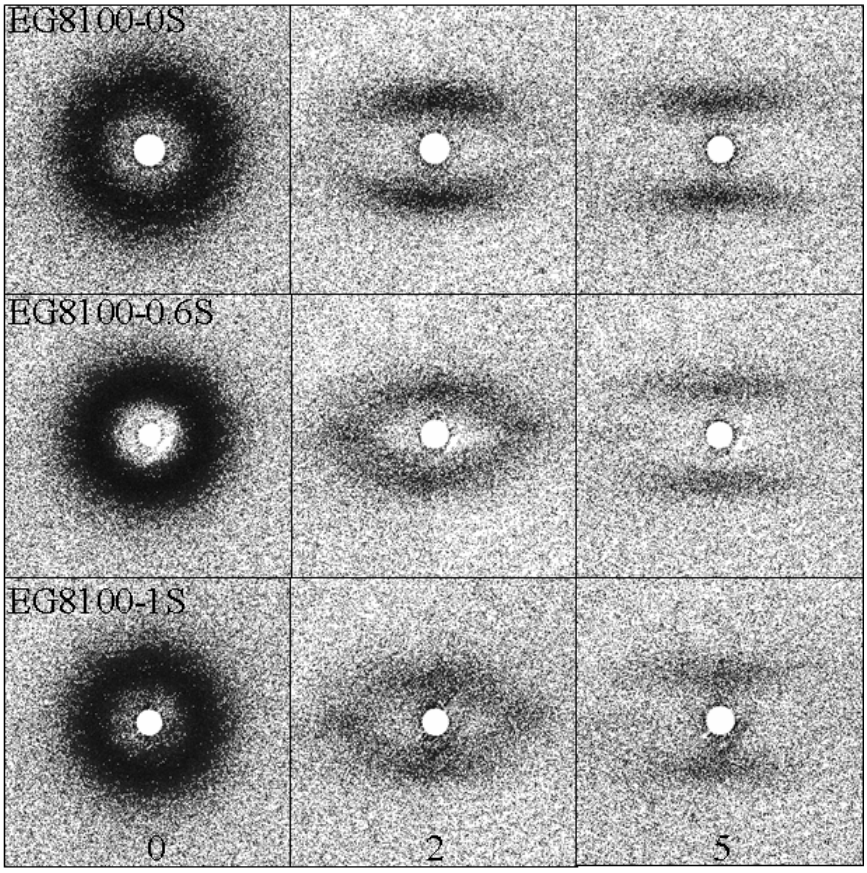

(B)

Figure 7.8. Radial (left) and angular (right) intensity profiles of EG8100-0S (black), EG8100-0.6S (blue), and EG8100-1S (red) at strain of 0 (bottom), 2 (middle), and 5 (top).

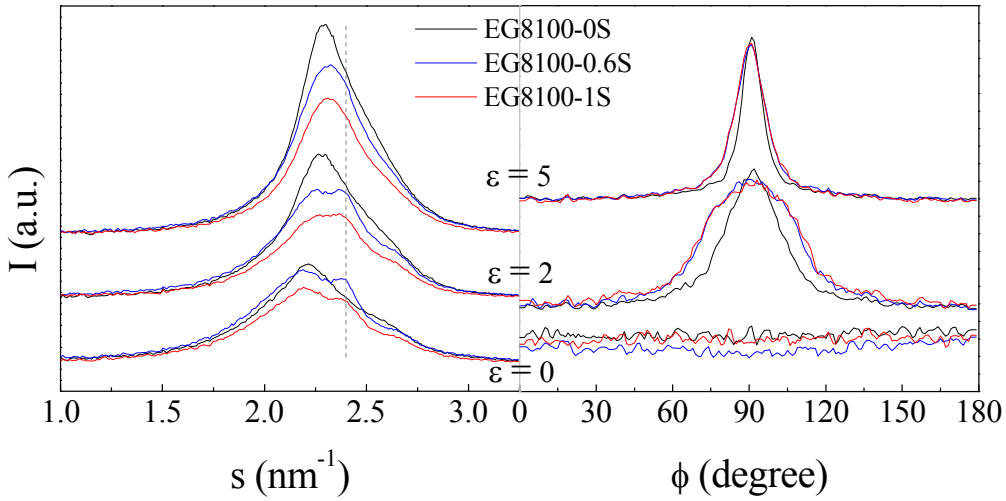

Figure 7.9. Time-evolution of angular intensity (normalized to the unoriented envelope intensity) distribution of (110) reflection during the uniaxial deformation of EG8100-0S at room temperature.

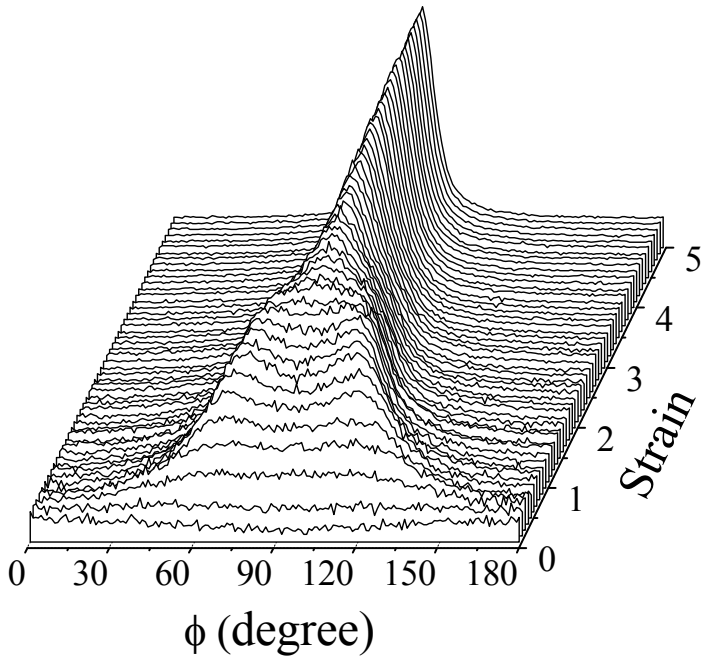

Figure 7.10. Selected 2D WAXD patterns of EG8100-0S and EG8100-0.6S during uniaxial deformation at 60 ^{o}C. Strain values were 0, 2, and 5, respectively.

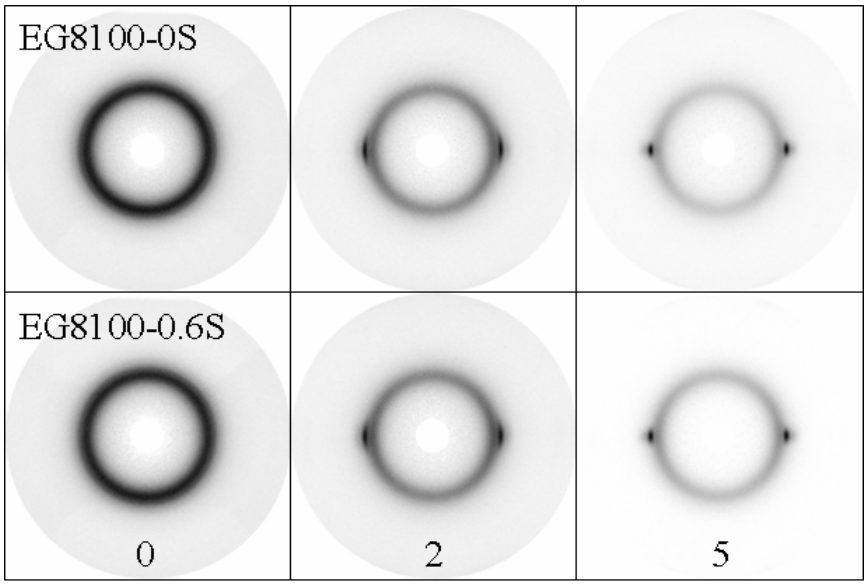

Figure 7.11. Engineering stress-strain curves of E-beam crosslinked KC8852 (A) and OBC (B) during uniaxial deformation at room temperature and 60 ^{o}C.

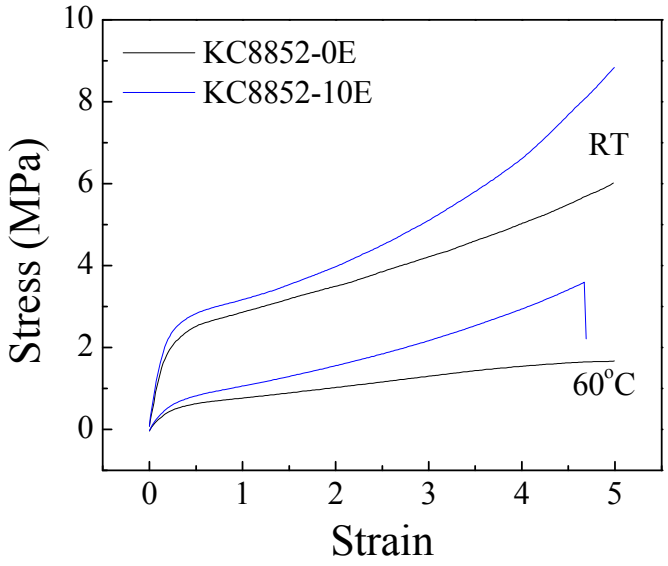

(A)

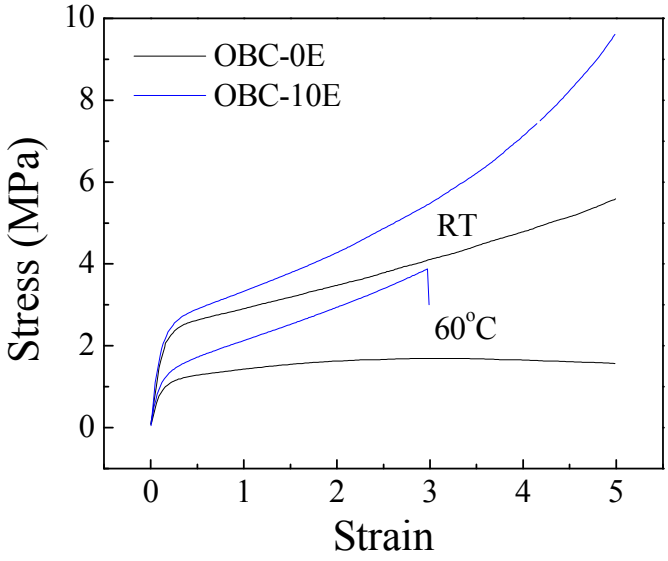

(B)

Figure 7.12. Radial (left) and angular (right) intensity profiles of KC8852 (A) and OBC (B) at room temperature (top) and 60 ^{o}C (bottom) with strain value of 2.

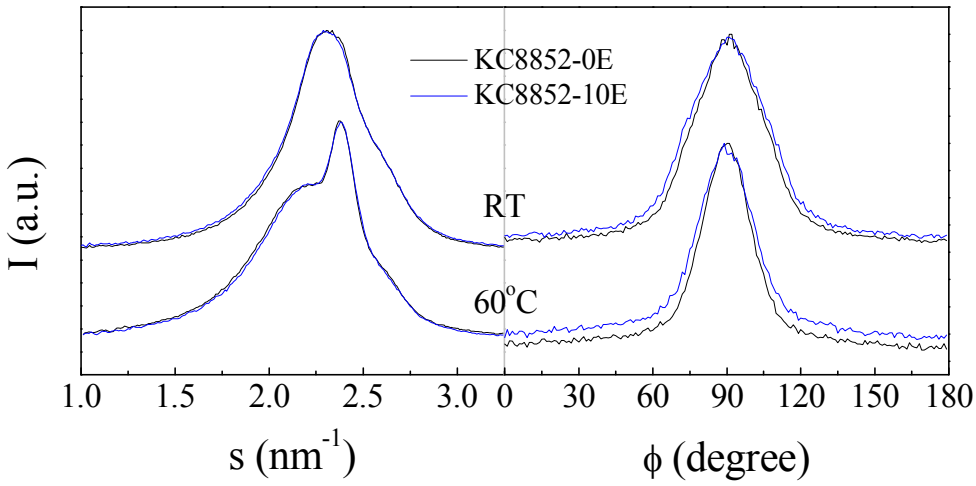

(A)

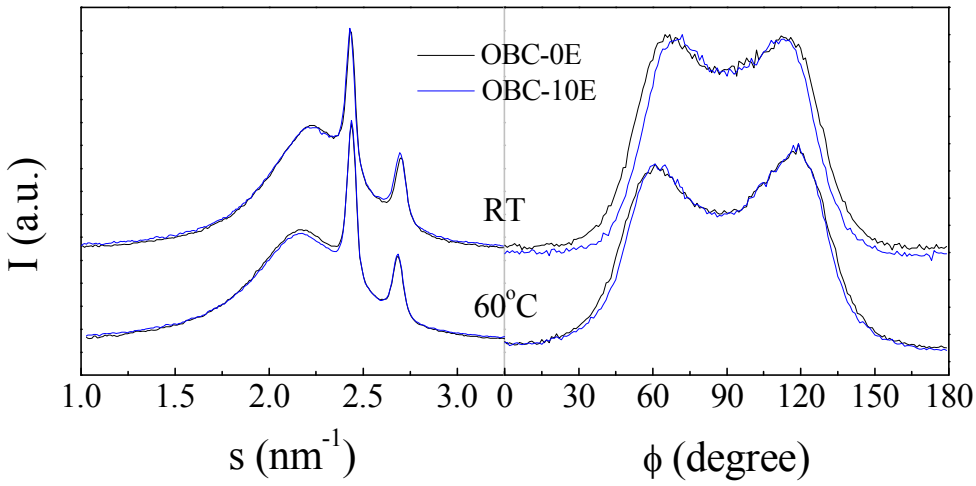

(B)

Figure 7.13. Engineering stress-strain curves of all samples during the step-cycle tests at room temperature.

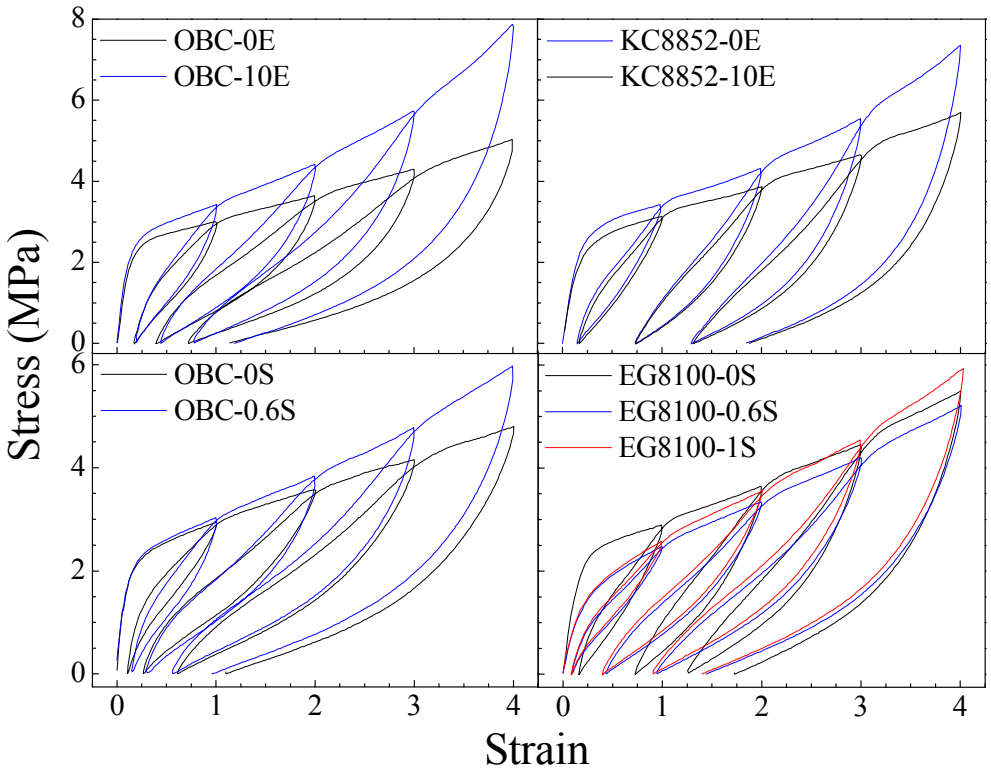

Bibliography

1.1 Keller, A.; Kolnaar, H. W. *Mater. Sci. Technol*, **1997**, vol 18, 189.

1.2 Ward, I. M. *Structure and Properties of Oriented Polymers*, Wiley, New York, **1975**.

1.3 Wunderlich, B. *Macromolecular physics*, vol 2, Academic Press, New York, **1973**.

1.4 Wilkinson, A. N. and Ryan, A. J. (Eds.), *Polymer Processing and Structure Development*, Kluwer, Dodrecht, **1998**.

1.5 Eder, G.; Janeschitz-Kriegl, H. *Mater. Sci. Technol.*, **1997**, 18, 268.

1.6 Hobbs, J. K.; Humphris, A. D. L.; Miles, M. J. *Macromolecules*, **2001**, 34, 5508.

1.7 Bashir, Z.; Odell, J. A.; Keller, A. *J. Mater. Sci.*, **1986**, 21, 3993.

1.8 Somani, R. H.; Hsiao, B. S.; Nogales, A.; Srinivas, S.; Tsou, A. H.; Sics, I.; Balta-Calleja, F. J.; Ezquerra, T. A. *Macromolecules*, **2000**, 33, 9385.

1.9 Jerschow, P.; Janeschitz-Kriegl, H. *Int. Polym. Process*. **1997**, 12, 72.

1.10 Sherwood, C.; Price, F.; Stein, R. J. *Polym. Sci. (Polym Symp.)*, **1978**, 63, 77.

1.11 Lagasse, R. R.; Maxwell, B. *Polym. Eng. Sci.*, **1976**, 16, 189.

1.12 Vleeshouwers, S.; Meijer, H. *Rheol. Acta*, **1996**, 35, 391.

1.13 Duplay, C.; Monasse, B.; Haudin, J. M.; Costa, J. L. *J. Mater. Sci.,* **2000**, 35, 6093.

1.14 Seki, M.; Thurman, D. W.; Oberhauser, J. P.; Kornfield, J. A. *Macromolecules*, **2002**, 35, 2583.

1.15 de Gennes, P. G.; *J. Chem. Phys.*, **1974**, 60, 5030.

1.16 Pope, D. P.; Keller, A. *Colloid Polym. Sci.*, **1978**, 256, 751.

1.17 Miles, M. J.; Keller, A. *Polymer*, **1980**, 21, 1295.

1.18 Dukovski, I.; Muthukumar, M. *J. Chem. Phys.*, **2003**, 118, 6648.

1.19 Na, B., Wang, Y.; Zhang, Q.; Fu, Q. *Polymer*, **2004**, 45, 6245.

1.20 Yamazaki, S.; Hikosaka, M.; Toda, A.; Wataoka, I.; Yamada, K.; Tagashira, K. *J. Macromol. Sci. Phys.*, **2003**, B42, 499.

1.21 Isayev, A. I.; Chan, T. W.; Shimojo, K.; Gmerek, M. *J. Appl. Polym. Sci.*, **1995**, 55, 807.

1.22 Gutierrez, M. G.; Alfonso, G. C.; Riekel, C.; Azzurri, F. *Macromolecules*, **2004**, 37, 478.

1.23 Azzurri, F.; Alfonso, G. C. *Macromolecules*, **2005**, 38, 1723.

1.24 Hill, M. J.; Barbam, P. J.; Keller, A. *Colloid Polym. Sci.*, **1980**, 258, 1023.

1.25 Hill, M. J.; Keller, A. *Colloid Polym. Sci.*, **1981**, 259, 335.

1.26 Hill, M. J.; Barbam, P. J.; Keller, A. *Colloid Polym. Sci.*, **1983**, 261, 721.

1.27 Liu, T.; Petermann, J.; He, C.; Liu, Z.; Chung, T. *Macromolecules*, **2001**, 34, 4305.

1.28 Liu, T.; Lieberwirth, I.; Petermann, J. *Macromol. Chem. Phys.*, **2001**, 202, 2921.

1.29 Liu, T.; Tjiu, W. C.; Petermann, J. *J. Crystal Growth*, **2002**, 243, 218.

1.30 Somani, R. H.; Hsiao, B. S.; Nogales, A.; Fruitwala, H.; Srinivas, S.; Tsou, A. H. *Macromolecules*, **2001**, 34, 5902.

1.31 Nogales, A.; Hsiao, B. S.; Somani, R. H.; Srinivas, S.; Tsou, A. H.; Balta-Calleja, F. J.; Ezquerra, T. A. *Polymer*, **2001**, 42, 5247.

1.32 Keum, J.; Somani, R. H.; Zuo, F.; Burger, C.; Sics, I.; Hsiao, B. S.; Chen, H.; Kolb, R.; Lue, C. *Macromolecules*, **2005**, 38, 5128.

1.33 de Gennes, P. G.; *Scaling Concepts in Polymer Physics*, Cornell University Press, Ithaca, New York, **1979**.

1.34 Ballard, D. G. H.; Cheshier, P.; Longman, G. W.; Schelten, J. *Polymer*, **1978**, 19, 379.

1.35 Yang, L; Somani, R. H.; Sics, I.; Hsiao, B. S.; Kolb, R.; Fruitwala, H.; Ong, C. *Macromolecules*, **2004**, 37, 4845.

1.36 Somani, R. H.; Hsiao, B. S.; Nogales, A.; Srinivas, S.; Tsou, A. H.; Scis, I,; Balta-Calleja, F. J.; Ezquerra, T. A. *Macromolecules*, **2000**, 33, 9385.

1.37 Keum, J.; Burger, C.; Hsiao, B. S.; Somani, R. H.; Yang, L.; Chu, B.; Kolb, R.; Chen, H.; Lue, C. *Prog. Colloid Polym. Sci.*, **2005**, 130, 114.

1.38 Milner, S. T.; McLeish, T. C. B. *Phys. Rev. Lett.*, **1998**, 31, 725.

1.39 Bent, J.; Hutchings, L. R.; Richards, R. W.; Gough, T.; Spares, R.; Coates, P. D.; Grillo, I.; Harlen, O. G.; Read, J. D.; Garham, R. S.; Likhtman, A. E.; Groves, D. J.; Nicholson, T. M.; McLeish, T. C. B. *Science*, **2003**, 301, 1692.

1.40 Doi, M.; Edwards, S. F. *The Theory of Polymer Dynamics*, Oxford Science Publications, Oxford, **1986**.

1.41 Hsiao, B. S.; Yang, L.; Somani, R. H.; Carlos, A. A.; Zhu, L. *Phys. Rev. Lett*, **2005**, 94, 117802.

2.1 Doi, M.; Edwards, S. F. *The Theory of Polymer Dynamics* (Clarendon Press, Oxford, 1986).

2.2 de Gennes, P. G. *Scaling Concepts in Polymer Physics* (Cornell Univ. Press, Ithaca, 1979).

2.3 Rastogi, S.; Lippits, D. R.; Peters, G. W. M.; Graf, R.; Yao, Y.; Spiess, H. W. *Natural Materials* **2005**, *4*, 635.

2.4 Yamada, K.; Kamezawa, M.; Takayanagi, M. *J. Appl. Polym. Sci.* **1981**, *26*, 49.

2.5 de Rosa, C.; Auriemma, F.; De Lucia, G.; Resconi, L. *Polymer* **2005**, *46*, 9461.

2.6 Hong, K.; Rastogi, A.; Strobl, G. *Macromolecules* **2004**, *37*, 10174.

2.7 Al-Hussein, M.; Strobl, G. *Macromolecules* **2002**, *35*, 8515.

2.8 Schrauwen, B. A. G.; Janssen, R. P. M.; Govaert, L. E.; Meijer, H. E. H. *Macromolecules* **2004**, *37*, 6069.

2.9 Schrauwen, B. A. G.; Breemen, L. C. A.; Spoelstra, A. B.; Govaert, L. E.; Peters, G. W M.; Meijer, H. E. H. *Macromolecules* **2004**, *37*, 8618.

2.10 Keith, H. D.; Padden, F. J. Jr.; Vadimsky, R. G. *J. Polym. Sci., Polym. Phys. Ed.* **1966**, *4*, 267.

2.11 Lustiger, A.; Markham, R. L. *Polymer* **1983**, *24*, 1647.

2.12 Huang, Y.; Brown, N. *J. Polym. Sci., Part B: Polym. Phys.* **1991**, *29*, 129.

2.13 Porter, R. S.; Wang, L. *J. Macromol. Sci., Rev. in Macromol. Chem. Phys.* **1995**, *C35*, 63.

2.14 Ishikawa, M.; Ushui, K.; Kondo, Y.; Hatada, K.; Gima, S. *Polymer* **1996**, *37*, 5375.

2.15 Nitta, K.; Takayanagi, M. *J. Polym. Sci., Part B: Polym. Phys.* **1999**, *37*, 357.

2.16 Janimak, J. J.; Stevens, G. C. *J. Mater. Sci.* **2001**, *36*, 1879.

2.17 Spitalsky, Z; Bleha, T. *Polymer* **2003**, *44*, 1603.

2.18 Seguela, R. *J. Polym. Sci. Part B: Polym. Phys.* **2005**, *43*, 1729.

2.19 Hay, I. L.; Keller, A. *Kolloid. Z. Z. Polym* **1965**, *204*, 43.

2.20 Shimamura, K. *In Morphology of Polymers. Proceedings 17th Europhysics Conference on Macromolecular Physics Pargue, Czechoslovakia,,* **1985**.

2.21 Peterlin, A. *J. Mater. Sci.* **1971**, *6*, 490.

2.22 Peterlin, A. *Colloid Polym. Sci.* **1987**, *265*, 357.

2.23 Flory, P.; Yoon, D. *Nature (London)* **1978**, *272*, 226.

2.24 Bowden, P.; Young, R. *J. Mater. Sci.* **1974**, *9*, 2034.

2.25 Popli, R.; Mandelkern, L. *J. Polym. Sci. Polym. Phys. Ed.* **1987**, *25*, 441.

2.26 Galeski, A. *Prog. Polym. Sci.* **2003**, *28*, 1643.

2.27 Hiss, R.; Hobeika, S.; Lynn, C.; Strobl, G. *Macromolecules* **1999**, *32*, 4390.

2.28 Ferreiro, V.; Coulon, G. *J. Polym. Sci., Polym. Phys. Ed.* **2004**, *42*, 687.

2.29 Hu, W. G.; Schmidt-Rohr, K. *Acta. Polym.* **1999**, *50*, 271.

2.30 de Rosa, C.; Auriemma, F.; de Ballesteros, O. R. *Phys. Rev. Lett.* **2006**, *96*, 167801.

2.31 Men, Y.; Riger, J.; Homeyer, J. *Macromolecules* **2004**, *37*, 9481.

2.32 Men, Y.; Rieger, J.; Strobl, G. *Phys. Rev. Lett.* **2003**, *91*, 095502.

2.33 Ran, S.; Zong, X.; Fang, D.; Hsiao, B. S.; Chu, B.; Phillips, R. A. *Macromolecules* **2001**, *34*, 2569.

2.34 Ran, S.; Zong, X.; Fang, D.; Hsiao, B. S.; Chu, B.; Cunniff P. M.; Phillips, R. A. *J. Materials Sci.* **2001**, *36*, 3071.

2.35 Ran, S.; Wang, Z.; Burger, C.; Chu, B.; Hsiao, B. S. *Macromolecules* **2002**, *35*, 10102.

2.36 Kawakami, D.; Ran, S.; Burger, C.; Fu, B.; Sics, I.; Hsiao, B. S. *Macromolecules* **2003**, *36*, 9275.

2.37 Kawakami, D.; Ran, S.; Burger, C.; Fu, B.; Sics, I; Hsiao, B. S.; Kikutani, T. *Polymer* **2004**, *45*, 905.

2.38 Kawakami, D.; Hsiao, B. S.; Ran, S.; Burger, C.; Avila-Orta, C.; Sics, I.; Kikutani, T.; Jacob, K.; Chu, B. *Macromolecules* **2005**, *38*, 91.

2.39 Natta, G.; Peraldo, M.; Corradini, P. *Rend. Accad. Naz. Lincei* **1959**, *26*, 14.

2.40 Natta, G.; Corradini, P. *Nuovo Cimento, Suppl.* **1960**, *15*, 40.

2.41 Wyckoff, H. W. *J. Polym. Sci.* **1962**, *62*, 83.

2.42 Morosoff, N.; Peterlin, A. *J. Polym. Sci.* **1972**, *A-2(10)*, 1237.

2.43 Jones, A. T.; Aizlewood, J. M.; Beckett, D. R. *Makromolekulare Chemie* **1964**, *75*, 134.

2.44 Brucker, S.; Meille, S. V.; Petraccone, V.; Pirozzi, B. *Prog. Polym. Sci.* **1991**, *16*, 361.

2.45 Lotz, B.; Wittmann, J. C.; Lovinger, A. J. *Polymer* **1996**, *37*, 4979.

2.46 Miller, R. L. *Polymer* **1960**, *1*, 135.

2.47 Zannetti, R.; Celotti, G.; Fichera, A. Francesconi, R. *Makromol. Chem*. **1969**, *128*, 137.

2.48 Zannetti, R.; Celotti, G.; Armigliato, A. *Eur. Polym. J.* **1970**, *6*, 879.

2.49 de Candia, F.; Iannelli, P.; Staulo, G.; Vittoria, V. *Colloid Polym. Sci.* **1988**, *266*, 608.

2.50 Vittoria, V. *J. Macromol. Sci. Phys.* **1989**, *B28(2&3)*, 489.

2.51 Song, Y.; Nitta, K.; Nemoto, N. *Macromolecules* **2003**, *36*, 1955.

2.52 Nozue, Y.; Shinohara, Y.; Ogawa, Y.; Sakurai, T.; Hori, H.; Kasahara, T.; Yamaguchi, N.; Yagi, N.; Amemiya, Y *Macromolecules* **2007**, *40*, 2036.

2.53 Sakurai, T.; Nozue, Y.; Kasahara, T.; Mizunuma, K.; Yamaguchi, N.; Tashiro, K.; Amemiya, Y. *Polymer* **2005**, *46*, 8846.

2.54 Koike, Y.; Cakmak, M. *Macromolecules* **2004**, *37*, 2171.

2.55 Koike, Y.; Cakmak, M. *Polymer* **2003**, *44*, 4249.

2.56 Koike, Y.; Cakmak, *J. Polym. Sci., Polym. Phys.* **2006**, *44*, 925.

2.57 Li, J. X.; Cheung, W. L.; Chan, C. M. *Polymer* **1999**, *40*, 3641.

2.58 Li, J. X.; Cheung, W. L.; Chan, C. M. *Polymer* **1999**, *40*, 2089.

2.59 Aboulfaraj, M.; G'Sell, C.; Ulrich, B.; Dahoun, A. *Polymer* **1995**, *36*, 731.

2.60 Zhang, X. C.; Butler, M. F.; Cameron, R. E. *Polymer* **2000**, *41*, 3797.

2.61 Chu, F.; Yamaoka, T.; Kimura, Y. *Polymer* **1995**, *36*, 2523.

2.62 Huy, T. A.; Adhikari, R.; Lupke, T.; Henning, S.; Michler, G. H. *J. Polym. Sci., Polym. Phys.* **2004**, *42*, 4478.

2.63 Hong, K.; Strobl, G. *Macromolecules* **2006**, *39*, 268.

2.64 Wu, J. *Polymer* **2003**, *44*, 8033.

2.65 Aerts, J. *J. Appl. Cryst.* **1991**, *24*, 709.

2.66 Wu, J.; Schultz, J. M.; Yeh, F.; Hsiao, B. S.; Chu, B. *Macromolecules* **2002**, *33*, 1765.

2.67 Fraser, R. D. B.; Macrae, T. P.; Miller, A.; Rowlands, R. J. *J. Appl. Cryst.* **1976**, *9*, 81.

2.68 Ran, S.; Zong, X.; Fang, D.; Hsiao, B. S.; Chu, B.; Ross, R. *J. Appl. Cryst.* **2000**, *33*, 1031.

2.69 Dukovski, I.; Muthukumar, M. *J. Chem. Phys.* **2003**, *118*, 6648.

2.70 Wilchinsky, W. Z. *J. Appl. Phys*. **1960**, *31*, 1969.

3.1 Keller, A.; Kolnaar, H. W. H. *Processing of Polymers*, **1997**, 18, 189-268.

3.2 Kornfield, J. A.; Kumaraswamy, G.; Issaian, A. M. *Ind. Eng. Chem. Res.*, **2002**, 41, 6383-6392.

3.3 Somani, R. H.; Yang, L.; Zhu, L.; Hsiao, B. S. *Polymer*, **2005**, 46, 8587-8623.

3.4 Pople, J. A.; Mitchell, G. R.; Chai, C. K.; *Polymer*, **1996**, 37, 4187-4191.

3.5 Androsch, R. *Polymer*, **1999**, 40, 2805-2812.

3.6 Stribeck, N; Camarillo, A. A.; Cunis, S.; Bayer, R. K.; Gehrke, R. *Macromol. Chem. Phys.*, **2004**, 205, 1445-1454.

3.7 Fukushima, H.; Ogino, Y.; Matsuba, G.; Nishida, K.; Kanaya, T. *Polymer*, **2005**, 46, 1878-1885.

3.8 Crist, B.; Howard, P. R. *Macromolecules*, **1999**, 32, 3057-3067.

3.9 Hu, W.; Srinivas, S.; Sirota, E. B. *Macromolecules*, **2002**, 35, 5013-5024.

3.10 Matsuba, G.; Shimizu, K.; Wang, H.; Wang, Z.; Han, C. C. *Polymer*, **2003**, 44, 7459-7465.

3.11 Silvestre, C.; Cimmino, S.; Triolo, R. *J. Polym. Sci.: Part B: Polym. Phys.*, **2003**, 41, 493-500.

3.12 Hafele, A.; Heck, B.; Kawai, T.; Kohn, P.; Strobl, G. *Eur. Phys, J. E*, **2005**, 16, 207-216.

3.13 Kim, M.; Phillips, P. J. *J Appl. Polym. Sci.*, **1998**, 70, 1893-1905.

3.14 Alizadeh, A.; Richardson, L.; Xu, J.; McCartney, S.; Marand, H.; Cheung, Y. W.; Chum, S. *Macromolecules*, **1999**, 32 6221-6235.

3.15 Zhang, M.; Lynch, D. T.; Wanke, S. E. *Polymer*, **2001**, 42, 3067-3075.

3.16 Zhang, F.; Liu, J.; Xie, F.; Fu, Q.; He, T. *J. Polym. Sci.: Part B: Polym. Phys.*, **2002**, 40, 822-830.

3.17 Bustos, F.; Cassagnau, P.; Fulchiron, R. *J. Polym. Sci.: Part B: Polym. Phys.*, **2006**, 44, 1597-1607.

3.18 Rangarajan, P.; Register, R. A.; Adamson, D. H.; Fetters, L. J.; Bras, W.; Naylor, S.; Ryan, A. J. *Macromolecules*, **1995**, 28, 1422-1428.

3.19 Rangarajan, P.; Register, R. A.; Fetters, L. J.; Bras, W.; Naylor, S.; Ryan, A. J. *Macromolecules*, **1995**, 28, 4932-4938.

3.20 Ryan, A. J.; Hamley, I. W.; Bras, W.; Bates, F. S. *Macromolecules*, **1995**, 28, 3860-3868.

3.21 Hamley, I. W.; Fairclough, J. P. A.; Ryan, A. J.; Bates, F. S.; Towns-Andrews, E. *Polymer*, **1996**, 37, 4425-4429.

3.22 Hamley, I. W.; Fairclough, J. P. A.; Bates, F. S.; Ryan, A. J. *Polymer*, **1998**, 39, 1429-1437.

3.23 Flory, P. J. *Principles of polymer chemistry*, Cornell University Press, **1953**, Ithaca.

3.24 Hamley, I. W.; *The Physics of Block Copolymers*, Oxford University Press, **1998**, Oxford.

3.25 Arriola, D. J.; Carnahan, E. M.; Hustad, P. D.; Kuhlman, R. L.; Wenzel, T. T. *Science*, **2006**, 312, 714-719.

3.26 Khariwala, D. U.; Taha, A.; Chum, S. P.; Hiltner, A.; Baer, E. *Polymer*, **2008**, 1365-1375.

4.1 Arriola, D. J.; Carnahan, E. M.; Hustad, P. D.; Kuhlman, R. L.; Wenzel, T. T. *Science*, **2006**, *312*, 714-719.

4.2 Arriola, D. J.; Carnahan, E. M.; Cheung, Y. W.; Devore, D. D.; Graf, D. D.; Hustad, P. D.; Kuhlman, R. L.; Shan, C. L. P.; Poon, B. C.; Roof, G. R.; Stevens, J. C.; Stirn, P. J.; Wenzel, T. T. Catalyst composition comprising shuttling agent for ethylene multi-block copolymer formation. *WO*, **2005090427**, *2005-US8917*.

4.3 Wang, H. P.; Khariwala, D. U.; Cheung, W.; Chum, S. P.; Hiltner, A.; Baer, E. *Macromolecules*, **2007**, *40*, 2852-2862.

4.4 Androsch, R.; Blackwell, J.; Chvalun, S. N.; Wunderlich, B. *Macromolecules*, **1999**, *32*, 3735-3740.

4.5 Androsch, R.; Stribeck, N.; Lupke, T.; Funari, S. S. *J Polym. Sci. Part B: Polym. Phys.*, **2002**, *40*, 1919-1930.

4.6 Androsch, R.; Wunderlich, B.; Lupke, T.; Wutzler, A. *J Polym. Sci. Part B: Polym. Phys.*, **2002**, *40*, 1223-1235.

4.7 Shan, H.; White J. *Plastics, Rubber and Composites*, **2006**, *35*, 155-164.

4.8 Hu, W.; Srinivas, S.; Sirota, E. B. *Macromolecules*, **2002**, *35*, 5013-5024.

4.9 Hu, W.; Sirota, E. B. *Macromolecules*, **2003**, *36*, 5144-5149.

4.10 Bensason, S.; Stepanov, E. V.; Chum, S.; Hiltner, A.; Baer, E. *Macromolecules*, **1997**, *30*, 2436-2444.

4.11 Eynde, S. V.; Rastogi, S.; Mathot, V. B. F.; Reynaers, H. *Macromolecules*, **2000**, *33*, 9696-9704.

4.12 Chen, X.; Yoon, K.; Burger, C.; Sics, I.; Fang, D.; Hsiao, B. S.; Chu, B. *Macromolecules*, **2005**, *38*, 3883-3893.

4.13 Kiho, H.; Peterlin, A.; Geil, P. H. *J. Appl. Phys.*, **1964**, *35*, 1599-1605.

4.14 Kiho, H.; Peterlin, A.; Geil, P. H. *Polym. Lett.*, **1965**, *3*, 157-160.

4.15 Seto, T.; Hara, T.; Tanaka, K.; *Japan. J. Appl. Phys.*, **1968**, *7*, 31-42.

4.16 Takahashi, Y.; Ishida, T. *J Polym. Sci. Part B: Polym. Phys.*, **1988**, *26*, 2267-2277.

4.17 Whttmann, J. C.; Lotz, B. *Polymer*, **1989**, *30*, 27-34.

4.18 Russell, K. E.; Hunter, B. K.; Heyding, R. D. *Polymer*, **1997**, *38*, 1409-1414.

4.19 Shan, H.; White, J. L. *Intern. Polymer Processing XXI*, **2006**, *4*, 361-373.

4.20 Zuo, F.; Keum, J. K.; Chen, X. M.; Hsiao, B. S.; Chen, H. Y.; Lai, S. Y.; Wevers, R.; Li, J. *Polymer*, Accepted.

4.21 Wilchinsky, W. Z. *J. Appl. Phys*. **1960**, *31*, 1969.

5.1 Holden, G.; Kricheldorf, H. R.; Quirk, R. P. *Thermoplastic elastomers* 3rd edition; Munich: Hanser, **2004**.

5.2 Holden, G. *J Elastoplastics* **1970**, *2*, 234-246.

5.3 Hepburn, C. *Polyurethane Elastomers* 2nd edition; Elsevier Applied Science: London, **1991**.

5.4 Wirpsza, Z. *Polyurethanes: Chemistry, Technology and Application*; Horwood: New York, **1993**.

5.5 Abdou-Sabet, S.; Puydak, R. C.; Rader, C. P. *Rubber Chem. Tech.* **1996**, *69*, 476-494.

5.6 Batistini, A. *Macromol. Symp.* **1995**, *100*, 137-142.

5.7 Arriola, D. J.; Carnahan, E. M.; Hustad, P. D.; Kuhlman, R. L.; Wenzel, T. T. *Science* **2006**, *312*, 714-719.

5.8 Wang, H. P.; Khariwala, D. U.; Cheung, W.; Chum, S. P.; Hiltner, A.; Baer, E. *Macromolecules* **2007**, *40*, 2852-2862.

5.9 Khariwala, D. U.; Taha, A.; Chum, S. P.; Hiltner, A.; Baer, E. *Polymer* **2008**, *49*, 1365-1375.

5.10 Martin, D. J.; Meijs, G. F.; Renwick, G. M.; McCarthy, S. J.; Gunatillake, P. A. *J. Appl. Polym. Sci.,* **1996**, *62*, 1377-1386.

5.11 Martin, D. J.; Meijs, G. F.; Gunatillake, P. A.; McCarthy, S. J.; Renwick, G. M. *J. Appl. Polym. Sci.,* **1997**, *64*, 803-817.

5.12 Gisselfalt, K.; Helgee, B. *Macromol. Mater. Eng.* **2003**, *288*, 265-271.

5.13 Chu, B.; Gao, T.; Li, Y.; Wang, J.; Desper, C. R.; Byrne, C. A. *Macromolecules* **1992**, *25*, 5724-5729.

5.14 Kong, X.; Tan, S.; Yang, X.; Li, G.; Zhou, E.; Ma, D. *J Polym. Sci. Part B: Polym. Phys.*, **2000**, *38*, 3230-3238.

5.15 Miller, J. A.; Lin, S. B.; Hwang, K. K. S.; Wu, K. S.; Gibson, P. E.; Cooper, S. L. *Macromolecules* **1985**, *18*, 32-44.

5.16 Versteegen, R. M.; Kleppinger, R.; Sijbesma, R. P.; Meijer, E. W. *Macromolecules* **2006**, *39*, 772-783.

5.17 Amitay-Sadovsky, E.; Komvopoulos, K.; Ward, R.; Somorjai, G. A. *Appl. Phys. Lett.* **2003**, *83*, 3066-3068.

5.18 Chen, S.; Hu, J.; Liu, Y.; Liem, H.; Zhu, Y.; Liu, Y. *J Polym. Sci. Part B: Polym. Phys.* **2007**, *45*, 444-454.

5.19 Kim, B. K.; Shin, Y. J.; Cho, S. M.; Jeong, H. M. *J Polym. Sci. Part B: Polym. Phys.* **2000**, *38*, 2652-2657.

5.20 O'sickey, M. J.; Lawrey, B. D.; Wilkes, G. L. *J. Appl. Polym. Sci,* **2002**, *84*, 229-243.

5.21 Puskas, J. E.; Antony, P.; Fray, M. E.; Altstadt, V. *Euro. Poly. J.* **2003**, *39*, 2041-2049.

5.22 Wilchinsky, W. Z. J. Appl. Phys. 1960, 31, 1969.

6.1 Bensason, S.; Stepanov, E. V.; Chum, S.; Hiltner, A.; Baer, E. *Macromolecules*, **1997**, 30, 2436-2444.

6.2 Androsch, R.; Stribeck, N.; Lupke, T.; Funari, S. S. *J. Polym. Sci.: Part B: Polym. Phys.*, **2002**, 40, 1919-1930.

6.3 Liu, L.; Hsiao, B. S.; Fu, B. X.; Ran, S.; Toki, S.; Chu, B.; Tsou, A. H.; Agarwal, P. K. *Macromolecules*, **2003**, 36, 1920-1929.

6.4 Men, Y.; Rieger, J.; Strobl, G. *Phys. Rev. Lett.*, **2003**, 91, 095502-1-4.

6.5 Schrauwen, B. A. G.; Janssen, R. P. M.; Govaert, L. E.; Meijer, H. E. H. *Macromolecules*, **2004**, 37, 6069-6078.

6.6 Shan, H.; White, J. L. *J. Appl. Polym. Sci.*, **2004**, 93, 9-22.

6.7 Shan, H.; White, J. L. *Plastics, Rubber and Composites*, **2006**, 35, 155-164.

6.8 Hong, K.; Strobl, G. *Macromolecules*, **2006**, 39, 268-273.

6.9 Kennedy, M. A.; Peacock, A. J.; Failla, M. D.; Lucas, J. C.; Mandelkern, L. *Macromolecules*, **1995**, 28, 1407-1421.

6.10 Fatou, J. G.; Macia, I. G.; Macro, C.; Gomez, M. A.; Arribas, J. M.; Fontecha, A.; Aroca, M.; Martinez, M. C. *J Mater. Sci.*, **1996**, 31, 3095-3107.

6.11 Chum, P. S.; Kruper, W. J.; Guest, M. *J. Adv. Mater.*, **2000**, 12, 1759-1767.

6.12 Chum, P. S.; Swogger, K. W. *Prog. Polym. Sci.*, **2008**, 33, 797-819.

6.13 Arriola, D. J.; Carnahan, E. M.; Hustad, P. D.; Kuhlman, R. L.; Wenzel, T. T. *Science*, **2006**, 312, 714-719.

6.14 Kiho, H.; Peterlin, A.; Geil, P. H. *J. Appl. Phys.*, **1964**, 35, 1599-1605.

6.15 Kiho, H.; Peterlin, A.; Geil, P. H. *Polym. Lett.*, **1965**, 3, 157-160.

6.16 Seto, T.; Hara, T.; Tanaka, K. Jap. *J. Appl. Phys.*, **1968**, 7, 31-42.

6.17 Hendra, P. J.; Taylor, M. A.; Willis, H. A. *Polymer*, **1985**, 26, 1501-1506.

6.18 Tashiro, K.; Sasaki, S.; Kobayashi, M. *Macromolecules*, **1996**, 29, 7460-7469.

6.19 Androsch, R.; Blackwell, J.; Chvalun, S. N.; Wunderlich, B. *Macromolecules*, **1999**, 32, 3735-3740.

6.20 Kuwabara, K.; Horii, F. *Macromolecules*, **1999**, 32, 5600-5605.

6.21 Hu, W.; Srinivas, S.; Sirota, E. B. *Macromolecules*, **2002**, 35, 5013-5024.

6.22 Hu, W.; Sirota, E. B. *Macromolecules*, **2003**, 36, 5144-5149.

6.23 Liu, L.; Hsiao, B. S.; Ran, S.; Fu, B. X.; Toki, S.; Zuo, F.; Tsou, A. H.; Chu, B. *Polymer*, **2006**, 47, 2884-2893.

6.24 Takahashi, Y.; Ishida, T. *J. Polym. Sci.: Part B: Polym. Phys.*, **1988**, 26, 2267-2277.

6.25 Wittmann, J. C.; Lotz, B. *Polymer*, **1989**, 30, 27-34.

6.26 Russell, K. E.; Hunter, B. K.; Heyding, R. D. *Polymer*, **1997**, 38, 1409-1414.

7.1 Lazar, M.; Rado, R.; Rychly, J. *Adv. Polym. Sci.*, **1990**, 95, 149-197.

7.2 Jiao, C.; Wang, Z.; Gui, Z.; Hu, Y. *Eur. Polym. J.*, **2005**, 41, 1204.

7.3 Manley, T. R.; Qayyum. M. M. *Polymer*, **1972**, 13, 587-592.

7.4 Robertson, M. B.; Ward, I. M.; Klein, P. G.; Packer, K. J. *Macromolecules*, **1997**, 30, 6893-6898.

7.5 Rizzo, P.; Baione, F.; Guerra, G.; Martinotto, L.; Albizzati, E. *Macromolecules*, **2001**, 34, 5175-5179.

7.6 Khonakdar, H. A.; Morshedian, J.; Wagenknecht, U.; Jafari, S. H. *Polymer*, **2003**, 44, 4301-4309.

7.7 Khonakdar, H. A.; Jafari, S. H.; Wagenknecht, U.; Jehnichen, D. *Rad. Phys. Chem.*, **2006**, 75, 78-86.

7.8 Sirisinha, K.; Chimdist, S. *J. Appl. Polym. Sci.*, **2008**, 109, 2522-2528.

7.9 Phillips, P. J.; Kao, Y. H. *Polymer*, **1986**, 27, 1679-1686.

7.10 Lambert, W. S.; Phillips, P. J. *Polymer*, **1990**, 31, 2077-2082.

7.11 Lambert, W. S.; Phillips, P. J.; Lin, J. S. *Polymer*, **1994**, 35, 1809-1818.

7.12 Klein, P. G.; Gonzalez-Orozco, J. A.; Ward, I. M. *Polymer*, **1994**, 35, 2044-2048.

7.13 Andersson, L. H. U.; Hjertberg, T. *Polymer*, **2006**, 47, 200-210.

7.14 Cerrada, M. L.; Benavente, R.; Fernandez-Garcia, M.; Perez, E.; Campos, J. M. ; Ribeiro, M. R. *Polymer*, **2009**, 50, 1095-1102.

7.15 Chodak, I. *Prog. Polym. Sci.*, **1995**, 20, 1165-1199.

7.16 Chodak, I. *Prog. Polym. Sci.*, **1998**, 23, 1409-1442.

7.17 Sirisinha, K.; Meksawat, D. *J. Appl. Polym. Sci.*, **2004**, 93, 901-906.

7.18 Sirisinha, K.; Meksawat, D. *J. Appl. Polym. Sci.*, **2004**, 93, 1179-1185.

7.19 Kamphunthong, W.; Sirisinha, K. *J. Appl. Polym. Sci.*, **2008**, 109, 2347-2353.

7.20 Mishra, J. K.; Chang, Y. W.; Lee, B. C. ; Ryu, S. H. *Rad. Phys. Chem.*, **2008**, 77, 675-679.

7.21 Nicolas, J.; Ressia, J. A.; Valles, E. M.; Merino, J. C.; Pastor, J. M. *J. Appl. Polym. Sci.*, **2009**, 112, 2691-2700.

7.22 Khonakdar, H. A.; Jafari, S. H.; Taheri, M. ; Wagenknecht, U.; Jehnichen, D.; Haussler, L. *J. Appl. Polym. Sci.*, **2006**, 100, 3264-3271.

7.23 Turcsanyi, B.; Fekete, E.; Pukanszky, B.; Tabor, I. *J. Thermal Anal.*, **1990**, 36, 1775-1784.

7.24 Ke, Q.; Huang, X.; Wei, P.; Wang, G.; Jiang, P. *J. Appl. Polym. Sci.*, **2007**, 104, 1920-1927.

7.25 Matsuo, M.; Sawatari, C. *Macromolecules*, **1986**, 19, 2028-2035.

7.26 Narkis, M.; Raiters, I.; Shkolnik, S.; Siegmann, A. Eyerer, P. *J. Macromol. Sci. Phys.*, **1987**, B26(1), 37-58.

7.27 van der Sanden, M. C. M.; Meijer, H. E. H. *Polymer*, **1993**, 34, 5063-5072.

7.28 Krupa, I.; Luyt, A. S. *J. Appl. Polym. Sci.*, **2001**, 81, 973-980.

7.29 Bocok, T.; Zicans, J.; Kalnins, M. *Mecha. Compos. Mat.*, **2005**, 41, 161-170.

7.30 Zhang, G.; Wang, G.; Zhang, J.; Wei, P.; Jiang, P. *J. Appl. Polym. Sci.*, **2006**, 102, 5057-5061.

7.31 Ali, Z.; Youssef, H.; Afify, T. *Polym. Compos.*, **2008**, 29, 1119-1124.

7.32 Nicolas, J.; Ressia, J. A.; Valles, E. M.; Merino, J. C.; Pastor, J. M. *J. Appl. Polym. Sci.*, **2009**, 112, 2691-2700.